



OFFICE OF THE DIRECTOR
CENTER FOR ADVANCED COMMUNICATIONS

March 20, 2018

Defense Technical Information Center
8725 John J Kingman Road Ste 0944
Fort Belvoir, VA 22060-6218

NOTE: Final Technical Report with SF298

Dear Sir/Madam,

Enclosed please find the Final ONR report of the project titled Co-Prime Frequency and Aperture Design for HF Surveillance, Wideband Radar Imaging, and Nonstationary Array Processing (Grant No. N00014-13-1-0061) which spanned the period from 01/01/2013 to 12/31/2017.

Regards,

Dr. Moeness Amin, PI
Director, Center for Advanced Communications
Professor, Electrical & Computer Engineering



Center for Advanced Communications

Villanova University

FINAL TECHNICAL REPORT

(1/1/2013 – 12/31/2017)

**Co-Prime Frequency and Aperture Design for HF Surveillance,
Wideband Radar Imaging, and Nonstationary Array Processing**

(Grant No. N00014-13-1-0061)

Submitted to

Office of Naval Research

Principal Investigators

Moeness G. Amin
Fauzia Ahmad
Yimin D. Zhang

March 2018

Table of Contents

1. Executive Summary	1
1.1. Generalized Co-Prime Array Design	1
1.2. Wideband DOA Estimation and Radar Sensing	2
1.3. Active Sensing Using Co-Prime Array	2
1.4. Mutual Coupling Effect and Reduction	2
1.5. Spectrum Estimation Based on Co-Prime Sampling	3
1.6 References	3
2. List of Publications	5
3. Selected Publications	9
3.1. Generalized coprime array configurations for direction-of-arrival estimation	10
3.2. Multi-frequency co-prime arrays for high-resolution direction-of-arrival estimation	43
3.3. DOA estimation exploiting a uniform linear array with multiple co-prime frequencies	76
3.4. Frequency diverse coprime arrays with coprime frequency offsets for multi-target localization	100
3.5. Sparsity-based direction finding of coherent and uncorrelated targets using active nonuniform arrays.....	136
3.6. Mutual coupling effect and compensation in non-uniform arrays for direction-of-arrival estimation	149
3.7. Generalized coprime sampling of Toeplitz matrix for spectrum estimation	180

Co-Prime Frequency and Aperture Design for HF Surveillance, Wideband Radar Imaging, and Nonstationary Array Processing

1. Executive Summary

This report presents the results of the research performed under Office of Naval Research (ONR) grant number N00014-13-1-0061 over the period of January 1, 2013 to December 31, 2017. The research team working on this project consists of Prof. Moeness Amin (PI, Villanova University), Prof. Yimin D. Zhang (Co-PI, Villanova University; moved to Temple University in 2015), and Prof. Fauzia Ahmad (Co-PI, Villanova University; moved to Temple University in 2016). This project supported two full-time Ph.D. students, Si Qin and Elie BouDaher, at Villanova University. We have also collaborated with Prof. Ahmad Hoorfar (Villanova University), Prof. Abdelhak M. Zoubir (Darmstadt University of Technology, Germany), Prof. Fulvio Gini (University of Pisa, Italy), Prof. Elias Aboutanios (University of New South Wales, Australia), Prof. Wei Liu (University of Sheffield, United Kingdom), Prof. Panos Markopoulos (Rochester Institute of Technology), and Prof. Xiangrong Wang (Beihang University, China).

The research objectives are to develop novel co-prime sampling and array design strategies that achieve high-resolution estimation of spectral power distributions and signal direction-of-arrivals (DOAs), and their applications in various surveillance, radar imaging applications, and array processing. The focus of our studies has been in the following five areas: (i) Generalized co-prime array design; (ii) Wideband DOA estimation and radar sensing; (iii) Active sensing using co-prime arrays; (iv) Mutual coupling effect and mitigation; (v) Spectrum estimation based on co-prime sampling. These efforts resulted in 12 journal papers and 27 conference papers.

Below is a summary of the research accomplishments in each of these individual areas. A list of the publications generated under the support of this project is provided in Section 2. The full text of selected journal publications are included in Section 3.

1.1. Generalized Co-Prime Array Design

A co-prime array uses two uniform linear subarrays to construct an effective difference coarray with certain desirable characteristics, such as a high number of degrees-of-freedom for DOA estimation. We have generalized the co-prime array concept with two operations [1]. The first operation is through the compression of the inter-element spacing of one subarray and the resulting structure treats the existing variations of co-prime array configurations as well as the nested array structure as its special cases. The second operation exploits two displaced subarrays, and the resulting co-prime array structure allows the minimum inter-element spacing to be much larger than the typical half-wavelength requirement, making them useful in applications where a small interelement spacing is infeasible. We have derived the analytical expressions for the coarray aperture, the achievable number of unique lags, and the maximum number of consecutive lags for quantitative evaluation, comparison, and design of co-prime arrays.

1.2. Wideband DOA Estimation and Radar Sensing

The co-prime array, which utilizes a co-prime pair of uniform linear sub-arrays, provides a systematical means for sparse array construction. On the other hand, utilizing spectrum bandwidth in co-prime array can achieve a number of advantages. (a) Utilizing multiple frequencies equivalently provides multiple virtual arrays to achieve a higher number of degrees of freedom; (b) Fusing multi-frequency signals improves the robustness of DOA estimation; and (c) The use of signal bandwidth and co-prime array provides DOA-range resolution for target localization. In one of our proposed schemes [2], a co-prime array is operated at multiple frequencies in order to fill the missing coarray elements, thereby enabling the co-prime array to form consecutive coarray lags and effectively utilize all of the offered degrees of freedom (DOFs) with subspace based DOA estimation methods. In another proposed scheme [3], a single sparse uniform linear array is used to exploit two or more continuous-wave signals whose frequencies satisfy a co-prime relationship. This extends the co-prime array and filtering to a joint spatio-spectral domain, thereby achieving high flexibility in array structure design to meet system complexity constraints. The DOA estimation is obtained using group sparsity-based compressive sensing techniques. The achievable number of DOFs is derived for the two-frequency case, and an upper bound of the available DOFs is provided for multi-frequency scenarios. In the third scheme [4], we considered the frequency diverse array (FDA) radar which offers a range-dependent beampattern capability. The spatial and range resolutions of an FDA radar are fundamentally limited by the array geometry and the frequency offset. We overcome this limitation by introducing a novel sparsity-based multi-target localization approach incorporating both coprime arrays and coprime frequency offsets. The covariance matrix of the received signals corresponding to all sensors and employed frequencies is formulated to generate a space-frequency virtual difference coarrays. The joint DOA and range estimation is cast as a two-dimensional sparse reconstruction problem and is solved within the Bayesian compressive sensing framework. The superiority of the proposed approach in terms of DOA-range resolution, localization accuracy, and the number of resolvable targets were evidently demonstrated.

1.3. Active Sensing Using Co-Prime Array

We performed DOA estimation of a mixture of coherent and uncorrelated targets using sparse reconstruction and active nonuniform arrays [5]. The data measurements from multiple transmit and receive elements can be considered as observations from the sum coarray corresponding to the physical transmit/receive arrays. The vectorized covariance matrix of the sum coarray observations emulates the received data at a virtual array whose elements are given by the difference coarray of the sum coarray. Sparse reconstruction is used to fully exploit the significantly enhanced degrees-of-freedom offered by the difference coarray of the sum coarray for DOA estimation. Simulated data from multiple-input multiple-output minimum redundancy arrays and transmit/receive co-prime arrays were used for performance evaluation of the proposed sparsity-based active sensing approach.

1.4. Mutual Coupling Effect and Reduction

We have investigated the effect of mutual coupling on DOA estimation using non-uniform arrays

[6]. We compared and contrasted the DOA estimation accuracy in the presence of mutual coupling for three different non-uniform array geometries, namely, minimum redundancy arrays, nested arrays, and co-prime arrays, and for two antenna types, namely dipole antennas and microstrip antennas. We demonstrated through numerical simulations that the mutual coupling, if unaccounted for, can, in general, lead to performance degradation, with the minimum redundancy array faring better against mutual coupling than the other two non-uniform structures for both antenna types. We also proposed two methods that can compensate for the detrimental effects of mutual coupling, leading to accurate and reliable DOA estimation.

1.5. Spectrum Estimation Based on Co-Prime Sampling

Increased demand on spectrum sensing over a broad frequency band requires a high sampling rate and thus leads to a prohibitive volume of data samples. In some applications, such as spectrum estimation, only the second-order statistics are required. In this case, we may use a reduced data sampling rate by exploiting a low-dimensional representation of the original high dimensional signals. In particular, the covariance matrix can be reconstructed from compressed data by utilizing its specific structure, e.g., the Toeplitz property. Among a number of techniques for compressive covariance sampler design, the coprime sampler is considered attractive because it enables a systematic design capability with a significantly reduced sampling rate. We have proposed a general coprime sampling scheme that implements effective compression of Toeplitz covariance matrices [7]. Given a fixed number of data samples, we examined different schemes on covariance matrix acquisition for performance evaluation, comparison and optimal design, based on segmented data sequences.

1.6. References

- [1] S. Qin, Y. D. Zhang, and M. G. Amin, "Generalized coprime array configurations for direction-of-arrival estimation," *IEEE Transactions on Signal Processing*, vol. 63, no. 6, pp. 1377-1390, March 2015.
- [2] E. BouDaher, Y. Jia, F. Ahmad, and M. G. Amin, "Multi-frequency co-prime arrays for high-resolution direction-of-arrival estimation," *IEEE Transactions on Signal Processing*, vol. 63, no.14, pp. 3797–3808, July 2015.
- [3] S. Qin, Y. D. Zhang, M. G. Amin, and B. Himed, "DOA estimation exploiting a uniform linear array with multiple co-prime frequencies," *Signal Processing*, vol. 130, pp. 37-46, Jan. 2017.
- [4] S. Qin, Y. D. Zhang, M. G. Amin, and F. Gini, "Frequency diverse coprime arrays with coprime frequency offsets for multi-target localization," *IEEE Journal of Selected Topics in Signal Processing*, vol. 11, no. 2, pp. 321-335, March 2017.
- [5] E. BouDaher, F. Ahmad, and M. G. Amin, "Sparsity-based direction finding of coherent and uncorrelated targets using active nonuniform arrays," *IEEE Signal Processing Letters*, vol. 22, no. 10, pp. 1628–1632, Oct. 2015.

- [6] E. BouDaher, F. Ahmad, M. G. Amin, and A. Hoorfar, "Mutual coupling effect and compensation in non-uniform arrays for direction-of-arrival estimation," *Digital Signal Processing*, vol. 61, pp. 3-14, Feb. 2017.
- [7] S. Qin, Y. D. Zhang, M. G. Amin, and A. Zoubir, "Generalized coprime sampling of Toeplitz matrix for spectrum estimation," *IEEE Transactions on Signal Processing*, vol. 65, no. 1, pp. 81-94, Jan. 2017.

2. List of Publications

Note that the full manuscripts of the papers listed in the bold font are included in Chapter 3.

Journal Articles

1. **S. Qin, Y. D. Zhang, and M. G. Amin, “Generalized coprime array configurations for direction-of-arrival estimation,” *IEEE Transactions on Signal Processing*, vol. 63, no. 6, pp. 1377-1390, March 2015.**
2. S. Qin, Y. D. Zhang, Q. Wu, and M. G. Amin, “Structure-aware Bayesian compressive sensing for near-field source localization based on sensor-angle distributions,” *International Journal on Antennas and Propagation*, vol. 2015, article ID 783467, March 2015.
3. **E. BouDaher, Y. Jia, F. Ahmad, and M. G. Amin, “Multi-frequency co-prime arrays for high-resolution direction-of-arrival estimation,” *IEEE Transactions on Signal Processing*, vol. 63, no.14, pp. 3797–3808, July 2015.**
4. Q. Shen, W. Liu, W. Cui, S. Wu, Y. D. Zhang, and M. G. Amin, “Low-complexity wideband direction-of-arrival estimation based on co-prime arrays,” *IEEE/ACM Transactions on Audio, Speech and Language Processing*, vol. 23, no. 9, pp. 1445-1456, Sept. 2015.
5. **E. BouDaher, F. Ahmad, and M. G. Amin, “Sparsity-based direction finding of coherent and uncorrelated targets using active nonuniform arrays,” *IEEE Signal Processing Letters*, vol. 22, no. 10, pp. 1628–1632, Oct. 2015.**
6. **S. Qin, Y. D. Zhang, M. G. Amin, and A. Zoubir, “Generalized coprime sampling of Toeplitz matrix for spectrum estimation,” *IEEE Transactions on Signal Processing*, vol. 65, no. 1, pp. 81-94, Jan. 2017.**
7. Q. Shen, W. Liu, W. Cui, S. Wu, Y. D. Zhang, and M. G. Amin, “Focused compressive sensing for underdetermined wideband DOA estimation exploiting high-order difference co-arrays,” *IEEE Signal Processing Letters*, vol. 24, no. 1, pp. 86-90, Jan. 2017.
8. **S. Qin, Y. D. Zhang, M. G. Amin, and B. Himed, “DOA estimation exploiting a uniform linear array with multiple co-prime frequencies,” *Signal Processing*, vol. 130, pp. 37-46, Jan. 2017.**
9. S. Qin, Y. D. Zhang, and M. G. Amin, “DOA estimation of mixed coherent and uncorrelated targets exploiting coprime MIMO radar,” *Digital Signal Processing*, special issue on Coprime Array and Sampling, vol. 61, pp. 26-34, Feb. 2017.
10. **E. BouDaher, F. Ahmad, M. G. Amin, and A. Hoorfar, “Mutual coupling effect and compensation in non-uniform arrays for direction-of-arrival estimation,” *Digital Signal Processing*, vol. 61, pp. 3-14, Feb. 2017.**
11. **S. Qin, Y. D. Zhang, M. G. Amin, and F. Gini, “Frequency diverse coprime arrays with coprime frequency offsets for multi-target localization,” *IEEE Journal of***

Selected Topics in Signal Processing, vol. 11, no. 2, pp. 321-335, March 2017.

12. X. Wang, M. G. Amin, F. Ahmad, and E. Aboutanios, "Interference DOA estimation and suppression for GNSS receivers using fully augmentable arrays," *IET Radar, Sonar, & Navigation*, vol. 11, no. 3, pp. 474 – 480, March 2017.

Conference Papers

1. Y. D. Zhang, M. G. Amin, and B. Himed, "Sparsity-based DOA estimation using co-prime arrays," *IEEE International Conference on Acoustics, Speech, and Signal Processing*, Vancouver, Canada, May 2013.
2. Y. D. Zhang, M. G. Amin, F. Ahmad, and B. Himed, "DOA estimation using a sparse uniform linear array with two CW signals of co-prime frequencies," *IEEE International Workshop on Computational Advances in Multi-Sensor Adaptive Processing*, Saint Martin, Dec. 2013.
3. S. Qin, Y. D. Zhang, and M. G. Amin, "DOA estimation exploiting coprime frequencies," *SPIE Wireless Sensing, Localization, and Processing Conference*, Baltimore, MD, May 2014.
4. Y. D. Zhang, S. Qin, and M. G. Amin, "DOA estimation exploiting coprime arrays with sparse sensor spacing," *IEEE International Conference on Acoustics, Speech, and Signal Processing*, Florence, Italy, May 2014.
5. S. Qin, Y. D. Zhang, and M. G. Amin, "Generalized coprime array configurations," *IEEE Sensor Array and Multichannel Signal Processing Workshop*, A Coruna, Spain, June 2014.
6. Q. Shen, W. Liu, W. Cui, S. Wu, Y. D. Zhang, and M. G. Amin, "Group sparsity based wideband DOA estimation for co-prime arrays," *IEEE China Summit and International Conference on Signal and Information Processing*, Xi'an, China, July 2014.
7. E. BouDaher, Y. Jia, F. Ahmad, and M. G. Amin, "Direction-of-arrival estimation using multi-frequency co-prime arrays," *European Signal Processing Conference*, Lisbon, Portugal, pp. 1034–1038, Sept. 2014.
8. S. Qin, Y. D. Zhang, and M. G. Amin, "DOA estimation of mixed coherent and uncorrelated signals exploiting a nested MIMO system," *IEEE Benjamin Franklin Symposium on Microwave and Antenna Sub-systems*, Philadelphia, PA, Sept. 2014. (**First Prize of Student Paper Competition**)
9. S. Qin, Q. Wu, Y. D. Zhang, and M. G. Amin, "DOA estimation of nonparametric spreading spatial spectrum based on Bayesian compressive sensing exploiting intra-task dependency," *IEEE International Conference on Acoustics, Speech, and Signal Processing*, Brisbane, Australia, April 2015.
10. X. Wang, M. G. Amin, F. Ahmad, and E. Aboutanios, "Bayesian compressive sensing For DOA estimation using the difference coarray," *IEEE International Conference on Acoustics, Speech, and Signal Processing*, Brisbane, Australia, pp. 2384–2388, April 2015.
11. S. Qin, Y. D. Zhang, and M. G. Amin, "High-resolution frequency estimation using generalized coprime sampling," *SPIE Mobile Multimedia/Image Processing, Security, and*

Applications Conference, Baltimore, MD, April 2015.

12. E. BouDaher, F. Ahmad, and M. G. Amin, "Sparsity-based DOA estimation of coherent and uncorrelated targets using transmit/receive co-prime arrays," *SPIE Compressive Sensing IV Conference*, Baltimore, MD, vol. 9484, pp. 94840E, April 2015.
13. Y. D. Zhang, S. Qin, and M. G. Amin, "Near-field source localization using thinned array based on sparse reconstruction of sensor-angle distributions," *IEEE International Radar Conference*, Arlington, VA, May 2015.
14. S. Qin, Y. D. Zhang, and M. G. Amin, "Sparsity-based multi-target localization exploiting multi-frequency coprime array," *IEEE China Summit and International Conference on Signal and Information Processing*, Chengdu, China, July 2015.
15. Q. Shen, W. Liu, W. Cui, S. Wu, Y. D. Zhang, and M. G. Amin, "Wideband DOA estimation for uniform linear arrays based on the co-Array concept," *European Signal Processing Conference*, Nice, France, Aug.-Sept. 2015.
16. E. BouDaher, F. Ahmad, M. G. Amin, and A. Hoorfar, "DOA estimation with co-prime arrays in the presence of mutual coupling," *European Signal Processing Conference*, Nice, France, Aug.-Sept. 2015.
17. S. Qin, Y. D. Zhang, M. G. Amin, and A. Zoubir, "Generalized coprime sampling of Toeplitz matrices," *IEEE International Conference on Acoustics, Speech, and Signal Processing*, Shanghai, China, March 2016.
18. E. BouDaher, F. Ahmad, and M. G. Amin, "Sparsity-based extrapolation for direction-of-arrival estimation using co-prime arrays," *SPIE Compressive Sensing V Conference*, Baltimore, MD, April 2016.
19. S. Qin, Y. D. Zhang, and M. G. Amin, "Multi-target localization using frequency diverse coprime arrays with coprime frequency offsets," *IEEE Radar Conference*, Philadelphia, PA, May 2016.
20. E. BouDaher, F. Ahmad, M. G. Amin, and A. Hoorfar, "Effect of mutual coupling on direction-of-arrival estimation using sparse dipole arrays," *IEEE International Symposium on Antennas and Propagation/USNC-URSI National Radio Science Meeting*, Fajardo, Puerto Rico, June-July 2016.
21. S. Qin, Y. D. Zhang, and M. G. Amin, "Two-dimensional DOA estimation using parallel coprime subarrays," *IEEE Sensor Array and Multichannel Signal Processing Workshop*, Rio de Janeiro, Brazil, July 2016.
22. B. Wang, S. Qin, Y. D. Zhang, and M. G. Amin, "Robust DOA estimation in the presence of mis-calibrated sensors," *IEEE International Conference on Acoustics, Speech, and Signal Processing*, New Orleans, LA, March 2017.
23. E. BouDaher, F. Ahmad, and M. G. Amin, "Performance analysis of sparsity-based interpolation for DOA estimation with non-uniform arrays," *SPIE Compressive Sensing VI Conference*, Anaheim, CA, April 2017.
24. A. Ahmed, Y. D. Zhang, and B. Himed, "Effective nested array design for fourth-order cumulant-based DOA estimation," *IEEE Radar Conference*, Seattle, WA, May 2017.
(Student Paper Competition Award – Third Place)

25. A. Ahmed, Y. D. Zhang, and B. Himed, "Cumulant-based direction-of-arrival estimation using multiple co-prime frequencies," *Asilomar Conference on Signals, Systems, and Computers*, Pacific Grove, CA, Oct. 2017.
26. D. Chachlakis, P. P. Markopoulos, and F. Ahmad, "The mean-squared-error of autocorrelation sampling in coprime arrays," *IEEE International Workshop on Computational Advances in Multi-sensor Adaptive Processing*, Curacao, Dutch Antilles, Dec. 2017.
27. D. Chachlakis, P. P. Markopoulos, and F. Ahmad, "MMSE-based autocorrelation sampling for coprime arrays," *IEEE International Conference on Acoustics, Speech, and Signal Processing*, Calgary, Canada, April 2018.

3. Selected Publications

1. Generalized coprime array configurations for direction-of-arrival estimation

Published in *IEEE Transactions on Signal Processing*, vol. 63, no. 6, pp. 1377-1390, March 2015

2. Multi-frequency co-prime arrays for high-resolution direction-of-arrival estimation

Published in *IEEE Transactions on Signal Processing*, vol. 63, no.14, pp. 3797–3808, July 2015

3. DOA estimation exploiting a uniform linear array with multiple co-prime frequencies

Published in *Signal Processing*, vol. 130, pp. 37-46, January 2017

4. Frequency diverse coprime arrays with coprime frequency offsets for multi-target localization

Published in *IEEE Journal of Selected Topics in Signal Processing*, vol. 11, no. 2, pp. 321-335, March 2017

5. Sparsity-based direction finding of coherent and uncorrelated targets using active nonuniform arrays

Published in *IEEE Signal Processing Letters*, vol. 22, no. 10, pp. 1628–1632, October 2015

6. Mutual coupling effect and compensation in non-uniform arrays for direction-of-arrival estimation

Published in *Digital Signal Processing*, vol. 61, pp. 3-14, February 2017

7. Generalized coprime sampling of Toeplitz matrix for spectrum estimation

Published in *IEEE Transactions on Signal Processing*, vol. 65, no. 1, pp. 81-94, January 2017

3.1. Generalized Coprime Array Configurations for Direction-of-Arrival Estimation

Abstract

A coprime array uses two uniform linear subarrays to construct an effective difference coarray with certain desirable characteristics, such as a high number of degrees-of-freedom for direction-of-arrival (DOA) estimation. In this paper, we generalize the coprime array concept with two operations. The first operation is through the compression of the inter-element spacing of one subarray and the resulting structure treats the existing variations of coprime array configurations as well as the nested array structure as its special cases. The second operation exploits two displaced subarrays, and the resulting coprime array structure allows the minimum inter-element spacing to be much larger than the typical half-wavelength requirement, making them useful in applications where a small inter-element spacing is infeasible. The performance of the generalized coarray structures is evaluated using their difference coarray equivalence. In particular, we derive the analytical expressions for the coarray aperture, the achievable number of unique lags, and the maximum number of consecutive lags for quantitative evaluation, comparison, and design of coprime arrays. The usefulness of these results is demonstrated using examples applied for DOA estimations utilizing both subspace-based and sparse signal reconstruction techniques.

I. INTRODUCTION

Direction-of-arrival (DOA) estimation, which determines the spatial spectra of the impinging electromagnetic waves, is an important application area of antenna arrays. It is well known that conventional subspace-based DOA estimation methods, such as MUSIC and ESPRIT [3], [4], resolve up to $N - 1$ sources with an N -element array. However, the problem of detecting more sources than the number of sensors is of tremendous interest in various applications [5], [6]. Toward this purpose, a higher number of degrees-of-freedom (DOFs) is usually achieved by exploiting a sparse array under the coarray equivalence. For example, the minimum redundancy array (MRA) [7] is a linear array structure that, for a given number of physical sensors, maximizes the number of consecutive virtual sensors in the resulting difference coarray. The minimum hole array (also known as the Golomb array) minimizes the number of holes in the difference coarray [8]. However, there are no general expressions for the MRA and Golomb array configurations as well as the achievable DOFs for an arbitrary number of sensors. Therefore, the optimum design and performance analysis of such arrays are not easy in general. In addition, finding the suitable

covariance matrix corresponding to a large array requires a rather complicated time-consuming iterative process.

Recently, several array configurations have been proposed as attractive alternatives for sparse array construction. The nested array [9], which is obtained by combining two uniform linear subarrays, in which one subarray has a unit inter-element spacing, can resolve $O(N^2)$ sources with N sensors. Unlike the MRA, the nested array configuration is easy to construct and it is possible to obtain the exact expressions of the sensor locations and the available DOFs for a given number of the sensors. The total aperture and the number of unique and consecutive coarray sensors can be subsequently obtained [9]. Note that, as some of the sensors in a nested array are closely located, the mutual coupling effects between antennas may become significant and thus compromise the coarray reconstruction capability and the DOA estimation performance [10], [11]. The recently developed coprime array [12], which is referred to as the prototype coprime array in this paper, utilizes a coprime pair of uniform linear subarrays, where one is of M sensors with an inter-element spacing of N units, whereas the other is of N elements with an inter-element spacing of M units. By choosing the integer numbers M and N to be coprime, a coprime array can resolve $O(MN)$ sources with $M + N - 1$ sensors. This is attractive when it is necessary to reduce mutual coupling between elements. A different coprime array structure was proposed in [13] by extending the number of elements in one subarray. The result is a larger number of consecutive virtual sensors under the coarray equivalence. By considering the difference coarray of $N + 2M - 1$ sensors, they demonstrated that continuous correlation lags can be created from $-MN$ to MN .

A close examination of the extended coprime configuration reveals that there is at least one pair of adjacent sensors that is separated only by the unit spacing, which is typically half wavelength to avoid the grating lobe problem. In addition to the mutual coupling effect as described above, there are situations that such half-wavelength minimum spacing is infeasible or impractical. One of the examples is when the physical size of the antenna sensors is larger than half-wavelength (e.g., [14]). Indeed, many parabola antennas are designed to have a large size for enhanced directivity [15]. This problem is alleviated through an effective array configuration design in which the minimum inter-element spacing is much larger than the typical half-wavelength requirement [1].

In this paper, we propose the generalization of the coprime array concept, which comprises two operations. The first operation is the compression of the inter-element spacing of one constituting subarray in the coprime array by a positive integer. The resulting coarray structure is referred to as *coprime array with compressed inter-element spacing (CACIS)*. As such, the coprime array structure developed in [13], which doubles the number of sensors in a constituting subarray, becomes a special case of the proposed CACIS structure. The second operation introduces a displacement between the two subarrays, yielding a *coprime*

array with displaced subarrays (CADiS). The resulting CADiS structure allows the minimum inter-element spacing to be much larger than the typical half-wavelength requirement. These two operations can be performed separately or jointly. We evaluate the performance of each individual generalized coarray structure corresponding to these operations using their respective difference coarray equivalence. In particular, we derive the analytical expressions of the coarray aperture, the achievable number of unique lags, and the maximum number of consecutive lags for quantitative evaluation, comparison, and optimal design.

It is noted that the focus of this paper is the examination of the generalized coprime array structures in the context of narrowband DOA estimation. Wideband or multi-frequency signals may further permit the utilization of frequency-domain DOFs for enhanced DOA estimation capability. For example, it is shown in [16] that coprime arrays that handle wideband signals can benefit from frequency diversity to achieve improved DOA estimation performance. On the other hand, the exploitation of two coprime frequencies in a uniform linear array can generate an equivalent coprime array with an increased number of DOFs [17], [18].

The rest of the paper is organized as follows. In Section II, we first review the coprime array concept based on the difference coarray concept. Then two different DOA estimation approaches, which are respectively based on the MUSIC algorithm and compressive sensing (CS) techniques, exploiting coprime arrays are summarized in Section III. The two generalized coprime array structures, i.e., CACIS and CADiS, are respectively described in Sections IV and V with the analytical expressions of array aperture, unique coarray lags, and consecutive coarray lags. Different nested array structures are clarified and compared in Section VI. Simulation results are provided in Section VII to numerically compare the performance of the different generalized coprime array configurations with the two DOA estimation techniques. Such results reaffirm and demonstrate the usefulness of the results presented in Sections IV and V. Section VIII concludes this paper.

Notations: We use lower-case (upper-case) bold characters to denote vectors (matrices). In particular, \mathbf{I}_N denotes the $N \times N$ identity matrix. $(\cdot)^*$ implies complex conjugation, whereas $(\cdot)^T$ and $(\cdot)^H$ respectively denote the transpose and conjugate transpose of a matrix or vector. $\text{vec}(\cdot)$ denotes the vectorization operator that turns a matrix into a vector by stacking all columns on top of the another, and $\text{diag}(\mathbf{x})$ denotes a diagonal matrix that uses the elements of \mathbf{x} as its diagonal elements. $\|\cdot\|_2$ and $\|\cdot\|_1$ respectively denote the Euclidean (l_2) and l_1 norms, and $\mathbb{E}(\cdot)$ is the statistical expectation operator. \otimes denotes the Kronecker product, and $\text{real}(\cdot)$ and $\text{imag}(\cdot)$ represent the real and imaginary part operations. $\mathcal{CN}(\mathbf{a}, \mathbf{B})$ denotes joint complex Gaussian distribution with mean vector \mathbf{a} and covariance matrix \mathbf{B} .

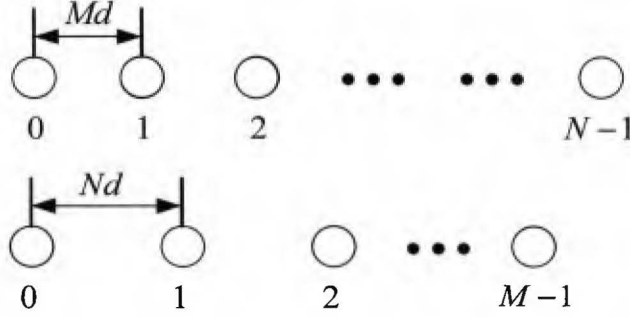


Fig. 1. The prototype coprime array configuration.

II. COPRIME ARRAY CONCEPT

A. Prototype coprime array structure

A prototype coprime array [12], as described in the previous section, is illustrated in Fig. 1, where M and N are coprime integers. Without loss of generality, we assume $M < N$. The unit inter-element spacing d is set to $\lambda/2$, where λ denotes the wavelength. The array sensors are positioned at

$$\mathbb{P} = \{Mnd \mid 0 \leq n \leq N-1\} \cup \{Nmd \mid 0 \leq m \leq M-1\}. \quad (1)$$

Because the two subarrays share the first sensor at the zeroth position, the total number of the sensors used in the coprime array is $M + N - 1$. Note that the minimum inter-element spacing in this coprime array is $\lambda/2$.

Denote $\mathbf{p} = [p_1, \dots, p_{M+N-1}]^T$ as the positions of the array sensors where $p_i \in \mathbb{P}$, $i = 1, \dots, M+N-1$, and the first sensor is assumed as the reference, i.e., $p_1 = 0$. Assume that Q uncorrelated signals impinging on the array from angles $\Theta = [\theta_1, \dots, \theta_Q]^T$, and their discretized baseband waveforms are expressed as $s_q(t)$, $t = 1, \dots, T$, for $q = 1, \dots, Q$. Then, the data vector received at the coprime array is expressed as,

$$\mathbf{x}(t) = \sum_{q=1}^Q \mathbf{a}(\theta_q) s_q(t) + \mathbf{n}(t) = \mathbf{A}\mathbf{s}(t) + \mathbf{n}(t), \quad (2)$$

where

$$\mathbf{a}(\theta_q) = \left[1, e^{j\frac{2\pi p_2}{\lambda} \sin(\theta_q)}, \dots, e^{j\frac{2\pi p_{M+N-1}}{\lambda} \sin(\theta_q)} \right]^T \quad (3)$$

is the steering vector of the array corresponding to θ_q , $\mathbf{A} = [\mathbf{a}(\theta_1), \dots, \mathbf{a}(\theta_Q)]$, and $\mathbf{s}(t) = [s_1(t), \dots, s_Q(t)]^T$. The elements of the noise vector $\mathbf{n}(t)$ are assumed to be independent and identically distributed (i.i.d.) random variables following the complex Gaussian distribution $CN(0, \sigma_n^2 \mathbf{I}_{M+N-1})$.

The covariance matrix of data vector $\mathbf{x}(t)$ is obtained as

$$\begin{aligned}\mathbf{R}_{\mathbf{xx}} &= \mathbb{E}[\mathbf{x}(t)\mathbf{x}^H(t)] = \mathbf{A}\mathbf{R}_{\mathbf{ss}}\mathbf{A}^H + \sigma_n^2\mathbf{I}_{M+N-1} \\ &= \sum_{q=1}^Q \sigma_q^2 \mathbf{a}(\theta_q)\mathbf{a}^H(\theta_q) + \sigma_n^2\mathbf{I}_{M+N-1},\end{aligned}\quad (4)$$

where $\mathbf{R}_{\mathbf{ss}} = \mathbb{E}[\mathbf{s}(t)\mathbf{s}^H(t)] = \text{diag}([\sigma_1^2, \dots, \sigma_Q^2])$ is the source covariance matrix, with σ_q^2 denoting the input signal power of the q th source, $q = 1, \dots, Q$. In practice, the covariance matrix is estimated using the T available samples, i.e.,

$$\hat{\mathbf{R}}_{\mathbf{xx}} = \frac{1}{T} \sum_{t=1}^T \mathbf{x}(t)\mathbf{x}^H(t). \quad (5)$$

From a pair of antennas located at the i th and k th positions in \mathbf{p} , the correlation $\mathbb{E}[x_i(t)x_k^*(t)]$ yields the (i, k) th entry in $\mathbf{R}_{\mathbf{xx}}$ with lag $p_i - p_k$. As such, all the available values of i and k , where $0 \leq i \leq M+N-1$ and $0 \leq k \leq M+N-1$, yield virtual sensors of the following difference coarray:

$$\mathbb{C}_P = \{\mathbf{z} \mid \mathbf{z} = \mathbf{u} - \mathbf{v}, \mathbf{u} \in \mathbb{P}, \mathbf{v} \in \mathbb{P}\}. \quad (6)$$

The significance of the difference coarray is that the correlation of the received signal can be calculated at all differences in set \mathbb{C}_P . Any application which depends only on such correlation (e.g., DOA estimation) can exploit all the DOFs offered by the resulting coarray structure. Using a part or the entire set of the distinct auto-correlation terms in set \mathbb{C}_P , instead of the original array, to perform DOA estimation, we can increase the number of detectable sources by the array. The maximum number of the DOFs is determined by the number of unique elements in the following set

$$\mathbb{L}_P = \{l_P \mid l_P d \in \mathbb{C}_P\}. \quad (7)$$

To gain more insights about the difference coarrays, we separately consider the self-differences of the two subarrays and their cross-differences. Since the coarray is obtained from the Hermitian matrix $\mathbf{R}_{\mathbf{xx}}$, the self-difference in the coarray has positions

$$\mathbb{L}_s = \{l_s \mid l_s = Mn\} \cup \{l_s \mid l_s = Nm\}, \quad (8)$$

and the corresponding mirrored positions $\mathbb{L}_s^- = \{-l_s \mid l_s \in \mathbb{L}_s\}$, whereas the cross-difference has positions

$$\mathbb{L}_c = \{l_c \mid l_c = Nm - Mn\}, \quad (9)$$

and the corresponding mirrored positions $\mathbb{L}_c^- = \{-l_c \mid l_c \in \mathbb{L}_c\}$, for $0 \leq n \leq N-1$ and $0 \leq m \leq M-1$. Consequently, the full set of lags in the virtual array is given by,

$$\mathbb{L}_P = \mathbb{L}_s \cup \mathbb{L}_s^- \cup \mathbb{L}_c \cup \mathbb{L}_c^-. \quad (10)$$

An example is illustrated in Fig. 2, where $M=6$ and $N=7$. Fig. 2(a) show the self- and cross-lags described in (8) and (9). If we include the negative mirror of the above set, then the full set of lags becomes symmetric, as shown in Fig. 2(b). Notice that some “holes”, e.g., $\pm 13, \pm 19, \pm 20$, still exist in the difference coarray and are indicated by \times in this figure. The total number of lags in the symmetric set gives a global upper bound of the achievable DOFs.

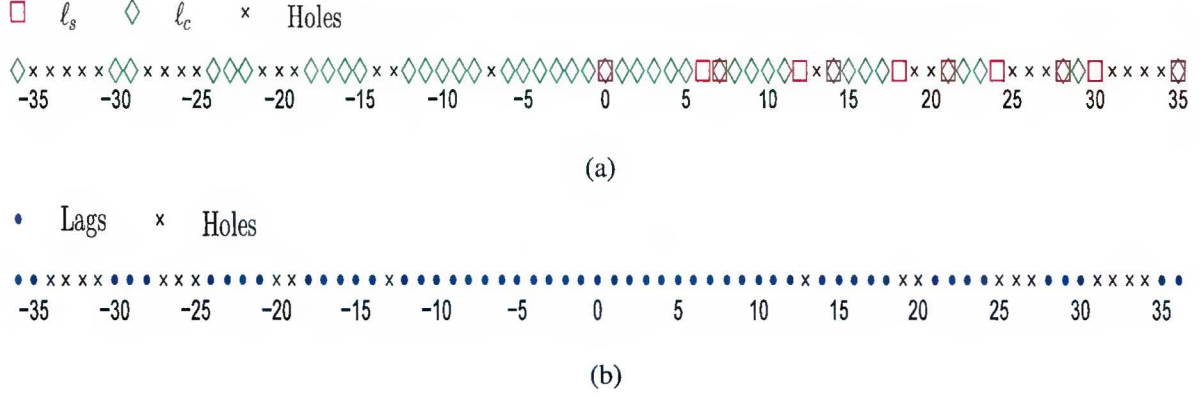


Fig. 2. An example of prototype coprime configuration coarrays, where $M=6$ and $N=7$. (a) The set \mathbb{L}_s and \mathbb{L}_c . (b) The lag positions in full set \mathbb{L}_P

III. DOA ESTIMATION TECHNIQUES

To better understand the significance of the performance metrics to be examined, i.e., the coarray aperture, the number of consecutive coarray lags, and the number of unique lags of coarray lags, we briefly review the two representative DOA estimation techniques that are recently developed for coprime array configurations. The first one is based on the well-known MUSIC algorithm, and the spatial smoothing technique [19], [20], [21] is applied to construct a suitable covariance matrix from the virtual sensor output prior to performing MUSIC spectrum estimation [12], [13]. Notice that, while the use of virtual sensors substantially increases the available number of DOFs, the application of spatial smoothing essentially halves the number of available virtual sensors. A different approach to perform DOA estimation exploiting coprime arrays is through sparse signal reconstruction by taking advantages of the fact that the spatial signal spectra are sparse. Such sparse signal reconstruction is achieved using the recently developed compressive sensing techniques [22], [23]. These two DOA estimation techniques are summarized below.

A. MUSIC Algorithm

Vectorizing \mathbf{R}_{xx} in (4) yields

$$\mathbf{z} = \text{vec}(\mathbf{R}_{xx}) = \tilde{\mathbf{A}}\mathbf{b} + \sigma_n^2 \tilde{\mathbf{I}} = \mathbf{B}\mathbf{r}, \quad (11)$$

where $\tilde{\mathbf{A}} = [\tilde{\mathbf{a}}(\theta_1), \dots, \tilde{\mathbf{a}}(\theta_Q)]$, $\tilde{\mathbf{a}}(\theta_q) = \mathbf{a}^*(\theta_q) \otimes \mathbf{a}(\theta_q)$, $\mathbf{b} = [\sigma_1^2, \dots, \sigma_Q^2]^T$, $\tilde{\mathbf{I}} = \text{vec}(\mathbf{I}_{M+N-1})$. In addition, $\mathbf{B} = [\tilde{\mathbf{A}}, \tilde{\mathbf{I}}]$ and $\mathbf{r} = [\mathbf{b}^T, \sigma_n^2]^T = [\sigma_1^2, \dots, \sigma_Q^2, \sigma_n^2]$ are used for notational simplicity. The vector \mathbf{z} amounts to the received data from a virtual array with an extended coarray aperture whose corresponding steering matrix is defined by $\tilde{\mathbf{A}}$. However, the virtual source signal becomes a single snapshot of \mathbf{b} . In addition, the rank of the noise-free covariance matrix of \mathbf{z} , $\mathbf{R}_{\mathbf{z}\mathbf{z}} = \mathbf{z}\mathbf{z}^H$, is one. As such, the problem is similar to handling fully coherent sources, and subspace-based DOA estimation techniques, such as MUSIC, fail to yield reliable DOA estimates when multiple signals impinge to the array.

To overcome this problem, it is proposed in [13] to apply spatial smoothing technique to the covariance matrix so that its rank can be restored. Since spatial smoothing requires a consecutive difference lag set so that every subarray has similar manifold, we extract all the consecutive lag samples of \mathbf{z} and form a new vector \mathbf{z}_1 . Denote $[-l_\xi, l_\xi]$ as the consecutive lag range in \mathbb{L}_P . Then, \mathbf{z}_1 can be expressed as

$$\mathbf{z}_1 = \tilde{\mathbf{A}}_1 \mathbf{b} + \sigma_n^2 \tilde{\mathbf{I}}_1, \quad (12)$$

where $\tilde{\mathbf{A}}_1$ is identical to the manifold of a uniform linear array (ULA) with $2l_\xi + 1$ sensors located from $-l_\xi d$ to $l_\xi d$ and $\tilde{\mathbf{I}}_1$ is a $(2l_\xi + 1) \times 1$ vector of all zeros except a 1 at the $(l_\xi + 1)$ th position. We divide this virtual array into $l_\xi + 1$ overlapping subarrays, \mathbf{z}_{1i} , $i = 1, \dots, l_\xi + 1$, each with $l_\xi + 1$ elements, where the i th subarray has sensors located at $(-i + 1 + k)d$, with $k = 0, 1, \dots, l_\xi$ denoting the index of the overlap subarray used in the spatial smoothing.

Define

$$\mathbf{R}_i = \mathbf{z}_{1i} \mathbf{z}_{1i}^H. \quad (13)$$

Taking the average of \mathbf{R}_i over all i , we obtain

$$\mathbf{R}'_{\mathbf{z}\mathbf{z}} = \frac{1}{l_\xi + 1} \sum_{i=1}^{l_\xi+1} \mathbf{R}_i, \quad (14)$$

which yields a full-rank covariance matrix so that the MUSIC algorithm can be performed for DOA estimation directly. As a result, l_ξ DOFs are achieved, which are roughly equal to half of the available consecutive lags of the resulting coarray.

B. Compressive Sensing Approach

Alternatively, (11) can be solved using the CS approach [23]. The desired result of \mathbf{b} , whose elements are the first Q entries of vector \mathbf{r} , can be obtained from the solution to the following constrained l_0 -norm minimization problem

$$\hat{\mathbf{r}}^\circ = \arg \min_{\mathbf{r}^\circ} \|\mathbf{r}^\circ\|_0 \quad \text{s.t.} \quad \|\mathbf{z} - \mathbf{B}^\circ \mathbf{r}^\circ\|_2 < \epsilon, \quad (15)$$

where ϵ is a user-specific bound, \mathbf{B}° is a sensing matrix consisting of the searching steering vectors and $\tilde{\mathbf{i}}$, whereas \mathbf{r}° is the sparse entries in these search grids to be determined. The sensing matrix \mathbf{B}° and the entry vector \mathbf{r}° are defined over a finite grid $\theta_1^g, \dots, \theta_G^g$, where $G \gg Q$. The last entry of \mathbf{r}° denotes the estimate of σ_n^2 , whereas the positions and values of the non-zero entries in the other elements of \mathbf{r}° represent the estimated DOAs and the corresponding signal power.

This type of problems has been the objective of intensive studies in the area of CS, and a number of effective numerical computation methods have been developed [24], [25], [26], [27], [28]. In [23], the batch Lasso method was used, but other methods may also be used. The objective function of the Lasso algorithm is defined as

$$\hat{\mathbf{r}}^\circ = \arg \min_{\mathbf{r}^\circ} \left[\frac{1}{2} \|\mathbf{z} - \mathbf{B}^\circ \mathbf{r}^\circ\|_2 + \lambda_t \|\mathbf{r}^\circ\|_1 \right], \quad (16)$$

where the l_2 norm in the objective function denotes the ordinary least-squares (OLS) cost function, and the l_1 norm involves the sparsity constraint. In addition, λ_t is a penalty parameter which can be tuned to trade off the OLS error for the number of nonzero entries (degree of sparsity) in the estimates [24]. The above Lasso objective is convex in \mathbf{r}° , and can be optimized using linear programming techniques [29].

IV. COPRIME ARRAY WITH COMPRESSED INTER-ELEMENT SPACING

Now we present our main results that generalize coarray structures in two operations, i.e., CACIS and CADiS. The CACIS is presented in this section, whereas the CADiS is examined in the following section.

We consider two subarrays with M and N sensors, where M and N are coprime. Note that, in the sequel, the condition that $M < N$ is no longer assumed. Unlike the prototype coprime array, an integer compression factor p is introduced for changing the inter-element spacing of one subarray. Assume that M can be expressed as a product of two positive integers p and \check{M} , i.e.,

$$M = p\check{M}, \quad (17)$$

for some p that takes a value between 2 and M . It is easy to confirm that \check{M} and N are also coprime since M and N do not have common factors other than unity. As shown in Fig. 3, in the generalized coprime array, the M -element subarray has an inter-element spacing of Nd , whereas the N -element subarray has an inter-element space of $\check{M}d = Md/p$. As such, the generalized coprime array can be considered that the inter-element spacing of one constituting subarray is compressed by an integer factor of p , thus comes the term of coprime array with compressed inter-element spacing (CACIS). Note that all arrays consist of the same $M + N - 1$ physical antenna sensors and their aperture is $(M - 1)N$,

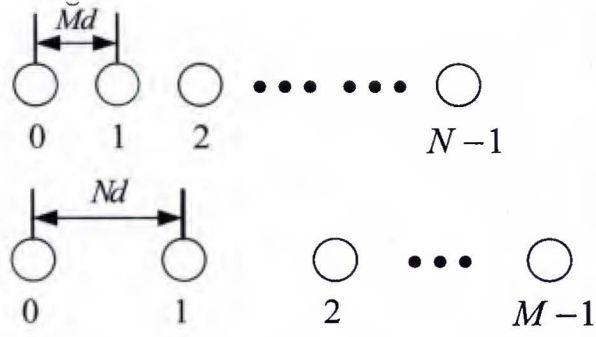


Fig. 3. The CACIS configuration.

regardless the value of p . It is shown that the variation of the coprime array configuration used in [13] is a special case of the CACIS configuration by choosing $p = 2$.

In this array configuration, the self-lags of the two subarrays are given by the following set ¹,

$$\tilde{\mathbb{L}}_s = \{\tilde{l}_s | \tilde{l}_s = \check{M}n\} \cup \{\tilde{l}_s | \tilde{l}_s = Nm\}, \quad (18)$$

and the corresponding mirrored positions $\tilde{\mathbb{L}}_s^-$, whereas the cross-lags between the two subarrays are given by

$$\tilde{\mathbb{L}}_c = \{\tilde{l}_c | \tilde{l}_c = Nm - \check{M}n\}, \quad (19)$$

and the corresponding $\tilde{\mathbb{L}}_c^-$, where $0 \leq m \leq M - 1$ and $0 \leq n \leq N - 1$.

To completely exploit the DOFs of the CACIS configuration, we summarize the properties of $\tilde{\mathbb{L}}_s$ and $\tilde{\mathbb{L}}_c$ in the following proposition.

Proposition 1: The following facts hold for the CACIS:

- (a) There are MN distinct integers in set $\tilde{\mathbb{L}}_c$.
- (b) $\tilde{\mathbb{L}}_c$ contains all the contiguous integers in the range $-(N - 1) \leq \tilde{l}_c \leq MN - \check{M}(N - 1) - 1$.
- (c) The negative values form a subset of the flipped positive values in set $\tilde{\mathbb{L}}_c$, i.e.,

$$\{\tilde{l}_c | \tilde{l}_c < 0, \tilde{l}_c \in \tilde{\mathbb{L}}_c\} \subseteq \{-\tilde{l}_c | \tilde{l}_c > 0, \tilde{l}_c \in \tilde{\mathbb{L}}_c\}.$$
- (d) The self-lags form a subset of the cross-lags, i.e., $(\tilde{\mathbb{L}}_s^- \cup \tilde{\mathbb{L}}_s) \subseteq (\tilde{\mathbb{L}}_c^- \cup \tilde{\mathbb{L}}_c)$.
- (e) There are “holes” located at both positive range and negative ranges of $\tilde{\mathbb{L}}_c$. The holes falling in the negative range are located at $-(a\check{M} + bN)$, where $a \geq 0, b > 0$ are integers.

The proof is provided in Appendix A.

¹($\tilde{\cdot}$) is used to emphasize variables corresponding to the CACIS structure.

Based on the properties (c) and (d) of Proposition 1, the entire lag set in the virtual array defined in (10) consists of $\{\tilde{l}_c | \tilde{l}_c \geq 0, \tilde{l}_c \in \tilde{\mathbb{L}}_c\} \cup \{-\tilde{l}_c | \tilde{l}_c \geq 0, \tilde{l}_c \in \tilde{\mathbb{L}}_c\}$, thus resulting in Proposition 2.

Proposition 2: The CACIS configuration defined in equation (17) yields a virtual array such that:

- (a) It contains $2MN - (M + 1)(N - 1) - 1$ unique lags of virtual sensors;
- (b) Among the unique lags, there are $2\check{M}(N - 1) - 1$ consecutive integers within the range $[-MN + \check{M}(N - 1) + 1, MN - \check{M}(N - 1) - 1]$.

The proof is provided in Appendix B. In Fig. 4, $M = 2\check{M}$ is considered as an illustrative example of above properties. It is equivalent to the configuration proposed in [13]. In this case, the virtual array consists of $3\check{M}N + \check{M} - N$ unique lags, among which $[-\check{M}N - \check{M} + 1, \check{M}N + \check{M} - 1]$ are consecutive. Note that our result contains more consecutive lags and is more precise than the result provided in [13], which is $[-\check{M}N + 1, \check{M}N - 1]$. The difference, which is based on property (b) of Proposition 1, is clarified in Appendix A.

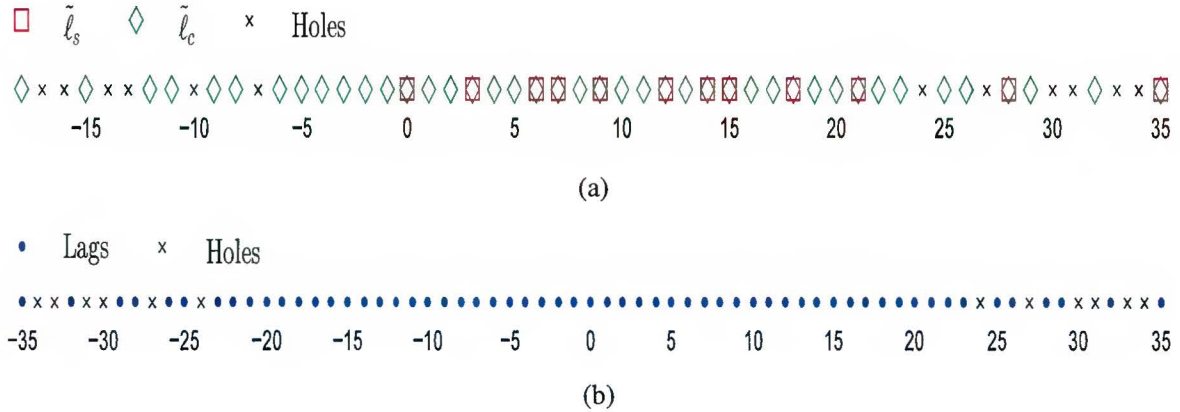


Fig. 4. An example of CACIS configuration coarrays, where $\check{M}=3$, $p=2$ and $N=7$. (a) The set $\tilde{\mathbb{L}}_s$ and $\tilde{\mathbb{L}}_c$. (b) The full set $\tilde{\mathbb{L}}_P$.

According to Proposition 2, we can draw a conclusion that, for a specific pair of M and N , smaller values of \check{M} led to more unique and consecutive coarray lags. In other words, both numbers increase with the compression factor p . The minimum value that \check{M} can take is 1. In this case, the CACIS configuration becomes a nested array structure, which provides the highest numbers of the unique and consecutive virtual sensors. More detailed discussions about nested array configurations will be given in Section VI.

V. COPRIME ARRAY WITH DISPLACED SUBARRAYS

Sharing the same property as MRA, the prototype coprime array and the CACIS structure provide sparse configurations in which the minimum inter-element spacing remains the unit spacing, which is

typically half wavelength, to avoid the grating lobe problem. In addition to the aforementioned challenges associated with half wavelength minimum spacing in regards of antenna size and mutual coupling, there is a high number of overlapping between the self- and cross-lags. This is the case for both the prototype coprime array and the CACIS structures and is consequence of the colocated subarray placement. By introducing a proper displacement between the two subarrays, the new coprime array structure achieves a larger minimum inter-element spacing, a higher number of unique lags, and a larger virtual array aperture. As we will see, however, the number of consecutive lags is reduced because the positive and negative lags are no longer connected.

Consider two collinearly located uniform linear subarrays, as depicted in Fig. 5, where one consists of N antennas and the other with $M - 1$ antennas. As such, the total number of the sensors is kept to $M + N - 1$. We refer to this coprime array structure as coprime array with displaced subarrays (CADiS). Similar to the CACIS configuration, we assume M and N are coprime. The N -element subarray has an inter-element spacing of $\check{M}d$, and the $(M - 1)$ -element subarray has an inter-element spacing of Nd , where, as indicated in (17), $M = p\check{M}$. The difference to the CASIS structure lies in the fact that these two subarrays in the CADiS structure are placed collinearly with the closest spacing between the two subarrays set to Ld , where $L \geq \min\{\check{M}, N\}$. Note that $\check{M} > 1$ is required to guarantee the minimum inter-element spacing to be larger than unit spacing, but the nested structure under this configuration, i.e., $\check{M} = 1$, will also be discussed later as a special case. The total number of array sensors in the CADiS structure remains $M + N - 1$, which is the same as the CACIS configuration discussed earlier. Note that the minimum inter-element spacing in the CADiS is $\min\{\check{M}, N\}d$, as compared to d in the CACIS structure. In addition, the total array aperture of the CADiS is $(MN + \check{M}N - \check{M} - 2N + L)d$, which is much larger than the $(M - 1)Nd$ of the CACIS. In practical application, however, a small value of displacement L should be chosen to avoid false peaks.

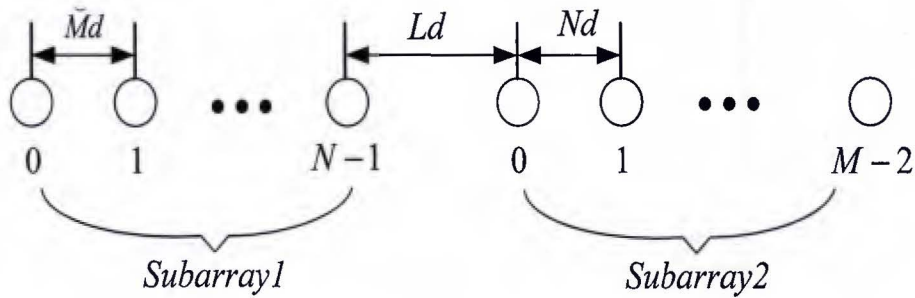


Fig. 5. The CADiS configuration.

For the CADiS configuration, the corresponding self-lags \bar{l}_s and cross-lags \bar{l}_c are respectively given by²

$$\bar{\mathbb{L}}_s = \{\bar{l}_s \mid \bar{l}_s = Nm\} \cup \{\bar{l}_s \mid \bar{l}_s = \check{M}n\}, \quad (20)$$

$$\bar{\mathbb{L}}_c = \{\bar{l}_c \mid \bar{l}_c = \check{M}(N-1) + Nm - \check{M}n + L\}, \quad (21)$$

and their corresponding mirrored positions $\bar{\mathbb{L}}_s^-$ and $\bar{\mathbb{L}}_c^-$, respectively, where $0 \leq m \leq M-2$ and $0 \leq n \leq N-1$.

The following proposition reveals the properties of the resulting virtual sensors of the CADiS configuration.

Proposition 3: Set $\bar{\mathbb{L}}_s$ and $\bar{\mathbb{L}}_c$ have the following properties in the CADiS configuration:

- (a) There are $(M-1)N$ distinct integers in set $\bar{\mathbb{L}}_c$.
- (b) $\bar{\mathbb{L}}_c$ contains all the contiguous integers in the range $(\check{M}-1)(N-1) + L \leq \bar{l}_c \leq MN - N - 1 + L$.
- (c) There are “holes” located at $\check{M}(N-1) - (a\check{M} + bN) + L$ in set $\bar{\mathbb{L}}_c$, where $a \geq 0$, $b > 0$ are integers.
- (d) $(\bar{\mathbb{L}}_s^- \cup \bar{\mathbb{L}}_s) \not\subseteq (\bar{\mathbb{L}}_c^- \cup \bar{\mathbb{L}}_c)$.

The proof is provided in Appendix C.

In the CACIS configuration, the negative lags form a subset of the flipped positive counterpart. Therefore, only non-negative lags in $\bar{\mathbb{L}}_c$ are used. In the CADiS configuration, however, the negative lags do not generally overlap with the flipped positive lags because of the displacement between two subarrays, necessitating the consideration of both positive and negative lags. As such, the CADiS configuration enjoys a higher number of unique lags than the CACIS because of the utilization of negative lags. In addition, the self-lags are less likely to coincide with the cross-lags in the CADiS configuration. Consequently, the CADiS offers a larger virtual array aperture and a higher number of virtual sensors. The role of the displacement L is as follows. On one hand, it reduces the overlaps between the self- and cross-lags. On the other hand, because $\bar{\mathbb{L}}_c$ has holes located at $\check{M}(N-1) - (a\check{M} + bN) + L$ for integers $a \geq 0$ and $b > 0$, the number of consecutive lags can be extended by choosing an approximate value of L so that some self-lags are aligned to the cross-lag holes. For illustrative purpose, we consider the case of $p = 2$, $\check{M} = 3$, $N = 7$ and $L = \check{M} + N$ as an example. The corresponding $\bar{\mathbb{L}}_s$ and $\bar{\mathbb{L}}_c$ are shown in Fig. 6. It is clear that some holes in $\bar{\mathbb{L}}_c$ (12, 14, 15, 18 and 21) are aligned by elements of $\bar{\mathbb{L}}_s$. The following proposition describes the selection of the value of L that maximizes the number of unique and consecutive lags.

²($\bar{\cdot}$) is used to emphasize variables corresponding to the CADiS structure.

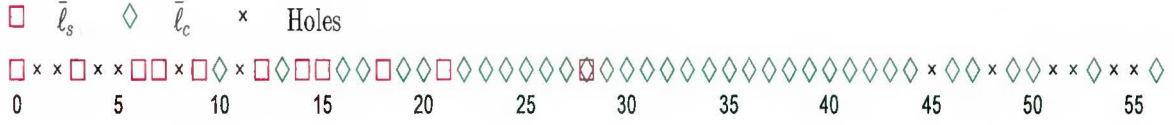


Fig. 6. An example of CADiS configuration coarrays, where $p = 2$, $\check{M} = 3$, $N = 7$ and $L = \check{M} + N$.

Proposition 4: For the CADiS configuration,

- (a) The maximum number of unique lags $2MN + 2M - 5$ can be achieved with $L > N(M - 2)$.
- (b) $L = \check{M} + N$ is the choice that yields the largest number of consecutive lags. In this case, there are $2MN + 2\check{M} - 1$ unique lags, among which the range $[(\check{M} - 1)(N - 1), MN + \check{M} - 1]$ and its corresponding negative range $[-MN - \check{M} + 1, -(\check{M} - 1)(N - 1)]$ are respectively consecutive.

The proof is provided in Appendix D. Based on property (2) of Proposition 4, it is clear that the number of unique lags increases as \check{M} increases, whereas the number of the consecutive lags decreases. Particularly, for the nested array structure, i.e., $\check{M} = 1$, the positive range of consecutive lags is $[0, MN]$ and its corresponding negative range becomes $[-MN, 0]$, resulting in all unique lags to be consecutive.

For comparison, we enlist in Table I the coarray aperture, the maximum number of unique and consecutive lags for both proposed configurations. As the results show, for a given coprime pair of M and N , the nested structure achieves the maximum number of consecutive and unique lags when using CACIS configurations. In other word, it offers the highest number of DOFs for DOA estimation. As for CADiS, the nested structure provides the highest number only for the consecutive lags. The number of its unique lags, $2MN + 1$, on the other hand, is less than that of the CADiS structure with a large separation between the two subarrays. That is, the nested CADiS provides the highest number of DOFs only when MUSIC or other subspace based methods are used for DOA estimation, but it becomes less effective when CS based DOA estimation methods are applied. It is noted that, to estimate DOAs of up to MN sources, the nested CADiS structure requires only $M + N - 1$ sensors, which are much less than the result of $2M + N - 1$ sensors as exploited in [13].

VI. COMPARISON OF DIFFERENT NESTED STRUCTURES

The nested structure is referred to a structure consisting of two uniform linear subarrays, where one subarray has a unit inter-element spacing [9]. A nested array is usually designed such that the virtual sensors in the resulting coarray are all contiguous. The nested structure proposed in [9], as shown in Fig. 7, consists of an inner N_1 -element subarray with a unit spacing d and an outer N_2 -element subarray with spacing $(N_1 + 1)d$, resulting in $2N_2(N_1 + 1) - 1$ contiguous lags. Note that the nested array concept

TABLE I
COMPARISON OF THE COARRAY APERTURE, NUMBER OF UNIQUE LAGS, AND NUMBER OF CONSECUTIVE LAGS

	Coarray aperture	Maximum number of unique lags	Maximum number of consecutive lags
CACIS	$(M - 1)N$	$2MN - \check{M}(N - 1) - N$	$2MN - 2\check{M}(N - 1) - 1$
CADiS ($\check{M} > 1$) (displacement L)	$(N - 1)\check{M}$ $+(M - 2)N + L$ (arbitrary L)	$2MN + 2\check{M} - 5$ ($L > N(M - 2)$)	$MN - (\check{M} - 1)(N - 2) + 1$ ($L = \check{M} + N$)
Nested CADiS ($\check{M} = 1$) (displacement L)	MN ($L = N + 1$)	$2MN + 1$ ($L = N + 1$)	$2MN + 1$ ($L = N + 1$)

TABLE II
OPTIMUM SOLUTION FOR DIFFERENT NESTED STRUCTURES THAT MAXIMIZES THE DOFS

	Number of physical sensors		Optimal values	Maximum number of DOFs
CACIS	$K = M + N - 1$	K is even	$M = \frac{K+2}{2}, N = \frac{K}{2}$	$(M - 1)N = \frac{K^2}{4}$
		K is odd	$M = \frac{K+1}{2}, N = \frac{K+1}{2}$	$(M - 1)N = \frac{K^2 - 1}{4}$
CADiS	$K = M + N - 1$	K is even	$M = \frac{K+2}{2}, N = \frac{K}{2}$	$MN = \frac{K^2 + 2K}{4}$
		K is odd	$M = \frac{K+1}{2}, N = \frac{K+1}{2}$	$MN = \frac{K^2 + 2K + 1}{4}$
Configuration in [9]	$K = N_1 + N_2$	K is even	$N_1 = \frac{K}{2}, N_2 = \frac{K}{2}$	$N_2(N_1 + 1) - 1 = \frac{K^2 + 2K - 4}{4}$
		K is odd	$N_1 = \frac{K-1}{2}, N_2 = \frac{K+1}{2}$	$N_2(N_1 + 1) - 1 = \frac{K^2 + 2K - 3}{4}$

does not require a coprimality between N_1 and N_2 . It is also important to note that, in the extension of the generalized coprime array framework, different nested array configurations can be defined, by setting \check{M} to be one to the CACIS and CADiS structures. These different nested configurations yield different numbers of DOFs. For comparison of the three nested array structures, we consider the same number, K , of physical sensors, and optimize the array configuration for each structure to maximize the respective number of DOFs. Such optimal solutions are summarized in Table II. It is clear that the structure in [9] offers a higher number of DOFs than the nested CACIS structure, but less than the nested CADiS.

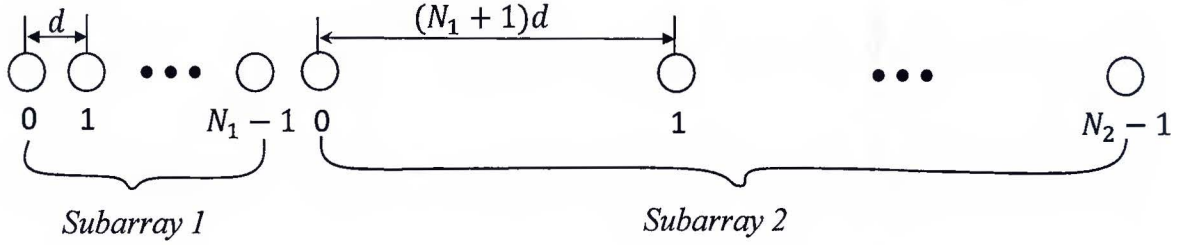


Fig. 7. The nested configuration proposed in [9].

For better illustrative purposes, we compare three different optimized nested configurations with $K = 8$ physical sensors in Fig. 8. Fig. 8(a) shows the optimized nested CACIS configuration. One subarray is of $N = 4$ sensors with an inter-element spacing of $\check{M}d = d$, whereas the other is of $M = 5$ elements with an inter-element spacing of $Nd = 4d$. In addition, the two subarrays share the first sensor at the zeroth position and form a coarray with 33 lag positions. The nested CADiS structure is illustrated in Fig. 8(b). One 4-element subarray has an inter-element spacing of $\check{M}d = d$, and the other subarray has an inter-element spacing of $Nd = 4d$. In addition, there is a displacement $Ld = (\check{M} + N)d = 5d$ between the two subarrays. As a result, its coarray has 41 lag positions. Finally, the nested array configuration proposed in [9] is depicted in Fig. 8(c), where the inner subarray has $N_1 = 4$ elements with spacing d and the outer subarray has $N_2 = 4$ elements with spacing $(N_1 + 1)d = 5d$. In this case, the coarray has 39 lag positions. As a result, the nested CADiS structure achieves a higher number of DOFs.

VII. SIMULATION RESULTS

For illustrative purposes, we consider $M = 6$ and $N = 7$ with different values of the compression factor p of the two configurations, i.e., CACIS and CADiS. $L = \check{M} + N$ are considered for the CADiS configuration for the convenience of performance comparison between both MUSIC and CS techniques.

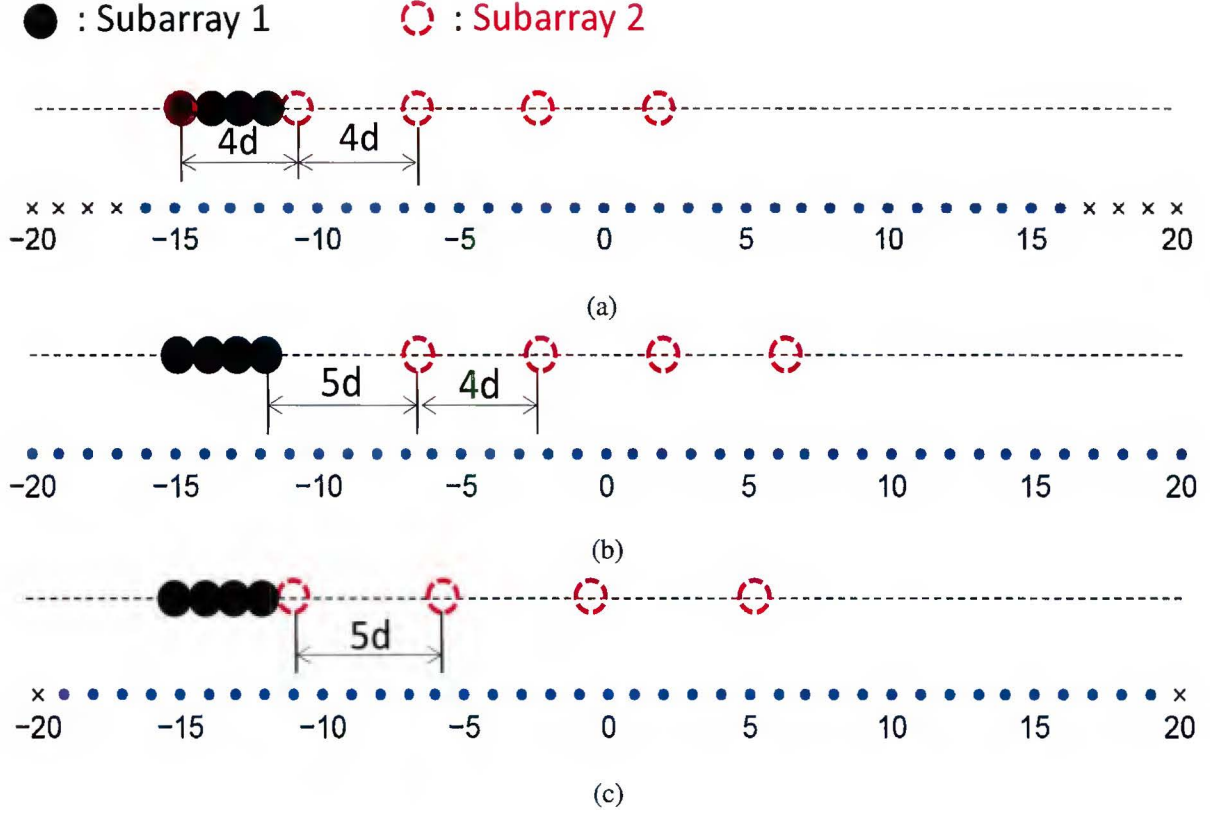
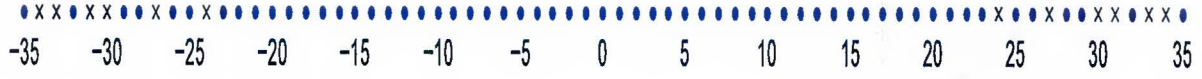


Fig. 8. Three different optimized nested configurations and their coarrays ($K=8$). (a) The nested CACIS. (b) The nested CADiS. (c) The nested configuration proposed in [9].

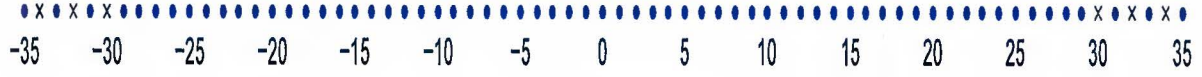
All configurations consist of $M + N - 1 = 12$ physical antenna sensors and the unit inter-element spacing is $d = \lambda/2$.

A. Array Configurations

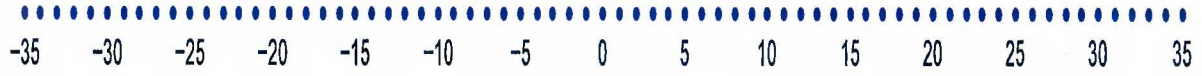
The virtual sensors corresponding to the CACIS and CADiS structures are respectively shown in Fig. 9 and Fig. 10. Fig. 9(a) depicts the CACIS configuration example for $p = 2$, where the coprime array form a virtual array with 59 unique lags, among which 47 lags within $[-23, 23]$ are consecutive. Fig. 9(b) shows for the case of $p = 3$, and the resulting virtual array has 65 unique lags, among which 59 lags within $[-29, 29]$ are consecutive. When $p = M = 6$, i.e., $\check{M} = 1$, as shown in Fig. 9(c), the coprime array becomes the nested array structure with 71 unique lags, which are all consecutive. It is clear that both numbers of the unique and consecutive lags increase with p , and the nested array achieves the maximum number for both. For the CADiS configuration with $L = \check{M} + N$, the case of $p = 2$ is presented in Fig. 10(a). In this case, the entire virtual array has 89 unique lags, among which lags within $[-44, -12]$ and $[12, 44]$ are respectively consecutive. For $p = 3$, there are 87 distinct lags, resulting consecutive lags in



(a)

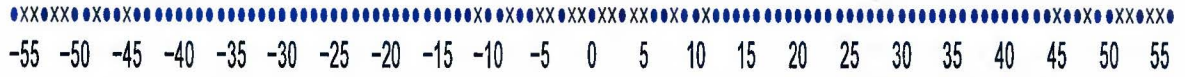


(b)



(c)

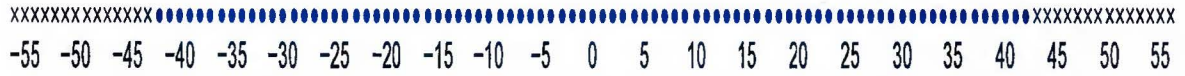
Fig. 9. CACIS configuration coarrays, for different compression factor p ($M=6$ and $N=7$). (a) $p = 2$ and $\check{M} = 3$. (b) $p = 3$ and $\check{M} = 2$. (c) $p = 6$ and $\check{M} = 1$.



(a)



(b)



(c)

Fig. 10. CADiS configuration coarrays with displacement $L = \check{M} + N$, corresponding the compression factor p ($M=6$ and $N=7$). (a) $p = 2$, $\check{M} = 3$ and $L = 10$. (b) $p = 3$, $\check{M} = 2$ and $L = 9$. (c) $p = 6$, $\check{M} = 1$ and $L = 8$.

$[-43, -6]$ and in $[6, 43]$ as shown in Fig. 10(b). In Fig. 10(c), the nested CADiS with $p = 6$ and $\check{M} = 1$ is considered as a special case. It is noted that all 85 lags in the full symmetric set of $[-42, 42]$ are consecutive.

B. MUSIC and CS Spectra

In Figs. 11 and 12, we present numerical examples to demonstrate the number of achievable DOFs for DOA estimation using the generalized coprime arrays. As the virtual sensor lags are obtained from the estimated covariance matrix based on the received data samples as in (5), the virtual steering matrix is sensitive to the noise contamination. To clearly demonstrate the number of achievable DOFs, therefore, we use 2000 noise-free snapshots to obtain a relatively clean covariance matrix. $Q = 33$ uncorrelated narrowband sources are considered, which are uniformly distributed between -60° and 60° . For the MUSIC algorithm which requires consecutive lags, we respectively obtain 23, 29 and 35 DOFs of CACIS configuration for $p = 2$, $p = 3$ and $p = 6$ as shown in Figs. 11(a), 11(c) and 11(e). On the other hand, 17, 19 and 42 DOFs are obtained using the CADiS configuration as shown in Figs. 11(b), 11(d) and 11(f). Note that only the nested structures have a sufficient number of DOFs to resolve all 33 impinging signals. This is verified in Fig. 11 in which only the cases of $p = 6$ resolve all the 33 signals for both configurations, whereas not all sources are correctly identified for the cases of $p = 2$ and $p = 3$. In addition, it is evident that the “nested CADiS” has better performance than “nested CACIS” due to the higher DOFs of the former. When the CS technique is applied for DOA estimation, a higher number of DOFs is achieved because all unique lags are exploited. The results obtained from the Lasso are shown in Fig. 12, where a grid interval of $\theta_i^g = 0.25^\circ$ and the penalty parameter of $\lambda_t = 0.85$ are used. It is clearly shown that only the nested structure can recover all 33 sources using the CACIS configuration, whereas all these signals can be detected for all the CADiS configurations examined in Fig. 12 due to their higher unique lags. In addition, the CS based technique results in better estimated spectra, when comparing the MUSIC spectra depicted in Fig. 11.

To compare the performance between the CACIS and CADiS structures as well as between the MUSIC and CS methods, we use the respective nested structures and compute the results in the presence of noise with a 0 dB SNR for all signals, and the number of snapshots is reduced to 500. In this case, the perturbation in the covariance matrix becomes higher due to noise and the limited number of samples, and the resulting DOA estimation performance degrades. The DOA estimation results are compared in Fig. 13 for $Q = 33$ sources, which is smaller than the available DOFs for both array configurations. It is evident that the nested CADiS outperforms the nested CACIS, and the CS based method achieves a better spatial spectrum estimation performance.

C. Root Mean Square Error versus SNR and Number of Snapshots

We further compare the DOA estimation performance of different CACIS and CADiS configurations through Monte Carlo simulations. The average root mean square error (RMSE) of the estimated DOAs,

expressed as

$$\text{RMSE} = \sqrt{\frac{\sum_{i=1}^I \sum_{q=1}^Q (\hat{\theta}_q(i) - \theta_q)^2}{IQ}},$$

is used as the performance metric, where $\hat{\theta}_q(i)$ is the estimate of θ_q for the i th Monte Carlo trial, $i = 1, \dots, I$. We use $I = 500$ independent trials in all simulations.

To enable comparison, we consider $Q = 16$ narrowband uncorrelated sources, which are lower than the available DOFs for all cases with both MUSIC and CS techniques. Fig. 14 compares the RMSE performance as a function of the input SNR, where 500 snapshots are used. In Fig. 15, we compare the performance of different array configurations and DOA techniques with respect to the number of snapshots, where the input SNR is set to 0 dB. It is evident that the DOA estimation performance is improved with the increase of the input SNR and the number of snapshots. For the CACIS structure, the performance of both MUSIC and CS approaches improves as the compression factor p increases because of the increased number of consecutive and unique lags. As a result, the nested array structure achieves the best performance. For CADiS, MUSIC-based DOA estimation for non-nested CADiS structures suffers from significant performance degradation because of the disconnected coarray lags. As such, the nested array is the preferred CADiS structure when the MUSIC algorithm is used for DOA estimation. Furthermore, the nested CADiS slightly outperforms the nested CACIS as a result of higher number of consecutive lags. However, because it has the fewest unique lags, the nested structure is least effective among the three CADiS array structures when the CS technique is exploited. As a conclusion, the CS-based method obtains better performance than the MUSIC counterparts. In addition, when the CS-based technique is used, the CADiS outperforms the corresponding CACIS structures.

VIII. CONCLUSIONS

We have proposed the generalized coprime array concept in two aspects: compression of the inter-element of spacing of one constituting subarray, and the displacement of the two subarrays. The first operation yields flexibility of trading-off between unique lags and consecutive lags for effective direction-of-arrival (DOA) estimation based on different algorithms, whereas the second operation further allows a larger minimum inter-element spacing beyond the typical half-wavelength requirement. The performance of the generalized coarray structures was evaluated using their difference coarray equivalence, and the analytical expressions of the coarray aperture, the achievable number of unique lags, and the maximum number of consecutive lags were derived for quantitative evaluation, comparison, and optimal design. The usefulness of these results was demonstrated using examples applied for DOA estimations.

IX. ACKNOWLEDGEMENT

The authors would like to thank the reviewers for the many constructive suggestions and comments.

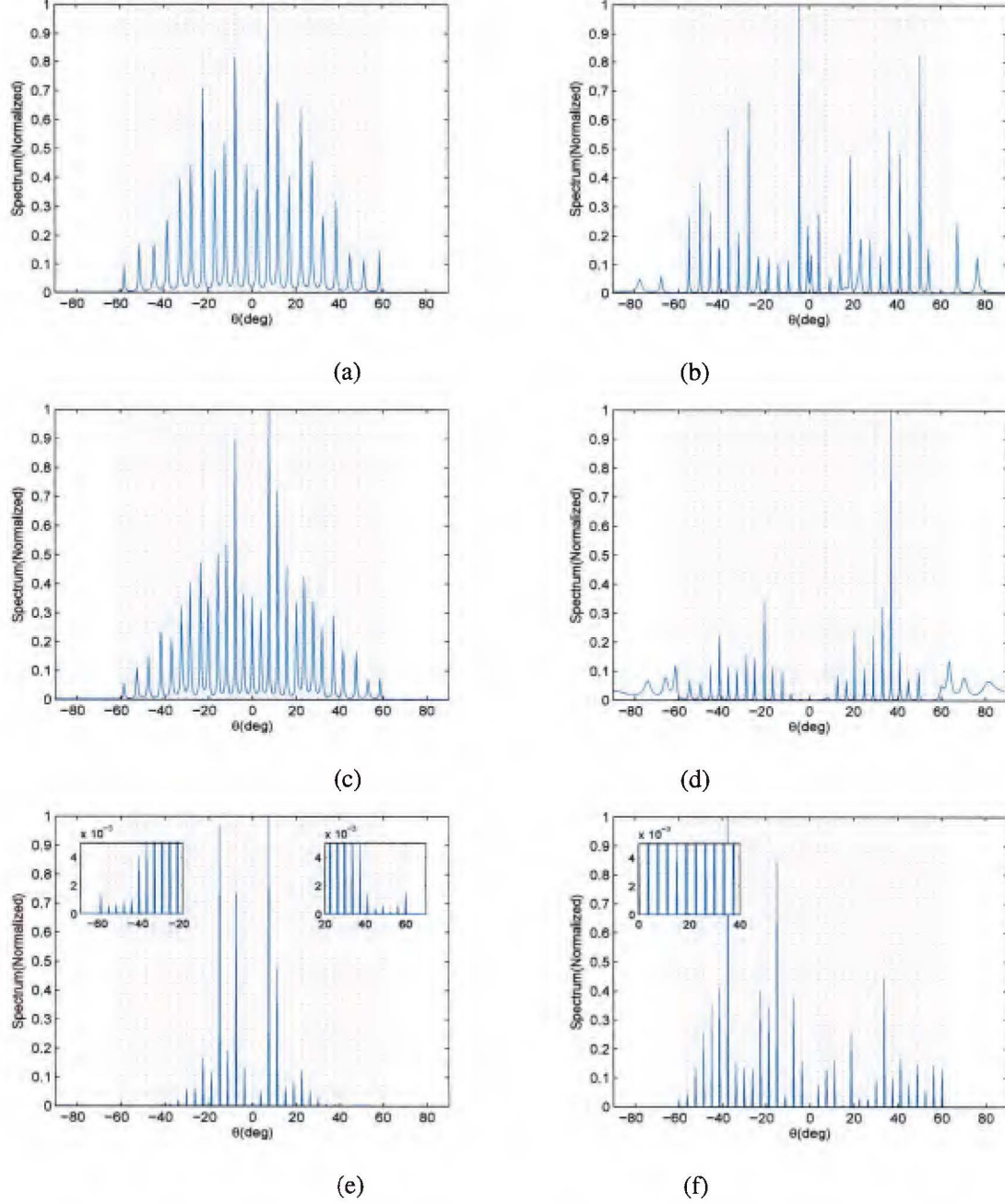


Fig. 11. Spatial spectra estimated using MUSIC for both configurations ($Q=33$, $M=6$ and $N=7$). (a) CACIS with $p=2$. (b) CADiS with $p=2$. (c) CACIS with $p=3$. (d) CADiS with $p=3$. (e) CACIS with $p=6$. (f) CADiS with $p=6$.

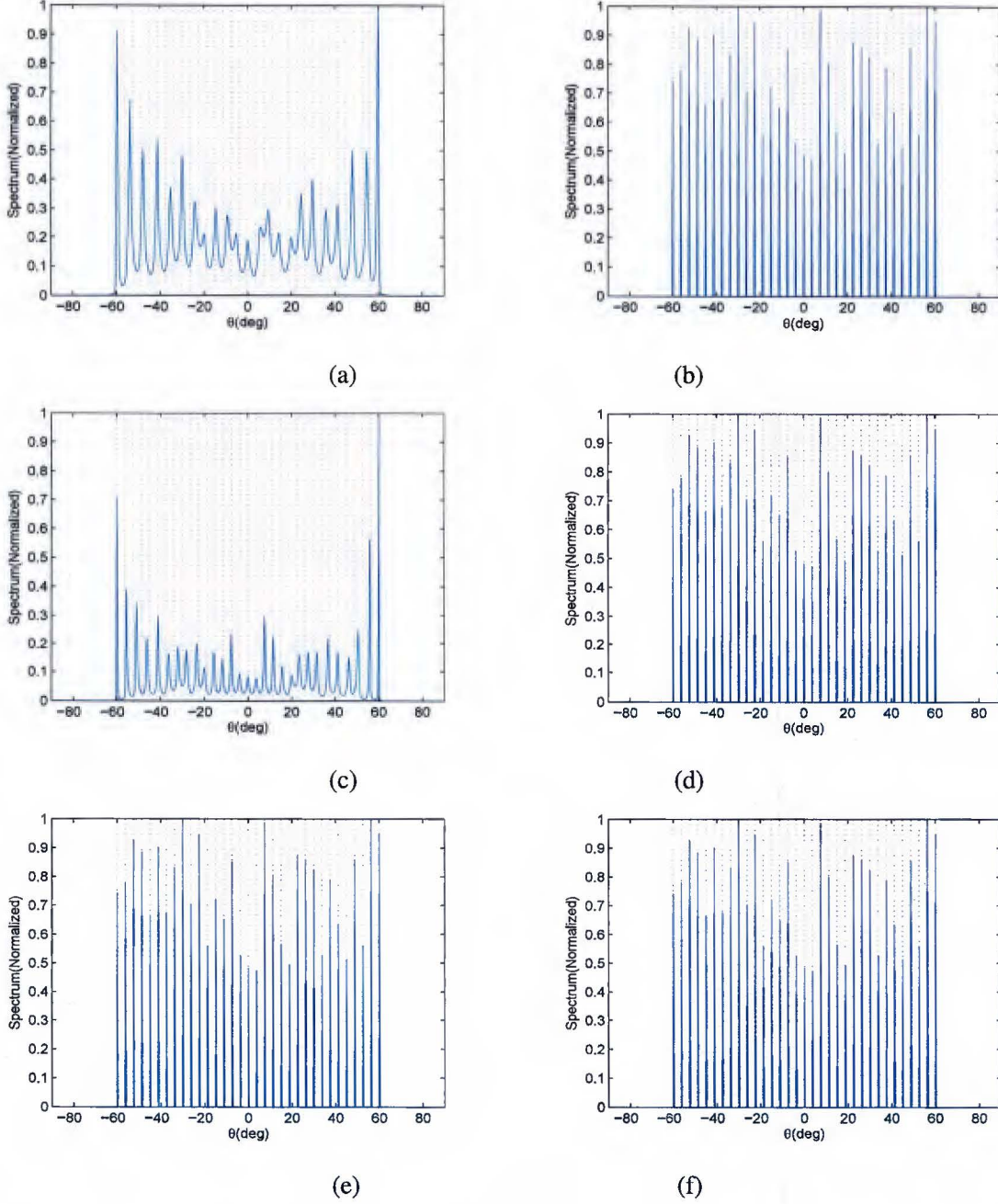


Fig. 12. Spatial spectra estimated using Lasso for both configurations ($Q=33$, $M = 6$ and $N = 7$). (a) CACIS with $p=2$. (b) CADiS with $p=2$. (c) CACIS with $p=3$. (d) CADiS with $p=3$. (e) CACIS with $p=6$. (f) CADiS with $p=6$.

X. APPENDIX

A. Proof of Proposition 1

(a) We prove it using contradiction. Denote $\tilde{l}_{c_1} = Nm_1 - \check{M}n_1$ and $\tilde{l}_{c_2} = Nm_2 - \check{M}n_2$ as two arbitrary

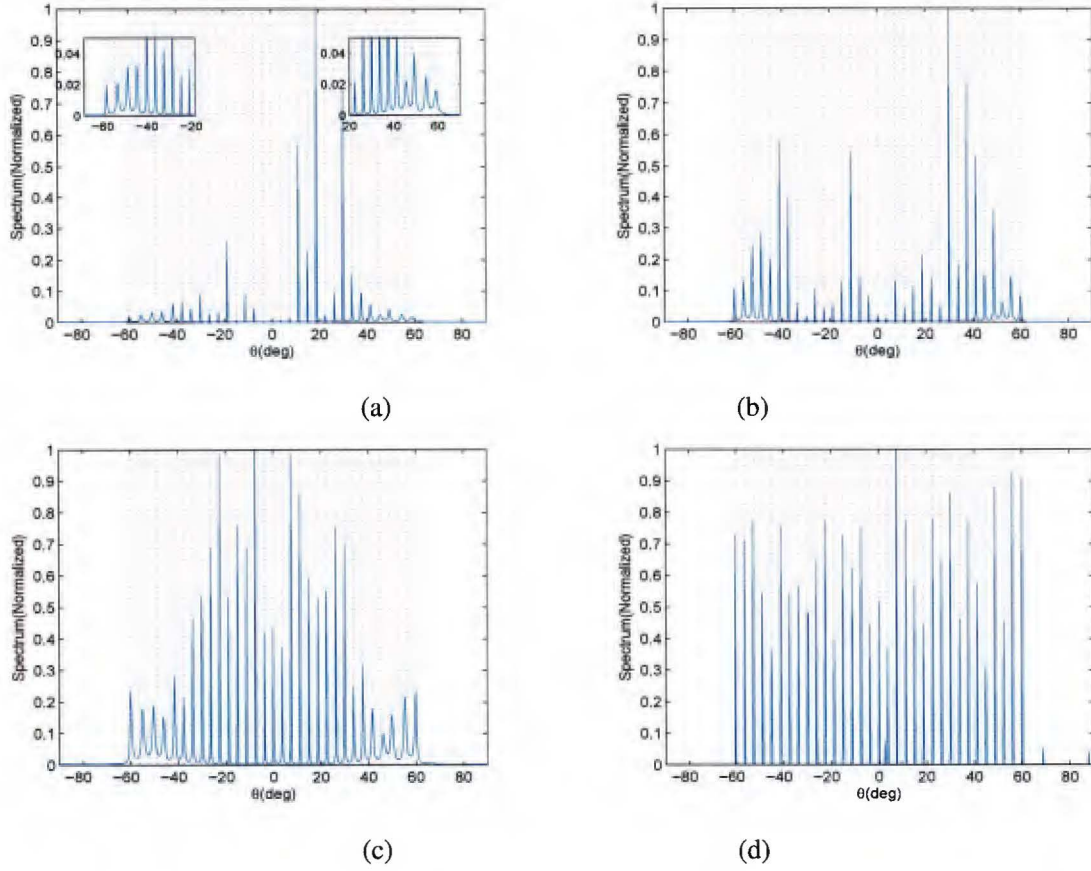


Fig. 13. Estimated spatial spectra (SNR=0 dB, 500 snapshots, $Q=33$). (a) MUSIC with nested CACIS. (b) MUSIC with nested CADiS. (c) LASSO with nested CACIS. (d) LASSO with nested CADiS.

lags in set $\tilde{\mathcal{L}}_c$, where $0 \leq m_1 \leq M-1$, $0 \leq m_2 \leq M-1$, $0 \leq n_1 \leq N-1$ and $0 \leq n_2 \leq N-1$. Had $\tilde{l}_{c_1} = \tilde{l}_{c_2}$ been held, we would have

$$\frac{\check{M}}{N} = \frac{m_1 - m_2}{n_1 - n_2}. \quad (22)$$

Since $n_1 - n_2 < N$, (22) cannot hold due to the coprimality of \check{M} and N . That is, \tilde{l}_{c_1} and \tilde{l}_{c_2} cannot be equal. Thus, $\tilde{\mathcal{L}}_c$ has MN distinct integers.

(b) Given an arbitrary integer \tilde{l}_c in set $\tilde{\mathcal{L}}_c$ satisfying

$$-(N-1) \leq \tilde{l}_c \leq MN - \check{M}(N-1) - 1, \quad (23)$$

we need to prove that there exist integers $m \in [0, M-1]$ and $n \in [0, N-1]$ such that $\tilde{l}_c = Nm - \check{M}n$ holds. The requirement $n \in [0, N-1]$ is equivalent to

$$0 \leq \check{M}n \leq \check{M}(N-1). \quad (24)$$

Because $Nm = \tilde{l}_c + \check{M}n$, we obtain the following relationship by combining (23) and (24),

$$-(N-1) \leq Nm \leq MN-1. \quad (25)$$

This result can be equivalently expressed as $-N < Nm < MN$, which implies $-1 < m < M$.

Because m is an integer, this requirement is equivalent to

$$0 \leq m \leq M-1, \quad (26)$$

which is satisfied in the underlying coprime array.

Remark: The configuration proposed in [13] becomes a special case of CACIS configuration, as $M = 2\check{M}$. As a result, the set $\tilde{\mathbb{L}}_c$ contains all the integers in the range $-(N-1) \leq \tilde{l}_c \leq \check{M}N + \check{M} - 1$. Apparently, our result contains more consecutive lags and more precise than the results provided in [13] using the same configuration. In [13], they only count the consecutive \tilde{l}_c in the range $[0, \check{M}N]$.

- (c) Given an arbitrary integer in set $\tilde{\mathbb{L}}_c$ satisfying $\tilde{l}_c = Nm - \check{M}n < 0$, where $m \in [0, M-1]$ and $n \in [0, N-1]$, the following relationship can be obtained

$$0 \leq Nm < \check{M}n \leq \check{M}(N-1) < \check{M}N. \quad (27)$$

Consequently, the set $\tilde{\mathbb{L}}_{c-}$, which consists of the negative elements in $\tilde{\mathbb{L}}_c$, can be expressed as

$$\tilde{\mathbb{L}}_{c-} = \{\tilde{l}_c | \tilde{l}_c = Nm - \check{M}n, Nm < \check{M}n\}, \quad (28)$$

where $0 \leq m \leq M-1$ and $0 < n \leq N-1$.

Considering an arbitrary integer $\tilde{l}_{c_1} = Nm_1 - \check{M}n_1$ in set $\tilde{\mathbb{L}}_{c-}$, where $Nm_1 < \check{M}n_1$, $m_1 \in [0, M-1]$ and $n_1 \in (0, N-1]$, then we need to prove that there always exists \tilde{l}_{c_2} in set $\tilde{\mathbb{L}}_c$ to satisfy

$$\tilde{l}_{c_2} = Nm_2 - \check{M}n_2 = -\tilde{l}_{c_1} = \check{M}n_1 - Nm_1, \quad (29)$$

where integers $m_2 \in [0, M-1]$ and $n_2 \in [0, N-1]$.

Then the relationship

$$\frac{\check{M}}{N} = \frac{m_1 + m_2}{n_1 + n_2}, \quad (30)$$

must be valid. Since $n_1 + n_2 \in (0, 2N)$ and \check{M} and N are coprime, it is indicated that \check{M}/N cannot be reduced to a ratio of smaller integers. As a result, the requirement is equivalent to

$$\begin{aligned} m_2 &= \check{M} - m_1, \\ n_2 &= N - n_1, \end{aligned} \quad (31)$$

It is clear that there always exists $m_2 \in [1, \check{M}] \subseteq [0, M-1]$ and $n_2 \in [0, N-1]$ to satisfy (31).

(d) Because the two subarrays share the first sensor at the zeroth position, the self-lags can be taken as cross-lags between every sensor of one subarray and the first sensor of the other subarray. Thus, $(\tilde{\mathbb{L}}_s^- \cup \tilde{\mathbb{L}}_s) \subseteq (\tilde{\mathbb{L}}_c^- \cup \tilde{\mathbb{L}}_c)$.

(e) We prove the proposition by contradiction. Based on (28), we suppose $Nm - \check{M}n = -(a\check{M} + bN)$ holds for some integers $m \in (0, \check{M})$ and $n \in (0, N)$, where $a \geq 0$ and $b > 0$ are integers, then relationship

$$\frac{\check{M}}{N} = \frac{m+b}{n-a} \quad (32)$$

must be valid. From $0 < n < N$ and $a \geq 0$, we find $n - a < N$. As such, due to the coprimality between \check{M} and N , we cannot find an integer m that satisfies (32). Therefore, $Nm - \check{M}n \neq -(a\check{M} + bN)$, i.e., there are holes at $-(a\check{M} + bN)$ in set $\tilde{\mathbb{L}}_c$.

B. Proof of Proposition 2

(a) In line with the property (d) of Proposition 1, the full symmetric set of lags which defined in (10) can be expressed as

$$\tilde{\mathbb{L}}_P = \tilde{\mathbb{L}}_c^- \cup \tilde{\mathbb{L}}_c. \quad (33)$$

Because $\tilde{\mathbb{L}}_c$ can be denoted as

$$\tilde{\mathbb{L}}_c = \{\tilde{l}_c | \tilde{l}_c \geq 0, \tilde{l}_c \in \tilde{\mathbb{L}}_c\} \cup \{\tilde{l}_c | \tilde{l}_c < 0, \tilde{l}_c \in \tilde{\mathbb{L}}_c\}, \quad (34)$$

(33) is equivalent to

$$\tilde{\mathbb{L}}_P = \{\pm \tilde{l}_c | \tilde{l}_c \geq 0, \tilde{l}_c \in \tilde{\mathbb{L}}_c\} \cup \{\pm \tilde{l}_c | \tilde{l}_c < 0, \tilde{l}_c \in \tilde{\mathbb{L}}_c\}. \quad (35)$$

Based on the property (c) of Proposition 1, the negative values form a subset of the flipped positive values in set $\tilde{\mathbb{L}}_c$. It is indicated that $\{\tilde{l}_c | \tilde{l}_c < 0, \tilde{l}_c \in \tilde{\mathbb{L}}_c\} \subseteq \{-\tilde{l}_c | \tilde{l}_c > 0, \tilde{l}_c \in \tilde{\mathbb{L}}_c\}$ and $\{-\tilde{l}_c | \tilde{l}_c < 0, \tilde{l}_c \in \tilde{\mathbb{L}}_c\} \subseteq \{\tilde{l}_c | \tilde{l}_c > 0, \tilde{l}_c \in \tilde{\mathbb{L}}_c\}$. Finally, the set $\tilde{\mathbb{L}}_P$ becomes

$$\tilde{\mathbb{L}}_P = \{\tilde{l}_c | \tilde{l}_c \geq 0, \tilde{l}_c \in \tilde{\mathbb{L}}_c\} \cup \{-\tilde{l}_c | \tilde{l}_c \geq 0, \tilde{l}_c \in \tilde{\mathbb{L}}_c\}, \quad (36)$$

Denote $\tilde{\eta}_c$ and $\tilde{\eta}_{c-}$ as the number of distinct lags in set $\tilde{\mathbb{L}}_c$ and $\tilde{\mathbb{L}}_{c-}$, respectively. As a result of (36), the number of distinct lags in set $\tilde{\mathbb{L}}_P$ can be expressed as

$$\tilde{\eta}_P = 2(\tilde{\eta}_c - \tilde{\eta}_{c-}) - 1, \quad (37)$$

where $\tilde{\eta}_c - \tilde{\eta}_{c-}$ represents the number of non-negative lags in set $\tilde{\mathbb{L}}_c$.

Due to the property (a) of Proposition 1, there are MN distinct integers in set $\tilde{\mathbb{L}}_c$. It is easy to confirm that

$$\tilde{\eta}_c = MN. \quad (38)$$

$\tilde{\eta}_P$ can be obtained easily if given $\tilde{\eta}_{c-}$. Next, the derivation of $\tilde{\eta}_{c-}$ is given as follows.

According to the definition of $\tilde{\mathbb{L}}_{c-}$ defined in (28),

$$\tilde{\mathbb{L}}_{c-} = \{\tilde{l}_c | \tilde{l}_c = Nm - \check{M}n, Nm < \check{M}n\},$$

where $0 \leq m \leq \check{M} - 1$ and $0 < n \leq N - 1$.

For illustration, the geometry distribution of m and n , is shown in Fig. 16. As such, the boundary and interior of the shadow part **R1** represents all elements in $\tilde{\mathbb{L}}_{c-}$. Since \check{M} and N are coprime, there is no integer point on the diagonal line between OB. In addition, the shadow part **R1** is symmetric with **R2**. As a consequence, for obtaining the number of elements in set $\tilde{\mathbb{L}}_{c-}$, we can first calculate the number of integer points in the rectangle within $[0, \check{M}]$ and $[1, N - 1]$ and then get the half of that number.

There are $(\check{M} + 1)$ and $(N - 1)$ integers in the range $[0, \check{M}]$ and $[1, N - 1]$, respectively, thus, we obtain

$$\tilde{\eta}_{c-} = \frac{(\check{M} + 1)(N - 1)}{2}, \quad (39)$$

Finally, substituting (38) and (39) into (37),

$$\tilde{\eta}_P = 2MN - (\check{M} + 1)(N - 1) - 1, \quad (40)$$

is derived analytically.

- (b) On the basis of property (b) of Proposition 1, $\tilde{\mathbb{L}}_c$ contains all the contiguous integers in the range $-(N - 1) \leq \tilde{l}_c \leq MN - \check{M}(N - 1) - 1$. Then, it is easy to confirm that $\tilde{\mathbb{L}}_P$ contains $2MN - 2\check{M}(N - 1) - 1$ consecutive integers in the range $[-MN + \check{M}(N - 1) + 1, MN - \check{M}(N - 1) - 1]$ in terms of (36).

C. Proof of Proposition 3

- (a) The proof can be extended from the proof of property (a) of Proposition 1, i.e., two arbitrary lags \bar{l}_{c_1} and \bar{l}_{c_2} in set $\bar{\mathbb{L}}_c$ cannot be equal. Thus, $\bar{\mathbb{L}}_c$ has $(M - 1)N$ distinct integers.
- (b) The set $\bar{\mathbb{L}}_c$ can be rewritten as

$$\bar{\mathbb{L}}_c = \{\bar{l}_c | \bar{l}_c = \check{M}(N - 1) + z + L\}, \quad (41)$$

where $0 \leq m \leq M - 2$ and $0 \leq n \leq N - 1$, for different values of z that falls into the following set,

$$\mathbb{Z} = \{z | z = Nm - \check{M}n, 0 \leq m \leq M - 2, 0 \leq n \leq N - 1\}. \quad (42)$$

Extended from the proof of the property (b) of Proposition 1, we can conclude that z is consecutive in the range

$$-(N-1) \leq z \leq MN - \check{M}(N-1) - N - 1. \quad (43)$$

Combining (41) and (43), $\bar{\mathbb{L}}_c$ contains all the contiguous integers in the range

$$(\check{M}-1)(N-1) + L \leq \bar{l}_c \leq MN - N - 1 + L. \quad (44)$$

- (c) Based on the the proof of property (e) of Proposition 1, it is easy to confirm that there are some holes located at $-(a\check{M} + bN)$ in the negative range of set \mathbb{Z} , where $a \geq 0, b > 0$ are integers. Then we can draw a conclusion that there are holes located at $\check{M}(N-1) - (a\check{M} + bN) + L$ in set $\bar{\mathbb{L}}_c$ by combining (41) and (42).
- (d) Due to the displacement, the two subarray do not share the first sensor any more. Considering the elements in set $\bar{\mathbb{L}}_s$, $0 \notin \bar{\mathbb{L}}_c$ because the minimum value in $\bar{\mathbb{L}}_c$ is L , which is larger than 1. Consequently, $(\bar{\mathbb{L}}_s^- \cup \bar{\mathbb{L}}_s) \not\subseteq (\bar{\mathbb{L}}_c^- \cup \bar{\mathbb{L}}_c)$.

D. Proof of Proposition 4

- (a) Denote $\bar{\eta}_s$ and $\bar{\eta}_c$ as the number of the distinct lags in sets $\bar{\mathbb{L}}_s$ and $\bar{\mathbb{L}}_c$, respectively, and $\bar{\eta}_o$ as the number of overlaps between the $\bar{\mathbb{L}}_s$ and $\bar{\mathbb{L}}_c$. Based on the definition of $\bar{\mathbb{L}}_P$ and $\bar{\mathbb{L}}_s$ in (21), all lags in these sets are positive. As a consequence of this, the number of full symmetric set of lags in the virtual array can be expressed as

$$\bar{\eta}_P = 2(\bar{\eta}_s + \bar{\eta}_c - \bar{\eta}_o) - 1. \quad (45)$$

Because of the coprimality of \check{M} and N , $\check{M}n \neq Nm$ for $n \in (0, N-1]$ and $m \in (0, M-2]$. As such,

$$\bar{\eta}_s = M + N - 2. \quad (46)$$

In line with the property (a) of Proposition 1, we can obtain

$$\bar{\eta}_c = (M-1)N. \quad (47)$$

Substituting (46) and (47) into (45), the relationship is equivalent to

$$\bar{\eta}_P = 2(MN + M - 2 - \bar{\eta}_o) - 1. \quad (48)$$

When $L > N(M-2)$, the maximum value in $\bar{\mathbb{L}}_s$ is less than the minimum value in $\bar{\mathbb{L}}_c$. It signifies that there is no overlap between \bar{l}_s and \bar{l}_c , i.e., $\bar{\eta}_o = 0$. Then the maximum number of unique lags, which is $2MN + 2M - 5$, can be achieved.

- (b) Due to the coprimality of \check{M} and N , any integer value for displacement, L , can be realized by an appropriate choice of integers c_1 and c_2 , i.e., [30]

$$L = c_1\check{M} + c_2N. \quad (49)$$

Based on the property (c) of the Proposition 3, there are holes located at $\check{M}(N-1) - (a\check{M} + bN) + L$ in set $\bar{\mathbb{L}}_c$, where with a and b are integers and $a \in [0, \infty)$, $b \in (0, \infty)$. If some holes are aligned by the elements in $\bar{\mathbb{L}}_s$, the following relationship

$$\check{M}(N-1) - (a\check{M} + bN) + L = Nm, \quad (50)$$

or

$$\check{M}(N-1) - (a\check{M} + bN) + L = \check{M}n \quad (51)$$

must be valid. Substituting (49) into (50) and (51), the requirement is equivalent to

$$\check{M}N + (c_1 - a - 1)\check{M} + (c_2 - b)N = Nm,$$

or

$$\check{M}N + (c_1 - a - 1)\check{M} + (c_2 - b)N = \check{M}n,$$

i.e.,

$$c_1 = a + 1 \quad \text{or} \quad c_2 = b. \quad (52)$$

Then the requirement further becomes

$$c_1 = 1 \quad \text{or} \quad c_2 = 1, \quad (53)$$

so that the first hole ($a = 0$ and $b = 1$), which is outside the consecutive range of $\bar{\mathbb{L}}_c$, can be aligned.

When $c_1 = 1$, i.e., $L = \check{M} + c_2N$, the holes, where $a = 0$ and arbitrary $b > 0$,

$$\begin{aligned} & \check{M}(N-1) - bN + L \\ &= \check{M}(N-1) - bN + \check{M} + c_2N \\ &= (\check{M} - b + c_2)N, \end{aligned} \quad (54)$$

are aligned.

When $c_2 = 1$, i.e., $L = c_1\check{M} + N$, the holes, where arbitrary $a \geq 0$ and $b = 1$,

$$\begin{aligned} & \check{M}(N-1) - (a\check{M} + N) + L \\ &= \check{M}(N-1) - (a\check{M} + N) + c_1\check{M} + N \\ &= (N-1-a+c_1)\check{M}, \end{aligned}$$

are aligned.

Thus, $c_1 = c_2 = 1$, i.e., $L = \check{M} + N$, is the optimal choice since all above holes can be aligned. In this case, the holes, where $a = 0$ and $b = 1$, $a = 0$ and $b = 2$, $a = 1$ and $b = 1$, are aligned. As a result, the first hole outside the consecutive range of $\bar{\mathbb{L}}_c$ becomes $\check{M}(N - 1) - (\check{M} + 2N) + L$ where $a = 1$ and $b = 2$. Then, the set $\bar{\mathbb{L}}_c$ contains all the consecutive integers in the range

$$\check{M}(N - 1) - (\check{M} + 2N - 1) + L \leq \bar{l}_c \leq MN - N - 1 + L, \quad (55)$$

where $L = \check{M} + N$.

It is simplified as,

$$(\check{M} - 1)(N - 1) \leq \bar{l}_c \leq MN + \check{M} - 1. \quad (56)$$

Next, we give the proof of the number of the unique lags when $L = \check{M} + N$. The following relationship

$$\check{M}(N - 1) + (Nm_1 - \check{M}n_1) + \check{M} + N = Nm_2, \quad (57)$$

or

$$\check{M}(N - 1) + (Nm_1 - \check{M}n_1) + \check{M} + N = \check{M}n_2, \quad (58)$$

must be valid if $\bar{\mathbb{L}}_s$ overlaps with $\bar{\mathbb{L}}_c$. It is equivalent to

$$\check{M} + m_1 + 1 - n_1 \frac{\check{M}}{N} = m_2, \quad (59)$$

or

$$N - n_1 + (m_1 + 1) \frac{N}{\check{M}} = n_2. \quad (60)$$

In (59), n_1 must be equal to 0 because m_2 is an integer, yielding

$$\check{M} + m_1 + 1 = m_2. \quad (61)$$

It is clear to confirm $m_2 \in [0, M - \check{M} - 3]$ since $m_1 \in [0, M - 2]$. This suggests that the number of the overlaps in (59) is $M - \check{M} - 2$. Similarly, we can show the number of overlaps in (60) is 0. Hence,

$$\bar{\eta}_o = M - \check{M} - 2. \quad (62)$$

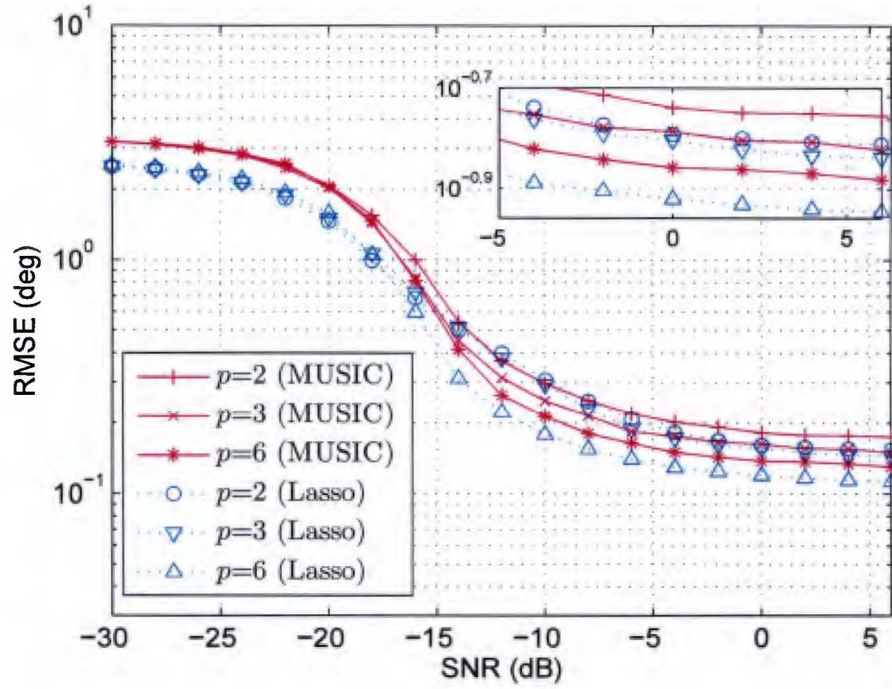
Substituting (62) into (48), we can obtain the number of unique lags $\bar{\eta}_P$ to be

$$\bar{\eta}_P = 2MN + 2\check{M} - 1. \quad (63)$$

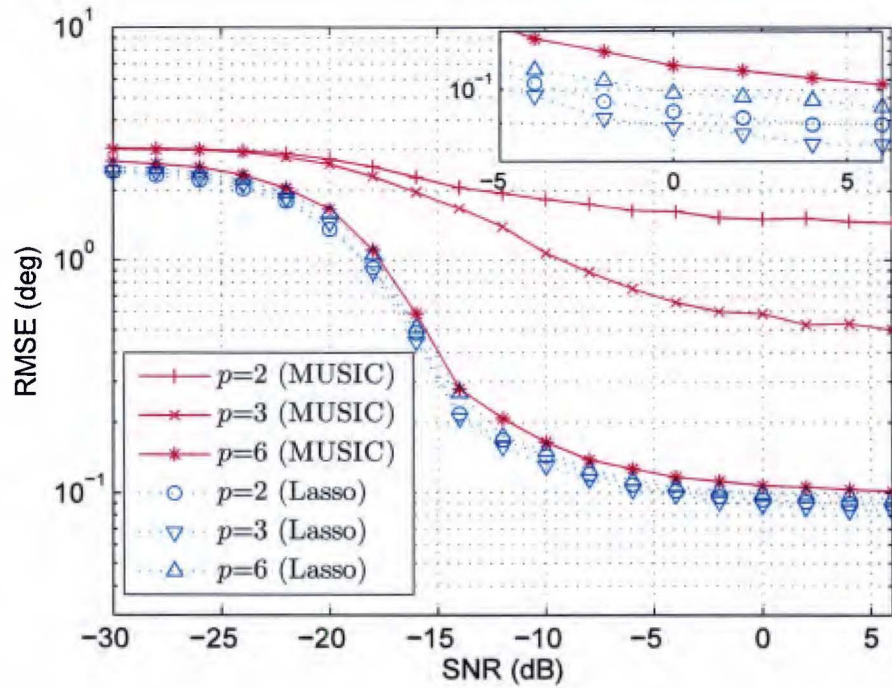
REFERENCES

- [1] Y. D. Zhang, S. Qin, and M. G. Amin, "DOA estimation exploiting coprime arrays with sparse sensor spacing," in *Proc. IEEE ICASSP*, Florence, Italy, pp. 2267–2271, May 2014.
- [2] S. Qin, Y. D. Zhang, and M. G. Amin, "Generalized coprime array configurations," in *Proc. IEEE Sensor Array and Multichannel Signal Processing Workshop*, A Coruña, Spain, June 2014.
- [3] R. O. Schmidt, "Multiple emitter location and signal parameter estimation," *IEEE Trans. Antennas Propagat.*, vol. 34, no. 3, pp. 276–280, March 1986.
- [4] R. Roy and T. Kailath, "ESPRIT – Estimation of signal parameters via rotation invariance techniques," *IEEE Trans. Acoust., Speech, Signal Proc.*, vol. 17, no. 7, pp. 984–995, July 1989.
- [5] S. Pillai, *Array Signal Processing*, Springer, 1989.
- [6] R. T. Hoctor and S. A. Kassam, "The unifying role of the co-array in aperture synthesis for coherent and incoherent imaging," *Proc. IEEE*, vol. 78, no. 4, pp. 735–752, April 1990.
- [7] A. Moffet, "Minimum-redundancy linear arrays," *IEEE Trans. Antennas Propagat.*, vol. 16, no. 2, pp. 172–175, March 1968.
- [8] G. S. Bloom and S. W. Golomb, "Application of numbered undirected graphs," *Proc. IEEE*, vol. 65, no. 4, pp. 562–570, April 1977.
- [9] P. Pal and P. P. Vaidyanathan, "Nested arrays: A novel approach to array processing with enhanced degrees of freedom," *IEEE Trans. Signal Proc.*, vol. 58, no. 8, pp. 4167–4181, Aug. 2010.
- [10] I. J. Gupta and A. A. Ksienski, "Effect of mutual coupling on the performance of adaptive arrays," *IEEE Trans. Antennas Propagat.*, vol. AP-31, no. 5, Sept. 1983.
- [11] Y. Zhang, K. Hirasawa, and K. Fujimoto, "Signal bandwidth consideration of mutual coupling effects on adaptive array performance," *IEEE Trans. Antennas Propagat.*, vol. AP-35, no. 3, pp. 337–339, March 1987.
- [12] P. P. Vaidyanathan and P. Pal, "Sparse sensing with co-prime samplers and arrays," *IEEE Trans. Signal Proc.*, vol. 59, no. 2, pp. 573–586, Feb. 2011.
- [13] P. Pal and P. P. Vaidyanathan, "Coprime sampling and the MUSIC algorithm," in *Proc. IEEE Digital Signal Proc. Workshop and IEEE Signal Proc. Education Workshop*, Sedona, AZ, Jan. 2011.
- [14] W. C. Barott and P. G. Steffes, "Grating lobe reduction in aperiodic linear arrays of physically large antennas," *IEEE Antennas and Wireless Propagation Letters*, vol. 8, pp. 406–408, 2009.
- [15] Y. Rahmat-Samii, "Reflector antennas," Chapter 15, in J. L. Volakis (Ed.), *Antenna Engineering Handbook, Fourth Edition*. New York, NY: McGraw-Hill, 2007.
- [16] Q. Shen, W. Liu, W. Cui, S. W. Y. D. Zhang, and M. G. Amin, "Group sparsity based wideband DOA estimation for co-prime arrays," in *Proc. IEEE China Summit and International Conference on Signal and Information Processing*, Xi'an, China, July 2014.
- [17] Y. D. Zhang, M. G. Amin, F. Ahmad, and B. Himed, "DOA estimation using a sparse uniform linear array with two CW signals of co-prime frequencies," in *Proc. IEEE Int. Workshop on Comp. Adv. in Multi-Sensor Adaptive Proc.*, Saint Martin, pp. 404–407, Dec. 2013.

- [18] S. Qin, Y. D. Zhang, and M. G. Amin, "DOA estimation exploiting coprime frequencies," in *Proc. SPIE Wireless Sensing, Localization, and Processing Conference*, vol. 9103, Baltimore, MD, May 2014.
- [19] T.-J. Shan, M. Wax, and T. Kailath, "On spatial smoothing for direction-of-arrival estimation of coherent signals," *IEEE Trans. Acoust., Speech Signal Process.*, vol. 33, no. 4, pp. 806-811, Aug. 1985.
- [20] B. Friedlander and A. J. Weiss, "Direction finding using spatial smoothing with interpolated arrays," *IEEE Trans. Aerosp., Electron. Syst.*, vol. 28, pp. 574-587, Apr. 1992.
- [21] S. U. Pillai and B. H. Kwon, "Forward/backward spatial smoothing techniques for coherent signal identification," *IEEE Trans. Acoust., Speech Signal Process.*, vol. 37, no. 1, pp. 8-15, Jan. 1989.
- [22] P. Pal and P. P. Vaidyanathan, "On application of LASSO for sparse support recovery with imperfect correlation awareness," in *Proc. Asilomar Conf. Signals, Systems and Computers*, Pacific Grove, CA, Nov. 2012.
- [23] Y. D. Zhang, M. G. Amin, and B. Himed, "Sparsity-based DOA estimation using co-prime arrays," in *Proc. IEEE ICASSP*, Vancouver, Canada, pp. 3967-3971, May 2013.
- [24] R. Tibshirani, "Regression shrinkage and selection via the lasso," *J. Royal Statistical Society, Series B*, vol. 58, no. 1, pp. 267-288, 1996.
- [25] S. S. Chen, D. L. Donoho, and M. A. Saunders, "Atomic decomposition by basis pursuit," *SIAM Journal on Scientific Computing*, vol. 20, no. 1, pp. 33-61, 1998.
- [26] J. A. Tropp and A. C. Gilbert, "Signal recovery from random measurements via orthogonal matching pursuit," *IEEE Trans. Info. Theory*, vol. 53, no. 12, pp. 4655-4666, 2007.
- [27] S. Ji, D. Dunson, and L. Carin, "Multi-task compressive sampling," *IEEE Trans. Signal Proc.*, vol. 57, no. 1, pp. 92-106, Jan. 2009.
- [28] Q. Wu, Y. D. Zhang, M. G. Amin, and B. Himed, "Complex multitask Bayesian compressive sensing," in *Proc. IEEE ICASSP*, Florence, Italy, pp. 3375-3379, May 2014.
- [29] D. P. Bertsekas, *Nonlinear Programming, Second Edition*. Athena Scientific, 1999.
- [30] P. P. Vaidyanathan and P. Pal, "Sparse sensing with coprime arrays," in *Proc. Asilomar Conf. Signals, Systems and Computers*, Pacific Grove, CA, Nov. 2010.

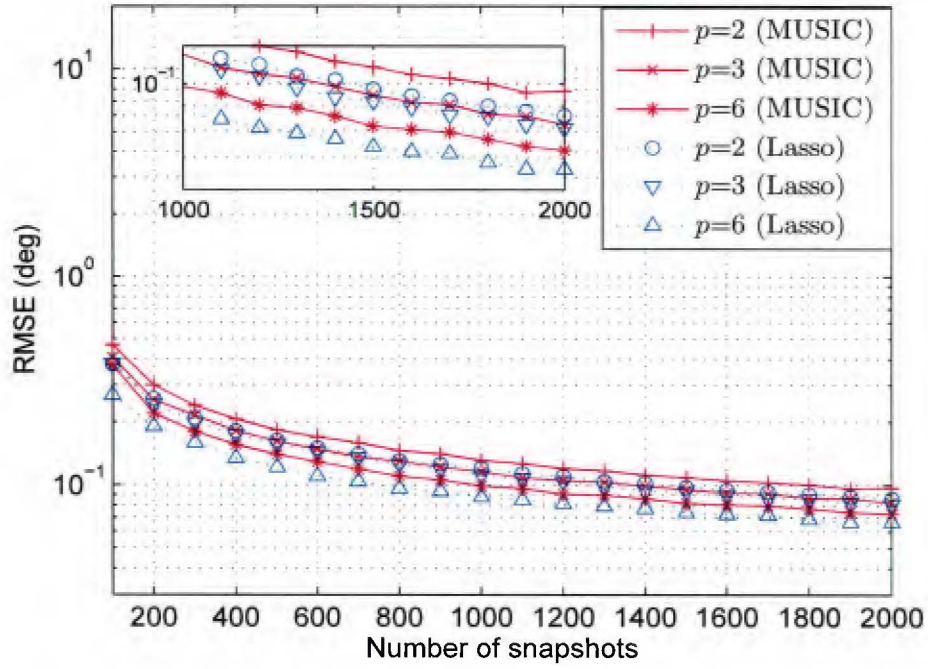


(a)

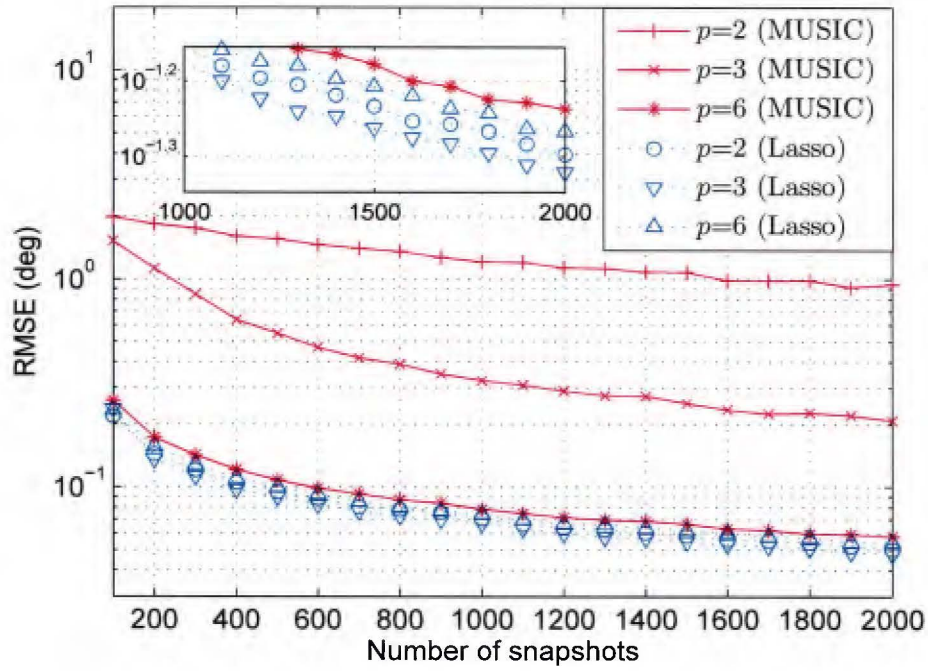


(b)

Fig. 14. RMSE versus SNR (500 snapshots, $Q=16$). (a) The CACIS configurations. (b) The CADiS configurations.



(a)



(b)

Fig. 15. RMSE versus the number of snapshots (SNR=0 dB, $Q=16$). (a) The CACIS configurations. (b) The CADiS configurations.

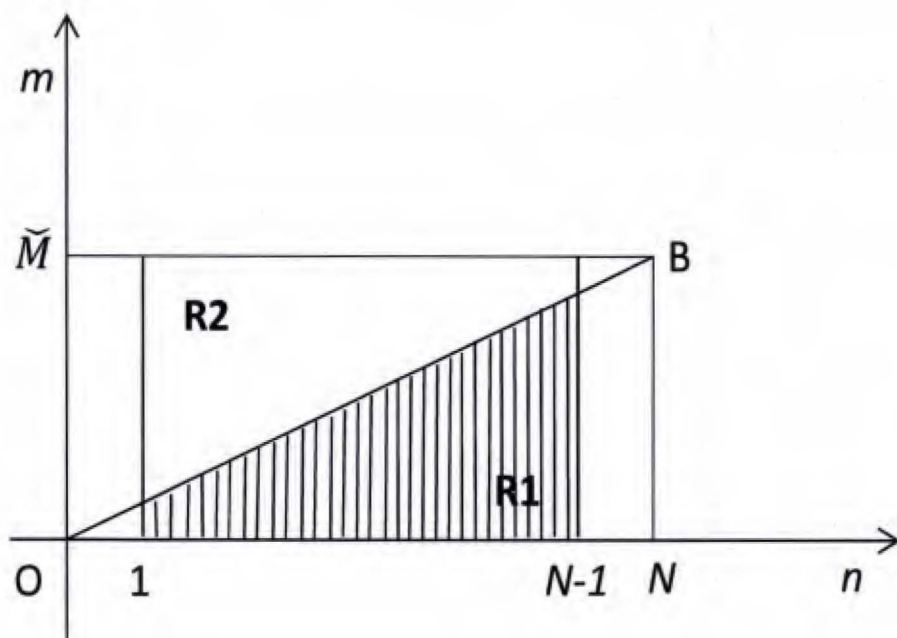


Fig. 16. The geometry of m and n .

3.2. Multi-Frequency Co-Prime Arrays for High-Resolution Direction-of-Arrival Estimation

Abstract

This paper presents multi-frequency operation for increasing the number of resolvable sources in high-resolution direction-of-arrival (DOA) estimation using co-prime arrays. A single-frequency operation requires complicated and involved matrix completion to utilize the full extent of the degrees of freedom (DOFs) offered by the co-prime configuration. This processing complexity is attributed to the missing elements in the corresponding difference coarray. Alternate single-frequency schemes avoid such complexity by utilizing only the filled part of the coarray and, thus, cannot exploit all of the DOFs for DOA estimation. We utilize multiple frequencies to fill the missing coarray elements, thereby enabling the co-prime array to effectively utilize all of the offered DOFs. The sources are assumed to have a sufficient bandwidth to cover all the required operational frequencies. We consider both cases of sources with proportional and nonproportional power spectra at the employed frequencies. The former permits the use of multi-frequency measurements at the co-prime array to construct a virtual covariance matrix corresponding to a filled uniformly spaced coarray at a single frequency. This virtual covariance matrix can be employed for DOA estimation. The nonproportionality of the source spectra casts a more challenging situation, as it is not amenable to producing the same effect as that of an equivalent single-frequency filled coarray. Performance evaluation of the multi-frequency approach based on computer simulations is provided under both cases of proportional and nonproportional source spectra.

I. INTRODUCTION

Nonuniform linear arrays provide the ability to estimate the direction-of-arrival (DOA) of more sources than the number of physical sensors [1]-[6]. Recently, a new structure of nonuniform linear arrays, known as co-prime arrays, has been proposed [7], [8]. A co-prime configuration comprises two undersampled uniformly spaced subarrays with co-prime number of elements and co-prime spatial sampling rates. Co-prime configurations have many advantages over other popular nonuniform configurations, including

minimum redundancy arrays (MRA) [9], minimum hole arrays (MHA) [10], and nested arrays [11]. For a given number of physical sensors, MRAs and MHAs require an exhaustive search through all possible combinations of the sensors to find the optimal design [12], [13]. On the other hand, the positions of the sensors constituting the co-prime configuration have closed-form expressions. Although the same is true of nested arrays, the elements of one of the subarrays constituting the nested structure are closely separated, which may lead to problems due to mutual coupling between the sensors. Co-prime arrays reduce the mutual coupling between most adjacent sensors by spacing them farther apart [7]. Because of all of the aforementioned characteristics, co-prime arrays are finding broad applications in the areas of communications, radar, and sonar [14]-[20].

Similar to other nonuniform arrays, high-resolution DOA estimation with co-prime arrays can be performed using two main approaches. The first approach employs covariance matrix augmentation [21]-[23], while the second method vectorizes the data covariance matrix to emulate observations at a virtual array whose elements are given by the difference coarray (the set of all spatial lags generated by the physical array [24]) [8], [11]. Since the difference coarray of a co-prime array contains multiple missing elements or ‘holes’, the latter approach employs only that part of the difference coarray which has contiguous elements with no holes. As such, only a subset of the total degrees of freedom (DOFs) offered by the co-prime structure can be utilized for high-resolution DOA estimation using the vectorized covariance matrix approach. The augmented covariance matrix approach, on the other hand, can exploit all the DOFs but at the expense of additional complicated matrix completion processing [23].

In this paper, we consider multi-frequency operation to utilize all of the DOFs for DOA estimation in co-prime arrays. More specifically, a set of additional frequencies is employed to recover the missing lags through dilations of the coarray [25]. The sources are assumed to have a bandwidth large enough to cover all specific frequencies required for filling the holes. Only the array elements involved in filling the missing holes in the difference coarray are required to be operated at one or more of the additional frequencies. The multi-frequency measurements are used to construct a virtual covariance matrix corresponding to an equivalent filled uniformly spaced coarray at a single frequency [26]. High-resolution subspace techniques,

such as MUSIC [27], can then be applied to this virtual covariance matrix for DOA estimation. It is important to note that full utilization of the DOFs using multiple additional frequencies comes with a restriction on the sources' spectra. More specifically, the source spectra at all operational frequencies are required to be proportional. Deviations from this restriction can lead to higher DOA estimation errors.

Multiple frequencies have previously been used for alias-free DOA estimation of broadband sources [28], [29]. In [28], frequency diversity was exploited on a single spatial sampling interval to mitigate spatial aliasing in DOA estimation with a sparse nonuniformly spaced array. Ambiguities in the source location estimates were resolved by proper choice of chosen operational frequencies in [29] for arrays with periodic spatial spectra. Spatial sampling interval diversity at a single narrowband frequency was exploited in [7] to disambiguate aliased DOAs. Both spatial sampling and frequency diversity were exploited in [26] through multi-frequency coarray augmentation for high-resolution DOA estimation. However, no attempt was made therein to select the best number of employed frequencies or determine their best values. We effectively apply the multi-frequency coarray augmentation to co-prime arrays in this paper. Our main contribution lies in exploiting the specific structure of the coarray corresponding to co-prime configuration to determine the number and values of the additional frequencies required for recovering the missing lags. We provide closed-form expressions for the additional frequencies, which are 'best' in the sense of minimum operational bandwidth requirements. We also describe when and how the redundancy in the coarray can be exploited to reduce the system hardware complexity for multi-frequency co-prime arrays. Further, we investigate the effects of noise and deviation from the proportional source spectra constraint on the DOA estimation performance of the multi-frequency co-prime arrays.

The remainder of the paper is organized as follows. The single-frequency based high-resolution DOA estimation using co-prime arrays is reviewed in Section II. In Section III, we describe the multi-frequency approach for filling the missing elements in the coarray and utilizing all the DOFs offered by the co-prime configuration for DOA estimation. Section IV delineates the system bandwidth requirement for the multi-frequency operation, taking into account the specificities of the coarray structure corresponding to co-prime arrays. Coarray redundancy is also examined to reduce the number of antennas engaging in multiple

frequency operation. In Section V, performance of the proposed method is evaluated through extensive simulations under both proportional and nonproportional source spectra and Section VI concludes the paper.

II. HIGH-RESOLUTION DOA ESTIMATION USING SINGLE-FREQUENCY CO-PRIME ARRAYS

A co-prime array consists of two undersampled uniform linear subarrays, one having M sensors positioned at $\{Nmd_0, 0 \leq m \leq M-1\}$, and the other comprising N sensors with positions $\{Mnd_0, 0 \leq n \leq N-1\}$ [11], M and N being co-prime integers and d_0 equal to one-half wavelength at the operating frequency ω_0 . Without loss of generality, we assume $M < N$. With the two subarrays sharing the element at location 0, the co-prime array has a total of $M + N - 1$ physical sensors. The element positions of the corresponding difference coarray form the set

$$S_0 = \{\pm(Mnd_0 - Nmd_0)\}, 0 \leq n \leq N-1, 0 \leq m \leq M-1, \quad (1)$$

which extends from $-N(M-1)d_0$ to $N(M-1)d_0$, but only the elements from $-(M+N-1)d_0$ and $(M+N-1)d_0$ are contiguous. As such, high-resolution schemes, such as MUSIC, can estimate only up to $M + N - 1$ sources.

An extended co-prime configuration was proposed in [8], wherein the number of elements in the subarray with fewer sensors were doubled, as depicted in Fig. 1. The difference coarray of this configuration, shown in Fig. 2, extends from $-(2M-1)Nd_0$ to $(2M-1)Nd_0$, and has a contiguous set of elements between $-(MN+M-1)d_0$ and $(MN+M-1)d_0$. Thus, high-resolution DOA estimation can be performed to estimate $(MN+M-1)$ sources using the extended co-prime configuration. We will consider the extended co-prime configuration with $M < N$ in the remainder of this paper.

Assume that D sources with powers $\sigma_1^2(\omega_0), \sigma_2^2(\omega_0), \dots, \sigma_D^2(\omega_0)$ impinge on the extended co-prime array from directions $[\theta_1, \theta_2, \dots, \theta_D]$ where θ is measured relative to broadside. The received data vector at frequency ω_0 can be expressed as

$$\mathbf{x}(\omega_0) = \mathbf{A}(\omega_0)\mathbf{s}(\omega_0) + \mathbf{n}(\omega_0), \quad (2)$$

where $\mathbf{s}(\omega_0) = [s_1(\omega_0) s_2(\omega_0) \dots s_D(\omega_0)]^T$ is the source signal vector at ω_0 , $\mathbf{n}(\omega_0)$ is the corresponding

noise vector, $\mathbf{A}(\omega_0)$ is the array manifold matrix at ω_0 , and the superscript $(\cdot)^T$ denotes matrix transpose. The (i, j) th element of the array manifold can be expressed as

$$[\mathbf{A}(\omega_0)]_{i,j} = e^{jk_0 x_i \sin(\theta_j)}, i = 1, 2, \dots, 2M + N - 1, \quad j = 1, 2, \dots, D \quad (3)$$

where x_i is the location of the i th physical sensor of the array, θ_j is the DOA of the j th source, and $k_0 = \omega_0/c$ is the wavenumber at ω_0 with c being the speed of propagation in free space. Assuming that the sources are uncorrelated and the noise is spatially and temporally white, the covariance matrix is obtained as

$$\mathbf{R}_{xx}(\omega_0) = E\{\mathbf{x}(\omega_0)\mathbf{x}^H(\omega_0)\} = \mathbf{A}(\omega_0)\mathbf{R}_{ss}(\omega_0)\mathbf{A}^H(\omega_0) + \sigma_n^2(\omega_0)\mathbf{I}, \quad (4)$$

where $\mathbf{R}_{ss}(\omega_0) = \text{diag}([\sigma_1^2(\omega_0) \ \sigma_2^2(\omega_0) \ \dots \ \sigma_D^2(\omega_0)])$ is the source covariance matrix, $\sigma_n^2(\omega_0)$ is the noise variance, \mathbf{I} is an identity matrix, the superscript $(\cdot)^H$ denotes Hermitian operation, and $E\{\cdot\}$ denotes the statistical expectation operator. In practice, (4) is replaced by a sample average.

After forming the covariance matrix, two approaches can be employed to perform high-resolution DOA estimation. The first approach uses covariance matrix augmentation [21]-[23]. Following [22], since the difference coarray is filled between $-(MN + M - 1)d_0$ and $(MN + M - 1)d_0$, a virtual covariance matrix corresponding to an equivalent $(MN + M)$ -element filled ULA can be formed by collecting specific elements of the estimated spatial covariance matrix $\mathbf{R}_{xx}(\omega_0)$ into a Toeplitz matrix. The resulting augmented covariance matrix may not always be positive definite and, thus, requires positive definite Toeplitz completion [22]. Subspace-based high-resolution methods can then be applied to the augmented covariance matrix for estimating up to $(MN + M - 1)$ sources. The number of resolvable sources can be increased to $(2M - 1)N$ by considering a partially specified virtual covariance matrix corresponding to an equivalent $(2M - 1)N + 1$ -element filled ULA [23]. However, this comes at the expense of increased computational complexity due to a complicated and involved matrix completion process.

The second approach vectorizes the covariance matrix $\mathbf{R}_{xx}(\omega_0)$ as [7]

$$\mathbf{z}(\omega_0) = \text{vec}(\mathbf{R}_{xx}(\omega_0)) = \tilde{\mathbf{A}}(\omega_0)[\sigma_1^2(\omega_0) \ \sigma_2^2(\omega_0) \ \dots \ \sigma_D^2(\omega_0)]^T + \sigma_n^2(\omega_0)\mathbf{\tilde{I}}, \quad (5)$$

where $\tilde{\mathbf{A}}(\omega_0) = \mathbf{A}^*(\omega_0) \odot \mathbf{A}(\omega_0)$, the symbol ' \odot ' denotes the Khatri-Rao product, the superscript '**' denotes complex conjugate.

denotes complex conjugation, and $\tilde{\mathbf{I}}$ is the vectorized form of \mathbf{I} . The vector $\mathbf{z}(\omega_0)$ acts as the received signal vector of a longer array whose elements positions are given by the difference coarray. However, as the sources are replaced by their powers, the model in (5) is similar to that of a fully coherent source environment. Spatial smoothing can be used to decorrelate the sources [8], [30], provided that only the filled part of the difference coarray between $-(MN + M - 1)d_0$ and $(MN + M - 1)d_0$ is employed. As such, the rank of the smoothed covariance matrix is equal to $(MN + M)$ [8], [11], which allows a maximum of $(MN + M - 1)$ sources to be estimated by applying high-resolution techniques.

In the sequel, we employ the filled part of the coarray and covariance matrix augmentation for DOA estimation under single frequency operation.

III. HIGH RESOLUTION DOA ESTIMATION WITH MULTI-FREQUENCY CO-PRIME ARRAYS

In this section, we describe how dual and multiple frequencies can be utilized to fill the holes in the coarray, thereby permitting the exploitation of the full DOFs that the co-prime configuration has to offer. The sources are assumed to have a bandwidth large enough to cover all frequencies required for filling the holes. Discrete Fourier transform (DFT) or filterbanks are used to decompose the array output vector into multiple non-overlapping narrowband components and extract the received signal at each considered frequency [31], [32]. The observation time is assumed to be sufficiently long to resolve the different frequencies.

Consider the extended co-prime configuration of Fig. 1, where the unit spacing d_0 is assumed to be half-wavelength at the reference frequency ω_0 . The received signal at ω_0 is the same as in (2), whereas that obtained by operating the physical co-prime array at a different frequency, $\omega_q = \alpha_q \omega_0$, has the form

$$\mathbf{x}(\omega_q) = \mathbf{A}(\omega_q)\mathbf{s}(\omega_q) + \mathbf{n}(\omega_q), \quad (6)$$

where $\mathbf{A}(\omega_q)$ is the $(2M + N - 1) \times D$ array manifold at ω_q with its (i, j) th element given by

$$[\mathbf{A}(\omega_q)]_{i,j} = e^{jk_q x_i \sin(\theta_j)}. \quad (7)$$

In (7), $k_q = \omega_q/c$ is the wavenumber at ω_q . Since $k_q = \alpha_q k_0$, (7) can be rewritten as

$$[\mathbf{A}(\omega_q)]_{i,j} = e^{jk_0 \alpha_q x_i \sin(\theta_j)}. \quad (8)$$

Comparing (3) and (8), we observe that the array manifold at ω_q is equivalent to the array manifold at ω_0 of a scaled version of the physical co-prime array. The position of the i th element in the equivalent scaled array is given by $\alpha_q x_i$. This results in the difference coarray at ω_q to be a scaled version of the coarray at the reference frequency ω_0 [33]. Values of ω_q higher than ω_0 cause an expansion of the coarray, while the coarray contracts if ω_q is lower than ω_0 . In other words, operation at the additional frequency adds extra points at specific locations in the coarray. A suitable choice of additional operating frequencies will cause some of these extra points to occur at the locations of the holes in the difference coarray at ω_0 .

A. Virtual Covariance Matrix Formation

Let the total number of operational frequencies, including the reference, be Q . As shown below, a virtual covariance matrix can be constructed using the multi-frequency measurements, which is equivalent to that of a ULA with $(2M - 1)N + 1$ elements operating at the reference frequency [26], [34]. This would allow DOA estimation of $(2M - 1)N$ sources instead of $(MN + M - 1)$ sources using $(2M + N - 1)$ physical sensors of the co-prime array.

A $(2M + N - 1) \times (2M + N - 1)$ support matrix $\mathbf{C}(\omega_q)$ is defined such that its (i, j) th element is given by [26], [34]

$$[\mathbf{C}(\omega_q)]_{i,j} = \alpha_q x_i - \alpha_q x_j. \quad (9)$$

That is, the (i, j) th element of $\mathbf{C}(\omega_q)$ is the spatial lag or the coarray element position which is the support of the (i, j) th element of the covariance matrix $\mathbf{R}_{xx}(\omega_q)$

$$\mathbf{R}_{xx}(\omega_q) = E \left\{ \mathbf{x}(\omega_q) \mathbf{x}(\omega_q)^H \right\} = \mathbf{A}(\omega_q) \mathbf{R}_{ss}(\omega_q) \mathbf{A}^H(\omega_q) + \sigma_n^2(\omega_q) \mathbf{I}, \quad (10)$$

where $\mathbf{R}_{ss}(\omega_q) = \text{diag}([\sigma_1^2(\omega_q) \sigma_2^2(\omega_q) \dots \sigma_D^2(\omega_q)])$ is the source covariance matrix at frequency ω_q .

It should be noted that $\mathbf{C}(\omega_q) = \alpha_q \mathbf{C}(\omega_0)$, where $\mathbf{C}(\omega_0)$ is the support matrix at the reference frequency ω_0 . Let $\mathbf{C}_v(\omega_0)$ and $\mathbf{R}_v(\omega_0)$ be the support and the covariance matrices corresponding to the desired ULA with $(2M - 1)N + 1$ sensors operating at ω_0 . Given that the Q operational frequencies are sufficient to

fill all the holes in the difference coarray of the co-prime array, then

$$[\mathbf{C}_v(\omega_0)]_{i,j} = [\mathbf{C}(\omega_q)]_{p,r} \text{ for some } q, p, r \text{ and all } i, j \quad (11)$$

Let h be the map that arranges selected elements of the multi-frequency support matrices, $\{\mathbf{C}(\omega_q)\}_{q=0}^{Q-1}$, into the desired virtual support matrix $\mathbf{C}_v(\omega_0)$. Using the same map, the virtual covariance matrix $\mathbf{R}_v(\omega_0)$ corresponding to the equivalent ULA can then be constructed from the covariance matrices $\{\mathbf{R}_{xx}(\omega_q)\}_{q=0}^{Q-1}$ corresponding to the Q operational frequencies [26].

For illustration, we consider a co-prime array with $M = 2$ and $N = 3$. The sensor positions of the two uniform linear subarrays are given by $[0, 2d_0, 4d_0]$ and $[3d_0, 6d_0, 9d_0]$, respectively. The support matrix $\mathbf{C}(\omega_0)$ at the reference frequency takes the form

$$\mathbf{C}(\omega_0) = \begin{bmatrix} 0 & -2 & -3 & -4 & -6 & -9 \\ 2 & 0 & -1 & -2 & -4 & -7 \\ 3 & 1 & 0 & -1 & -3 & -6 \\ 4 & 2 & 1 & 0 & -2 & -5 \\ 6 & 4 & 3 & 2 & 0 & -3 \\ 9 & 7 & 6 & 5 & 3 & 0 \end{bmatrix} d_0. \quad (12)$$

The difference coarray of this configuration is shown in Fig. 3. It has holes at $-8d_0$ and $8d_0$. In order to fill these holes and form the virtual covariance matrix, an additional frequency $\omega_1 = 8/9\omega_0$ is required.

With this choice of the second operational frequency, the support matrix at ω_1 is given by

$$\mathbf{C}(\omega_1) = \begin{bmatrix} 0 & -16/9 & -8/3 & -32/9 & -16/3 & -8 \\ 16/9 & 0 & -8/9 & -16/9 & -32/9 & -56/9 \\ 8/3 & 8/9 & 0 & -8/9 & -8/3 & -16/3 \\ 32/9 & 16/9 & 8/9 & 0 & -16/9 & -40/9 \\ 16/3 & 32/9 & 8/3 & 16/9 & 0 & -8/3 \\ 8 & 56/9 & 16/3 & 40/9 & 8/3 & 0 \end{bmatrix} d_0. \quad (13)$$

The support matrix $\mathbf{C}_v(\omega_0)$ of the desired 10-element ULA, whose elements are positioned at $[0, 1, \dots, 9]d_0$, has the structure

$$\mathbf{C}_v(\omega_0) = \begin{bmatrix} 0 & -1 & -2 & \dots & -8 & -9 \\ 1 & 0 & -1 & \dots & -7 & -8 \\ 2 & 1 & 0 & \dots & -6 & -7 \\ \vdots & \vdots & \vdots & \ddots & \vdots & \vdots \\ 8 & 7 & 6 & \dots & 0 & -1 \\ 9 & 8 & 7 & \dots & 1 & 0 \end{bmatrix}. \quad (14)$$

From (12)-(14), we observe that several possibilities exist for constructing $\mathbf{C}_v(\omega_0)$ using $\mathbf{C}(\omega_0)$ and $\mathbf{C}(\omega_1)$, since several elements of $\mathbf{C}(\omega_0)$ and $\mathbf{C}(\omega_1)$ correspond to the same element of $\mathbf{C}_v(\omega_0)$. Either a single element or an average of all such elements can be used to specify the map for forming the desired virtual support matrix and, subsequently, the virtual covariance matrix $\mathbf{R}_v(\omega_0)$ [26], [34].

It should be noted that since the difference coarray at ω_0 has two holes at $\pm 8d_0$, only those elements of $\mathbf{R}_{xx}(\omega_1)$ that correspond to these two lags are required to form $\mathbf{R}_v(\omega_0)$. This means that instead of operating the entire co-prime array at ω_1 , only the sensors that produce the $\pm 8d_0$ lags at ω_1 should be operated at the additional frequency. For example, operating the two sensors with positions $[0 \ 9]d_0$ at ω_1 produces the following reduced support matrix

$$\mathbf{C}_r(\omega_1) = \frac{8}{9} \mathbf{C}_r(\omega_0) = \frac{8}{9} \begin{bmatrix} 0 & -9 \\ 9 & 0 \end{bmatrix} d_0 = \begin{bmatrix} 0 & -8 \\ 8 & 0 \end{bmatrix} d_0. \quad (15)$$

The two support matrices $\mathbf{C}(\omega_0)$ and $\mathbf{C}_r(\omega_1)$ can then be combined to form $\mathbf{C}_v(\omega_0)$. This procedure results in reducing hardware complexity. A more detailed discussion in this regard is provided in Section IV-D.

B. Proportional Spectra Requirement

For multi-frequency DOA estimation, the normalized covariance matrices are employed instead of $\{\mathbf{R}_{xx}(\omega_q)\}_{q=0}^{Q-1}$. The (i, j) th element of the normalized covariance matrix $\bar{\mathbf{R}}_{xx}(\omega_q)$ at frequency ω_q can be expressed as [34]

$$[\bar{\mathbf{R}}_{xx}(\omega_q)]_{i,j} = \frac{E\{[\mathbf{x}(\omega_q)]_i [\mathbf{x}^*(\omega_q)]_j\}}{\frac{1}{N_s(\omega_q)} E\{\mathbf{x}^H(\omega_q) \mathbf{x}(\omega_q)\}}, \quad (16)$$

where $[\mathbf{x}(\omega_q)]_i$ is the i th element of the data vector at frequency ω_q , and $N_s(\omega_q)$ is the number of sensors that are operated at ω_q . This results in the source and noise powers in the covariance matrix representation of (10) being replaced by the normalized powers [26], which are given by

$$\bar{\sigma}_k^2(\omega_q) = \frac{\sigma_k^2(\omega_q)}{\sum_{d=1}^D \sigma_d^2(\omega_q) + \sigma_n^2(\omega_q)} \quad (17)$$

$$\bar{\sigma}_n^2(\omega_q) = \frac{\sigma_n^2(\omega_q)}{\sum_{d=1}^D \sigma_d^2(\omega_q) + \sigma_n^2(\omega_q)}. \quad (18)$$

where $\bar{\sigma}_k^2(\omega_q)$ is the normalized power of the k th source at frequency ω_q and $\bar{\sigma}_n^2(\omega_q)$ is the normalized noise power at the same frequency. The virtual covariance matrix $\mathbf{R}_v(\omega_0)$, constructed by using the normalized covariance matrices $\{\bar{\mathbf{R}}_{xx}(\omega_q)\}_{q=0}^{Q-1}$ following the procedure outlined in Section III.A, must appear to have been generated by the virtual array as if it were the actual array operating at frequency ω_0 . However, some of the elements of the constructed virtual covariance matrix have contributions from frequencies other than ω_0 . The virtual covariance matrix will be exact provided that the normalized power of each source is independent of frequency,

$$\bar{\sigma}_k^2(\omega_q) = \sigma_k^2, \text{ for all } q \in \{0, 1, \dots, Q-1\} \text{ and all } k \in \{1, 2, \dots, D\}. \quad (19)$$

For a high signal-to-noise ratio (SNR), a sufficient condition for the virtual covariance matrix to be exact is that the sources must have proportional spectra at the employed frequencies [34]. That is,

$$\frac{\sigma_k^2(\omega_q)}{\sigma_l^2(\omega_q)} = \beta_{k,l}, \quad (20)$$

where $\beta_{k,l}$ is a constant for each source pair (k, l) over all frequencies ω_q . This condition is satisfied, for example, when the D sources are BPSK or chirp-like signals.

IV. FREQUENCY SELECTION FOR MULTI-FREQUENCY OPERATION USING EXTENDED CO-PRIME ARRAYS

In order to quantify the operational frequency set for filling the holes, we first need to examine the specific structure of the difference coarray corresponding to an extended co-prime configuration. Consider the difference coarray of Fig. 2, which corresponds to the co-prime array of Fig. 1. The total number of filled and missing elements in the coarray equals $2(2M-1)N+1$, whereas the total number of holes is determined to be $(M-1)(N-1)$. As the coarray is symmetric, we only focus on the portion corresponding to the non-negative lags. We observe that the portion of the coarray extending from 0 to $(MN+M-1)d_0$ is uniform and has no holes. The first hole appears at $(MN+M)d_0$, followed by another filled part from

$(MN + M + 1)d_0$ to $(MN + 2M - 1)d_0$. The final part of the coarray from $(MN + 2M)d_0$ to $(2M - 1)Nd_0$ is non-uniform and contains $((M - 1)(N - 1)/2) - 1$ holes.

A. One Additional Frequency (Dual-Frequency Operation)

The two holes at $-(MN + M)d_0$ and $(MN + M)d_0$ can be filled using only one additional frequency. The choice of the additional frequency is not unique. The value of ω_1 that minimizes the separation between ω_0 and ω_1 is given by

$$\omega_1 = \alpha_1 \omega_0 = \frac{MN + M}{MN + M + 1} \omega_0, \quad (21)$$

where the numerator and the denominator of the scaling factor α_1 correspond to the respective positions of the hole to be filled and the adjacent filled element to the right of the hole (considering the non-negative lags) that is used to fill it. Note that the value of ω_1 in (21) is less than ω_0 . It can be readily shown that using neighboring elements other than the right adjacent one yields values of ω_1 , which result in a larger separation from ω_0 .

Filling the two holes at $\pm(MN + M)d_0$ causes the uniform part of the difference coarray to extend from $-(MN + 2M - 1)d_0$ to $(MN + 2M - 1)d_0$. As a result, up to $(MN + 2M - 1)$ sources can be estimated after forming the corresponding virtual covariance matrix. This implies that, compared to the single frequency operation, M additional sources can be estimated using one extra frequency in addition to ω_0 .

B. Multiple Additional Frequencies (Multiple Frequency Operations)

The remaining $(M - 1)(N - 1) - 2$ holes in the difference coarray can also be filled through the use of additional frequencies. The exact number and values of the frequencies are tied to the non-uniformity pattern in the coarray beyond $\pm(MN + 2M)d_0$, which varies from one co-prime configuration to the other. Assuming that each additional frequency is used to fill only two holes (one missing positive element and its negative counterpart), we require at the most $\frac{1}{2}((M - 1)(N - 1) - 2) = (MN - M - N)/2$ additional frequencies to yield a filled uniform coarray extending from $-(2M - 1)Nd_0$ to $(2M - 1)Nd_0$.

C. Maximum Frequency Separation

The maximum frequency separation from the reference frequency determines the required operational bandwidth of the antennas and receiver front end for the proposed multi-frequency approach. It is determined by the distance of the farthest hole from its nearest filled right neighbor and the location of the neighbor. The maximum number of consecutive holes in the difference coarray is $(M - 1)$ and this pattern of $(M - 1)$ consecutive holes repeats $\lfloor N/M \rfloor$ times at each end of the difference coarray, as shown in Fig. 4 for the non-negative lags. However, it is the first set of $(M - 1)$ consecutive holes (those on extreme left in Fig. 4) that requires operational frequencies with the maximum separation from ω_0 in order to be filled. The repeated hole patterns at larger lags yield smaller frequency separation values. The first missing element in the leftmost set of consecutive holes occurs at $\left[(2M - 1)N - (M - 1) - \left(\left\lfloor \frac{N}{M} \right\rfloor - 1 \right) M \right] d_0$, while the nearest right filled element is positioned at $\left[(2M - 1)N - \left(\left\lfloor \frac{N}{M} \right\rfloor - 1 \right) M \right] d_0$. Therefore, the required frequency to fill this hole is given by

$$\tilde{\omega} = \frac{(2M - 1)N - (M - 1) - \left(\left\lfloor \frac{N}{M} \right\rfloor - 1 \right) M}{(2M - 1)N - \left(\left\lfloor \frac{N}{M} \right\rfloor - 1 \right) M} \omega_0 \quad (22)$$

The maximum frequency separation can, thus, be computed as

$$\Delta\omega_{max} = |\omega_0 - \tilde{\omega}| = \left| \frac{1 - M}{(2M - 1)N - \left(\left\lfloor \frac{N}{M} \right\rfloor - 1 \right) M} \right| \omega_0. \quad (23)$$

Table I shows the maximum frequency separation for different co-prime array configurations under two cases: i) when one additional frequency is used to fill the first pair of holes, and ii) when all holes are filled using multiple frequencies. For each of the aforementioned cases, the additional number of estimated sources compared to single frequency operation are also specified in Table I. We observe that the maximum frequency separation decreases with increasing values of M and N . This is because both the holes and the elements that are used to fill them occur at larger spatial lags for higher values of M and N , which, in turn, implies a smaller value of the scaling factor in (23).

D. Reduced Hardware Complexity

Since only a few observations at each employed frequency other than ω_0 are used for the proposed multi-frequency high-resolution DOA estimation scheme and the remaining observations are discarded, it is not economical to operate the entire physical array at each of the additional $Q - 1$ frequencies. Therefore, only the receive elements that generate the desired spatial lags for filling the holes need to be operating at more than one frequency. As determined in Section IV.C, the bandwidth requirement for the multi-frequency operation is not that high, especially for larger values of M and N . As such, only the multi-frequency receive elements require a DFT or a filterbank to extract the information at the different frequencies, leading to a significant reduction in system hardware complexity.

It becomes of interest to determine the smallest number of sensors that are required to operate at the additional frequency or frequencies. As the holes occur in symmetric pairs, the lags corresponding to each pair can be generated using only two sensors in the physical array. In case of redundancy in the difference coarray, there is more than one antenna pair that can generate the same spatial lag. In order to reduce the number of antennas engaging in multiple frequency processing, one should therefore seek and identify each sensor that participates in filling all the holes or at least many of them. This becomes important when there is flexibility in sensor participation choices implied by the redundancy property of the spatial lags. Clearly, only the redundant spatial lags occurring beyond the first symmetric hole pair at $\pm(MN + M)d_0$ need to be considered, since these are used to fill the holes in the difference coarray. It can be readily shown that there are a total of $2(M - 2)$ redundant lags beyond $\pm(MN + M)d_0$ at $\pm(MN + kN)d_0$ with weights given by

$$W(\pm(MN + kN)d_0) = M - k, \text{ for } k = 1, 2, \dots, M - 2. \quad (24)$$

For illustration, we consider an example where $M = 4$ and $N = 5$. The co-prime array consists of 12 elements positioned at $[0 \ 4 \ 5 \ 8 \ 10 \ 12 \ 15 \ 16 \ 20 \ 25 \ 30 \ 35]d_0$. Fig. 5 shows the difference coarray weighting function corresponding to this array. The first hole pair in the coarray occurs at $\pm(MN + M)d_0 = \pm 24d_0$. Beyond the first holes, $2(M - 2) = 4$ redundant lags exist. The first redundant lag pair occurs at $\pm(MN + N)d_0 = \pm 25d_0$ with weight equal to $(M - 1) = 3$. The second redundant pair occurs at

$\pm(MN + 2N)d_0 = \pm 30d_0$ and has a weight of $(M - 2) = 2$. In order to minimize the maximum frequency separation, only the redundant lags that occur immediately to the right of the holes (considering the nonnegative lags) can be used. For the case where $\text{mod}(N, M) = 1$, all the redundant lags in the nonuniform part of the coarray occur immediately after the holes. This can be confirmed by observing the weighting function in Fig. 5. For the case where $\text{mod}(N, M) = M - 1$, none of the redundant lags are immediately to the right of the holes, as illustrated in Fig. 6 for the case where $M = 4$ and $N = 7$. For the remaining cases, only a subset of the redundant lags in the nonuniform part is immediately after the holes.

For the illustration of the role of redundancy in reducing sensor engagement in hole filling, we provide the following two examples. Table II shows the additional frequencies and the corresponding sensor pairs that are required to fill all nine holes in the difference coarray for the case where $M = 4$ and $N = 7$. The corresponding physical array consists of 14 sensors at $[0\ 4\ 7\ 8\ 12\ 14\ 16\ 20\ 21\ 24\ 28\ 35\ 42\ 49]d_0$. It is clear from Table II that only the 6 sensors located at $[0\ 4\ 8\ 12\ 16\ 49]d_0$ are required to operate at more than one frequency in order to fill all the holes in the coarray. It should be noted that since $\text{mod}(N, M) = M - 1$ in this example, the redundant lags in the difference coarray cannot be used to further decrease the number of antennas that would operate at more than one frequency. Table III shows the required frequencies and the corresponding sensor pairs for the case where $M = 4$ and $N = 5$. Since $\text{mod}(N, M) = 1$, different sensor pairs can be used to fill the same holes. As shown in Table III, the pairs that include common sensors at different frequencies are chosen in order to minimize the number of sensors that operate at more than one frequency. Table IV shows the percentage of sensors that need to be operated at more than one frequency for different co-prime array configurations. We observe that the number of sensors that need to be operated at multiple frequencies has a lower bound of one-third of the total number of sensors in the array, which is achieved for co-prime configurations with $N = M + 1$. It should be noted that the same choice of $N = M + 1$ also minimizes the total number of sensors in the co-prime arrays, as demonstrated in [15].

V. NUMERICAL RESULTS

In this section, we present DOA estimation results based on the MUSIC algorithm using multi-frequency co-prime arrays. Both proportional and nonproportional source spectra cases are considered and performance comparison with single-frequency operation is provided. We employ the filled part of the coarray and covariance matrix augmentation for DOA estimation using MUSIC under single frequency operation. The root mean squared error (RMSE) in all examples in this section is based on a single realization, unless stated otherwise.

A. Proportional Spectra

We first consider a co-prime array configuration with six physical sensors, corresponding to $M = 2$ and $N = 3$. The first uniform linear subarray consists of three elements positioned at $[0, 2d_0, 4d_0]$ and the second subarray has four elements with positions $[0, 3d_0, 6d_0, 9d_0]$, with d_0 equal to one-half wavelength at ω_0 . The difference coarray of this configuration, shown in Fig. 3, has two holes at $\pm 8d_0$, which can be filled using an additional frequency $\omega_1 = (8/9)\omega_0$. We consider 9 sources with proportional spectra, where $\sigma_d^2(\omega_1) = 3\sigma_d^2(\omega_0)$ for $d = 0, 1, \dots, 8$. The sources are uniformly spaced between -0.95 and 0.95 in the reduced angular coordinate $\sin(\theta)$. A total of 2000 snapshots are used and the SNR is set to 0 dB for both frequencies. The estimated spatial spectrum, where only the reference frequency ω_0 is used, is provided in Fig. 7. The elements in the covariance matrix corresponding to the holes in the difference coarray have been filled with zeros. This is equivalent to the case where the sources have zero powers at the additional frequency. The vertical lines in the figure indicate the true DOAs of the sources. We observe from Fig. 7 that the single frequency approach fails to correctly estimate the DOAs of most of the targets. The RMSE is found to be 2.55° . This is expected since the considered co-prime array operating at a single frequency can resolve a maximum of 7 sources. Fig. 8 depicts the estimated spatial spectrum using the dual-frequency approach. We can clearly see that the DOAs of all sources have been correctly estimated. In this case, the RMSE of the DOA estimates is equal to 0.67° .

In the second example, we consider a co-prime configuration with $M = 5$ and $N = 7$. The 7 sensors of the first ULA are positioned at $[0, 5, 10, 15, 20, 25, 30]d_0$, and the second ULA has 10 elements with positions $[0, 7, 14, 21, 28, 35, 42, 49, 56, 63]d_0$. The corresponding coarray extends from $-63d_0$ to $63d_0$ and has a total of 24 holes. The uniform portion of the coarray only extends from $-39d_0$ to $39d_0$. Thus, the single frequency operation can resolve a maximum of 39 sources. One additional frequency $\omega_1 = (40/41)\omega_0$ is first used to fill the holes at $\pm 40d_0$ in the coarray. As a result, the uniform part of the coarray now includes the lags from $-44d_0$ to $44d_0$, thereby increasing the maximum number of resolvable sources from 39 to 44. We consider 44 sources with $\sin(\theta_d)$ uniformly distributed between -0.97 and 0.97 . The sources are assumed to have identical power spectra at the two frequencies. A total of 2000 snapshots are considered and the SNR is set to 0 dB for both frequencies. Fig. 9 shows the estimated spatial spectrum, wherein the DOAs of all 44 sources have been accurately estimated. The RMSE is determined to be 0.31° in this case. Next, we employ 12 additional frequencies to fill all 24 holes in the coarray. The additional frequencies and the corresponding holes they fill are listed in Table V. It should be noted that the holes could have also been filled using only six additional frequencies. These frequencies are $\omega_1 = 5\omega_0$, $\omega_2 = 2\omega_0$, $\omega_3 = (47/49)\omega_0$, $\omega_4 = 3\omega_0$, $\omega_5 = 59/63\omega_0$, and $\omega_6 = (61/63)\omega_0$. However, this choice of frequencies results in a maximum frequency separation of $4\omega_0$, compared to $0.064\omega_0$ for the set of frequencies in Table V. Fig. 10 shows the estimated spatial spectrum corresponding to 63 sources with $\sin(\theta_d)$ uniformly distributed between -0.97 and 0.97 and equal power spectra at the 12 frequencies. The SNR and the number of snapshots are taken to be the same as for Fig. 9. Again, the multi-frequency approach has estimated all sources accurately and the RMSE is 0.2° .

B. Nonproportional Spectra

We evaluate the DOA estimation performance of the multi-frequency co-prime arrays when the condition of proportional source spectra is violated. In the first example, we consider the same array and source configuration as in the first example in Section V.A with $M = 2$ and $N = 3$. However, the 9 sources are now assumed to have nonproportional spectra at ω_0 and $\omega_1 = (8/9)\omega_0$. More specifically, the source

powers at ω_0 are assumed to be identical and equal to unity, whereas the source powers associated with ω_1 are assumed to independently follow a truncated Gaussian distribution with a mean of 5.5 and a common variance. Two different values of 2.25 and 5.06 are considered for the variance. The variance controls the degree of non-proportionality. A higher variance increases the degree of non-proportionality of the source spectra, whereas a lower variance results in smaller variations in the source powers. Fig. 11 depicts the RMSE as a function of the variance and the SNR, averaged over 2000 Monte Carlo runs. For comparison, the RMSE corresponding to both single-frequency operation and dual-frequency operation for the case when the sources have proportional spectra are also included. As expected, the single-frequency approach, wherein the elements of the virtual covariance matrix corresponding to the holes in the coarray are filled with zeros, provides the worst performance. Further, the RMSE corresponding to the multi-frequency approach for nonproportional spectra increases with increasing variance. This results in a degradation of the estimation performance. Finally, the multi-frequency approach works best when the spectra are proportional and the SNR is higher.

In the following example, we compare the performance of the multi-frequency approach to single-frequency DOA estimation as a function of the assumed model order. The same array configuration with $M = 2$ and $N = 3$ is used. Two cases are considered in this example. The first case deals with sources with proportional spectra, while the second considers sources with nonproportional spectra. For the nonproportional case, the source powers associated with ω_0 are assumed to be identical and equal to unity, and the source powers associated with ω_1 follow a truncated Gaussian distribution with a mean of 5.5 and a variance 2. In both cases, the actual number of sources is set to 4, and the assumed model order is varied between 4 and 7. 1000 Monte Carlo are considered in this example. Fig. 12 shows the RMSE, averaged over 1000 Monte Carlo runs, as a function of the assumed model order for both cases. In computing the RMSE, only the detected peaks that are closest to the actual source directions were considered. From Fig. 12, we observe that, as expected, the performance of the single-frequency approach is not affected by the nonproportionality of the source spectra. On the other hand, the multi-frequency DOA estimation exhibits superior performance for sources with proportional spectra compared to those with nonproportional spectra.

Further, the multi-frequency approach is less sensitive to errors in model order as compared to the single-frequency approach.

The effect of the degree of non-proportionality on DOA estimation performance is next examined for the co-prime configuration of the second example in Section V.A with $M = 5$ and $N = 7$ under both dual and multi-frequency operation. Again, the source powers at ω_0 are assumed to be all equal to unity, whereas the source powers at additional frequencies follow a truncated Gaussian distribution with a mean of 5.5 and a common variance. Fig. 13 provides the RMSE, averaged over 2000 Monte Carlo runs, as a function of SNR and variance under the dual-frequency operation for 44 sources. Similar observations to those in Fig. 11 can be made in this case as well. However, two differences can be noticed by comparing the RMSE plots in Figs. 11 and 13. First, the RMSE takes on lower values for all considered DOA estimation methods and variances for the co-prime configuration with $M = 5$ and $N = 7$. Second, the difference in performance between the single and dual frequency operations for the nonproportional spectra cases is much smaller at higher SNR values in this example. This is due to the fact that the ratio of the number of missing elements to the total number of elements in the filled part of the difference coarray is smaller in this example. This results in a smaller percentage of elements in the virtual covariance matrix to come from a different frequency or be filled with zeros for single frequency operation. The RMSE plots for the multi-frequency operation to fill all 24 holes are provided in Fig. 14, which corresponds to 60 sources with $\sin(\theta_d)$ uniformly distributed between -0.97 and 0.97. The performance difference between multi-frequency operation for sources with non-proportional spectra and those with proportional spectra is even less noticeable in this case, though the RMSE values themselves are slightly higher for high SNR. Also, the single-frequency operation exhibits a higher RMSE since a higher percentage of the virtual covariance matrix elements now have a zero value compared to that for Fig. 13.

The final example in this section examines the estimation performance for varying degree of nonproportionality of the source spectra for different values of M and N with the SNR fixed at 0 dB. Both dual-frequency operation for filling only the first hole pair and multi-frequency operation for filling all the holes are considered for each co-prime configuration. For each case, the maximum number of resolvable

sources was used. A total of 2000 Monte Carlo runs were considered in this example. The source powers associated with the reference frequency ω_0 are identical and equal to unity. For the additional frequencies, the source powers follow a truncated Gaussian distribution with a mean of 5.5 and a common variance. The corresponding RMSE plots as a function of the variance of the source powers are depicted in Fig. 15. In order to have a fair comparison among co-prime arrays of different sizes, each RMSE plot is normalized by the Cramer Rao Bound (CRB) of an equivalent ULA with total number of elements equal to the number of contiguous nonnegative lags in the corresponding difference coarray. By examining Fig. 15, the following observations are in order. First, as expected, a decrease in the variance of the sources spectra results in a reduced estimation error. Second, by comparing the results of dual and multiple frequency operation for fixed M and N , we observe that, in general, the normalized RMSE error is smaller for the case when more than one additional frequencies are used.

C. Comparison with Sparse Reconstruction

Sparse reconstruction can be used in lieu of MUSIC for DOA estimation using multi-frequency co-prime arrays [35]. Unlike the proposed MUSIC-based approach, all of the lags generated by the multi-frequency operation, in addition to those that fill the holes in the difference coarray, can be utilized for DOA estimation using sparse reconstruction. This is because sparse reconstruction does not require the additional lags to fall on a uniform grid (integer multiples of the unit spacing). Utilization of all generated lags, in this case, enhances the number of DOFs for DOA estimation, leading to an increased number of resolvable sources. However, the performance of the sparse reconstruction approach is affected by the coherence of the data measurement operator. In addition, it is computationally more expensive than MUSIC.

In order to compare the performance of sparse reconstruction and MUSIC based multi-frequency approaches, we consider the following example. The same array configuration as in the first example in Section V.A is used. Two frequencies, ω_0 and $\omega_1 = (8/9)\omega_0$, are employed; the latter can fill the holes in the corresponding difference coarray so that the multi-frequency MUSIC technique can be applied. Nine

sources with directions uniformly spaced between -0.9 and 0.9 in the reduced angular coordinate $\sin(\theta)$ are used, which is the maximum number of sources that can be resolved using the multi-frequency MUSIC approach. Two separate cases are considered in this example. The first case assumes sources with proportional spectra, while the second considers sources with nonproportional spectra. For the latter, the source powers at ω_0 are assumed to be identical and equal to unity, whereas the source powers associated with ω_1 are assumed to independently follow a truncated Gaussian distribution with a mean of 5.5 and a variance of 2. Fig. 16 shows the RMSE, averaged over 1000 Monte Carlo runs, as a function of the SNR for both cases. The SNR is assumed to be identical at both frequencies and is varied from -10 dB to 10 dB with a 2.5 dB increment. It can be readily observed that the multi-frequency MUSIC approach outperforms the sparse reconstruction method for all SNR values when the sources have proportional spectra. In case of sources with nonproportional spectra, the multi-frequency MUSIC method outperforms the sparse reconstruction approach for low values of SNR, whereas both methods achieve similar performance at high SNR values. For both proportional and nonproportional spectra cases, the sparse reconstruction approach exhibits significantly degraded performance at low SNR values. This is expected since the accuracy of the sparse reconstruction methods suffers in high noise cases.

VI. CONCLUSION

A multi-frequency technique has been presented for high-resolution DOA estimation using co-prime arrays. A virtual covariance matrix at the reference frequency is created using elements of the narrowband covariance matrices corresponding to the different employed frequencies. The virtual covariance matrix corresponds to a uniform linear array with a difference coarray of the same extent as that of the co-prime array, except that the coarray of the ULA is filled whereas that of the co-prime array has holes. This permits the co-prime array to handle all of the degrees of freedom offered by the co-prime configuration. Simulation examples were used to evaluate the DOA estimation performance of the multi-frequency approach under both proportional and nonproportional spectra. It was shown that the DOAs are estimated with high accuracy under multi-frequency operation for sources with proportional spectra, while for non-proportional

spectra, the estimation error varies with the SNR as well as the values of M and N . The effect of nonproportionality was shown to be not as significant at high SNR for higher values of M and N as for lower values.

REFERENCES

- [1] S. Chandran, *Advances in Direction-of-Arrival Estimation*, Norwood, MA: Artech House, 2006.
- [2] H. L. Van Trees, *Optimum Array Processing: Part IV of Detection, Estimation and Modulation Theory*, New York, NY: Wiley, 2002.
- [3] T. E. Tuncer and B. Friedlander, *Classical and Modern Direction-of-Arrival Estimation*, Boston, MA: Academic Press (Elsevier), 2009.
- [4] L. C. Godara, "Application of antenna arrays to mobile communications. II. Beam-forming and direction-of-arrival considerations," *Proc. IEEE*, vol. 85, no. 8, pp. 1195–1245, 1997.
- [5] R. A. Monzingo and T. W. Miller, *Introduction to Adaptive Arrays*, New York, NY: Wiley, 1980.
- [6] D. H. Johnson and D. E. Dudgeon, *Array Signal Processing: Concepts and Techniques*, Englewood, NJ: Prentice Hall, 1993.
- [7] P. P. Vaidyanathan and P. Pal, "Sparse sensing with co-prime samplers and arrays," *IEEE Trans. Signal Process.*, vol. 59, no. 2, pp. 573–586, 2011.
- [8] P. Pal and P. P. Vaidyanathan, "Coprime sampling and the MUSIC algorithm," in *Proc. IEEE Digital Signal Process. Workshop and IEEE Signal Process. Education Workshop*, Sedona, AZ, 2011.
- [9] A. Moffet, "Minimum-redundancy linear arrays," *IEEE Trans. Antennas Propag.*, vol. AP-16, no. 2, pp. 172–175, Mar. 1968.
- [10] G. S. Bloom and S. W. Golomb, "Application of numbered undirected graphs," *Proc. IEEE*, vol. 65, no. 4, pp. 562–570, Apr. 1977.
- [11] P. Pal and P. P. Vaidyanathan, "Nested arrays: a novel approach to array processing with enhanced degrees of freedom," *IEEE Trans. Signal Process.*, vol. 58, no. 8, pp. 4167–4181, Aug. 2010.

- [12] J. C. P. Miller, "Difference bases, three problems in additive number theory," in A. D. L. Atkin and B. J. Birch (Eds.), *Computers in Number Theory*, pp. 299–322, London, UK: Academic Press, 1971.
- [13] K. A. Blanton and J. H. McClellan, "New search algorithm for minimum redundancy linear arrays," in *Proc. IEEE Int. Conf. Acoustics, Speech, and Signal Process.*, vol.2, Apr. 1991, pp. 1361–1364.
- [14] Q. Wu and Q. Liang, "Coprime sampling for nonstationary signal in radar signal processing," *EURASIP Journal on Wireless Communications and Networking* 2013, 2013:58.
- [15] K. Adhikari, J. R. Buck, and K. E. Wage, "Beamforming with extended co-prime sensor arrays," in *Proc. IEEE Int. Conf. Acoustics, Speech and Signal Process.*, May 2013, pp. 4183–4186.
- [16] Y. Zhang, M. Amin, F. Ahmad, and B. Himed, "DOA estimation using a sparse uniform linear array with two CW signals of co-prime frequencies," in *Proc. IEEE 5th Int. Workshop Computational Advances in Multi-Sensor Adaptive Process.*, Dec. 2013, pp. 404–407.
- [17] Z. Tan and A. Nehorai, "Sparse direction of arrival estimation using co-prime arrays with off-grid targets," *IEEE Signal Process. Lett.*, vol. 21, no. 1, pp. 26–29, Jan. 2014.
- [18] A. T. Pyzdek and R. L. Culver, "Processing methods for coprime arrays in complex shallow water environments," *J. Acoust. Soc. Am.*, vol. 135, no. 4, pp. 2392–2392, 2014.
- [19] J. Chen and Q. Liang, "Rate distortion performance analysis of nested sampling and coprime sampling," *EURASIP Journal on Advances in Signal Process.* 2014, 2014:18.
- [20] J. Ramirez, J. Odom, and J. Krolik, "Exploiting array motion for augmentation of co-prime arrays," in *Proc. IEEE 8th Int. Sensor Array and Multichannel Signal Process. Workshop*, Jun. 2014, pp. 525–528.
- [21] S. U. Pillai, Y. Bar-Ness, and F. Haber, "A new approach to array geometry for improved spatial spectrum estimation," *Proc. IEEE*, vol. 73, pp. 1522–1524, Oct. 1985.
- [22] Y. I. Abramovich, D. A. Gray, A. Y. Gorokhov, and N. K. Spencer, "Positive-definite Toeplitz completion in DOA estimation for nonuniform linear antenna arrays. I. Fully augmentable arrays," *IEEE Trans. Signal Process.*, vol. 46, pp. 2458–2471, Sep. 1998.

- [23] Y. I. Abramovich, N. K. Spencer, and A. Y. Gorokhov, "Positive-definite Toeplitz completion in DOA estimation for nonuniform linear antenna arrays. II. Partially augmentable arrays," *IEEE Trans. Signal Process.*, vol. 47, pp. 1502–1521, Jun. 1999.
- [24] R. T. Hoctor and S. A. Kassam, "The unifying role of the coarray in aperture synthesis for coherent and incoherent imaging," *Proc. IEEE*, vol. 78, no. 4, pp. 735–752, Apr. 1990.
- [25] E. BouDaher, Y. Jia, F. Ahmad, and M. Amin, "Direction-of-arrival estimation using multi-frequency co-prime arrays," in *Proc. 22nd European Signal Process. Conf.*, Sep. 2014.
- [26] J. L. Moulton, and S. A. Kassam, "Resolving more sources with multi-frequency coarrays in high-resolution direction-of-arrival estimation," in *Proc. 43rd Annual Conference on Information Sciences and Systems*, Mar. 2009, pp. 772–777.
- [27] R. Schmidt, "Multiple emitter location and signal parameter estimation," *IEEE Trans. Antennas Propag.*, vol. 34, pp. 276–280, Mar. 1986.
- [28] M. J. Hinich, "Processing spatially aliased arrays," *J. Acoust. Soc. Am.*, vol. 64, no. 3, pp. 793–795, 1978.
- [29] M. G. Amin, "Sufficient conditions for aliased free direction of arrival estimation in periodic spatial spectra," *IEEE Transactions on Antenna and Propagation*, vol. 41, no. 4, pp. 508–511, April 1993.
- [30] T. J. Shan, M. Wax, and T. Kailath, "On spatial smoothing for direction-of-arrival estimation of coherent signals," *IEEE Trans. Acoust., Speech, Signal Process.*, vol. 33, no. 4, pp. 806–811, Aug. 1985.
- [31] Y. Yoon, L. M. Kaplan, and J. H. McClellan, "TOPS: New DOA estimator for wideband signals," *IEEE Trans. Signal Process.*, vol. 54, no. 6, pp. 1977–1989, Jun 2006.
- [32] H. Wang and M. Kaveh, "Coherent signal-subspace processing for the detection and estimation of angles of arrival of multiple wide-band sources," *IEEE Trans. Acoust., Speech, Signal Processing*, vol. 33, no. 4, pp. 823–831, Mar 1985.
- [33] F. Ahmad and S. A. Kassam, "Performance analysis and array design for wide-band beamformers," *Journal of Electronic Imaging*, vol. 7, no. 4, pp. 825–838, Oct. 1998.

- [34] J. L. Moulton, "Enhanced high-resolution imaging through multiple-frequency coarray augmentation," Ph.D. dissertation, Electrical and Systems Engineering, University of Pennsylvania, Philadelphia, PA, 2010.
- [35] E. BouDaher, F. Ahmad, and M. G. Amin, "Sparse reconstruction for direction-of-arrival estimation using multi-frequency co-prime arrays," *EURASIP Journal on Advances in Signal Processing*, 2014, pp. 2014:168.

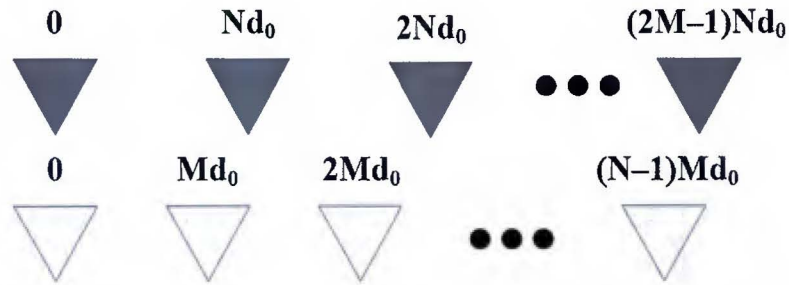


Figure 1. Extended co-prime array configuration

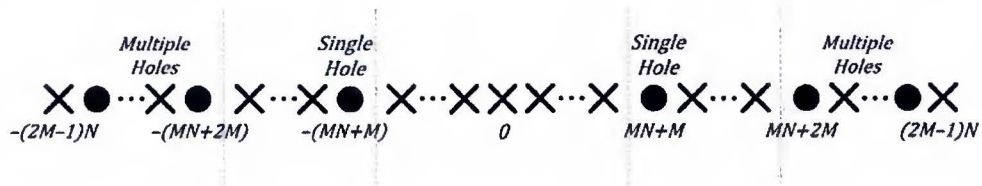


Figure 2. Difference coarray of the extended co-prime array.

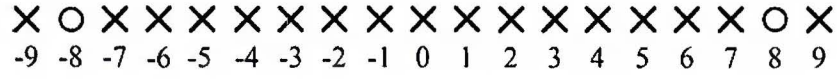


Figure 3. Difference coarray at the reference frequency ω_0 for $M=2$, $N=3$.

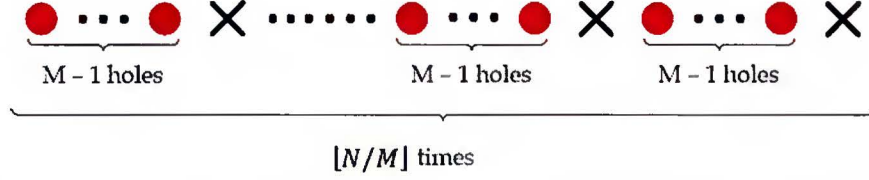


Figure 4. Positive end part of the difference coarray corresponding to the co-prime array.

TABLE I
MAXIMUM FREQUENCY SEPARATION FOR DUAL AND MULTI-FREQUENCY

M	N	Dual-frequency		Multi-frequency	
		Additional estimated sources	$\Delta\omega_{max}$	Additional estimated sources	$\Delta\omega_{max}$
2	3	2	11.11%	2	11.11%
3	4	3	6.25%	6	10.00%
3	5	3	5.26%	8	8.00%
5	7	5	2.44%	24	6.35%
7	9	7	1.41%	48	5.13%

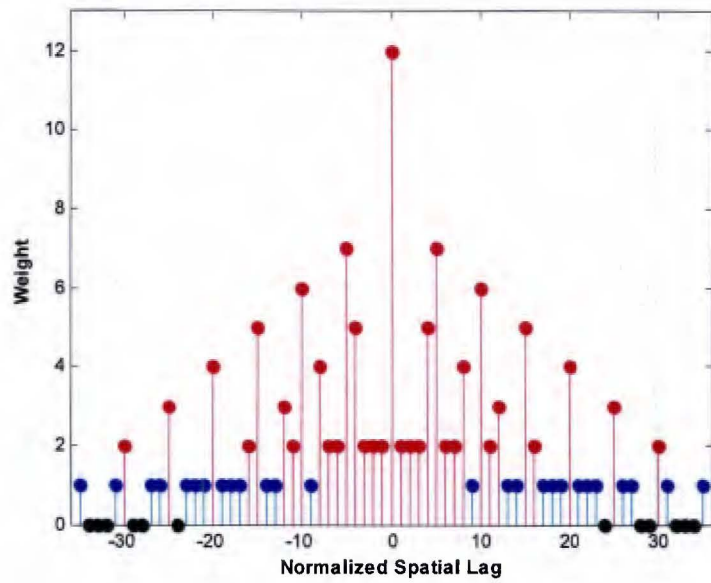


Figure 5. Difference coarray weight function: $M=4$, $N=5$.

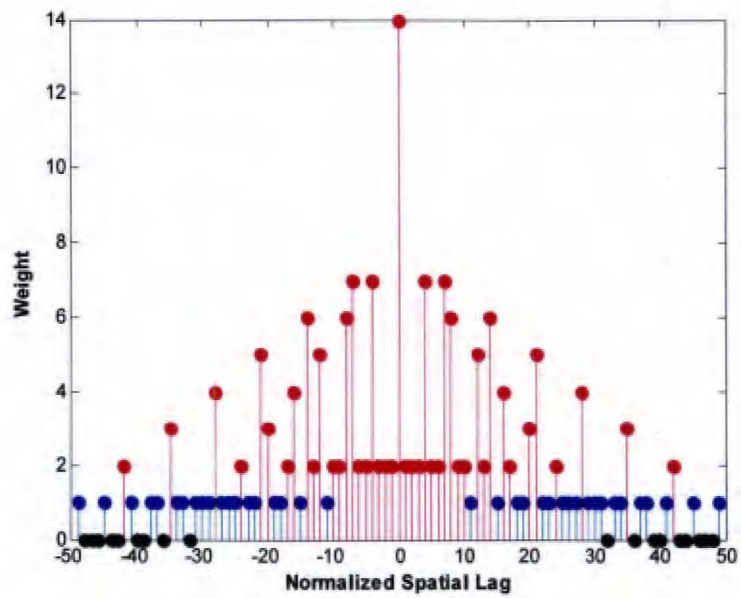


Figure 6. Difference coarray weight function: $M=4$, $N=7$.

TABLE II
REQUIRED FREQUENCIES AND SENSOR PAIRS, $M = 4, N = 7$

Frequencies	Holes	Sensor Pairs
$\omega_1 = (32/33)\omega_0$	$\pm 32d_0$	$[16\ 49]d_0$
$\omega_2 = (36/37)\omega_0$	$\pm 36d_0$	$[12\ 49]d_0$
$\omega_3 = (39/41)\omega_0$	$\pm 39d_0$	$[8\ 49]d_0$
$\omega_4 = (40/41)\omega_0$	$\pm 40d_0$	$[8\ 49]d_0$
$\omega_5 = (43/45)\omega_0$	$\pm 43d_0$	$[4\ 49]d_0$
$\omega_6 = (44/45)\omega_0$	$\pm 44d_0$	$[4\ 49]d_0$
$\omega_7 = (46/49)\omega_0$	$\pm 46d_0$	$[0\ 49]d_0$
$\omega_8 = (47/49)\omega_0$	$\pm 47d_0$	$[0\ 49]d_0$
$\omega_9 = (48/49)\omega_0$	$\pm 48d_0$	$[0\ 49]d_0$

TABLE III
REQUIRED FREQUENCIES AND SENSOR PAIRS, $M = 4, N = 5$

Frequencies	Holes	Sensor Pairs	Chosen Pairs
$\omega_1 = (24/25)\omega_0$	$\pm 24d_0$	$[0\ 25]d_0, [5\ 30]d_0, [10\ 35]d_0,$	$[0\ 25]d_0$
$\omega_2 = (28/30)\omega_0$	$\pm 28d_0$	$[0\ 30]d_0, [5\ 35]d_0$	$[0\ 30]d_0$
$\omega_3 = (29/30)\omega_0$	$\pm 29d_0$	$[0\ 30]d_0, [5\ 35]d_0$	$[0\ 30]d_0$
$\omega_4 = (32/35)\omega_0$	$\pm 32d_0$	$[0\ 35]d_0$	$[0\ 35]d_0$
$\omega_5 = (33/35)\omega_0$	$\pm 33d_0$	$[0\ 35]d_0$	$[0\ 35]d_0$
$\omega_6 = (34/35)\omega_0$	$\pm 34d_0$	$[0\ 35]d_0$	$[0\ 35]d_0$

TABLE IV
PERCENTAGE OF MULTI-FREQUENCY SENSORS FOR DIFFERENT CO-PRIME PAIRS

M	N	Multi-frequency sensors
2	3	$2/6 = 33.3\%$
3	4	$3/9 = 33.3\%$
3	5	$4/10 = 40.0\%$
4	5	$4/12 = 33.3\%$
4	7	$6/14 = 42.8\%$
5	7	$6/16 = 37.5\%$
6	7	$6/18 = 33.3\%$

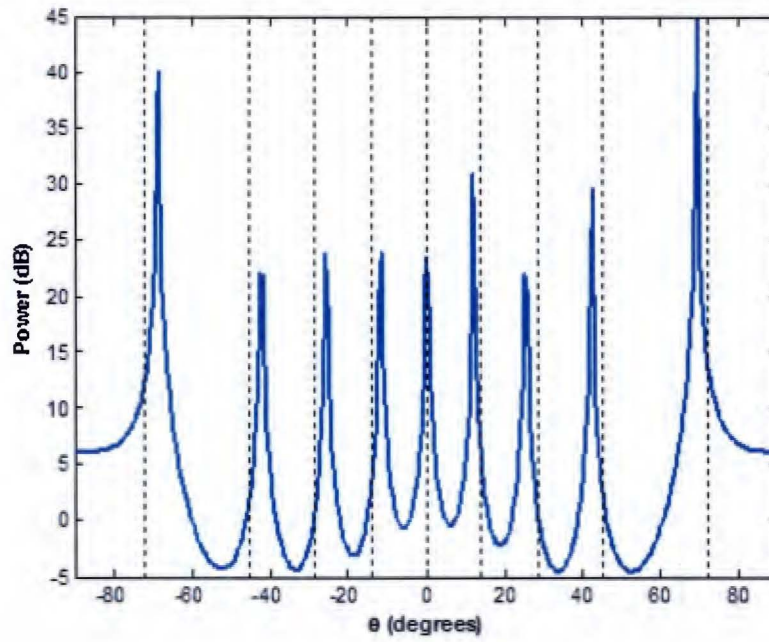


Figure 7. MUSIC spectrum using single frequency, $D = 9$ sources with proportional spectra.

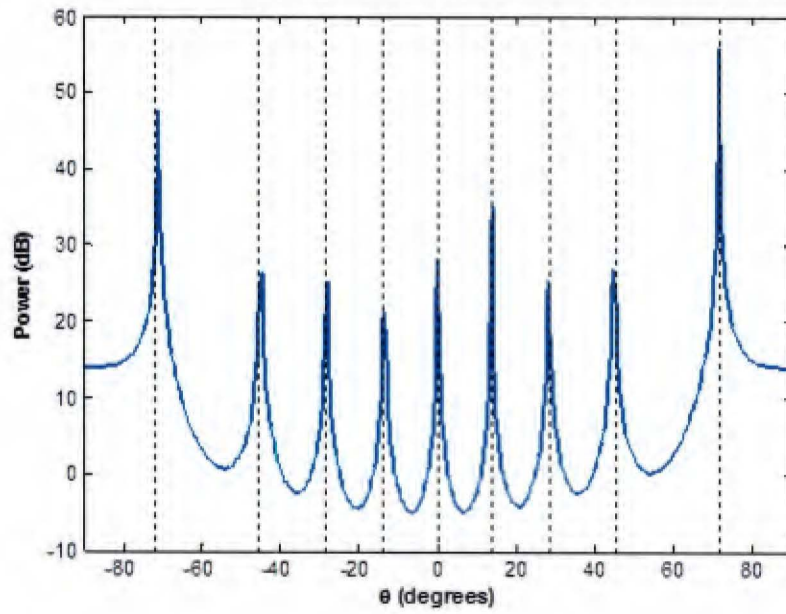


Figure 8. MUSIC spectrum using two frequencies, $D = 9$ sources with proportional spectra.

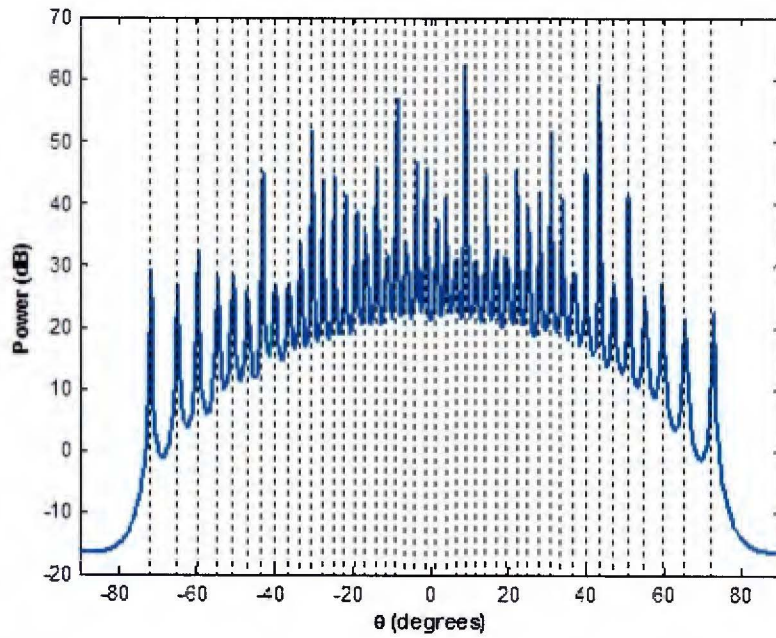


Figure 9. MUSIC spectrum with dual frequencies, $D = 44$ sources with proportional spectra.

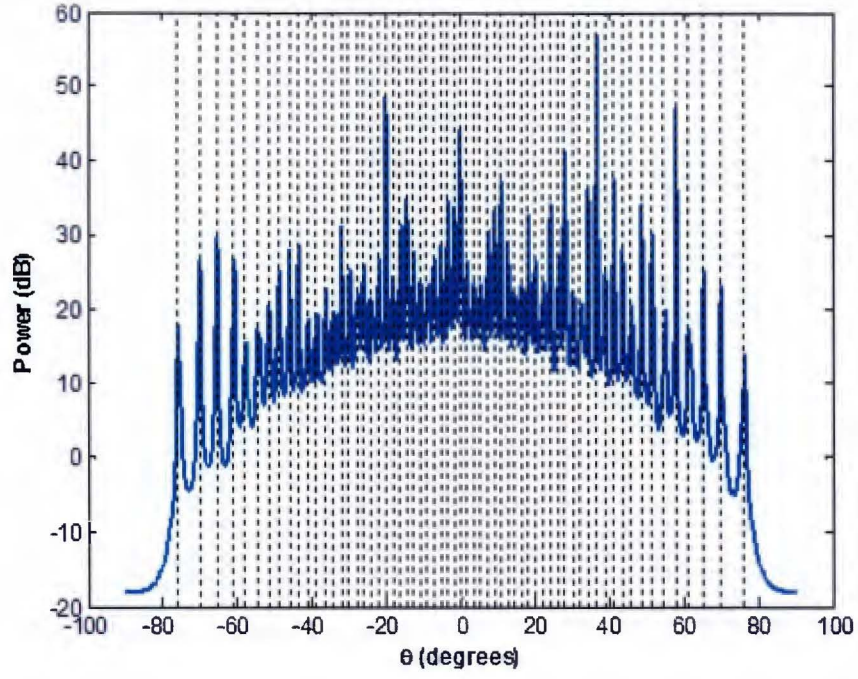


Figure 10. MUSIC spectrum with multiple frequencies, $D = 63$ sources with proportional spectra.

TABLE V
ADDITIONAL FREQUENCIES AND CORRESPONDING HOLES, $M = 5, N = 7$

Frequency	Holes	Frequency	Holes
$\omega_1 = (40/41)\omega_0$	$\pm 40d_0$	$\omega_7 = (55/56)\omega_0$	$\pm 55d_0$
$\omega_2 = (45/46)\omega_0$	$\pm 45d_0$	$\omega_8 = (57/58)\omega_0$	$\pm 57d_0$
$\omega_3 = (47/48)\omega_0$	$\pm 47d_0$	$\omega_9 = (59/63)\omega_0$	$\pm 59d_0$
$\omega_4 = (50/51)\omega_0$	$\pm 50d_0$	$\omega_{10} = (60/63)\omega_0$	$\pm 60d_0$
$\omega_5 = (52/53)\omega_0$	$\pm 52d_0$	$\omega_{11} = (61/63)\omega_0$	$\pm 61d_0$
$\omega_6 = (54/56)\omega_0$	$\pm 54d_0$	$\omega_{12} = (62/63)\omega_0$	$\pm 62d_0$

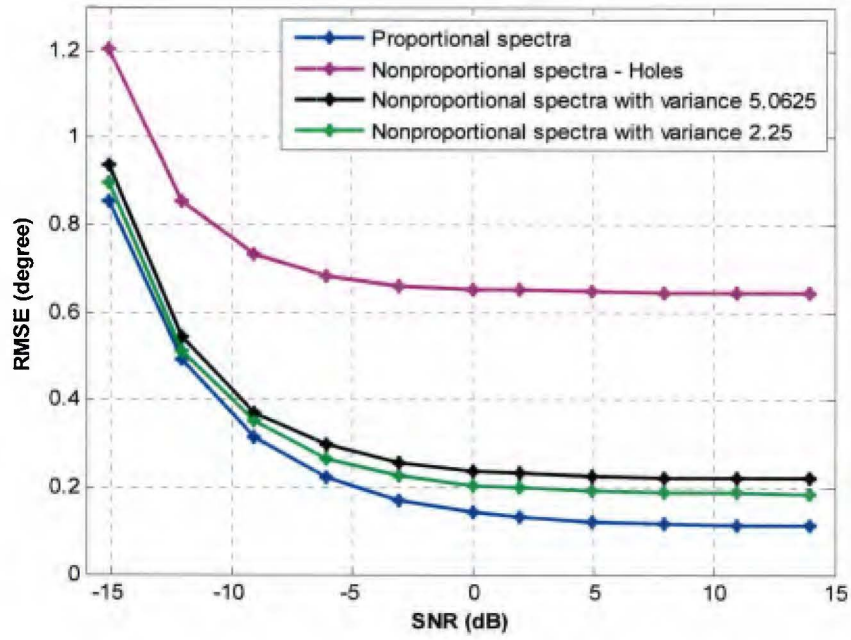


Figure 11. RMSE vs. SNR for $M = 2$, $N = 3$, $D = 9$.

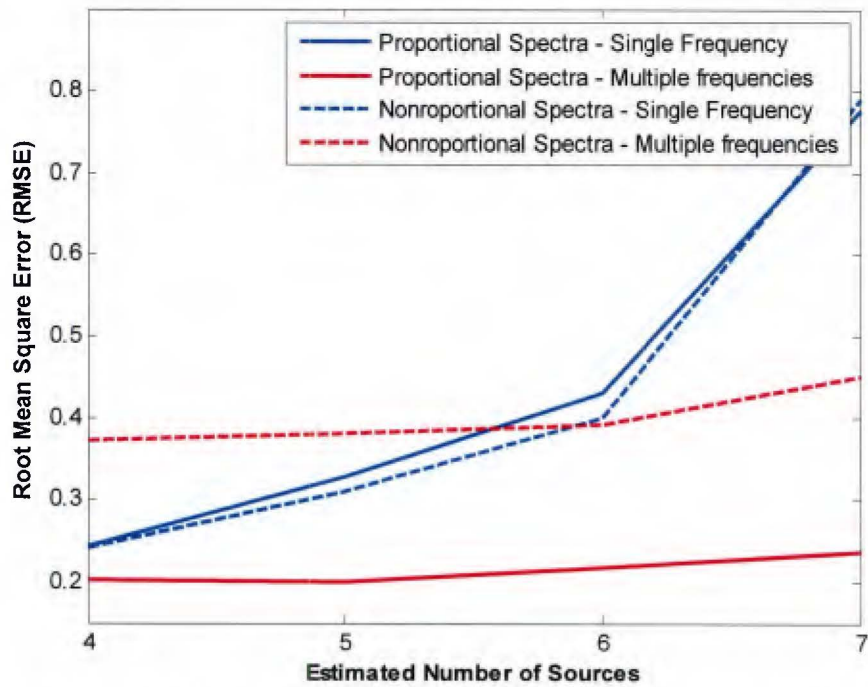


Figure 12. RMSE vs. Assumed Model Order for $M = 2$, $N = 3$, $D = 4$.

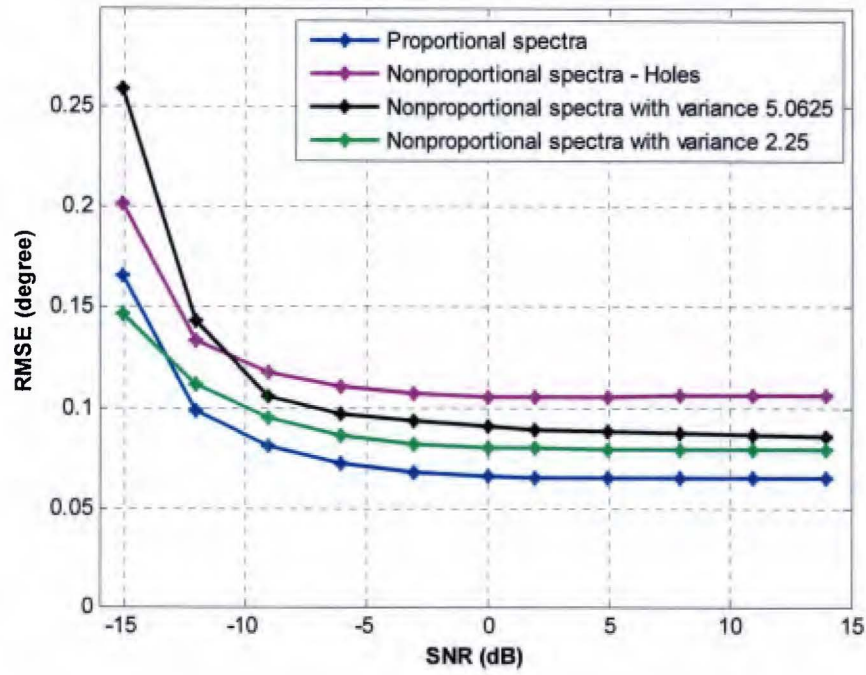


Figure 13. RMSE vs. SNR for $M=5$, $N=7$, $D=44$.

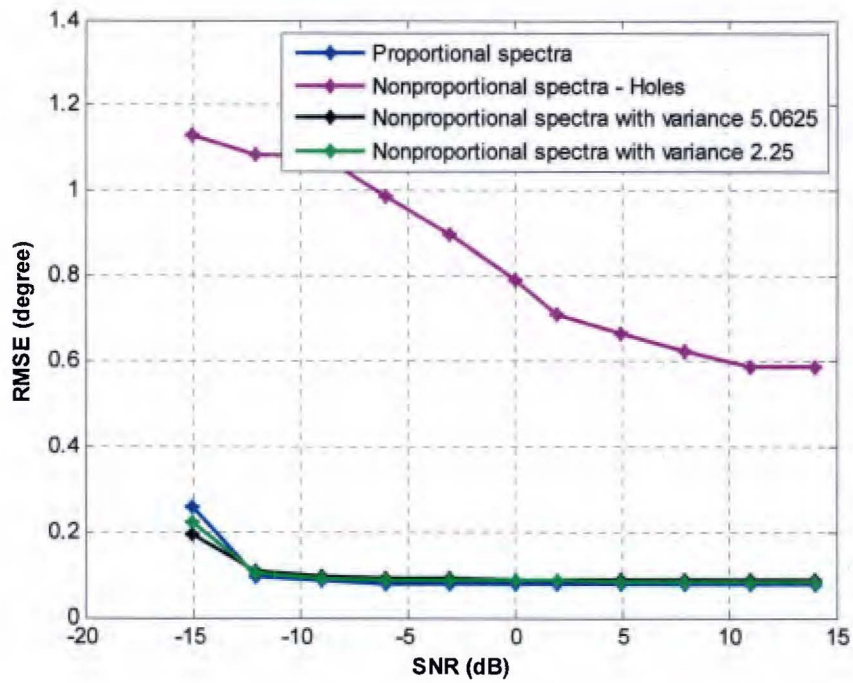


Figure 14. RMSE vs. SNR for $M=5$, $N=7$, $D=60$.

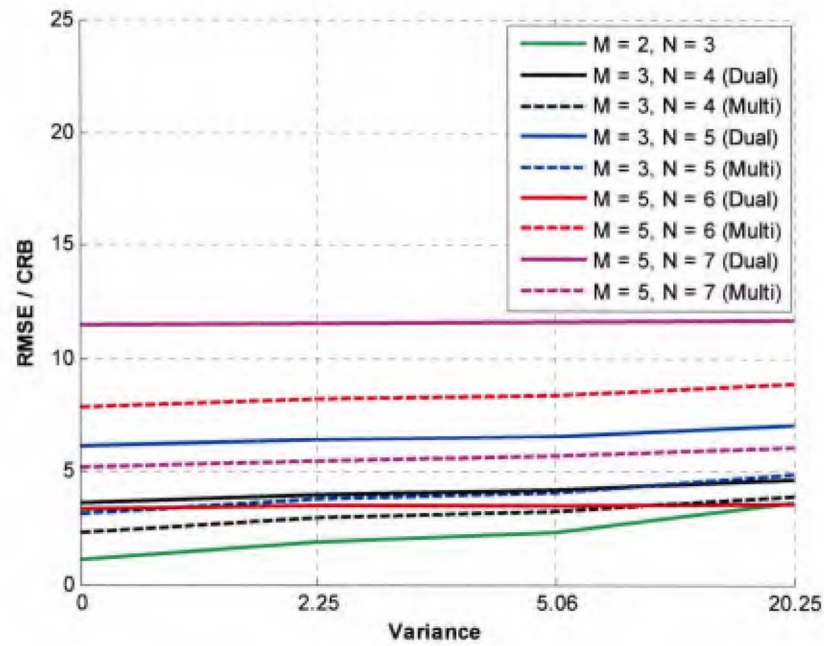


Figure 15. RMSE vs. variance, SNR = 0 dB

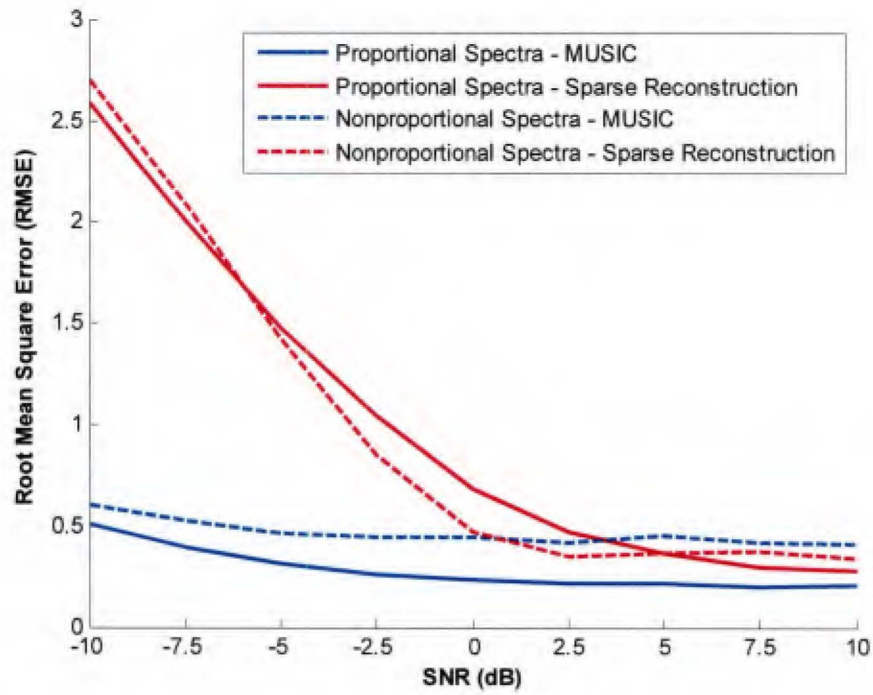


Figure 16. RMSE vs. SNR comparison between MUSIC and sparse reconstruction based multi-frequency approaches.

3.3. DOA Estimation Exploiting A Uniform Linear Array with Multiple Co-prime Frequencies

Abstract

The co-prime array, which utilizes a co-prime pair of uniform linear sub-arrays, provides a systematic means for sparse array construction. By choosing two co-prime integers M and N , $\mathcal{O}(MN)$ co-array elements can be formed from only $\mathcal{O}(M + N)$ physical sensors. As such, a higher number of degrees-of-freedom (DOFs) is achieved, enabling direction-of-arrival (DOA) estimation of more targets than the number of physical sensors. In this paper, we propose an alternative structure to implement co-prime arrays. A single sparse uniform linear array is used to exploit two or more continuous-wave signals whose frequencies satisfy a co-prime relationship. This extends the co-prime array and filtering to a joint spatio-spectral domain, thereby achieving high flexibility in array structure design to meet system complexity constraints. The DOA estimation is obtained using group sparsity-based compressive sensing techniques. In particular, we use the recently developed complex multitask Bayesian compressive sensing for group sparse signal reconstruction. The achievable number of DOFs is derived for the two-frequency case, and an upper bound of the available DOFs is provided for multi-frequency scenarios. Simulation results demonstrate the effectiveness of the proposed technique and verify the analysis results.

I. INTRODUCTION

An important application of array signal processing is direction-of-arrival (DOA) estimation, which determines the spatial spectrum of the impinging electromagnetic waves. It is well known that an N -element uniform linear array (ULA) has $N - 1$ degrees-of-freedom (DOFs), i.e., it resolves up to $N - 1$ sources or targets by using conventional DOA estimation methods, such as MUSIC and ESPRIT [3, 4]. On the other hand, a higher number of DOFs can be achieved to resolve more targets by using the same number of array sensors if they are sparsely placed [5, 6]. An increased number of DOFs is usually achieved by exploiting the extended difference co-array whose virtual sensor positions are determined by the lag differences between the physical sensors.

Among a number of techniques that are available for sparse array construction, co-prime array [7] is considered attractive due to its capability of the systematic sparse array design. By choosing two integer numbers M and N to be co-prime, $\mathcal{O}(MN)$ targets can be resolved with $M + N - 1$ physical sensors [8]. This co-prime array concept can be generalized by introducing an integer factor that compresses the inter-element spacing of one constituting sub-array, thereby achieving increased DOFs [9, 11]. In addition,

by placing the two sub-arrays co-linearly instead of co-located, the number of unique virtual sensors is further increased, which benefits DOA estimation based on sparse signal reconstruction techniques [10, 11].

While the co-prime array concept has been developed using physical uniform linear sub-arrays, we propose in this paper an effective scheme that implements co-prime array configurations using a single sparse ULA with two or more co-prime frequencies. As such, the ULA, whose inter-element spacing is respectively M_1 and M_2 half-wavelengths of the two respective frequencies, with M_1 and M_2 to be mutually co-prime integers, acts as virtual sub-arrays, resulting in an equivalent structure to co-prime arrays. In essence, the proposed approach integrates the concept of co-prime array and co-prime filter to reduce complexity and achieve high system performance. Unlike co-prime arrays, wherein the numbers of sub-array sensors and the inter-element spacings have to satisfy the co-prime relationship, only the frequencies are required to be co-prime in the proposed scheme.

The proposed scheme can be adopted for both passive and active radar systems. The former requires filtering the signal arrivals at the employed co-prime frequencies, whereas the latter requires emitting those frequencies from a single antenna or a phased array and receiving the target backscattering with ULA. The transmitter and receiver can be located or widely separated. For active sensing, sum co-array of the transmit and receive arrays replaces the difference co-array of the two structures which is associated with receive only operations [12].

In this paper, we derive the analytical expression of the available number of DOFs as a function of the number of physical sensors, L , and the selected co-prime frequencies for the two-frequency case. The results resemble those derived in [9, 11] for a physical co-prime array. The key difference lies in the fact that, unlike the co-prime array where each sub-array uses a different number of sensors, the two virtual sub-arrays in the underlying structure refer to the same physical ULA and thus share the same number of sensors. In addition, the number of physical sensors is not tied to the co-prime frequency multipliers M_1 and M_2 . The property enables a higher flexibility in array design and operation. In particular, for a fixed number of physical array sensors, L , we demonstrate that a high number of DOFs, proportional to L^2 , can be achieved with large values of M_1 and M_2 . When K mutually co-prime frequencies are used, each pair of these frequencies can form a virtual co-prime array as discussed above. Accordingly, $\mathcal{O}(K^2 L^2)$ DOFs can be achieved.

It is shown that, in the proposed scheme, the self-lags in the co-array corresponding to each sub-array form a subset of the sub-array cross-lags. As such, the available DOFs are solely determined by the number of cross-lags between the two sub-arrays. Because of the frequency-dependent characteristics of the source, channel and target radar cross section (RCS), the received signal vectors corresponding to the

different frequencies have a common spatial support, i.e., DOA, but generally have distinct coefficients. Thus, DOA estimations become a group sparse signal reconstruction problem. In this case, the self-lags obtained for each sub-array can also be exploited for possible performance improvement.

A large number of compressive sensing (CS) techniques have been proposed to deal with this problem. In this paper, we consider the problem under the Bayesian compressive sensing (BCS) or sparse Bayesian learning framework [13–17], which generally achieves a better reconstruction performance over those on the basis of the greedy algorithms and dynamic programming approaches, such as the orthogonal matching pursuit (OMP) [18] and the least absolute shrinkage and selection operator (LASSO) [19] algorithms. In particular, we use the complex multitask Bayesian compressive sensing (CMT-BCS) algorithm [20] to determine the DOAs of group sparse complex signals. This algorithm jointly treats the real and imaginary components of a complex value, in lieu of decomposing them into independent real and imaginary components. As a result, the sparsity of the estimated weight vectors can be improved, yielding better signal recovery. Group sparsity treatments for real and imaginary entries have been reported in, e.g., [21, 22].

The remainder of the paper is organized as follows. In Section II, we first review the co-prime array concept based on the difference co-array. Then, the array signal model exploiting co-prime frequencies is summarized in Section III. Analytical expressions of array aperture and the number of DOFs are derived in Section IV with respect to two and multiple co-prime frequencies. Sparsity-based DOA estimation exploiting the CMT-BCS is described in Section V. Simulation results are provided in Section VI to compare the performance of DOA estimation for different scenarios and validate the usefulness of the results presented in Section V. Section VII concludes this paper.

Notations: We use lower-case (upper-case) bold characters to denote vectors (matrices). In particular, \mathbf{I}_N denotes the $N \times N$ identity matrix. $(\cdot)^*$ implies complex conjugation, whereas $(\cdot)^T$ and $(\cdot)^H$ respectively denote the transpose and conjugate transpose of a matrix or vector. $\text{vec}(\cdot)$ denotes the vectorization operator that turns a matrix into a vector by stacking all columns on top of each other, and $\text{diag}(\mathbf{x})$ denotes a diagonal matrix that uses the elements of \mathbf{x} as its diagonal elements. $\|\cdot\|_2$ and $\|\cdot\|_1$ respectively denote the Euclidean (l_2) and l_1 norms, and $\mathbb{E}(\cdot)$ is the statistical expectation operator. \otimes denotes the Kronecker product, and $\lfloor \cdot \rfloor$ denotes the floor function and returns the largest integer not exceeding the argument. $P_r(\cdot)$ denotes the probability density function (pdf), and $\mathcal{N}(x|a, b)$ denotes that random variable x follows a Gaussian distribution with mean a and variance b . $\text{Re}(x)$ and $\text{Im}(x)$ denote the real and imaginary parts of complex element x , respectively.

II. CO-PRIME ARRAY CONCEPT

In this section, we first review the co-prime array configuration that achieves a higher number of DOFs based on the difference co-array concept. A co-prime array [7] is illustrated in Fig. 1, where M and N are co-prime integers, i.e., their greatest common divisor is one. Without loss of generality, we assume $M < N$. The unit inter-element spacing d is typically set to $\lambda/2$, where λ denotes the wavelength. The array sensors are positioned at

$$\mathbb{P} = \{Mnd \mid 0 \leq n \leq N-1\} \cup \{Nmd \mid 0 \leq m \leq M-1\}. \quad (1)$$

Because the two sub-arrays share the first sensor at the zeroth position, the total number of sensors used in the co-prime array is $M + N - 1$. Note that the minimum inter-element spacing in this co-prime array is $d = \lambda/2$.

Denote $\mathbf{p} = [p_1, \dots, p_{M+N-1}]^T$ as the positions of the array sensors, where $p_i \in \mathbb{P}$, $i = 1, \dots, M+N-1$, and the first sensor, located at $p_1 = 0$, is assumed as the reference. Assume that Q uncorrelated signals impinging on the array from angles $\Theta = [\theta_1, \dots, \theta_Q]^T$, and their discretized baseband waveforms are expressed as $s_q(t)$, $t = 1, \dots, T$, for $q = 1, \dots, Q$. Then, the data vector received at the co-prime array is expressed as,

$$\mathbf{x}(t) = \sum_{q=1}^Q \mathbf{a}(\theta_q) s_q(t) + \mathbf{n}(t) = \mathbf{A} \mathbf{s}(t) + \mathbf{n}(t), \quad (2)$$

where

$$\mathbf{a}(\theta_q) = \left[1, e^{j \frac{2\pi p_2}{\lambda} \sin(\theta_q)}, \dots, e^{j \frac{2\pi p_{M+N-1}}{\lambda} \sin(\theta_q)} \right]^T \quad (3)$$

is the steering vector of the array corresponding to θ_q , $\mathbf{A} = [\mathbf{a}(\theta_1), \dots, \mathbf{a}(\theta_Q)]$, and $\mathbf{s}(t) = [s_1(t), \dots, s_Q(t)]^T$. The elements of the noise vector $\mathbf{n}(t)$ are assumed to be independent and identically distributed (i.i.d.) random variables following the complex Gaussian distribution $\mathcal{CN}(0, \sigma_n^2 \mathbf{I}_{M+N-1})$.

The covariance matrix of the data vector $\mathbf{x}(t)$ is obtained as

$$\begin{aligned} \mathbf{R}_{\mathbf{xx}} &= \mathbb{E}[\mathbf{x}(t) \mathbf{x}^H(t)] = \mathbf{A} \mathbf{R}_{\mathbf{ss}} \mathbf{A}^H + \sigma_n^2 \mathbf{I}_{M+N-1} \\ &= \sum_{q=1}^Q \sigma_q^2 \mathbf{a}(\theta_q) \mathbf{a}^H(\theta_q) + \sigma_n^2 \mathbf{I}_{M+N-1}, \end{aligned} \quad (4)$$

where $\mathbf{R}_{\mathbf{ss}} = \mathbb{E}[\mathbf{s}(t) \mathbf{s}^H(t)] = \text{diag}([\sigma_1^2, \dots, \sigma_Q^2])$ with σ_q^2 denoting the input signal power of the q th target, $q = 1, \dots, Q$. In practice, the covariance matrix is estimated using the T available samples, i.e.,

$$\hat{\mathbf{R}}_{\mathbf{xx}} = \frac{1}{T} \sum_{t=1}^T \mathbf{x}(t) \mathbf{x}^H(t). \quad (5)$$

By vectorizing the matrix $\hat{\mathbf{R}}_{\mathbf{xx}}$, we obtain the following measurement vector:

$$\mathbf{z} = \text{vec}(\hat{\mathbf{R}}_{\mathbf{xx}}) = \tilde{\mathbf{A}} \mathbf{b} + \sigma_n^2 \mathbf{i}, \quad (6)$$

where $\tilde{\mathbf{A}} = [\tilde{\mathbf{a}}(\theta_1), \dots, \tilde{\mathbf{a}}(\theta_Q)]$, $\tilde{\mathbf{a}}(\theta_q) = \mathbf{a}^*(\theta_q) \otimes \mathbf{a}(\theta_q)$, for $1 \leq q \leq Q$. In addition, $\mathbf{b} = [\sigma_1^2, \dots, \sigma_Q^2]^T$ and $\mathbf{i} = \text{vec}(\mathbf{I}_{M+N-1})$. Benefiting from the Vandermonde vector $\mathbf{a}(\theta_q)$, we can regard \mathbf{z} as a received signal from a single snapshot \mathbf{b} and the matrix $\tilde{\mathbf{A}}$ behaves as the manifold matrix of a larger virtual array which has sensors located at the lags between two sub-arrays. From a pair of antennas located at the i th and k th positions in \mathbf{p} , the correlation $E[x_i(t)x_k^*(t)]$ yields the (i, k) th entry in $\mathbf{R}_{\mathbf{xx}}$ with lag $p_i - p_k$. As such, all the available values of i and k , where $0 \leq i \leq M + N - 1$ and $0 \leq k \leq M + N - 1$, yield virtual sensors of the following difference co-array:

$$\mathbb{C}_P = \{\mathbf{z} \mid \mathbf{z} = \mathbf{u} - \mathbf{v}, \mathbf{u} \in \mathbb{P}, \mathbf{v} \in \mathbb{P}\}. \quad (7)$$

The significance of the difference co-array is that the correlation of the received signal can be calculated at all lags in the set \mathbb{C}_P . Any application which depends only on such correlation (e.g., DOA estimation) can exploit all the DOFs offered by the resulting co-array structure. Using a part or the entire set of the distinct lag entries in the set \mathbb{C}_P , instead of the original physical array, to perform DOA estimation, we can increase the parameter identifiability. The maximum number of the DOFs is determined by the number of unique elements in the following set

$$\mathbb{L}_P = \{l_P \mid l_P d \in \mathbb{C}_P\}. \quad (8)$$

III. SYSTEM MODEL

As described in the previous section, a higher number of DOFs is achieved using a co-prime array. Such a co-prime array structure was originally developed using two physical uniform linear sub-arrays with co-prime inter-element spacing [7]. In this paper, we extend that concept to a sparse ULA with two or multiple co-prime frequencies, offering improved capabilities and flexibilities to achieve better performance using a single ULA.

Assume K continuous-wave (CW) signals with co-prime frequencies are received at an L -element ULA with inter-element spacing D . By co-prime frequencies, we mean that the ratio between carrier frequencies equals the ratio between co-prime integers. For a CW waveform with frequency f_k , $k = 1, \dots, K$, the return signal from the Q far-field targets, located at DOAs θ_q , $q = 1, 2, \dots, Q$, are expressed in a vector form as

$$\tilde{\mathbf{x}}_k(t) = \exp(j2\pi f_k t) \sum_{q=1}^Q \rho_{kq}(t) \mathbf{a}_k(\theta_q) + \tilde{\mathbf{n}}_k(t), \quad k = 1, \dots, K, \quad (9)$$

where $\rho_{kq}(t)$ is the complex envelop of the signal q corresponding to f_k , which does not vary with the receive antennas, but is in general frequency-dependent due to the different propagation phase delays. We assume $\rho_{kq}(t)$ to be uncorrelated for different targets over one scan due to target motion or RCS

fluctuations (Swerling II). In addition, $\mathbf{a}_k(\theta_q)$ is the steering vector corresponding to θ_q for frequency f_k , expressed as

$$\mathbf{a}_k(\theta_q) = \left[1, e^{-j\frac{2\pi D}{\lambda_k} \sin(\theta_q)}, \dots, e^{-j\frac{2\pi(L-1)D}{\lambda_k} \sin(\theta_q)} \right]^T, \quad (10)$$

where $\lambda_k = c/f_k$ denotes the wavelength corresponding to f_k , and c is the velocity of wave propagation. Furthermore, $\mathbf{n}_k(t)$ is the additive noise vector whose elements are assumed to be spatially and temporally white, and are independent of the target signals.

After converting the received signal vector to baseband using the respective frequencies, followed by low-pass filtering, we obtain

$$\mathbf{x}_k(t) = \sum_{q=1}^Q \rho_{kq}(t) \mathbf{a}_k(\theta_q) + \mathbf{n}_k(t) = \mathbf{A}_k \mathbf{s}_k(t) + \mathbf{n}_k(t), \quad k = 1, \dots, K, \quad (11)$$

where $\mathbf{A}_k = [\mathbf{a}_k(\theta_1), \dots, \mathbf{a}_k(\theta_Q)]$ and $\mathbf{s}_k(t) = [\rho_{k1}(t), \dots, \rho_{kQ}(t)]^T$. We denote the noise variance at the filter output as $\sigma_{n_k}^2$.

For convenience, $M_k, k = 1, \dots, K$, are denoted as mutually co-prime integers. Without loss of generality, we assume that they are sorted in a descending order, i.e., $M_1 < M_2 < \dots < M_K$. In addition, we assume that D is integer multiples of the half-wavelengths of all frequencies, such that $M_k = 2D/\lambda_k, k = 1, \dots, K$. As such, the ULA is sparse (spatially undersampled) at each frequency by a factor of M_k . In this case and for clarity, we can rewrite the steering vectors in a frequency-independent form, expressed as

$$\mathbf{a}_k(\theta_q) = \left[1, e^{-jM_k \pi \sin(\theta_q)}, \dots, e^{-jM_k(L-1)\pi \sin(\theta_q)} \right]^T. \quad (12)$$

It is clear that the DOA estimation problem is similar to the co-prime arrays considered in [7, 11]. There are K uniform linear sub-arrays with a respective co-prime inter-element spacing. It is noted, however, that unlike a co-prime array, in which the numbers of sub-array sensors are different, all sub-arrays in the underlying virtual co-prime array structure share the same number of sensors, L . In addition, the DOA estimation method needs to account for the fact that signals corresponding to different virtual arrays have distinct phases. In the next two sections, we respectively analyze the achievable DOFs and describe group sparse CS-based DOA estimation technique.

IV. ANALYSIS OF ACHIEVABLE DOFs

Similar to the co-prime array, the parameter identifiability can be improved using correlation-aware techniques. In this section, we consider the virtual array constructed by exploiting multiple co-prime frequencies and derive the analytical expressions of the number of DOFs.

A. Analysis of DOFs with two co-prime frequencies

We first consider the problem when two frequencies M_1 and M_2 , $M_1 < M_2$, are used. As shown in Fig. 2, the sensors of the two equivalent sub-arrays are located at

$$\tilde{\mathbb{P}} = \{M_1 l_1 d_0 | 0 \leq l_1 \leq L-1\} \cup \{M_2 l_2 d_0 | 0 \leq l_2 \leq L-1\}, \quad (13)$$

where d_0 denotes a half-wavelength unit inter-element spacing in a normalized frequency sense (i.e., no specific frequency is referred to), and l_1 and l_2 are the respective indices of the sensor positions of the two equivalent sub-arrays. As such, the aperture of this equivalent co-prime array structure is $M_2(L-1)d_0$. In addition, the two uniform linear sub-arrays in the underlying problem have the same L sensors, which align in the zeroth position and whenever l_2/M_2 is an integer. Therefore, there are $2L-1 - \lfloor (L-1)/M_2 \rfloor$ equivalent sensors. It is noted that, when $M_2 < L$, there are overlaps among the equivalent sensors, resulting in a reduced number of DOFs. Therefore, we only consider the $M_2 \geq L$ case in the remainder of this paper.

Because each sub-array is linear and uniformly spaced and the two sub-arrays share the first sensor at the zeroth position, a self-lag position of a sub-array can always be taken as the cross-lag position between a sensor of this sub-array and the first sensor of the other sub-array. In other words, the self-lag positions form a subset of the cross-lag positions [11]. Therefore, we only consider the cross-lags when determining the number of DOFs. In this array configuration, the cross-lags of the two equivalent sub-arrays are given by the following set,

$$\tilde{\mathbb{L}}_c = \{\tilde{l}_c | \tilde{l}_c = M_1 l_1 - M_2 l_2\}, \quad (14)$$

and the corresponding mirrored set,

$$\tilde{\mathbb{L}}_c^- = \{\tilde{l}_c | \tilde{l}_c = M_2 l_2 - M_1 l_1\} = \{-\tilde{l}_c | \tilde{l}_c \in \tilde{\mathbb{L}}_c\}, \quad (15)$$

where $0 \leq l_1 \leq L-1$ and $0 \leq l_2 \leq L-1$. The achievable DOFs from the difference co-array is determined by the unique elements in the following set

$$\tilde{\mathbb{L}}_P = \tilde{\mathbb{L}}_c \cup \tilde{\mathbb{L}}_c^-. \quad (16)$$

Overall, there are $2L^2$ lags in the set $\tilde{\mathbb{L}}_P$, which contains both non-overlapping and overlapping lags. To obtain a higher number of DOFs, which is determined by the number of unique lags in the set $\tilde{\mathbb{L}}_P$, we can choose different pairs of M_1 and M_2 to reduce the redundancies in both $\tilde{\mathbb{L}}_c$ and $\tilde{\mathbb{L}}_c^-$, as well as the overlapping lags between $\tilde{\mathbb{L}}_c$ and $\tilde{\mathbb{L}}_c^-$.

Denote η as the number of unique lags in the set $\tilde{\mathbb{L}}_P$. The following proposition reveals the analytical relationship between η and different choice of M_1 and M_2 .

Proposition 1: For a virtual array constructed from a ULA with inter-element spacing D using two co-prime frequencies with $D = \frac{1}{2}M_1\lambda_1 = \frac{1}{2}M_2\lambda_2$, the number of unique lags is given by

$$\eta = 2L^2 - 1 - \max\{0, 2L - 1 - M_2\}\min\{M_1 + 1, 2L - 1 - M_1\}. \quad (17)$$

It can be expressed for three different cases:

- (a) For $M_2 \geq 2L - 1$, $\eta = 2L^2 - 1$;
- (b) For $L \leq M_2 < 2L - 1$ and $L \leq M_1 < M_2$, $\eta = 2L^2 - 1 - (2L - 1 - M_2)(2L - 1 - M_1)$;
- (c) For $L \leq M_2 < 2L - 1$ and $1 \leq M_1 < L$, $\eta = 2L^2 - 1 - (2L - 1 - M_2)(M_1 + 1)$.

The proof is provided in Appendix A.

The number of DOFs in the co-array can be obtained as $(\eta + 1)/2$ [23]. It indicates that η achieves the maximum value of $2L^2 - 1$ in case (a), irrespective of M_1 , provided that $M_1 < M_2$ is satisfied. In practice, however, a large value of M_2 would increase the number of missing positions, i.e., holes in the difference co-array. For cases (b) and (c), η depends on the values of both M_1 and M_2 and is maximized when $M_1 = 1$ or $M_1 = M_2 - 1$. The latter case yields a smaller frequency separation between f_1 and f_2 , whereas the former configuration represents a nested structure [24]. A nested array is usually designed such that the virtual sensors in the resulting co-array are all contiguous and is considered as a special case of the generalized co-prime array in [11].

For an illustrative purpose, examples for different pairs of M_1 and M_2 are presented in Fig. 3 and Fig. 4, where the physical ULA has 4 sensors in all cases. The equivalent sensor positions are illustrated in Fig. 3, whereas the respective co-arrays are presented in Fig. 4. Note that the holes are indicated by “ \times ”. It is clear that the difference co-arrays for all cases have more virtual sensors than the number of physical sensors in the original ULA. Compared to the other examples, there are more duplications in the $M_1 = 2$ and $M_2 = 3 < L$ case depicted in Fig. 3(a), leading to a reduction of the DOFs in the co-array, as shown in Fig. 4(a). Also, there are 19 unique lags for the $M_1 = 3$ and $L < M_2 = 4 < 2L - 1$ case in Fig. 4(b), whereas it increases to 31 in Fig. 4(c) for $M_1 = 6$ and $M_2 = 7 \geq 2L - 1$, due to fewer overlapping lags between $\tilde{\mathbb{L}}_c$ and $\tilde{\mathbb{L}}_c^-$. The nested structure with $M_1 = 1$ and $M_2 = L = 4$ is depicted in Fig. 4(d) as a special case of $L \leq M_2 < 2L - 1$. It is evident that, in this case, all 25 lags are contiguous.

B. Analysis of DOFs with multiple co-prime frequencies

When more than two mutually co-prime frequencies are used, each co-prime frequency pair forms a virtual co-prime array corresponding to the two frequencies. Therefore, for K mutually co-prime frequencies, there are $\binom{K}{2} = \frac{K(K-1)}{2}$ co-prime frequency pairs. As a consequence, the number of DOFs in the resulting co-array is determined by the cardinality of the unique sum set of lags obtained in each

co-prime frequency pair, which generally increases with the number of frequencies being used. However, a general expression of the DOF for different choices of the co-prime frequencies is rather complicated and does not necessarily provide meaningful insights. Instead, we provide the maximum number of achievable DOFs in the following proposition, which corresponds to the case where each pair achieves the maximum number of DOFs with minimum overlapping between different frequency pairs.

Proposition 2: The maximum number of achievable unique lags of the co-array generated from the equivalent sub-arrays is given by

$$\eta = (L^2 - 1)(K^2 - K) - 2(L - 1)(K^2 - 2K) + 1. \quad (18)$$

The proof is provided in Appendix B.

It is clear that $\eta \propto O(K^2 L^2)$, since there are $O(K^2)$ frequency pairs and $O(L^2)$ unique lags for each pair. To achieve the upper bound of DOFs, however, it requires a large separation between different multipliers $M_k, k = 1, \dots, K$, so that the number of overlapping lags between different frequency pairs is minimized.

V. COMPRESSIVE SENSING BASED DOA ESTIMATION

While the DOA estimation problem considered here appears to be similar to that discussed in [7, 25], the CS method exploited therein cannot be readily applied to the underlying problem. A major distinction is that the target reflection coefficients $\rho_{kq}, q = 1, \dots, Q$, differ at different frequencies $k = 1, \dots, K$, due to differences in their propagation phase delays and target reflectivities. As such, the phase term of the cross-correlation between the received data vectors for different frequencies depends not only on the spatial angle, but also on the unknown phase difference in the reflection coefficients and propagation delays. In this section, we formulate the DOA estimation problem as a group sparsity based signal recovery problem.

A. DOA estimation using only cross-lags

As discussed earlier, a full number of unique lags is achieved in the resulting co-array by using the cross-lags between the sub-arrays. As such, the spatial spectra can be estimated based only on the cross-lag correlations without loss of DOFs.

The cross-lag covariance matrix $\mathbf{R}_{\mathbf{xx}}^{(i,k)}$ between the $L \times 1$ received data vectors $\mathbf{x}_i(t)$ and $\mathbf{x}_k(t)$, for $1 \leq i \neq k \leq K$, is obtained as

$$\mathbf{R}_{\mathbf{xx}}^{(i,k)} = \mathbb{E} [\mathbf{x}_i(t) \mathbf{x}_k^H(t)] = \mathbf{A}_i \mathbf{R}_{\mathbf{ss}}^{(i,k)} \mathbf{A}_k^H = \sum_{q=1}^Q \sigma_q^{(i,k)} \mathbf{a}_i(\theta_q) \mathbf{a}_k^H(\theta_q), \quad (19)$$

where $\mathbf{R}_{\text{ss}}^{(i,k)} = \mathbb{E}[\mathbf{s}_i(t)\mathbf{s}_k^H(t)] = \text{diag}([\sigma_1^{(i,k)}, \dots, \sigma_Q^{(i,k)}])$ is the cross-correlation matrix between the received signals at the i th and k th frequencies. Note that $\sigma_q^{(i,k)}$, $q = 1, \dots, Q$, in general, takes a complex value. Vectorizing $\mathbf{R}_{\text{xx}}^{(i,k)}$ in (19), we obtain

$$\mathbf{z}_{ik} = \text{vec}(\mathbf{R}_{\text{xx}}^{(i,k)}) = \tilde{\mathbf{A}}_{ik} \mathbf{b}_{ik}, \quad i \neq k \in [1, \dots, K], \quad (20)$$

where $\tilde{\mathbf{A}}_{ik} = [\tilde{\mathbf{a}}_{ik}(\theta_1), \dots, \tilde{\mathbf{a}}_{ik}(\theta_Q)]$ with $\tilde{\mathbf{a}}_{ik}(\theta_q) = \mathbf{a}_i^*(\theta_q) \otimes \mathbf{a}_k(\theta_q)$, and $\mathbf{b}_{ik} = [\sigma_1^{(i,k)}, \dots, \sigma_Q^{(i,k)}]^T$. It is noted that the $L^2 \times 1$ vector \mathbf{z}_{ik} can be sparsely represented in the spatial domain over the entire angular grids as

$$\mathbf{z}_{ik} = \tilde{\mathbf{A}}_{ik}^o \mathbf{b}_{ik}^o, \quad i \neq k \in [1, \dots, K], \quad (21)$$

where $\tilde{\mathbf{A}}_{ik}^o$ is defined as the collection of steering vectors $\tilde{\mathbf{a}}_{ik}$ over the entire possible grids θ_g for $g = 1, \dots, G$, with $G \gg Q$. It is important to note that the angle positions of the signal arrivals θ_q , $q = 1, \dots, Q$, are indicated by the non-zero entries in vector \mathbf{b}_{ik}^o , whose values describe the corresponding coefficients. Generally, the non-zero entries take different values with respect to different frequency pairs but share the same positions because they correspond to the DOAs of the same Q targets. Therefore, \mathbf{b}_{ik}^o exhibits a group sparsity across the K frequencies and, as such, the DOA estimation problem can be solved in the context of group sparse reconstruction.

B. DOA estimation using both self- and cross-lags

While CS-based DOA estimation can be performed based only on the cross-lag correlations without losing the available co-array DOFs, the utilization of both self- and cross-lags makes full use of the observed data and may yield performance improvement.

The self-lag covariance matrix for the data vector $\mathbf{x}_k(t)$, corresponding to the k th frequency for $1 \leq k \leq K$, can be obtained as

$$\mathbf{R}_{\text{xx}}^{(k,k)} = \mathbb{E}[\mathbf{x}_k(t)\mathbf{x}_k^H(t)] = \mathbf{A}_k \mathbf{R}_{\text{ss}}^{(k,k)} \mathbf{A}_k^H + \sigma_{n_k}^2 \mathbf{I}_L = \sum_{q=1}^Q \sigma_{kq}^2 \mathbf{a}_k(\theta_q) \mathbf{a}_k^H(\theta_q) + \sigma_{n_k}^2 \mathbf{I}_L, \quad (22)$$

where $\mathbf{R}_{\text{ss}}^{(k,k)} = \mathbb{E}[\mathbf{s}_k(t)\mathbf{s}_k^H(t)] = \text{diag}([\sigma_{k1}^2, \dots, \sigma_{kQ}^2])$ is the auto-covariance matrix corresponding to the k th frequency, and the signal power σ_{kq}^2 , $q = 1, \dots, Q$, is real and positive. Similarly, vectorizing $\mathbf{R}_{\text{xx}}^{(k,k)}$ in (22) yields an $L^2 \times 1$ vector

$$\mathbf{z}_{kk} = \text{vec}(\mathbf{R}_{\text{xx}}^{(k,k)}) = \tilde{\mathbf{A}}_k \mathbf{b}_k + \sigma_{n_k}^2 \mathbf{i}, \quad k \in [1, \dots, K], \quad (23)$$

where $\tilde{\mathbf{A}}_k = [\tilde{\mathbf{a}}_k(\theta_1), \dots, \tilde{\mathbf{a}}_k(\theta_Q)]$, $\tilde{\mathbf{a}}_k(\theta_q) = \mathbf{a}_k^*(\theta_q) \otimes \mathbf{a}_k(\theta_q)$, $\mathbf{b}_k = [\sigma_{k1}^2, \dots, \sigma_{kQ}^2]^T$, and $\mathbf{i} = \text{vec}(\mathbf{I}_L)$. Similarly, \mathbf{z}_{kk} can be sparsely represented as

$$\mathbf{z}_{kk} = \tilde{\mathbf{B}}_{kk}^o \tilde{\mathbf{b}}_{kk}^o, \quad k \in [1, \dots, K], \quad (24)$$

where $\tilde{\mathbf{B}}_{kk}^o = [\tilde{\mathbf{A}}_k^o, \mathbf{i}]$ and $\tilde{\mathbf{b}}_{kk}^o = [\mathbf{b}_{kk}^{o^T}, \sigma_{n_k}^2]^T$. Herein, $\tilde{\mathbf{A}}_k^o$ is the collection of steering vectors $\tilde{\mathbf{a}}_k(\theta_g)$ with $g = 1, \dots, G$, and \mathbf{b}_{kk}^o is the sparse vector whose non-zero entry positions correspond to the DOAs of the signals. Similar to \mathbf{b}_{ik}^o in Eqn. (21), $\tilde{\mathbf{b}}_{kk}^o$ also exhibits a group sparsity across the K frequencies and shares the same sparsity pattern with \mathbf{b}_{ik}^o . Thus, by combining the results of \mathbf{z}_{ik} and \mathbf{z}_{kk} , both self- and cross-lag covariances can be fully utilized for possible performance improvement based on group sparsity.

By using $\tilde{\mathbf{z}}_{ik}, i, k \in [1, \dots, K]$, to denote both cross-lag vector $\mathbf{z}_{ik}, i \neq k$, and self-lag vector \mathbf{z}_{kk} , the DOA estimation problem using both self- and cross-lag covariances can be reformulated as:

$$\tilde{\mathbf{z}}_{ik} = \tilde{\mathbf{B}}_{ik}^o \tilde{\mathbf{b}}_{ik}^o + \epsilon_{ik}, \quad i, k \in [1, \dots, K], \quad (25)$$

where each vector $\tilde{\mathbf{z}}_{ik}$ employs its respective $L^2 \times (G+1)$ dictionary matrix,

$$\tilde{\mathbf{B}}_{ik}^o = \begin{cases} [\tilde{\mathbf{A}}_{kk}^o, \mathbf{i}], & i = k, \\ [\tilde{\mathbf{A}}_{ik}^o, \mathbf{0}], & i \neq k, \end{cases} \quad (26)$$

and $\mathbf{0}$ denotes the all zero vector of $L^2 \times 1$. An $L^2 \times 1$ error vector ϵ_{ik} is included in (25) to account for the discrepancies between the statistical expectation and the sample average in computing the covariance matrices $\mathbf{R}_{\mathbf{xx}}^{(i,k)}, i, k = 1, \dots, K$. The discrepancies are modelled as i.i.d. complex Gaussian as a result of a sufficiently large number of samples employed in the averaging.

Note that exploiting the self-lag covariances, together with the cross-lags, requires expanding the dimension of the unknown sparse vector $\tilde{\mathbf{b}}_{ik}^o$ by an additional element of the noise power $\sigma_{n_k}^2$. In this case, the first G elements of the obtained estimates of $\tilde{\mathbf{b}}_{ik}^o$ are used to determine the DOAs, whereas the last element of $\tilde{\mathbf{b}}_{ik}^o$ is discarded.

A number of effective algorithms within the convex optimization and Bayesian sparse learning frameworks are available to solve the complex-valued group sparse reconstruction problem. In this paper, the CMT-BCS algorithm proposed in [20] and summarized in Section V-C is used due to its superior performance and robustness to dictionary coherence.

C. CMT-BCS algorithm

We use the CMT-BCS to determine the DOAs of the targets which are treated as group sparse complex observations. In this subsection, we briefly review the CMT-BCS approach based on [20]. Assume that the entries in the sparse vectors \mathbf{r}_{ik} are drawn from the product of the following zero-mean Gaussian distributions:

$$\tilde{\mathbf{b}}_{ik}^{o^g} \sim \mathcal{N}(\tilde{\mathbf{b}}_{ik}^{o^g} | \mathbf{0}, \alpha_g \mathbf{I}_2), \quad g \in [1, \dots, G], \quad (27)$$

where $\tilde{\mathbf{b}}_{ik}^{o^g}$ is a vector consisting of the real part coefficient, $\tilde{\mathbf{b}}_{ik}^{o^{gR}}$, and the imagery part coefficient, $\tilde{\mathbf{b}}_{ik}^{o^{gI}}$, with respect to the g th grid in $\tilde{\mathbf{b}}_{ik}^o$. In addition, $\alpha = [\alpha_1, \dots, \alpha_G]^T$ is a vector that contains variances of $\tilde{\mathbf{b}}_{ik}^{o^g}$, $g = 1, \dots, G$. Note that the vector α is shared by all groups to enforce the group sparsity. It is easy to confirm that $\tilde{\mathbf{b}}_{ik}^{o^g}$ trends to be zero when α_g is set to zero [14].

To encourage the sparsity of $\tilde{\mathbf{b}}_{ik}^o$, a Gamma prior is placed on α_g^{-1} , which is conjugate to the Gaussian distribution,

$$\alpha_g^{-1} \sim \text{Gamma}(\alpha_g^{-1}|a, b), \quad g \in [1, \dots, G], \quad (28)$$

where $\text{Gamma}(x^{-1}|a, b) = \Gamma(a)^{-1} b^a x^{-(a+1)} e^{-\frac{b}{x}}$, with $\Gamma(\cdot)$ denoting the Gamma function, and a and b are hyper-parameters.

As the covariance matrix is estimated from the received data samples, a Gaussian prior $\mathcal{N}(\mathbf{0}, \beta_0 \mathbf{I}_2)$ is also placed on the ϵ_{ik} . Similarly, the Gamma prior is placed on β_0^{-1} with hyper-parameters c and d .

The CMT-BCS algorithm carries out a Bayesian inference by the Gibbs samplers [20]. Once the parameters α and β_0 are estimated by maximizing the marginal likelihood, the joint posterior density function of $\tilde{\mathbf{b}}_{ik}^o$ can be obtained analytically using Bayes' rule. Define $\tilde{\mathbf{b}}_{ik}^{o_{RI}} = [(\tilde{\mathbf{b}}_{ik}^{o_R})^T, (\tilde{\mathbf{b}}_{ik}^{o_I})^T]^T$, with $\tilde{\mathbf{b}}_{ik}^{o_R} = [b_{ik}^{o_{1R}}, \dots, b_{ik}^{o_{GR}}]^T$ and $\tilde{\mathbf{b}}_{ik}^{o_I} = [b_{ik}^{o_{1I}}, \dots, b_{ik}^{o_{GI}}]^T$. Then,

$$\Pr(\tilde{\mathbf{b}}_{ik}^{o_{RI}} | \tilde{\mathbf{z}}_{ik}, \tilde{\mathbf{B}}_{ik}^o, \alpha, \beta_0) = \mathcal{N}(\tilde{\mathbf{b}}_{ik}^{o_{RI}} | \boldsymbol{\mu}_{ik}, \boldsymbol{\Sigma}_{ik}),$$

where

$$\tilde{\mathbf{z}}_{ik}^{o_{RI}} = [\text{Re}(\tilde{\mathbf{z}}_{ik})^T, \text{Im}(\tilde{\mathbf{z}}_{ik})^T]^T \quad (29)$$

$$\boldsymbol{\mu}_{ik} = \beta_0^{-1} \boldsymbol{\Sigma}_{ik} \boldsymbol{\Psi}_{ik}^T \tilde{\mathbf{z}}_{ik}^{o_{RI}}, \quad (30)$$

$$\boldsymbol{\Sigma}_{ik} = [\beta_0^{-1} \boldsymbol{\Psi}_{ik}^T \boldsymbol{\Psi}_{ik} + \mathbf{F}^{-1}]^{-1}, \quad (31)$$

$$\boldsymbol{\Psi} = \begin{bmatrix} \text{Re}(\tilde{\mathbf{B}}_{ik}^o) & -\text{Im}(\tilde{\mathbf{B}}_{ik}^o) \\ \text{Im}(\tilde{\mathbf{B}}_{ik}^o) & \text{Re}(\tilde{\mathbf{B}}_{ik}^o) \end{bmatrix}, \quad (32)$$

$$\mathbf{F} = \text{diag}(\alpha_1, \dots, \alpha_G, \alpha_1, \dots, \alpha_G). \quad (33)$$

Note that the mean and variance of each scattering coefficients can be derived using Eqns. (30) and (31) when α and β_0 are given. On the other hand, the values of α and β_0 are determined by maximizing the logarithm of the marginal likelihood, i.e.,

$$\{\alpha, \beta_0\} = \arg \max_{\alpha, \beta_0} \mathcal{L}(\alpha, \beta_0), \quad (34)$$

where

$$\begin{aligned}\mathcal{L}(\boldsymbol{\alpha}, \beta_0) &= \sum_{i,k=1}^K \log \Pr(\tilde{\mathbf{b}}_{ik}^{oRI} | \boldsymbol{\alpha}, \beta_0) \\ &= \text{const} - \frac{1}{2} \sum_{i,k=1}^K \log |\mathbf{C}_{ik}| + (\tilde{\mathbf{z}}_{ik}^{RI})^T \mathbf{C}_{ik}^{-1} \tilde{\mathbf{z}}_{ik}^{RI},\end{aligned}\quad (35)$$

and $\mathbf{C}_{ik} = \beta_0 \mathbf{I} + \boldsymbol{\Psi}_{ik} \mathbf{F} \boldsymbol{\Psi}_{ik}^T$. A type-II maximum likelihood (ML) approximation [26] employs the point estimates for $\boldsymbol{\alpha}$ and β_0 to maximize Eqn. (35), which can be implemented via the expectation maximization (EM) algorithm to yield

$$\alpha_g^{(\text{new})} = \frac{1}{K^2} \sum_{i,k=1}^K (\mu_{ik,g}^2 + \mu_{ik,g+G}^2 + \Sigma_{ik,gg} + \Sigma_{ik,(g+G)(g+G)}), \quad g \in [1, \dots, G], \quad (36)$$

$$\beta_0^{(\text{new})} = \frac{1}{2GK^2} \sum_{i,k=1}^K (\text{Tr}[\Sigma_{ik} \boldsymbol{\Psi}_{ik}^T \boldsymbol{\Psi}_{ik}] + \|\tilde{\mathbf{z}}_{ik}^{RI} - \boldsymbol{\Psi}_{ik} \boldsymbol{\mu}_{ik}\|_2^2), \quad (37)$$

where $\mu_{ik,g}^2$ and $\mu_{ik,g+G}^2$ are the g th and $(g+G)$ th elements in vector $\boldsymbol{\mu}_{ik}$, and $\Sigma_{ik,gg}$ and $\Sigma_{ik,(g+G)(g+G)}$ are the (g, g) and $(g+G, g+G)$ entries in matrix Σ_{ik} . Because $\boldsymbol{\alpha}$ and β_0 depend on $\boldsymbol{\mu}_{ik}$ and Σ_{ik} , the CMT-BCS algorithm is iterative and iterates between Eqns. (30)-(31) and Eqns. (36)-(37), until a convergence criterion is satisfied or the maximum number of iterations is reached.

VI. SIMULATION RESULTS

In the simulations, the CMT-BCS algorithm is used to estimate the DOAs of the signal arrivals with hyper-parameters $a = b = c = d = 0$. The maximum number of iterations in the Gibbs sampling is set to 200, and the sampler with the maximum marginal likelihood in the last 20 samples is chosen as the estimate of $\tilde{\mathbf{b}}_{ik}^o$.

We present four examples to demonstrate the effectiveness of the proposed technique. For all examples, Q targets, which are uniformly distributed between -60° and 60° are assumed to impinge a ULA with $L = 4$. The grid interval in the angular space is set to 0.25° . In addition, the noise power at each frequency is assumed to be identical and the phase difference between the received signal corresponding to each frequency pair is independent and uniformly distributed over $[0, 2\pi)$. We evaluate the performance through Monte Carlo simulations. The root mean-square error (RMSE) of the estimated DOA of the signal arrivals, expressed as

$$\text{RMSE} = \sqrt{\frac{1}{IQ} \sum_{i=1}^I \sum_{q=1}^Q (\hat{\theta}_q(i) - \theta_q)^2},$$

is used as the metric for performance evaluation with respect to the input SNR, where $\hat{\theta}_q(i)$ is the estimate of θ_q for the i th Monte Carlo trial, $i = 1, \dots, I$. We use $I = 500$ independent trials in all simulations.

A. Example I: Achievable number of DOFs with two co-prime frequencies

The number of achievable DOFs from the 4-element ULA with two co-prime frequencies is first illustrated in Fig. 5. $Q = 9$ targets are considered, which are much larger than the number of physical sensors. Two co-prime frequencies with $M_1 = 3$ and $M_2 = 4$ are exploited. Because the virtual sensor lags are obtained from the estimated covariance matrix based on the received data samples, as in Eqn. (5), the virtual steering matrix is sensitive to the noise contamination. To clearly demonstrate the number of achievable DOFs, therefore, we use 10000 noise-free snapshots to obtain a relatively clean covariance matrix. Fig. 5(a) shows the estimated spatial spectrum from the proposed co-array, which yields a co-array with $\eta = 19$ virtual sensors, and the result of the conventional non-co-array scenario is depicted in Fig. 5(b). It is clear that the co-array provides a sufficient number of DOFs to correctly identify the DOAs of all 9 targets, whereas the non-co-array approach fails.

B. Example II: DOA estimation using only cross-lags vs. both self- and cross-lags

In Figs. 6 and 7, the results obtained by using both self- and cross-lags are compared to those using only the cross-lags. $Q = 6$ targets are considered and two co-prime frequencies with $M_1 = 3$ and $M_2 = 4$ are exploited. The RMSE with respect to the input SNR is depicted in Fig. 6, where 2000 snapshots are used. At a moderate or high SNR, the utilization of both self- and cross-lag covariances benefits from additional measurement offered by the self-lags, resulting in the improved performance than the cross-lag only scenario. In Fig. 7, such improvement is demonstrated with fewer false peaks in the estimated spectra, where the input SNR is 10 dB. On the other hand, in the low SNR region, as shown in Fig. 6, the performance of the algorithm using cross-lag covariances only is better than the results using both self- and cross-lag covariances. In this case, both vectors \mathbf{z}_{ik} and \mathbf{z}_{kk} are highly perturbed by the noise. The inclusion of self-lag covariance matrices causes additional errors in the noise power estimation in (25), whereas this term does not exist in the cross-lag covariances.

C. Example III: DOA estimation using different frequency pairs

This example compares the DOA estimation performance when different frequency pairs are used. In the first frequency pair, $M_1 = 3$ and $M_2 = 4$ are assumed, yielding $\eta = 19$ elements in the virtual co-array. In the second frequency pair, we assume $M_1 = 6$ and $M_2 = 7$, resulting in $\eta = 31$ virtual co-array lags. In Fig. 8, the RMSE performance is presented as a function of the number of targets, Q , where SNR is assumed to be 10 dB and 2000 snapshots are exploited. The result shows that the second frequency pair outperforms the first one due to its higher number of DOFs and the larger aperture.

D. Example IV: Performance of multiple co-prime frequency cases

To demonstrate the merits of exploiting multiple co-prime frequencies, we first consider a three frequency case with $M_1 = 5$, $M_2 = 6$ and $M_3 = 7$. Similarly, 10000 noise-free snapshots are used to obtain a relatively clean covariance matrix. Fig. 9 shows the estimated spectrum for $Q = 13$ targets. Note in this case that all targets are resolved correctly due to a high number of DOFs and a small number of missing positions in the co-array.

Then, the RMSE performance of the three frequency case is presented in Fig. 10 with respect to the input SNR, where $Q = 13$ and 2000 snapshots are assumed. For comparison purposes, a four frequency scenario with $M_1 = 5$, $M_2 = 6$, $M_3 = 7$, and $M_4 = 11$ is also considered. It is clearly shown that the performance is significantly improved as the number of frequencies is increased.

VII. CONCLUSIONS

In this paper, we developed a co-prime array implementation using a sparse uniform linear array with multiple co-prime frequencies. We derived the analytical expression for the number of unique lags of the yielding difference co-array to determine the number of detectable targets. The complex multitask Bayesian compressive sensing algorithm was used to exploit the group sparse direction-of-arrivals (DOAs) across different frequencies for effective spatial spectrum estimation. The number of detectable targets and the DOA performance are improved as the number of frequencies increases. The effectiveness of the proposed technique and analysis is verified using simulation results.

VIII. APPENDIX

A. Proof of Proposition 1

Denote η_t and η_o as the total number of lags in $\tilde{\mathbb{L}}_P$ and the number of overlaps between the set $\tilde{\mathbb{L}}_c$ and $\tilde{\mathbb{L}}_c^-$, respectively. Then, the number of distinct lags in $\tilde{\mathbb{L}}_P$ can be expressed as

$$\eta = \eta_t - \eta_o. \quad (38)$$

Both $\tilde{\mathbb{L}}_c$ and $\tilde{\mathbb{L}}_c^-$ have L^2 distinct lags due to the co-primality of M_1 and M_2 . It is easy to confirm that

$$\eta_t = 2L^2. \quad (39)$$

Given arbitrary lags $\tilde{l}_{c_m} = M_1 l_{1_m} - M_2 l_{2_m}$ and $\tilde{l}_{c_n} = M_2 l_{2_n} - M_1 l_{1_n}$ in set $\tilde{\mathbb{L}}_c$ and $\tilde{\mathbb{L}}_c^-$, respectively, where the indexes $0 \leq l_{1_m} \leq L - 1$, $0 \leq l_{2_m} \leq L - 1$, $0 \leq l_{1_n} \leq L - 1$ and $0 \leq l_{2_n} \leq L - 1$. Had $\tilde{l}_{c_m} = \tilde{l}_{c_n}$ been held, we would have $M_1(l_{1_m} + l_{1_n}) = M_2(l_{2_m} + l_{2_n})$. It is evident that they

overlap at 0 position provided $l_{1_m} = l_{1_n} = l_{2_m} = l_{2_n} = 0$. When $l_{1_m} + l_{1_n} \neq 0$, the requirement is equivalent to

$$\frac{M_1}{M_2} = \frac{l_{2_m} + l_{2_n}}{l_{1_m} + l_{1_n}}. \quad (40)$$

- (a) When $M_2 \geq 2L - 1$, the maximum value of $l_{1_m} + l_{1_n}$ is less than M_2 . Since M_1 and M_2 are co-prime, it is indicated that M_1/M_2 cannot be reduced to a ratio of smaller integers. As a result, (40) cannot be hold. In other word, $\tilde{\mathbb{L}}_c$ and $\tilde{\mathbb{L}}_c^-$ only coincide at 0 position, i.e.,

$$\eta_o = 1. \quad (41)$$

Substituting (39) and (41) into (38), we can obtain

$$\eta = 2L^2 - 1. \quad (42)$$

- (b) When $L \leq M_2 < 2L - 1$, the relationship $0 \leq l_{1_m} + l_{1_n} \leq 2L - 2 < 2M_2$ is guaranteed. Due to the co-primality of M_1 and M_2 , (40) is valid if and only if

$$\begin{aligned} l_{2_m} + l_{2_n} &= M_1, \\ l_{1_m} + l_{1_n} &= M_2. \end{aligned} \quad (43)$$

Since $0 \leq l_{1_m}, l_{2_m} \leq L - 1$, the requirement is equivalent to

$$\begin{aligned} M_1 - (L - 1) &\leq l_{2_n} \leq M_1, \\ M_2 - (L - 1) &\leq l_{1_n} \leq M_2. \end{aligned} \quad (44)$$

Because $0 \leq l_{1_n}, l_{2_n} \leq L - 1$, we obtain the following relationship

$$\begin{aligned} \max\{M_1 - (L - 1), 0\} &\leq l_{2_n} \leq \min\{M_1, L - 1\}, \\ M_2 - (L - 1) &\leq l_{1_n} \leq L - 1, \end{aligned} \quad (45)$$

where $\max\{a, b\}$ and $\min\{a, b\}$ are operators, returning maximum and minimum values between a and b , respectively. Since $L \leq M_1 < M_2$, Eqn. (45) becomes

$$\begin{aligned} M_1 - (L - 1) &\leq l_{2_n} \leq L - 1, \\ M_2 - (L - 1) &\leq l_{1_n} \leq L - 1. \end{aligned} \quad (46)$$

It is indicated that $2L - 1 - M_1$ and $2L - 1 - M_2$ integers are in the respective range of l_{2_n} and l_{1_n} . In addition to 0 position, there are $(2L - 1 - M_1)(2L - 1 - M_2)$ combination to satisfy (40), i.e.,

$$\eta_o = (2L - 1 - M_1)(2L - 1 - M_2) + 1. \quad (47)$$

Substituting (39) and (47) into (38), we can obtain

$$\eta = 2L^2 - 1 - (2L - 1 - M_1)(2L - 1 - M_2). \quad (48)$$

(c) When $L \leq M_2 < 2L - 1$ and $1 \leq M_1 < L$, (45) is equivalent to

$$\begin{aligned} 0 \leq l_{2n} &\leq M_1, \\ M_2 - (L - 1) \leq l_{1n} &\leq L - 1. \end{aligned} \quad (49)$$

As such, there are $(M_1 + 1)(2L - 1 - M_2)$ integers satisfying (40). Therefore,

$$\eta_o = (M_1 + 1)(2L - 1 - M_2) + 1. \quad (50)$$

Substituting (39) and (50) into (38), we can obtain

$$\eta = 2L^2 - 1 - (M_1 + 1)(2L - 1 - M_2). \quad (51)$$

B. Proof of Proposition 2

(a) When K multiple frequencies are exploited, there are $K(K - 1)/2$ pairs of frequencies. As such, the total number of lags, η_t , which includes both unique and overlapping lags, is

$$\eta_t = K(K - 1)L^2, \quad (52)$$

as each pair has $2L^2$ lags. To obtain the maximum number of achievable unique lags of the co-array, we consider the case that each pair achieves its respective maximum number of unique lags, as described in Section IV-A, and the number of overlapping lags between different pairs is minimum. In this case, redundancy between different co-prime pairs happens at the following two cases: (a) The zeroth entry is shared by all $K(K - 1)/2$ pairs of co-prime frequencies with a total number of $K(K - 1)$ overlapping lags, whereas the unique lag in this position is 1; (b) At all self-lag positions because the array sensors corresponding to each frequency are used to generate $K - 1$ co-prime frequency pairs. As each frequency yields $2(L - 1)$ non-zero self-lags in $\tilde{\mathbb{L}}_c \cup \tilde{\mathbb{L}}_c^-$, there are $K(K - 1) \times 2(L - 1)$ total lag entries with $2K(L - 1)$ unique lags, yielding $2K(K - 2)(L - 1)$ redundancies to be discounted in computing the available unique lags. As a result, we can obtain the maximum number of the achievable unique lags of the co-array as

$$\eta = \eta_t - \eta_o = (L^2 - 1)(K^2 - K) - 2(L - 1)(K^2 - 2K) + 1. \quad (53)$$

REFERENCES

- [1] Y. D. Zhang, M. G. Amin, F. Ahmad, and B. Himed, "DOA estimation using a sparse uniform linear array with two CW signals of co-prime frequencies," in *Proc. IEEE Int. Workshop on Comp. Adv. in Multi-Sensor Adaptive Proc.*, Saint Martin, Dec. 2013, pp. 404–407.
- [2] S. Qin, Y. D. Zhang, and M. G. Amin, "DOA estimation exploiting coprime frequencies," in *Proc. SPIE Wireless Sens., Localization, Process. Conf.*, Baltimore, MD, May 2014, vol. 9103, pp. 91030E1–91030E7.
- [3] R. O. Schmidt, "Multiple emitter location and signal parameter estimation," *IEEE Trans. Antennas Propagat.*, vol. 34, no. 3, pp. 276–280, March 1986.
- [4] R. Roy and T. Kailath, "ESPRIT – Estimation of signal parameters via rotation invariance techniques," *IEEE Trans. Acoust., Speech, Signal Process.*, vol. 17, no. 7, pp. 984–995, July 1989.
- [5] R. T. Hoorfar and S. A. Kassam, "The unifying role of the co-array in aperture synthesis for coherent and incoherent imaging," *Proc. IEEE*, vol. 78, no. 4, pp. 735–752, April 1990.
- [6] A. Moffet, "Minimum-redundancy linear arrays," *IEEE Trans. Antennas Propagat.*, vol. 16, no. 2, pp. 172–175, March 1968.
- [7] P. P. Vaidyanathan and P. Pal, "Sparse sensing with co-prime samplers and arrays," *IEEE Trans. Signal Process.*, vol. 59, no. 2, pp. 573–586, Feb. 2011.
- [8] P. Pal and P. P. Vaidyanathan, "Coprime sampling and the MUSIC algorithm," in *Proc. IEEE Digital Signal Process. Workshop and IEEE Signal Process. Education Workshop*, Sedona, AZ, Jan. 2011, pp. 289–294.
- [9] S. Qin, Y. D. Zhang, and M. G. Amin, "Generalized coprime array configurations," in *Proc. IEEE Sensor Array and Multichannel Signal Processing Workshop*, A Coruña, Spain, June 2014, pp. 529–532.
- [10] Y. D. Zhang, S. Qin, and M. G. Amin, "DOA estimation exploiting coprime arrays with sparse sensor spacing," in *Proc. IEEE ICASSP*, Florence, Italy, May 2014, pp. 2267–2271.
- [11] S. Qin, Y. D. Zhang, and M. G. Amin, "Generalized coprime array configurations for direction-of-arrival estimation," *IEEE Trans. Signal Process.*, vol. 63, no. 6, pp. 1377–1390, March 2015.
- [12] S. Qin, Y. D. Zhang, and M. G. Amin, "DOA estimation of mixed coherent and uncorrelated signals exploiting a nested MIMO system," in *Proc. IEEE Benjamin Franklin Symposium on Microwave and Antenna Sub-systems*, Philadelphia, PA, Sep. 2014.
- [13] M. E. Tipping, "Sparse Bayesian learning and the relevance vector machine," *J. Machine Learning Research*, vol. 1, no. 9, pp. 211–244, 2001.
- [14] S. Ji, Y. Xue, and L. Carin, "Bayesian compressive sensing," *IEEE Trans. Signal Process.*, vol. 56, no. 6, pp. 2346–2356, 2008.
- [15] S. Ji, D. Dunson, and L. Carin, "Multitask compressive sensing," *IEEE Trans. Signal Process.*, vol. 57, no. 1, pp. 92–106, 2009.
- [16] Z. Zhang and D. B. Rao, "Sparse signal recovery with temporally correlated source vectors using sparse Bayesian learning," *IEEE J. Sel. Topics Signal Process.*, vol. 57, no. 1, pp. 92–106, 2009.
- [17] Z. Zhang and D. B. Rao, "Extension of SBL algorithms for the recovery of block sparse signals with intrablock

- correlation,” *IEEE Trans. Signal Process.*, vol. 61, no. 8, pp. 2009–2015, April 2013.
- [18] J. A. Tropp and A. C. Gilbert, “Signal recovery from random measurements via orthogonal matching pursuit,” *IEEE Trans. Info. Theory*, vol. 53, no. 12, pp. 4655–4666, 2007.
- [19] R. Tibshirani, “Regression shrinkage and selection via the lasso,” *J. Royal Statistical Society, Series B*, vol. 58, no. 1, pp. 267–288, 1996.
- [20] Q. Wu, Y. D. Zhang, and M. G. Amin, “Complex multitask Bayesian compressive sensing,” in *Proc. IEEE ICASSP*, Florence, Italy, May 2014, pp. 3375–3379.
- [21] D. Wipf and S. Nagarajan, “Beamforming using the relevance vector machine,” in *Proc. Int. Conf. on Machine Learning*, Corvallis, OR, pp. 1023–1030, 2007.
- [22] L. Poli, G. Oliveri, F. Viani, and A. Massa, “MT-BCS-based microwave imaging approach through minimum-norm current expansion,” *IEEE Trans. Antennas Propagat.*, vol. 61, no. 9, pp. 4722–4732, Sept. 2013.
- [23] P. Pal and P. P. Vaidyanathan, “Pushing the limits of sparse support recovery using correlation information,” *IEEE Trans. Signal Process.*, vol. 63, no. 3, pp. 711–726, Feb. 2015.
- [24] P. Pal and P. P. Vaidyanathan, “Nested Arrays: A novel approach to array processing with enhanced degrees of freedom,” *IEEE Trans. Signal Process.*, vol. 58, no. 8, pp. 4167–4181, Aug. 2010.
- [25] Y. D. Zhang, M. G. Amin, and B. Himed, “Sparsity-based DOA estimation using co-prime arrays,” in *Proc. IEEE ICASSP*, Vancouver, Canada, May 2013, pp. 3967–3971.
- [26] D. J. C. MacKay, “Bayesian interpolation,” *Neural Comput.*, vol. 4, no. 3, pp. 415–447, 1992.

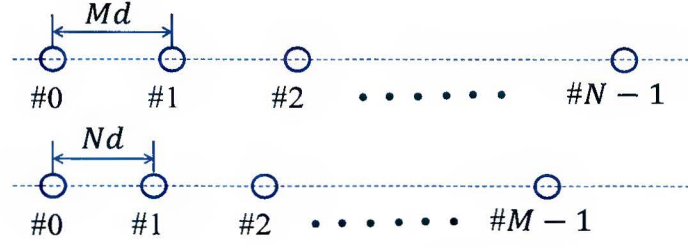
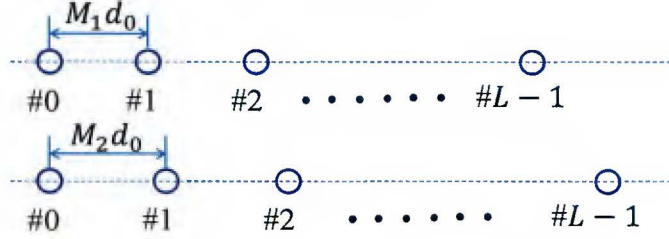


Fig. 1. The coprime array configuration.



(a) A sparse ULA



(b) Equivalent structure with two coprime frequencies

Fig. 2. A sparse ULA with two coprime frequencies configuration.

☆	x	▽	△	▽	x	☆	x	x	△
0	1	2	3	4	5	6	7	8	9

(a) $M_1=2$ and $M_2=3$

☆	x	x	▽	△	x	▽	x	△	▽	x	x	△
0	1	2	3	4	5	6	7	8	9	10	11	12

(b) $M_1=3$ and $M_2=4$

☆	x	x	x	x	x	▽	△	x	x	x	x	▽	x	△	x	x	x	▽	x	x	△
0	1	2	3	4	5	6	7	8	9	10	11	12	13	14	15	16	17	18	19	20	21

(c) $M_1=6$ and $M_2=7$

Fig. 3. Equivalent sensor positions for different M_1 and M_2 with $L = 4$ elements ULA (▽: Sub-array with M_1 ; △: Sub-array with M_2).

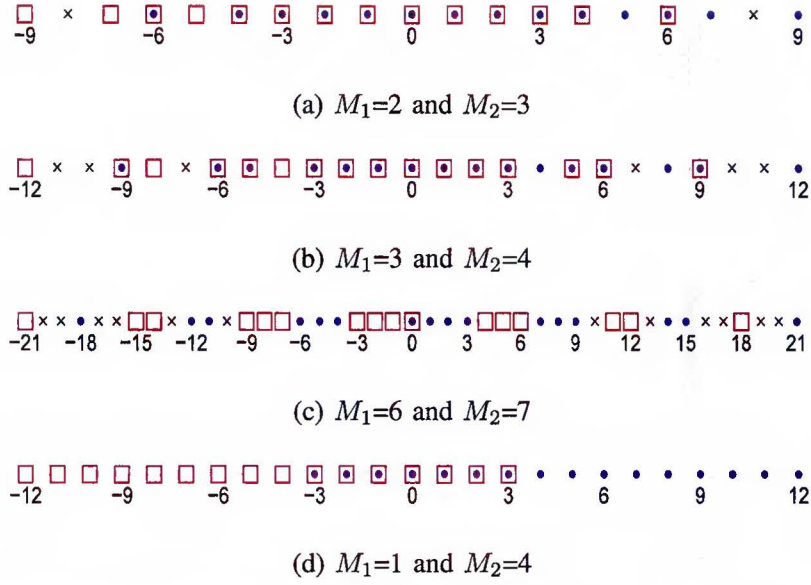


Fig. 4. The co-array lag positions in the set $\tilde{\mathcal{L}}_c \cup \tilde{\mathcal{L}}_c^-$ with $L = 4$ element ULA (\bullet : Positions in $\tilde{\mathcal{L}}_c$; \square : Positions in $\tilde{\mathcal{L}}_c^-$).

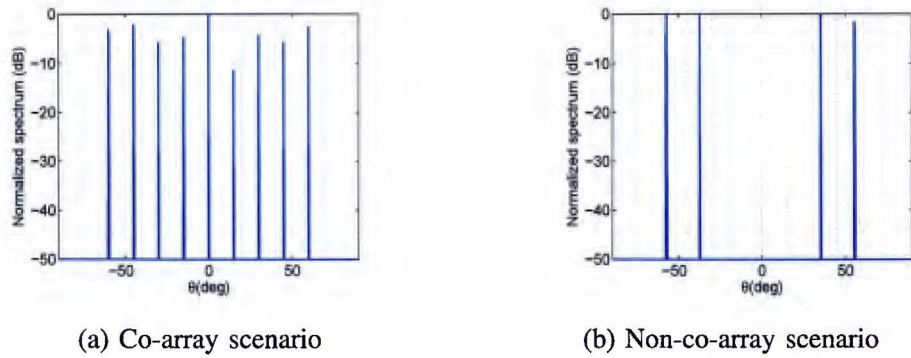


Fig. 5. Estimated spectrum using co-array and non-co-array scenarios ($M_1 = 3$, $M_2 = 4$, $Q = 9$, and 10000 noise-free snapshots).

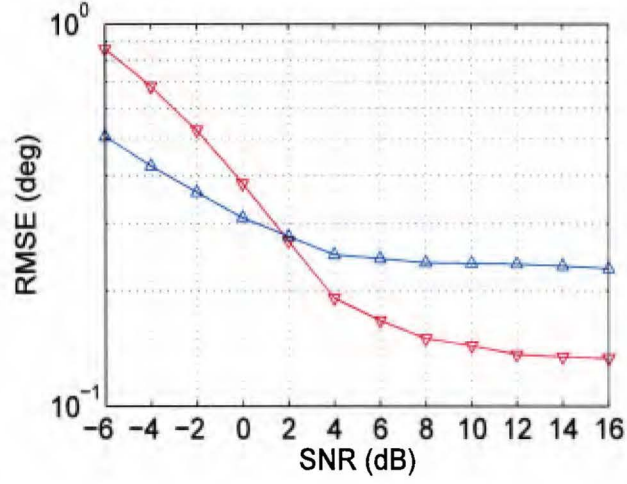
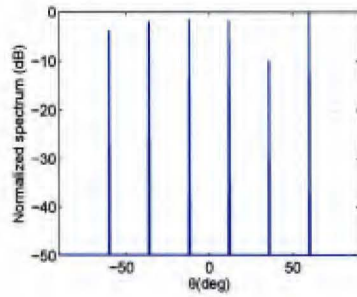
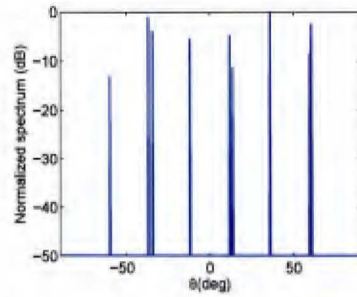


Fig. 6. RMSE versus input SNR ($M_1 = 3$, $M_2 = 4$, $Q = 6$, and 2000 snapshots; ∇ : Use self- and cross-lags; \triangle : Use cross-lags only).



(a) Using self- and cross-lags



(b) Using cross-lags only

Fig. 7. Spatial spectra estimated using different lags ($M_1 = 3$, $M_2 = 4$, $Q = 6$, SNR=10 dB, and 2000 snapshots).

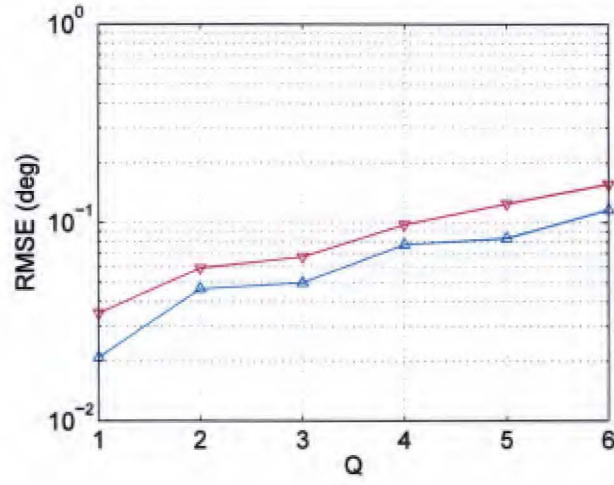
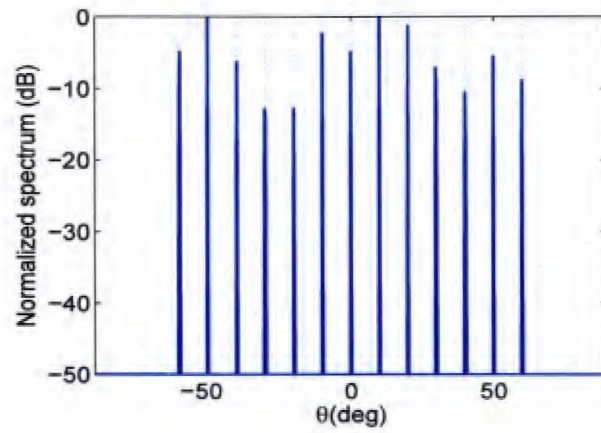


Fig. 8. RMSE versus signal number for different frequency pairs (SNR=10 dB and 2000 snapshots; ∇ : first pair ($M_1 = 3$ and $M_2 = 4$); \triangle : second pair ($M_1 = 6$ and $M_2 = 7$)).



$M_1 = 5, M_2 = 6$ and $M_3 = 7$

Fig. 9. Spatial spectra estimated for three frequency case ($M_1 = 5, M_2 = 6, M_3 = 7, Q = 13$ and 10000 noise-free snapshots).

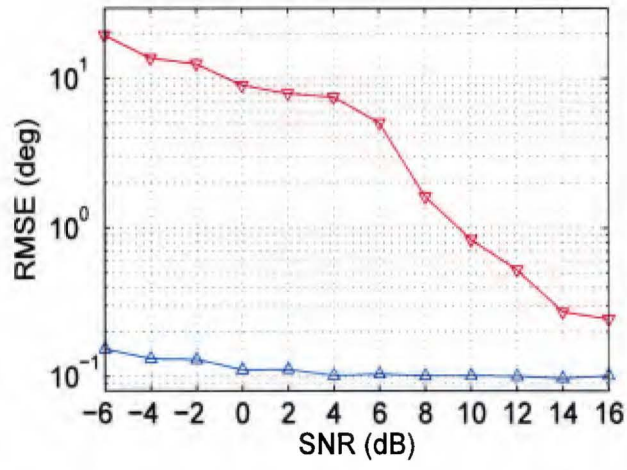


Fig. 10. RMSE versus SNR for different number of frequencies ($Q = 13$ and 2000 snapshots; ∇ : $M_1 = 5$, $M_2 = 6$ and $M_3 = 7$; \triangle : $M_1 = 5$, $M_2 = 6$, $M_3 = 7$ and $M_4 = 11$).

3.4. Frequency Diverse Coprime Arrays with Coprime Frequency Offsets for Multi-Target Localization

Abstract

Different from conventional phased-array radars, the frequency diverse array (FDA) radar offers a range-dependent beampattern capability that is attractive in various applications. The spatial and range resolutions of an FDA radar are fundamentally limited by the array geometry and the frequency offset. In this paper, we overcome this limitation by introducing a novel sparsity-based multi-target localization approach incorporating both coprime arrays and coprime frequency offsets. The covariance matrix of the received signals corresponding to all sensors and employed frequencies is formulated to generate a space-frequency virtual difference coarrays. By using $\mathcal{O}(M + N)$ antennas and $\mathcal{O}(M + N)$ frequencies, the proposed coprime arrays with coprime frequency offsets enables the localization of up to $\mathcal{O}(M^2 N^2)$ targets with a resolution of $\mathcal{O}(1/(MN))$ in angle and range domains, where M and N are coprime integers. The joint direction-of-arrival (DOA) and range estimation is cast as a two-dimensional sparse reconstruction problem and is solved within the Bayesian compressive sensing framework. We also develop a fast algorithm with a lower computational complexity based on the multitask Bayesian compressive sensing approach. Simulations results demonstrate the superiority of the proposed approach in terms of DOA-range resolution, localization accuracy, and the number of resolvable targets.

I. INTRODUCTION

Target localization finds a variety of applications in radar, sonar, communications, and navigation [2]–[5]. The phased array radars are known for their capability to electronically steer a beam for target detection and tracking in the angular domain [6]–[9]. To localize targets in both angle and range, beam-steering should be achieved across a signal bandwidth. This generally leads to a complicated waveform design and signal processing algorithms. Recently, the frequency diverse array (FDA) framework was introduced as an attractive multiple-input multiple-output (MIMO) structure that performs beam steering over a signal bandwidth and achieves joint estimation of targets direction-of-arrival (DOA) and range information [10]–[20]. As compared with conventional arrays that assume a fixed carrier frequency, FDA radars use a small frequency increment across array elements and thus achieve beam steering as a function of the angle and range in the far field. In FDA radars, the spatial and range resolutions are fundamentally limited by the array aperture and maximum frequency increment. In addition, the number of degrees-of-

freedom (DOFs) offered by the array sensors and frequency increments determines the maximum number of detectable targets.

The traditional FDA exploits a uniform linear array with a uniform frequency offset. The range and DOA estimation problem using such FDA radar has been discussed in [21]–[23]. In [21], [22], the target ranges and DOAs are jointly estimated by the minimum variance distortionless response (MVDR) and the MUSIC methods, respectively. Unlike [21], [22], an FDA utilizing coherent double pulse respectively with zero and non-zero frequency increments is considered in [23], where the ranges and DOAs are estimated in two steps. In the zero frequency increment case, the DOAs are first estimated using a non-adaptive beamformer. The estimated DOA information is then used as the prior knowledge by adaptive beamforming to obtain the range information in the other pulse. It is important to note that the above methods [21]–[23] use the traditional FDA radar and are discussed in the physical sensor framework rather than the virtual difference coarray. That is, for an array with N_t sensors, there are only $\mathcal{O}(N_t)$ DOFs with a resolution $\mathcal{O}(1/N_t)$ in both the range and angle domains. While the angular and range resolutions can be improved by exploiting a large interelement spacing and a large frequency increment, such structure generally requires a large number of array sensors, or otherwise yields undesirable aliasing problems, i.e., causes ambiguous estimations in angular and range dimensions.

Compared with uniform linear arrays (ULAs), sparse arrays use the same number of sensors to achieve a larger array aperture. A properly designed non-uniform array can achieve a desired trade-off between mainbeam width and sidelobe levels and, thereby, provide enhanced performance in terms of DOA accuracy and resolution. These attributes are achieved without changes in size, weight, power consumption, or cost. More importantly, sparse arrays offer a higher number of DOFs through the exploitation of the coarray concept [24] and, as such, significantly increases the number of detectable targets. Likewise, non-uniform frequency offsets can be used to achieve improved target identifiability and resolution in the range dimension [25]. Among different techniques that are available for sparse signal structures and array aperture synthesis, the recent proposed nested [26] and coprime configurations [27] offer systematical design capability and DOF analysis involving sensors, samples, or frequencies [28]–[41].

In [42], a nested array is employed to generate a coarray where the MUSIC algorithm together with spatial smoothing is applied. As a result, the number of the DOFs in the angular domain is increased to $\mathcal{O}(N_t^2)$. In [43], a sparsity-based method using the nested array is proposed. It achieves improved resolution and estimation accuracy when compared with the conventional covariance based methods. However, the number of the DOFs in the range domain is still $\mathcal{O}(N_t)$ since a uniform frequency offset is used. In addition, due to the large dimension of the joint range and angle dictionary, this method

results in a prohibitive computational complexity that limits its practical applicability, particularly when the number of antennas is large.

In this paper, we propose a novel configuration for the FDA radar, which incorporates both coprime array structure and coprime frequency offsets. In the proposed approach, the offsets of carrier frequencies assume a coprime relationship to further increase the number of DOFs beyond that achieved by only implementing the sparse arrays with uniform frequency increments. As a result, by using $\mathcal{O}(N_t)$ antennas and $\mathcal{O}(N_t)$ frequencies, the proposed approach achieves $\mathcal{O}(N_t^2)$ DOFs with a resolution of $\mathcal{O}(1/N_t^2)$ in both angular and range domains.

In this paper, we consider point-like targets and we exploit their sparsity in both range and angular domains. We propose both joint and sequential estimation methods based on the space-frequency coarray structure. For the joint estimation, the covariance matrix of the received signals corresponding to all sensors and employed frequencies is formulated to generate a virtual difference coarray structure in the joint space-frequency domain. Then, a joint-variable sparse reconstruction problem in the range and angular domain is presented as a single measurement vector (SMV) model. We further develop a novel sequential two-step algorithm in the context of group sparsity for reduced complexity. The cross-covariance matrices between the signals received at all sensors corresponding to different frequency pairs form space-only coarrays. Observations in these coarrays exhibit a group sparsity across all frequency pairs, since their sparse angular domain vectors share the same non-zero entry positions associated with the same target DOAs. Therefore, the DOAs can be first solved under a multiple measurement vector (MMV) model. The values of nonzero entries contain the range information, and their estimates across all frequency pairs are utilized to formulate a sparse reconstruction model with respect to the range. In so doing, the joint DOA and range estimation problem is recast as two sequential one-dimensional (1-D) estimation problems with a significantly reduced computational complexity.

The above sparse learning problems can be solved within the compressive sensing (CS) framework [44] and various CS methods can be used for this purpose. As a preferred approach, we exploit the algorithms developed in the sparse Bayesian learning context as they achieve superior performance and are insensitive to the coherence of dictionary entries [45]–[51]. In particular, the complex multitask Bayesian compressive sensing (BCS) method [45], which effectively handles complex-value observations in the underlying problem, is used in this paper.

The main contribution of this work is threefold: (a) We achieve a significantly increased number of DOFs and improve both angular and range resolutions by exploiting both coprime array and coprime frequency offsets under the coarray and frequency difference equivalence. (b) We employ a sparsity-based method to solve the joint DOA and range estimation problem which, when compared to conventional

MUSIC-based approach, enables more effective utilization of the available coarray aperture and frequency differences to resolve a higher number of targets and improve the localization accuracy. (c) We further develop a group-sparsity based algorithm which, by casting the joint DOA and range estimation as two sequential 1-D estimation problems, significantly reduces the computational complexity and processing time.

The rest of the paper is organized as follows. In Section II, the signal model of the traditional FDA radar is described. In Section III, we present a new FDA structure using coprime arrays and coprime frequency offsets. By effectively utilizing the available coarray aperture and frequency differences, two sparsity-based multi-target localization methods are proposed in Sections IV and V that resolve a higher number of targets and improve the localization accuracy. More specifically, in Section IV, the DOA and range are jointly estimated by a two-dimensional (2-D) sparse reconstruction algorithm, whereas a low-complexity algorithm through sequential 1-D sparse reconstruction is presented in Section V. Simulation results are provided in Section VI to numerically compare the localization performance of the proposed approach with other methods in terms of the number of resolvable targets, DOA-range resolution, and localization accuracy. Such results reaffirm and demonstrate the effectiveness of the proposed approach. Section VII concludes the paper.

Notations: We use lower-case (upper-case) bold characters to denote vectors (matrices). In particular, \mathbf{I}_N denotes the $N \times N$ identity matrix. $(\cdot)^*$ implies complex conjugation, whereas $(\cdot)^T$ and $(\cdot)^H$ respectively denote the transpose and conjugate transpose of a matrix or vector. $\text{vec}(\cdot)$ denotes the vectorization operator that turns a matrix into a vector by stacking all columns on top of the another, and $\text{diag}(\mathbf{x})$ denotes a diagonal matrix that uses the elements of \mathbf{x} as its diagonal elements. $\mathbb{E}(\cdot)$ is the statistical expectation operator and \otimes denotes the Kronecker product. $P_r(\cdot)$ denotes the probability density function (pdf), and $\mathcal{N}(x|a, b)$ denotes that random variable x follows a Gaussian distribution with mean a and variance b . Similarly, $\mathcal{CN}(a, b)$ denotes joint complex Gaussian distribution with mean a and variance b . $\Gamma(\cdot)$ is the Gamma function operator. $\delta_{q,p}$ is a delta function that returns the value of 1 when $p = q$ and 0 otherwise. \mathbb{N} and \mathbb{N}^+ respectively denote the set of non-negative integers and positive integers, whereas \mathbb{R}^+ denotes the set of positive real numbers. $|\cdot|$ denotes the determinant operation, whereas $\|\cdot\|_2$ and $\|\cdot\|_F$ represent the Euclidean (l_2) norm and Frobenious norm, respectively. $\text{Tr}(\mathbf{A})$ returns the trace of matrix \mathbf{A} .

II. FREQUENCY DIVERSE ARRAY RADAR

Without loss of generality, we limit our discussion to far-field targets in the 2-D space where the DOA is described by the azimuth angle only. Extension to three-dimensional (3-D) space is straightforward.

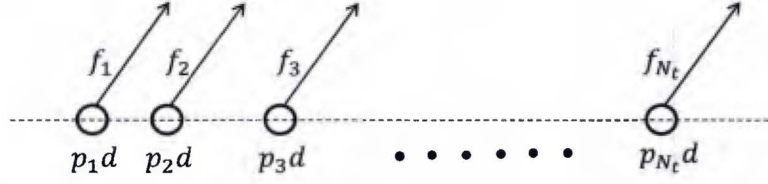


Fig. 1. The FDA configuration.

A. Signal Model

As shown in Fig. 1, an FDA radar utilizes a linear array with N_t antennas. Note that the array spacing can be either uniform or non-uniform. Denote $\mathbf{p} = [p_1 d, \dots, p_{N_t} d]^T$ as the positions of the array sensors where $p_k \in \mathbb{N}$, $k = 1, \dots, N_t$. The first sensor, located at $p_1 = 0$, is used as the reference. To avoid spatial ambiguity, d is typically taken as half wavelength, i.e., $d = \lambda_0/2 = c/(2f_0)$, where c is the velocity of electromagnetic wave propagation and f_0 is the base carrier frequency. Different from the conventional phased-array radar where all antennas transmit the same signal with carrier frequency f_0 , each FDA element radiates a signal with an incremental carrier frequency. That is, a continuous-wave (CW) signal transmitted from the k th element is expressed as

$$s_k(t) = A_k \exp(j2\pi f_k t), \quad (1)$$

where A_k is the amplitude and the radiation frequency $f_k = f_0 + \xi_k \Delta f$ is exploited with a unit frequency increment Δf , and $\xi_k \in \mathbb{N}$ is an integer coefficient of the frequency offset applied at the k th element, $k = 1, \dots, N_t$. The maximum increment is assumed to satisfy $\xi_{N_t} \Delta f \ll f_0$ so as to guarantee that the FDA radar works in a narrowband platform. Also, the frequency offsets are not necessary uniform.

An important objective of this paper is to improve the parameter identifiability using the FDA radar. Since the targets in different bins can be simple identified, we consider a scene with Q far-field targets within the same Doppler bin. Without loss of generality, the Doppler frequency is assumed to be 0. The locations of the targets are modeled as (θ_q, R_q) , $q = 1, 2, \dots, Q$. Then, the received signal at the l th sensor is modeled as

$$\begin{aligned} \tilde{x}_l(t) = & \sum_{k=1}^{N_t} \sum_{q=1}^Q \rho_q(t) \exp(j2\pi f_k t) e^{-j\frac{4\pi}{\lambda_k} R_q} e^{-j\frac{2\pi p_l d}{\lambda_k} \sin(\theta_q)} \\ & + \tilde{n}_l(t), \quad l = 1, \dots, N_t, \end{aligned} \quad (2)$$

where $\rho_q(t)$, $q = 1, \dots, Q$, are complex scattering coefficients of the targets, which are assumed to be uncorrelated zero-mean random variables with $\mathbb{E}[\rho_q^* \rho_p] = \sigma_q^2 \delta_{q,p}$, $1 \leq q, p \leq Q$, due to, e.g., the radar

cross section (RCS) fluctuations. In addition, $\lambda_k = c/f_k$ denotes the wavelength corresponding to carrier frequency f_k . Furthermore, $\tilde{n}_l(t)$ is the additive noise, which is assumed to be spatially and temporally white, and is independent of target signals.

By implementing the pass-band filtering, the received signal is converted to the signals corresponding to the respective frequencies. For a CW waveform with frequency f_k transmitted from the k th sensor, the baseband signal received at the l th sensor can be expressed as

$$\begin{aligned} x_{k,l}(t) &= \sum_{q=1}^Q \rho_q(t) e^{-j \frac{4\pi}{\lambda_k} R_q} e^{-j \frac{2\pi p_l d}{\lambda_k} \sin(\theta_q)} + n_{k,l}(t) \\ &= \sum_{q=1}^Q \rho_q(t) e^{-j \frac{4\pi f_k}{c} R_q} e^{-j \frac{\pi p_l (f_0 + \xi_k \Delta f)}{f_0} \sin(\theta_q)} + n_{k,l}(t), \end{aligned} \quad (3)$$

where $n_{k,l}(t)$ is the noise at the filter output with a variance σ_n^2 . Because $\xi_k \Delta f \ll f_0$, the above expression can be simplified as

$$x_{k,l}(t) = \sum_{q=1}^Q \rho_q(t) e^{-j \frac{4\pi f_k}{c} R_q} e^{-j \pi p_l \sin(\theta_q)} + n_{k,l}(t). \quad (4)$$

Stacking $x_{k,l}(t)$ for all $k, l = 1, \dots, N_t$ yields an $N_t^2 \times 1$ vector,

$$\begin{aligned} \mathbf{x}(t) &= \sum_{q=1}^Q \rho_q(t) \mathbf{a}_{p,f}(\theta_q, R_q) + \mathbf{n}(t) \\ &= \mathbf{A}_{p,f} \mathbf{d}(t) + \mathbf{n}(t), \end{aligned} \quad (5)$$

where $\mathbf{a}_{p,f}(\theta_q, R_q) = \mathbf{a}_p(\theta_q) \otimes \mathbf{a}_f(R_q)$ represents the steering vector associated with the angle-range pair (θ_q, R_q) . Herein, $\mathbf{a}_p(\theta_q)$ and $\mathbf{a}_f(R_q)$ are steering vectors corresponding to θ_q and R_q , respectively, expressed as

$$\mathbf{a}_p(\theta_q) = \left[1, e^{-j \pi p_2 \sin(\theta_q)}, \dots, e^{-j \pi p_{N_t} \sin(\theta_q)} \right]^T, \quad (6)$$

$$\mathbf{a}_f(R_q) = \left[e^{-j \frac{4\pi f_1}{c} R_q}, e^{-j \frac{4\pi f_2}{c} R_q}, \dots, e^{-j \frac{4\pi f_{N_t}}{c} R_q} \right]^T. \quad (7)$$

In addition, $\mathbf{A}_{p,f} = [\mathbf{a}_{p,f}(\theta_1), \dots, \mathbf{a}_{p,f}(\theta_Q)]$, $\mathbf{d}(t) = [\rho_1(t), \dots, \rho_Q(t)]^T$, and $\mathbf{n}_k(t)$ is the noise vector following the joint complex Gaussian distribution $\mathcal{CN}(0, \sigma_n^2 \mathbf{I}_{N_t^2})$.

The $N_t^2 \times N_t^2$ covariance matrix of data vector $\mathbf{x}(t)$ is obtained as

$$\begin{aligned} \mathbf{R}_x &= \mathbb{E}[\mathbf{x}(t) \mathbf{x}^H(t)] = \mathbf{A}_{p,f} \mathbf{R}_{dd} \mathbf{A}_{p,f}^H + \sigma_n^2 \mathbf{I}_{N_t^2} \\ &= \sum_{q=1}^Q \sigma_q^2 \mathbf{a}_{p,f}(\theta_q, R_q) \mathbf{a}_{p,f}^H(\theta_q, R_q) + \sigma_n^2 \mathbf{I}_{N_t^2}, \end{aligned} \quad (8)$$

where $\mathbf{R}_{dd} = \mathbb{E}[\mathbf{d}(t) \mathbf{d}^H(t)] = \text{diag}([\sigma_1^2, \dots, \sigma_Q^2])$ represents the target scattering power. Note that we assume the target scattering coefficients to be frequency-independent for the emitting signals since the

frequency offsets are relatively small. In practice, the covariance matrix is estimated using T available samples, i.e.,

$$\hat{\mathbf{R}}_{\mathbf{x}} = \frac{1}{T} \sum_{t=1}^T \mathbf{x}(t) \mathbf{x}^H(t). \quad (9)$$

Existing covariance matrix based techniques can then be applied to estimate the DOA and range of the targets, e.g., the Fourier-based power spectrum density (PSD) [52] and 2-D MUSIC [53].

B. Unambiguous Range

For each target, the DOA and range information are respectively determined by ϕ_{θ_q} and ϕ_{R_q} , which are defined as the minimum phase difference in angle and range dimensions, respectively, i.e., the phase terms of $e^{-j\pi \sin(\theta_q)}$ and $e^{-j4\pi \Delta f R_q/c}$. In reality, however, phase observations are wrapped within $[-\pi, \pi)$. Therefore, the true phase can be expressed as

$$\phi_{\theta_q}^{(\text{true})} = \phi_{\theta_q} + 2m_{\theta_q}\pi, \quad (10)$$

$$\phi_{R_q}^{(\text{true})} = \phi_{R_q} + 2m_{R_q}\pi, \quad (11)$$

where m_{θ_q} and m_{R_q} are unknown integers. As a result, the range estimate is subject to range ambiguity [54], i.e.,

$$R_q = \frac{c\phi_{R_q}}{4\pi\Delta f} + \frac{cm_{R_q}}{2\Delta f}. \quad (12)$$

The latter term in (12) implies ambiguity in range due to phase wrapping. Thus, the range can be assumed as infinite values separated by $R_{\max} = c/(2\Delta f)$, which is referred to as the maximum unambiguous range. Therefore, the use of a large value of Δf will reduce the maximum unambiguous range. As a large frequency bandwidth is required to achieve proper range resolution, uniform frequency offsets must trade off between the range resolution and unambiguous range estimation. On other other hand, coprime frequency offsets allows the use of small Δf while collectively spanning a large signal bandwidth.

III. FREQUENCY DIVERSE COPRIME ARRAYS WITH COPRIME FREQUENCY OFFSETS

For the traditional FDA radar with N_t -element ULA and uniform frequency increment, it can localize up to $N_t^2 - 1$ targets, with a resolution $\mathcal{O}(1/N_t)$ in the angle and range domains, respectively. Compared with the uniform case, sparse arrays and sparse frequency offsets use the same number of sensors and frequencies to achieve a larger array aperture and frequency bandwidth. As a result, they improve the resolution and estimation accuracy. However, the number of resolvable targets using sparse arrays and sparse frequency offsets is still upper bounded by $N_t^2 - 1$, if those covariance matrix based approaches are used directly. Such the limitation can be overcome by the improvement of DOFs under the coarray equivalence.

A. Coarray Equivalence

By vectorizing the matrix \mathbf{R}_x , we obtain the following $N_t^4 \times 1$ virtual measurement vector:

$$\mathbf{z} = \text{vec}(\mathbf{R}_x) = \tilde{\mathbf{A}}_{p,f} \mathbf{b}_{p,f} + \sigma_n^2 \tilde{\mathbf{i}}, \quad (13)$$

with

$$\tilde{\mathbf{A}}_{p,f} = [\tilde{\mathbf{a}}_{p,f}(\theta_1, R_1), \dots, \tilde{\mathbf{a}}_{p,f}(\theta_Q, R_Q)], \quad (14)$$

$$\mathbf{b}_{p,f} = [\sigma_1^2, \dots, \sigma_Q^2]^T, \quad (15)$$

$$\tilde{\mathbf{i}} = \text{vec}(\mathbf{I}_{N_t^2}), \quad (16)$$

where

$$\begin{aligned} \tilde{\mathbf{a}}_{p,f}(\theta_q, R_q) &= \mathbf{a}_{p,f}^*(\theta_q, R_q) \otimes \mathbf{a}_{p,f}(\theta_q, R_q) \\ &= \mathbf{a}_p^*(\theta_q) \otimes \mathbf{a}_f^*(R_q) \otimes \mathbf{a}_p(\theta_q) \otimes \mathbf{a}_f(R_q) \\ &= (\mathbf{a}_p^*(\theta_q) \otimes \mathbf{a}_p(\theta_q)) \otimes (\mathbf{a}_f^*(R_q) \otimes \mathbf{a}_f(R_q)) \\ &= \tilde{\mathbf{a}}_p(\theta_q) \otimes \tilde{\mathbf{a}}_f(R_q) \end{aligned} \quad (17)$$

for $1 \leq q \leq Q$. Benefiting from the Vandermonde structure of $\mathbf{a}_p(\theta_q)$ and $\mathbf{a}_f(R_q)$, the entries in $\tilde{\mathbf{a}}_p(\theta_q)$ and $\tilde{\mathbf{a}}_f(R_q)$ are still in the forms of $e^{-j\pi(p_i - p_j)\sin(\theta_q)}$ and $e^{-j4\pi(\xi_i - \xi_j)\Delta f R_q/c}$, for $i, j = 1, \dots, N_t$. As such, we can regard \mathbf{z} as a received signal vector from a single-snapshot signal vector $\mathbf{b}_{p,f}$, and the matrix $\tilde{\mathbf{A}}_{p,f}$ corresponds to the virtual array sensors and virtual frequency offsets which are respectively located at the sensor-lags between all sensor pairs and frequency-offsets between all frequency pairs. The targets can thus be localized by using the space-frequency coarray, in lieu of the original antennas and frequencies. Note that the number of elements in the space-frequency coarray structure are directly determined by the distinct values of $(p_i - p_j)$ and $(\xi_i - \xi_j)$ for $i, j = 1, \dots, N_t$. Non-uniform arrays can substantially increase the number of DOFs by reducing the number of redundant elements in the coarray. In other words, the number of DOFs would be reduced if different pairs of sensors or frequency offsets yield same lags when the uniform arrays are exploited.

B. Coprime Arrays with Coprime Frequency Offsets

Among the different choices that are available for sparse array and frequency offset designs, the recently proposed coprime configurations [27] offer a systematical design capability and DOF analysis involving sensors, samples, or frequencies. In this paper, we use the extended coprime structure which is proposed

in [55] as an example. Extensions to other generalized coprime structures that achieve higher DOFs are straightforward [34].

As shown in Fig. 2, the extended coprime array structure utilizes a coprime pair of uniform integers. The coprime array consists of a $2M$ -sensor uniform linear subarray with an interelement spacing of N , and an N -sensor uniform linear subarray with an interelement spacing of M . The two integers M and N are chosen to be coprime, i.e., their greatest common divisor is one. In addition, $M < N$ is assumed. Define

$$\mathbb{P}_{(M,N)} = \{Mn | 0 \leq n \leq N-1\} \cup \{Nm | 0 \leq m \leq 2M-1\} \quad (18)$$

as the union of two sparsely sampled integer subsets with respect to the pair of coprime integers (M, N) . As such, the yielding correlation terms have the positions

$$\mathbb{L}_{(M,N)} = \{\pm(Mn - Nm) | 0 \leq m \leq 2M-1, 0 \leq n \leq N-1\}. \quad (19)$$

An example is illustrated in Fig. 3, where $M = 2$ and $N = 3$. Fig. 3(a) shows the physical elements of extended coprime structure, and the positions of the corresponding correlation terms are depicted in Fig. 3(b). Notice that “holes”, e.g., ± 8 in this case, still exist in the virtual domain and are indicated by \times in the figure. It is proved in [56] that $\mathbb{L}_{(M,N)}$ can achieve at least MN (up to $(3MN + M - N + 1)/2$) DOFs with only $2M + N - 1$ (two subsets share the first element) entries in $\mathbb{P}_{(M,N)}$.

When coprime arrays and coprime frequency offsets with pairs of coprime integers (M, N) is exploited, there are at least MN available DOFs in each $\mathbf{a}_p(\theta_q)$ and $\mathbf{a}_f(R_q)$. That is, the resulting virtual array elements and virtual frequency offsets enable estimation of at least MN distinct DOAs and MN distinct ranges of targets. Benefitting from the sparse structure, the proposed coprime array with coprime frequency offsets offers a larger aperture and frequency span, thus resulting in an improved resolution in both angular and range domains. Further, it has less redundant entries in the covariance matrix \mathbf{R}_x , implying that the

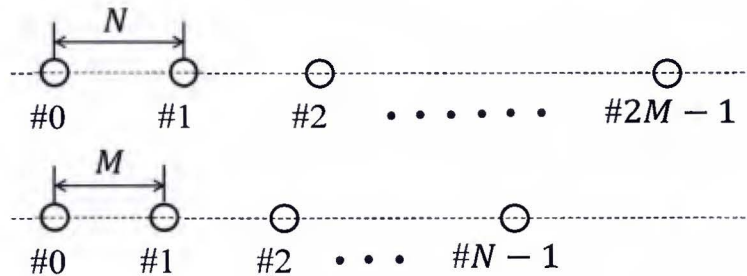


Fig. 2. The extended coprime structure.

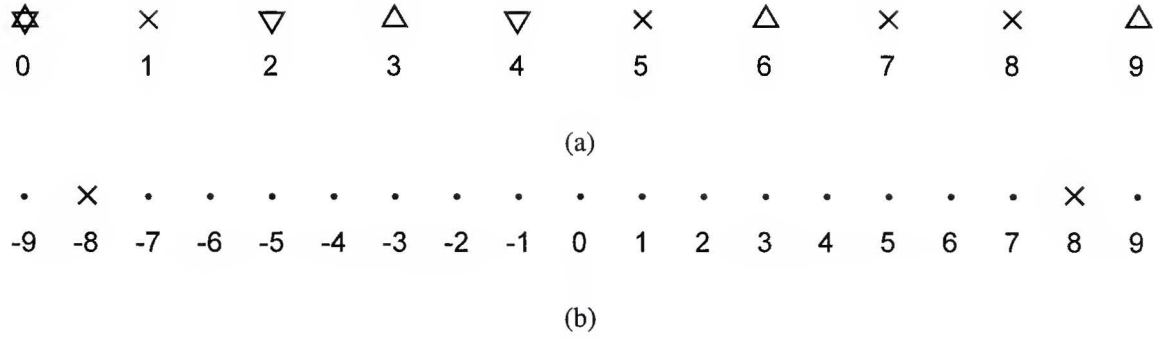


Fig. 3. An example for the extended coprime structure. (a) The physical elements in $\mathbb{P}_{(M,N)}$ (\triangle : Subset 1; ∇ : Subset 2); (b) The corresponding correlation term positions in $\mathbb{L}_{(M,N)}$.

resulting coarray structure and frequency lag sets provide a higher number of DOFs that can be used to identify more targets using the CS based methods.

The localization problem in (13) is similar to handling multiple targets that are fully coherent. In this case, the covariance matrix constructed from the virtual signal vector is rank-1 and, as a result, subspace-based localization approaches fail to function. A well-known approach that restores the rank of the covariance matrix is spatial smoothing [57], [58]. A major disadvantage of such approach is that only consecutive lags in the virtual observations can be used so that every subarray has a similar manifold (e.g., $[-7, 7]$ in Fig. 3(b)), whereas the virtual sensors that are separated by any holes have to be discarded. Alternatively, this problem can be solved by using sparse reconstruction methods (e.g., [34], [59]) which, by taking advantages of the fact that the targets are sparse in the angle-range domain, utilize all consecutive and non-consecutive lags (e.g., ± 9 and $[-7, 7]$ in Fig. 3(b)) in the coarray so as to fully utilize the available DOFs offered by the coarray configurations.

Provided that sufficient snapshots are available for reliable covariance matrix estimation, at least $\mathcal{O}(MN)$ targets (no same DOA and no same range), up to $\mathcal{O}(M^2N^2)$ targets (each of MN DOAs has MN distinct ranges), can thus be localized by using $N_t = 2M + N - 1$ antennas and $N_t = 2M + N - 1$ frequencies. For a given number of N_t , the maximum number of DOFs can be further optimized by

$$\begin{aligned}
 & \text{Maximize} \quad M^2N^2 \\
 & \text{subject to} \quad 2M + N - 1 = N_t, \\
 & \quad \quad \quad M < N, \quad M, N \in \mathbb{N}^+.
 \end{aligned} \tag{20}$$

It is demonstrated in [31] that the valid optimal coprime pair to maximize MN is the one that has $2M$ and N as close as possible. This is satisfied by choosing $N = 2M - 1$. In this case, more than

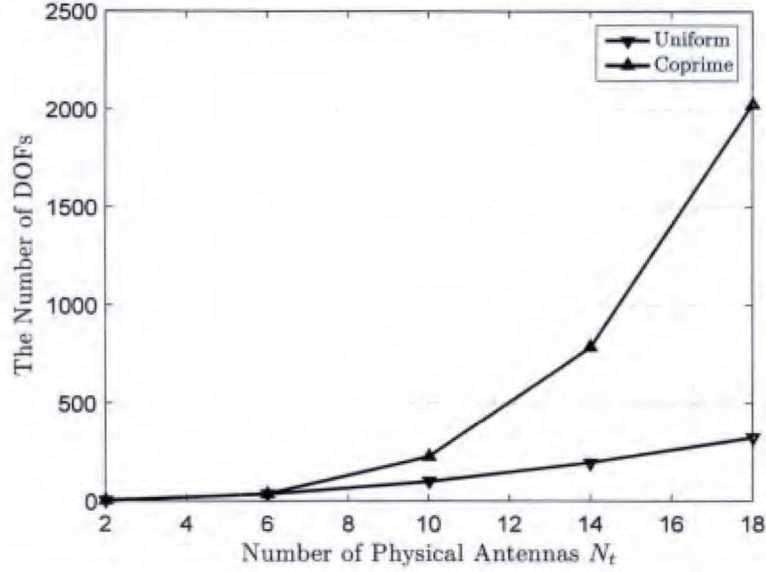


Fig. 4. The number of DOFs versus N_t .

$[N_t^2(N_t + 2)^2] / 64$ DOFs can be obtained. Therefore, the frequency diverse coprime arrays with coprime frequencies can resolve more targets than that of conventional FDA with ULA and uniform frequency increment (i.e., $N_t^2 - 1$) when $N_t \geq 6$, as shown in Fig. 4.

IV. TARGET LOCALIZATION USING MULTITASK BCS

In the following, we perform multi-target localization in the sparse reconstruction framework. The general focus of proposed methods is to resolve a higher number of targets and improve the localization accuracy by fully utilizing all the virtual observations achieved from lags in both sensor positions and frequencies. For the simplicity and clarity of the presentation, we assume the targets to be placed on a pre-defined grid. Direct application of the proposed method in the presence of dictionary mismatch would yield performance degradation. However, various techniques, such as those cited in [32], [33], [60], [61], can be used to overcome this problem by exploring the joint sparsity between signals and the grid mismatch variables.

The virtual signal vector \mathbf{z} in (13) can be sparsely represented over the entire discretized angular grids as

$$\mathbf{z} = \Phi \mathbf{b} + \epsilon, \quad (21)$$

where $\Phi = [\Phi_s, \tilde{\mathbf{I}}]$. Herein, Φ_s is defined as the collection of steering vectors $\tilde{\mathbf{a}}_{p,f}(\theta_{g_1}, R_{g_2})$ over all possible grids θ_{g_1} and R_{g_2} , $g_1 = 1, \dots, G_1, g_2 = 1, \dots, G_2$, with $G = G_1 G_2 \gg N_t^4 > Q$, and \mathbf{b}_s is

the sparse vector whose non-zero entry positions correspond to the DOAs and ranges of the targets, i.e., $(\theta_q, R_q), q = 1, \dots, Q$. The term $\tilde{\mathbf{I}}$ in the dictionary accounts for noise variance terms that have unequal values in the vectorized entries. In addition, an error vector ϵ is included to represent the discrepancies between the statistical expectation and the sample average in computing the covariance matrix \mathbf{R} . The discrepancies are modelled as i.i.d. complex Gaussian as a result of a sufficiently large number of samples employed in the averaging.

In this paper, we elect to perform the sparse signal reconstruction within the BCS framework [45]–[51] stemming from their superior performance and robustness to dictionary coherence. In particular, the complex multitask BCS approach developed in [45] is used to deal with all the sparse reconstruction problems. Thus, the following sparse Bayesian model is presented as an MMV model with P tasks (measurements), whereas the SMV problem in (21) can be considered as a special case with a single task, i.e., $P = 1$.

A. Sparse Bayesian Formulation

The MMV model is expressed as

$$\mathbf{Z} = \Phi \mathbf{B}, \quad (22)$$

where $\mathbf{Z} = [\mathbf{z}_1, \dots, \mathbf{z}_P]$ and $\mathbf{B} = [\mathbf{b}_1, \dots, \mathbf{b}_P]$. The matrix \mathbf{B} is jointly sparse (or row sparse), i.e., all columns of \mathbf{B} are sparses and share the same support.

Assume that the entries in jointly sparse matrix \mathbf{B} are drawn from the product of the following zero-mean complex Gaussian distributions:

$$\Pr(\mathbf{B}|\alpha) = \prod_{p=1}^P \mathcal{CN}(\mathbf{b}_p|\mathbf{0}, \mathbf{\Lambda}), \quad (23)$$

where $\alpha = [\alpha_1, \dots, \alpha_G]^T$ and $\mathbf{\Lambda} = \text{diag}(\alpha)$. It is noted that the g th row of \mathbf{B} tends to be zero when $\alpha_g, g = 1, \dots, G$ is set to zero [46]. In addition, α is placed on a complex variable directly. As such, it achieves improved sparse signal reconstruction because by utilizing the group sparsity of the real and imaginary components than the methods that simply decomposing them into independent real and imaginary components.

To encourage the sparsity, a Gamma prior is placed on α_g , which is conjugate to the Gaussian distribution,

$$\alpha_g \sim \Gamma(\alpha_g|1, \rho), g \in [1, \dots, G], \quad (24)$$

where $\rho \in \mathbb{R}^+$ is a fixed priori. It has been demonstrated in [62] that a proper choice of ρ encourages a sparse representation for the coefficients. Then, we have

$$\Pr(\boldsymbol{\alpha}|a, b) = \prod_{g=1}^G \Gamma(\alpha_g|1, \rho). \quad (25)$$

All columns of \mathbf{B} share the same prior due to the group sparse property. Base on [63], both of the real and image parts of \mathbf{b}_p , $p = 1, \dots, P$, are Laplace distributed and share the same pdf that is strongly peaked at the origin. As such, this two-stage hierarchical prior is a sparse prior that favors most rows of \mathbf{B} being zeros.

A Gaussian prior $\mathcal{CN}(\mathbf{0}, \beta_0^{-1}\mathbf{I}_2)$ is also placed on the error vector ϵ . Then, we have,

$$\Pr(\mathbf{Z}|\mathbf{B}, \beta_0) = \prod_{p=1}^P \mathcal{CN}(\mathbf{z}_p|\Phi\mathbf{b}_p, \beta_0^{-1}\mathbf{I}), \quad (26)$$

Likewise, the Gamma prior is placed on β_0 with hyper-parameters c and d , expressed as

$$\Pr(\beta_0|c, d) = \Gamma(\beta_0^{-1}|c, d), \quad (27)$$

where $\Gamma(\beta_0^{-1}|a, b) = \Gamma(a)^{-1}b^a\beta_0^{-(a+1)}e^{-\frac{b}{\beta_0}}$.

By combining the stages of the hierarchical Bayesian model, the joint pdf becomes

$$\Pr(\mathbf{Z}, \mathbf{B}, \boldsymbol{\alpha}, \beta_0) = \Pr(\mathbf{Z}|\mathbf{B}, \beta_0)\Pr(\mathbf{B}|\boldsymbol{\alpha})\Pr(\boldsymbol{\alpha}|1, \rho)\Pr(\beta_0|c, d). \quad (28)$$

To make this Gamma prior non-information, we set $c = d = 0$ in this paper as in [46]–[51].

B. Bayesian Inference

Assuming $\boldsymbol{\alpha}$ and β_0 are known, given the measurement \mathbf{Z} and the corresponding dictionary Φ , the posterior for \mathbf{B} can be obtained analytically using Bayes's rule, expressed as a Gaussian distribution with mean $\boldsymbol{\mu}$ and variance $\boldsymbol{\Sigma}$

$$\Pr(\mathbf{B}|\mathbf{Z}, \boldsymbol{\alpha}, \beta_0) = \prod_{p=1}^P \mathcal{CN}(\mathbf{b}_p|\boldsymbol{\mu}_p, \boldsymbol{\Sigma}), \quad (29)$$

where

$$\boldsymbol{\mu}_p = \beta_0^{-1}\boldsymbol{\Sigma}\Phi^H\mathbf{z}_p, \quad (30)$$

$$\boldsymbol{\Sigma} = [\beta_0^{-1}\Phi^H\Phi + \mathbf{F}^{-1}]^{-1}. \quad (31)$$

The associated learning problem, in the context of relevance vector machine (RVM), thus becomes the search for the $\boldsymbol{\alpha}$ and β_0 . In RVM, the values of $\boldsymbol{\alpha}$ and β_0 are estimated from the data by performing a

type-II maximum likelihood (ML) procedure [62]. Specially, by marginalizing over the \mathbf{B} , the marginal likelihood for α and β_0 , or equivalently, its logarithm $\mathcal{L}(\alpha, \beta_0)$ can be expressed analytically as

$$\begin{aligned}\mathcal{L}(\alpha, \beta_0) &= \sum_{p=1}^P \log \Pr(\mathbf{b}_p | \alpha, \beta_0) \\ &= \sum_{p=1}^P \log \int \Pr(\mathbf{z}_p | \mathbf{b}_p, \beta_0) \Pr(\mathbf{b}_p | \alpha) d\mathbf{b}_p \\ &= \text{const} - \frac{1}{2} \sum_{p=1}^P \log |\mathbf{C}| + (\mathbf{z}_p)^H \mathbf{C}^{-1} \mathbf{z}_p\end{aligned}\quad (32)$$

with

$$\mathbf{C} = \beta_0 \mathbf{I} + \Phi \mathbf{F} \Phi^H. \quad (33)$$

Denote $\mathbf{U} = [\mu_1, \dots, \mu_P] = \beta_0^{-1} \Sigma \Phi^H \mathbf{Z}$, $\underline{\mathbf{B}} = \mathbf{B} / \sqrt{P}$, $\underline{\mathbf{Z}} = \mathbf{Z} / \sqrt{P}$, $\underline{\mathbf{U}} = \mathbf{U} / \sqrt{P}$, and $\underline{\rho} = \rho / P$. An ML approximation employs the point estimates for α and β_0 to maximize (32), which can be implemented via the expectation maximization (EM) algorithm to yield

$$\alpha_g^{(\text{new})} = \frac{\sqrt{1 + 4\underline{\rho}(\|\underline{\mu}^g\|_2^2 + \Sigma_{g,g})} - 1}{2\underline{\rho}}, \quad g \in [1, \dots, G], \quad (34)$$

$$\beta_0^{(\text{new})} = \frac{\mathbb{E}\{\|\underline{\mathbf{Z}} - \Phi \underline{\mathbf{B}}\|_F^2\}}{N_\Phi}, \quad (35)$$

where $\underline{\mu}^g$ is the g th row of matrix $\underline{\mathbf{U}}$ and $\Sigma_{g,g}$ is the (g, g) th entry of matrix Σ . In addition, N_Φ is the number of rows of Φ .

It is noted that, because $\alpha^{(\text{new})}$ and $\beta_0^{(\text{new})}$ are a function of μ_p and Σ , while μ_p and Σ are a function of α and β_0 , this suggests an iterative algorithm that iterates between (30)–(31) and (34)–(35), until a convergence criterion is satisfied or the maximum number of iterations is reached. In each iteration, the computational complexity is $\mathcal{O}(\max(N_\Phi G^2, N_\Phi GP))$ with an $N_\Phi \times G$ dictionary Φ [48].

C. Complexity Analysis

For the case of 2-D BCS, the corresponding joint angle-range of targets, $(\hat{\theta}_q, \hat{R}_q)$, $q = 1, \dots, Q$, can be estimated by positions of the nonzero entries in \mathbf{b} in (21). In the sequel, we analyze its computational complexity, which can be divided into the following three stages:

- S1: Compute the $N_t^2 \times N_t^2$ covariance matrix $\hat{\mathbf{R}}_x$ with (9).
- S2: Generate the $N_t^4 \times 1$ virtual array data \mathbf{z} with (13) by vectorizing the covariance matrix.
- S3: Perform target localization to obtain $(\hat{\theta}_q, \hat{R}_q)$, $q = 1, \dots, Q$ using (30)–(31) and (34)–(35), based on the BCS ($P = 1$) with an $N_t^4 \times G_1 G_2$ dictionary.

In $S1$, there are $\mathcal{O}(N_t^4 T)$ complex multiplications, whereas no multiplication operation is needed for vectorization in $S2$. For the BCS, we might need $\mathcal{O}(\kappa N_t^4 G_1^2 G_2^2)$ complex multiplication operations, where κ is the number of iterations. Therefore, the total computational load, i.e., $\mathcal{O}(N_t^4 T + \kappa N_t^4 G_1^2 G_2^2)$, is very huge because the exhaustive 2-D searching process, which motivates the development of fast algorithms.

V. A FAST ALGORITHM FOR TARGET LOCALIZATION

In this section, we develop an algorithm based on the multitask BCS, wherein the 2-D sparse reconstruction problem is cast as separate 1-D sparse reconstruction problems. Therefore, the computational complexity can be reduced.

Stacking $x_{k,l}(t)$ for all $l = 1, \dots, N_t$ yields the following $N_t \times 1$ vector,

$$\mathbf{x}_k(t) = \sum_{q=1}^Q \rho_q(t) e^{-j \frac{4\pi f_k}{c} R_q} \mathbf{a}_p(\theta_q) + \mathbf{n}_k(t). \quad (36)$$

As such, the vector $\mathbf{x}_k(t)$ behaves as the received signal of the array, corresponding to the frequency f_k , $k = 1, \dots, N_t$.

The cross-covariance matrix between data vectors $\mathbf{x}_k(t)$ and $\mathbf{x}_{k'}(t)$, respectively corresponding to frequencies f_k and $f_{k'}$, $1 \leq k, k' \leq N_t$, is obtained as

$$\mathbf{R}_{\mathbf{x}_{kk'}} = \mathbb{E}[\mathbf{x}_k(t) \mathbf{x}_{k'}^H(t)] = \sum_{q=1}^Q \sigma_q^2 e^{-j \frac{4\pi \Delta f_{kk'}}{c} R_q} \mathbf{a}_p(\theta_q) \mathbf{a}_p^H(\theta_q), \quad (37)$$

where $\Delta f_{kk'} = f_k - f_{k'} = (\xi_k - \xi_{k'}) \Delta f$. Note that the dimension of $\mathbf{R}_{\mathbf{x}_{kk'}}$ is reduced to $N_t \times N_t$, compared to the $N_t^2 \times N_t^2$ matrix \mathbf{R}_x in (8). In practice, the cross-covariance matrix is estimated by using T available samples, i.e.,

$$\hat{\mathbf{R}}_{\mathbf{x}_{kk'}} = \frac{1}{T} \sum_{t=1}^T \mathbf{x}_k(t) \mathbf{x}_{k'}^H(t), 1 \leq k, k' \leq N_t. \quad (38)$$

Vectorizing this matrix yields the following $N_t^2 \times 1$ vector

$$\mathbf{z}_{kk'} = \text{vec}(\mathbf{R}_{\mathbf{x}_{kk'}}) = \bar{\mathbf{A}} \mathbf{b}_{f_{kk'}}, \quad (39)$$

where

$$\bar{\mathbf{A}} = [\bar{\mathbf{a}}_p(\theta_1), \dots, \bar{\mathbf{a}}_p(\theta_Q)], \quad (40)$$

$$\mathbf{b}_{f_{kk'}} = [\sigma_1^2 e^{-j \frac{4\pi \Delta f_{kk'}}{c} R_1}, \dots, \sigma_Q^2 e^{-j \frac{4\pi \Delta f_{kk'}}{c} R_Q}]^T. \quad (41)$$

Similarly, (39) can be sparsely represented over the entire angular grids as

$$\mathbf{z}_{kk'} = \bar{\Phi} \bar{\mathbf{b}}_{kk'}, \quad (42)$$

where the $N_t^2 \times G_1$ dictionary $\bar{\Phi}$ is defined as the collection of steering vectors $\tilde{\mathbf{a}}_p(\theta_g)$ over all possible grids θ_{g_1} , $g_1 = 1, \dots, G_1$, with $G_1 \gg Q$. As such, the DOAs θ_q , $q = 1, \dots, Q$, are indicated by the nonzero entries in the sparse vector $\bar{\mathbf{b}}_{kk'}$, whose values describe the corresponding coefficients $\sigma_q^2 e^{-j \frac{4\pi(\xi_k - \xi_{k'})\Delta f}{c} R_q}$. Note that the nonzero entries corresponding to different frequency pairs share the same positions as they are associated with the same DOAs of the Q targets. However, their values differ for each frequency pair. Therefore, $\mathbf{z}_{kk'}$ exhibits a group sparsity across all frequency pairs and the problem described in (42) can be solved in the MMV sparse reconstruction context.

Denote $\mathbf{Z} = [\mathbf{z}_1, \dots, \mathbf{z}_P]$ as the collection of vectors $\mathbf{z}_{kk'}$, corresponding to all $P = N_t^2$ frequency pairs. Then, the MMV sparse reconstruction problem is expressed as

$$\mathbf{Z} = \bar{\Phi} \bar{\mathbf{B}}, \quad (43)$$

where $\mathbf{B} = [\bar{\mathbf{b}}_1, \dots, \bar{\mathbf{b}}_P]$ is the sparse matrix that can be reconstructed by the multitask BCS.

Denote \bar{Q} as the number of distinct DOAs of Q targets, the $n_{\bar{q}}$, as the index of those nonzero positions in $\bar{\mathbf{B}}$ corresponding to $\theta_{\bar{q}}$, $\bar{q} = 1, \dots, \bar{Q}$. In addition, the $P \times 1$ vector $\mathbf{b}_{n_{\bar{q}}}$ is denoted as the $n_{\bar{q}}$ th column of $\bar{\mathbf{B}}^T$. Then, the range can be estimated by solving the following sparse reconstruction problem:

$$\mathbf{b}_{n_{\bar{q}}} = \Psi \mathbf{R}_{n_{\bar{q}}}, \quad \bar{q} = 1, \dots, \bar{Q}, \quad (44)$$

where Ψ is the $N_t^2 \times G_2$ dictionary, whose g_2 th column, $g_2 = 1, \dots, G_2$, is

$$\Psi_{g_2} = \left[1, \dots, e^{-j \frac{4\pi(\xi_k - \xi_{k'})}{c} R_{g_2}}, \dots, 1 \right]^T, \quad (45)$$

with $1 \leq k, k' \leq N_t$. Then, the range on $\theta_{\bar{q}}$, $\bar{q} = 1, \dots, \bar{Q}$ can be indicated by positions of nonzero entries in sparse vector $\mathbf{R}_{n_{\bar{q}}}$.

As a summary, the proposed approach can be divided into the following four stages:

- S1: Compute all $N_t \times N_t$ covariance matrix $\hat{\mathbf{R}}_{\mathbf{x}_{kk'}}$ using (38), $1 \leq k, k' \leq N_t$.
- S2: Generate all the $N_t^2 \times 1$ virtual array data $\mathbf{z}_{kk'}$ with (39) by vectorizing the covariance matrix, $1 \leq k, k' \leq N_t$.
- S3: Perform DOA estimation of the targets, based on the multitask sparse reconstruction ($P = N_t^2$) model in (43) with an $N_t^2 \times G_1$ dictionary.
- S4: Perform range estimation of the targets, based on the sparse reconstruction model in (44) with an $N_t^2 \times G_2$ dictionary.

In S1, there are $\mathcal{O}(N_t^4 T)$ multiplication operations. The complexity in S3 and S4 is $\mathcal{O}(\kappa_1 N_t^2 G_1^2)$ and $\mathcal{O}(\kappa_2 N_t^2 G_2^2)$, respectively, where κ_1 and κ_2 are the corresponding number of iterations. Thus, the total computation load is $\mathcal{O}(N_t^4 T + \kappa_1 N_t^2 G_1^2 + \kappa_2 \bar{Q} N_t^2 G_2^2)$, which is much lower than $\mathcal{O}(N_t^4 T + \kappa N_t^4 G_1^2 G_2^2)$ in Section IV.

Remarks: The following observations can be made regarding the relationship between the joint and the two-step estimation methods:

- (1) Both estimation methods achieve the same number of DOFs from the coarray;
- (2) The two-step estimation method requires a significantly reduced complexity. However, the corresponding performance becomes sub-optimal due to error propagation. i.e., errors in the DOA estimation stage may yield additional perturbations in the range estimation.

VI. SIMULATION RESULTS

For illustrative purposes, we consider an FDA radar exploiting coprime array and coprime frequency offset, where $M = 2$ and $N = 3$ are assumed. The extended coprime structure consist of $N_t = (2M + N - 1) = 6$ physical elements, and has $(3MN + M - N + 1)/2 = 9$ DOFs in the virtual domain. As such, the increased number of DOFs enables to localize more than $M^2N^2 = 36$ targets with only 6 antennas exploiting 6 frequencies.

The unit interelement spacing is $d = \lambda_0/2$, where λ_0 is the wavelength with respect to the carrier frequency $f_0 = 1$ GHz. We choose the unit frequency increment to be $\Delta f = 30$ KHz, resulting maximum unambiguous range $R_{\max} = c/(2\Delta f) = 5000$ m. In all simulations, Q far-field targets with identical target scattering powers are considered. The q th target is assumed to be on angle-range plane (θ_q, R_q) , where $\theta_q \in [-60^\circ, 60^\circ]$ and $R_q \in [1000, 5000]$ m, for $q = 1, \dots, Q$. The localization performance for the coprime array and coprime frequency offset (CA-CFO) is examined in terms of the resolution, accuracy, and the maximum number of resolvable targets. The average root mean square error (RMSE) of the estimated DOAs and ranges, expressed as

$$\begin{aligned} \text{RMSE}_\theta &= \sqrt{\frac{1}{IQ} \sum_{i=1}^I \sum_{q=1}^Q (\hat{\theta}_q(i) - \theta_q)^2}, \\ \text{RMSE}_R &= \sqrt{\frac{1}{IQ} \sum_{i=1}^I \sum_{q=1}^Q (\hat{R}_q(i) - R_q)^2}, \end{aligned} \quad (46)$$

are used as the metric for estimation accuracy, where $\hat{\theta}_q(i)$ and $\hat{R}_q(i)$ are the estimates of θ_q and R_q for the i th Monte Carlo trial, $i = 1, \dots, I$. We use $I = 500$ independent trials in simulations.

A. Joint Estimation Method versus Two-step Estimation Method

We first compare the performance of the joint estimation method and two-step estimation method. $Q = 1$ target with $(10^\circ, 1000\text{m})$ is considered. The dictionary matrices $\bar{\Phi}$ and Ψ are assumed to contain all possible grid entries within $(5^\circ, 15^\circ)$ and $(1250 \text{ m}, 1350 \text{ m})$ with uniform intervals $\theta_{g_1} = 0.2^\circ$ and

$R_{g_2} = 1$ m, respectively. Fig. 5 compares the RMSE performance of DOA and range estimations with respect to the input signal-to-noise ratio (SNR), where 500 snapshots are used. In Fig. 6, we compare the RMSE performance with respect to the number of snapshots, where the input SNR is set to -5 dB. It is clear that the joint estimation method achieves slightly better estimation accuracy at the cost of much higher computation complexity.

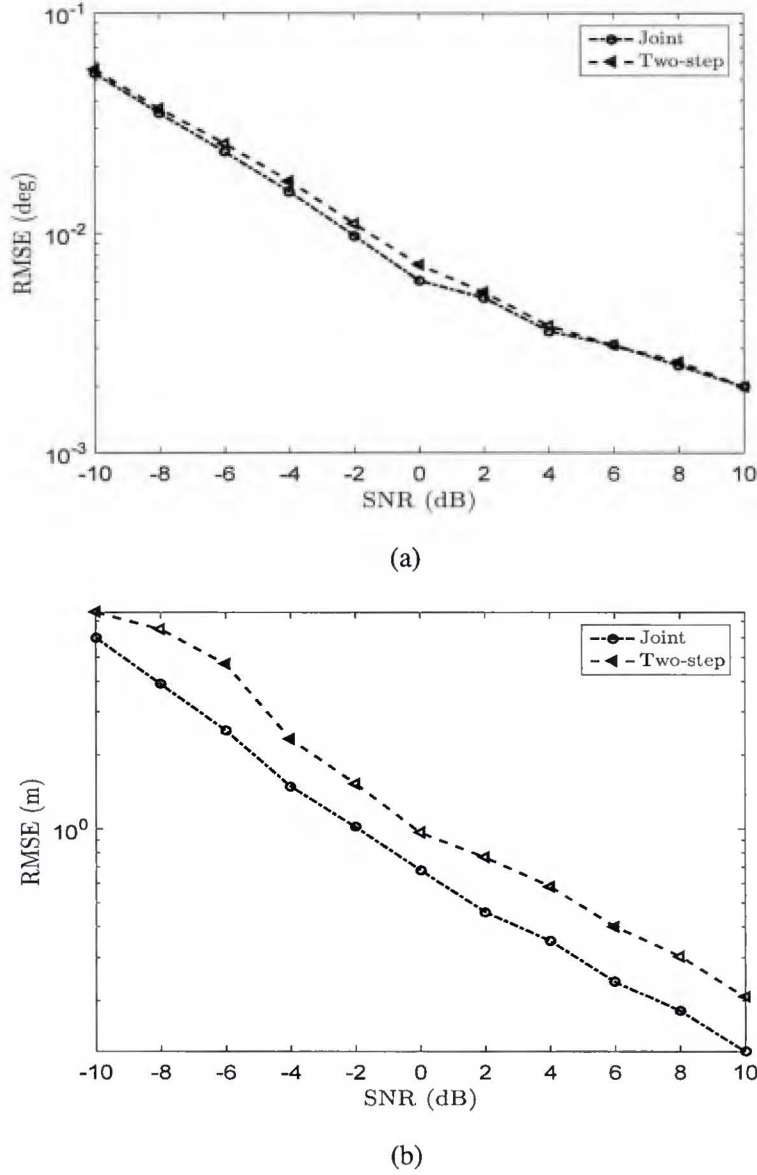


Fig. 5. RMSE versus SNR using the joint and two-step estimation methods ($Q = 1$ and $T = 500$). (a) $RMSE_{\theta}$; (b) $RMSE_R$

B. CA-CFO versus Other Array Configuration and Frequency Offset Designs

Next, we examine the localization performance for different array configuration and frequency offset designs. Particularly, the proposed CA-CFO is compared with uniform linear array and uniform frequency offset (ULA-UFO). Uniform linear array with coprime frequency offset (ULA-CFO), and coprime array and uniform frequency offset (CA-UFO) are also considered. In order to reduce the computational load, we use the fast algorithm in section V for target localization in simulations.

In Fig. 7, we compare the resolution performance of different schemes. $Q = 8$ targets whose true positions are shown in Fig. 7(a) are considered. The dictionary matrices $\bar{\Phi}$ and Ψ contain steering vectors over all possible grids in $(-60^\circ, 60^\circ)$ and $(1000 \text{ m}, 5000 \text{ m})$ with uniform intervals $\theta_{g_1} = 1^\circ$ and $R_{g_2} = 100 \text{ m}$, respectively. Note that the number of targets is larger than the number of antennas, and the traditional phased array radar does not have sufficient DOFs to resolve all targets. The covariance matrix are obtained by using 500 snapshots in the presence of noise with a 0 dB SNR, and the corresponding localization performance are illustrated in Figs. 7(b)–(e). It is evident that only the case of CA-CFO can identify targets correctly because the increased DOFs in both virtual array and frequency can estimate more DOAs than the number of antennas, and more ranges than the number of frequencies. In addition, the corresponding larger apertures in both angle and range domains enable the CA-CFO case to resolve the closely spaced targets. The conventional FDA with ULA-UFO fails to separate both pairs of the targets with closely spaced angle and closely spaced range. However, the scenario of CA-UFO can resolve the pair of targets with closely spaced angle and the ULA-CFO case can identify targets with closely spaced range, benefitting from the increased DOFs in the angle and range domains, respectively.

We further compare the estimation accuracy through Monte Carlo simulations. To proceed with the comparison, we consider $Q = 2$ targets with $(10^\circ, 1300 \text{ m})$ and $(25^\circ, 1700 \text{ m})$, which can be separated for all cases. The dictionary matrices $\bar{\Phi}$ and Ψ are assumed to contain entries corresponding to all possible grids in $(10^\circ, 30^\circ)$ and $(1000 \text{ m}, 2000 \text{ m})$ with uniform intervals $\theta_{g_1} = 0.2^\circ$ and $R_{g_2} = 10 \text{ m}$, respectively. Fig. 8 compares the RMSE performance of DOA and range estimations with respect to the input SNR for different array configurations and frequency offset structures, where 500 snapshots are used. In Fig. 9, we compare the RMSE performance with respect to the number of snapshots, where the input SNR is set to -5 dB . It is evident that the accuracy of both DOA and range estimates is improved as the SNR and the number of snapshots increase. In comparison with the uniform array/offset case, the coprime array/offset structure benefits from more independent measurements under the CS framework. It is shown that the CA-UFO and ULA-CFO respectively achieve improved estimation accuracy in the angular and range domains than that of the ULA-UFO owing to the coprime structure in the sensor positions and

frequency offsets. In particular, the CA-CFO achieves the best performance as the advantages of coprime structure are presented in both angular and range domains.

In Fig. 10, we consider $Q = 56$ targets. Note that this number is more than the available DOFs obtained from the cases of ULA-UFO (the conventional FDA radar), ULA-CFO, and CA-UFO. As the virtual array and virtual frequency offset are obtained from the estimated covariance matrix based on the received data samples, the virtual steering matrix is sensitive to the noise contamination. To clearly demonstrate the sufficient DOFs for localization of a large number of targets, we use 2000 snapshots in presence of noise with a 10 dB input SNR. It is evident that all 56 signals can be identified correctly, which demonstrates the effectiveness of the CA-CFO in resolving more targets.

C. Sparsity-based Method versus Subspace-based Method

In Figs. 11–13, we compare the sparsity-based method and the MUSIC algorithm with spatial smoothing (MUSIC-SS) applied to the CA-CFO configuration. Note that the spatial smoothing technique is applied to the covariance matrix of the virtual measurement vector \mathbf{z} so that its rank can be restored before the MUSIC algorithm is applied. In this case, only consecutive lags, i.e., $[-7, 7]$, can be used so that every sub-matrix has a similar manifold. The corresponding number of available DOFs is less than that of the proposed sparsity-based approach, which utilizes all unique lags [34]. In Fig. 11, we examine their resolution for $Q = 5$ closely spaced targets, whose true positions are shown in Fig. 11(a). The localization results, depicted in Figs. 11(b) and 11(c), are obtained by using 500 snapshots with a 0 dB SNR. It is clear that the sparsity-based method outperforms the MUSIC-SS approach for resolving the closely spaced targets, since it exploits all distinct lags to form a virtual space-frequency structure, thus yielding a larger array aperture and frequency span compared to the corresponding MUSIC-SS technique which only uses consecutive lags. The respective RMSE performance is compared in Figs. 12 and 13 under the same target scenario considered in Figs. 8 and 9, whereas $Q = 2$ targets located at $(10^\circ, 1300 \text{ m})$ and $(25^\circ, 1700 \text{ m})$ are present. In Fig. 12, 500 snapshots are used, while a -5 dB SNR is assumed in Fig. 13. It is evident that the proposed sparsity-based method achieves a lower RMSE than the MUSIC-SS due to the higher number DOFs in both angular and range domains. This simulation example shows that the sparsity-based method achieves better performance than the MUSIC-SS counterparts do.

D. Proposed Method versus Existing Methods

In Figs. 14–16, we compare the performance of the proposed method with the existing methods using sparse arrays. The methods in [42] and [43], which are referred to as the Nested-MUSIC and Nested-

CS, respectively, employ a nested array configuration but with the uniform time-delayer and frequency increment. As a consequence, it has only $\mathcal{O}(N_t)$ frequency DOFs with a smaller spectral span for a coarse range resolution, although it has the same $\mathcal{O}(N_t^2)$ spatial DOFs as the proposed coprime FDA radar configuration. The same target scenario considered in Figs. 11–13 is used for performance comparison. Fig. 14 depicts the angle-range resolution, wherein the true positions and results obtained from the proposed method are reproduced from Fig. 11(a) and Fig. 11(c) as Fig. 14(a) and Fig. 14(b) for the convenience of comparison. The corresponding results using the Nested-MUSIC and Nested-CS methods are presented in Figs. 14(c) and 14(d), respectively. It is evident that only the proposed method can resolve these closely spaced targets in the range. Furthermore, the Nested-MUSIC method produces more blurry spectra than the Nested-CS for targets with a small angular separation. The RMSE is compared in Figs. 15 and 16. It is clear that the Nested-MUSIC and Nested-CS methods suffer from significant performance degradation in the range domain due to the reduced spectral span and range-domain DOFs. Accordingly, the Nested-CS outperforms the Nested-MUSIC owing to its utilizations of all distinct lags in the coarray structure.

VII. CONCLUSIONS

In this paper, we proposed a novel sparsity-based multi-target localization algorithm, which incorporates both coprime arrays and coprime frequency offsets in an FDA radar platform. By exploiting the sensor position lags and frequency differences, the proposed technique achieved a high number of DOFs representing a larger array aperture and increased frequency increments compared to conventional approaches. These attributes enable high-resolution target localization of significantly more targets than the number of physical sensors. A fast algorithm was developed that cast the 2-D sparse reconstruction problem as separate 1-D sparse reconstruction problems, thus effectively reducing the computational complexity. The offerings of the proposed technique were demonstrated by simulation results.

REFERENCES

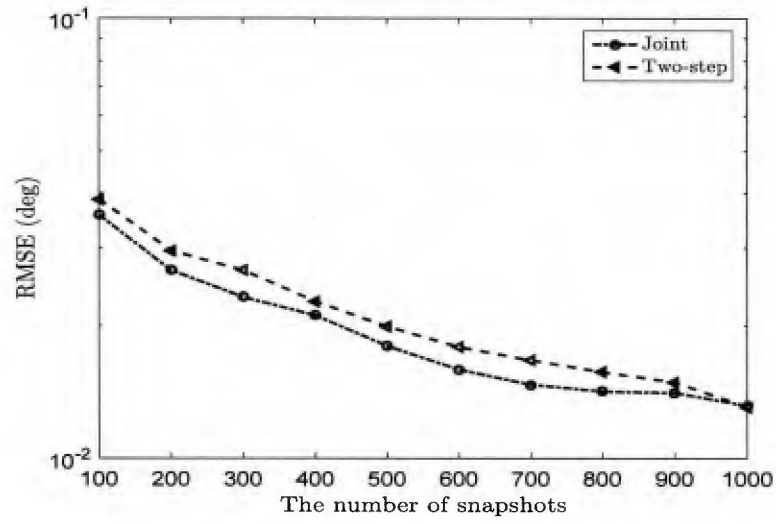
- [1] S. Qin, Y. D. Zhang, and M. G. Amin, “Multi-target localization using frequency diverse coprime arrays with coprime frequency offsets,” in *Proc. IEEE Radar Conf.*, Philadelphia, PA, 2016, pp. 1–5.
- [2] M. Skolnik, *Radar Handbook, Third Edition*. McGraw-Hill, 2008.
- [3] D. Ribas, P. Rida, and J. Neira, *Underwater SLAM for Structured Environments Using an Imaging Sonar*. Springer, 2010.
- [4] G. Mao and B. Fidan, Eds, *Localization Algorithms and Strategies for Wireless Sensor Networks*. Information Science Reference, 2009.

- [5] C. Gentile, N. Alsindi, R. Raulefs, and C. Teolis, *Geolocation Techniques: Principles and Applications*. Springer, 2012.
- [6] B. Bauman, A. Christianson, A. Wegener, and W. J. Chappell, "Dynamic visualization of antenna patterns and phased-array beam steering," *IEEE Antennas Propag. Mag.*, vol. 54, no. 3, pp. 184–193, 2012.
- [7] P. Rocca, R. L. Haupt, and A. Massa, "Interference suppression in uniform linear arrays through a dynamic thinning strategy," *IEEE Trans. Antennas Propag.*, vol. 59, no. 12, pp. 4525–4533, 2011.
- [8] J. R. Mosig, "An old tool and a new challenge for depicting antenna array radiation patterns," *IEEE Antennas Propag. Mag.*, vol. 53, no. 3, pp. 115–123, 2011.
- [9] T. F. Chun, A. Zamora, J. L. Bao, R. T. Iwami, and W. A. Shiroma, "An interleaved, interelement phase-detecting/phase-shifting retrodirective antenna array for interference reduction," *IEEE Antennas Wirel. Propag. Lett.*, vol. 10, pp. 919–922, 2011.
- [10] P. Antonik, M. C. Wicks, H. D. Griffiths, and C. J. Baker, "Frequency diverse array radars," in *Proc. IEEE Radar Conf.*, Verona, NY, 2006, pp. 215–217.
- [11] M. Secmen, S. Demir, A. Hizal, and T. Eker, "Frequency diverse array antenna with periodic time modulated pattern in range and angle," in *Proc. IEEE Radar Conf.*, Boston, MA, 2007, pp. 427–430.
- [12] P. Antonik, "An investigation of a frequency diverse array," Ph.D. dissertation, Univ. College London, London, U.K., 2009.
- [13] W.-Q. Wang, "Phased-MIMO radar with frequency diversity for range-dependent beamforming," *IEEE Sens. J.*, vol. 13, no. 4, pp. 1320–1328, 2013.
- [14] P. F. Sammartino, C. J. Baker, and H. D. Griffiths, "Frequency diverse MIMO techniques for radar," *IEEE Trans. Aerosp. Electron. Syst.*, vol. 49, no. 1, pp. 201–222, 2013.
- [15] W.-Q. Wang and H. C. So, "Transmit subaperturing for range and angle estimation in frequency diverse array radar," *IEEE Trans. Signal Process.*, vol. 62, no. 8, pp. 2000–2011, 2014.
- [16] W.-Q. Wang, "Frequency diverse array antenna: New opportunities," *IEEE Antennas Propag. Mag.*, vol. 57, no. 2, pp. 145–152, 2015.
- [17] Z. Xiang and B. Chen, "Optimal frequency increment selection in frequency diverse multiple-input-multiple-output radar," *IET Radar Sonar Navig.*, DOI:10.1049/iet-rsn.2015.0519, 2016.
- [18] K. Gao, W.-Q. Wang, and J. Cai, "Frequency diverse array and MIMO hybrid radar transmitter design via Cramer-Rao lower bound minimization," *IET Radar Sonar Navig.*, DOI:10.1049/iet-rsn.2015.0644, 2016.
- [19] W. Khan, I. M. Qureshi, A. Basit, and W. Khan, "Range-bins-based MIMO frequency diverse array radar with logarithmic frequency offset," *IEEE Antennas Wirel. Propag. Lett.*, vol. 15, pp. 885–888, 2016.
- [20] W.-Q. Wang, "Moving-target tracking by cognitive RF stealth radar using frequency diverse array antenna," *IEEE Trans. Geosci. Remote Sens.*, vol. 54, no. 7, pp. 3764–3773, 2016.
- [21] J. Xu, G. Liao, S. Zhu, L. Huang, and H. C. So, "Joint range and angle estimation using MIMO radar with

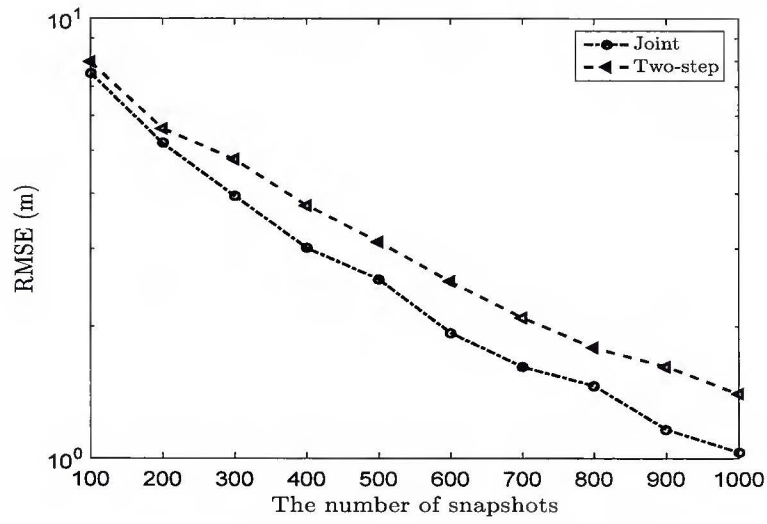
- frequency diverse array,” *IEEE Trans. Signal Process.*, vol. 63, no. 13, pp. 3396–3410, 2015.
- [22] K. Gao, H. Shao, H. Chen, J. Cai and W. -Q. Wang, “Impact of frequency increment errors on frequency diverse array MIMO in adaptive beamforming and target localization,” *Digital Signal Process.*, vol. 44, pp. 58–67, 2015.
- [23] W.-Q. Wang and H. Shao, “Range-angle localization of targets by a double-pulse frequency diverse array radar,” *IEEE J. Sel. Top. Signal Process.*, vol. 8, no. 1, pp. 106–114, 2014.
- [24] R. T. Hoorfar and S. A. Kassam, “The unifying role of the coarray in aperture synthesis for coherent and incoherent imaging,” *Proc. IEEE*, vol. 78, no. 4, pp. 735–752, 1990.
- [25] W.-Q. Wang, H. C. So, and H. Shao, “Nonuniform frequency diverse array for range-angle imaging of targets,” *IEEE Sens. J.*, vol. 14, no. 8, pp. 2469–2476, 2014.
- [26] P. Pal and P. P. Vaidyanathan, “Nested arrays: A novel approach to array processing with enhanced degrees of freedom,” *IEEE Trans. Signal Process.*, vol. 58, no. 8, pp. 4167–4181, 2010.
- [27] P. P. Vaidyanathan and P. Pal, “Sparse sensing with co-prime samplers and arrays,” *IEEE Trans. Signal Process.*, vol. 59, no. 2, pp. 573–586, 2011.
- [28] Y. D. Zhang, M. G. Amin, F. Ahmad, and B. Himed, “DOA estimation using a sparse uniform linear array with two CW signals of co-prime frequencies,” in *Proc. IEEE Workshop Comput. Adv. Multi-sensor Adapt. Process. (CAMSAP)*, Saint Martin, 2013, pp. 404–407.
- [29] Q. Wu and Q. Liang, “Coprime sampling for nonstationary signal in radar signal processing,” *EURASIP J. Wireless Commun. Netw.*, vol. 2013, no. 58, pp. 1–11, 2013.
- [30] J. Chen, Q. Liang, B. Zhang and X. Wu, “Spectrum efficiency of nested sparse sampling and coprime sampling,” *EURASIP J. Wireless Commun. Netw.*, vol. 2013, no. 47, pp. 1–15, 2015.
- [31] K. Adhikari, J. R. Buck and K. E. Wage, “Extending coprime sensor arrays to achieve the peak side lobe height of a full uniform linear array,” *EURASIP J. Adv. Signal Process.*, vol. 2014, no. 148, pp. 1–17, 2014.
- [32] Z. Tan and A. Nehorai, “Sparse direction-of-arrival estimation using co-prime arrays with off-grid targets,” *IEEE Signal Process. Lett.*, vol. 21, no. 1, pp. 26–29, 2014.
- [33] Z. Tan, Y. Eldar, and A. Nehorai, “Direction of arrival estimation using co-prime arrays: A super resolution viewpoint,” *IEEE Trans. Signal Process.*, vol. 62, no. 21, pp. 5565–5576, 2014.
- [34] S. Qin, Y. D. Zhang, and M. G. Amin, “Generalized coprime array configurations for direction-of-arrival estimation,” *IEEE Trans. Signal Process.*, vol. 63, no. 6, pp. 1377–1390, 2015.
- [35] S. Qin, Y. D. Zhang, Q. Wu, and M. G. Amin, “Structure-aware Bayesian compressive sensing for near-field source localization based on sensor-angle distributions,” *Int. J. Antennas Propag.*, vol. 2015, article ID 783467, 2015.
- [36] C. L. Liu and P. P. Vaidyanathan, “Coprime arrays and samplers for space-time adaptive processing,” in *Proc. IEEE Int. Conf. Acoust. Speech Signal Process. (ICASSP)*, Brisbane, Australia, 2015, pp. 2364–2368.

- [37] S. Qin, Y. D. Zhang, and M. G. Amin, "Sparsity-based multi-target localization exploiting multi-frequency coprime array," in *Proc. IEEE China Summit and Int. Conf. Signal and Inform. Process. (ChinaSIP)*, Chengdu, China, 2015, pp. 329–333.
- [38] Q. Shen, W. Liu, W. Cui, S. Wu, Y. D. Zhang, and M. G. Amin, "Low-complexity wideband direction-of-arrival estimation based on co-prime arrays," *IEEE/ACM Trans. Audio, Speech and Language Process.*, vol. 23, no. 9, pp. 1445–1456, 2015.
- [39] S. Qin, Y. D. Zhang, M. G. Amin, and A. Zoubir, "Generalized coprime sampling of Toeplitz matrices," in *Proc. IEEE Int. Conf. Acoust. Speech Signal Process. (ICASSP)*, Shanghai, China, 2016, pp. 4468–4472.
- [40] S. Qin, Y. D. Zhang, M. G. Amin, and B. Himed, "DOA estimation exploiting a uniform linear array with multiple co-prime frequencies," *Signal Process.*, vol. 130, pp. 37–46, 2017.
- [41] S. Qin, Y. D. Zhang, M. G. Amin, and A. Zoubir, "Generalized coprime sampling of Toeplitz matrix," *IEEE Trans. Signal Process.*, in press.
- [42] W.-Q. Wang and C. Zhu, "Nested array receiver with time-delayers for joint target range and angle estimation," *IET Radar Sonar Navig.*, DOI:10.1049/iet-rsn.2015.0450, 2016.
- [43] J. Xiong, W.-Q. Wang, H. Chen, and H. Shao, "Compressive sensing-based range and angle estimation for nested FDA radar," in *Proc. Asia-Pacific Signal Inf. Process. Assoc. Annu. Summit Conf. (APSIPA)*, 2015, pp. 608–611.
- [44] D. L. Donoho, "Compressed sensing," *IEEE Trans. Inf. Theory*, vol. 52, no. 4, pp. 1289–1306, 2006.
- [45] D. Wipf and S. Nagarajan, "Beamforming using the relevance vector machine," in *Proc. Int. Conf. Mach. Learn.*, Corvallis, OR, 2007, pp. 1023–1030.
- [46] S. Ji, Y. Xue, and L. Carin, "Bayesian compressive sensing," *IEEE Trans. Signal Process.*, vol. 56, no. 6, pp. 2346–2356, 2008.
- [47] S. Ji, D. Dunson, and L. Carin, "Multitask compressive sensing," *IEEE Trans. Signal Process.*, vol. 57, no. 1, pp. 92–106, 2009.
- [48] Z. Yang, L. Xie, and C. Zhang, "Off-grid direction-of-arrival estimation using sparse Bayesian inference," *IEEE Trans. Signal Process.*, vol. 61, no. 1, pp. 38–43, 2013.
- [49] Q. Wu, Y. D. Zhang, and M. G. Amin, "Complex multitask Bayesian compressive sensing," in *Proc. IEEE Int. Conf. Acoust. Speech Signal Process. (ICASSP)*, Florence, Italy, 2014, pp. 3375–3379.
- [50] X. Wang, M. G. Amin, F. Ahmad, and E. Aboutanios, "Bayesian compressive sensing for DOA estimation using the difference coarray," in *Proc. IEEE Int. Conf. Acoust. Speech Signal Process. (ICASSP)*, Brisbane, Australia, 2015, pp. 2384–2388.
- [51] Q. Wu, Y. D. Zhang, M. G. Amin, and B. Himed, "Multi-task Bayesian compressive sensing exploiting intra-task dependency," *IEEE Signal Process. Lett.*, vol. 22, no. 4, pp. 430–434, 2015.
- [52] R. Klemm, *Space-Time Adaptive Processing: Principles and Applications*. IEEE Press, 1998.

- [53] J. W. Odendaal, E. Barnard, and C. W. I. Pistorius, "Two-dimensional superresolution radar imaging using the MUSIC algorithm," *IEEE Trans. Antennas Propag.*, vol. 42, no. 10, pp. 1386–1391, 1994.
- [54] X-G. Xia and G. Wang, "Phase unwrapping and a robust Chinese remainder theorem," *IEEE Signal Process. Lett.*, vol. 14, no. 4, pp. 247–250, 2007.
- [55] P. Pal and P. P. Vaidyanathan, "Coprime sampling and the MUSIC algorithm," in *Proc. IEEE Digital Signal Process. Workshop and IEEE Signal Process. Educ. Workshop (DSP/SPE)*, Sedona, AZ, 2011, pp. 289–294.
- [56] Y. D. Zhang, S. Qin, and M. G. Amin, "DOA estimation exploiting coprime arrays with sparse sensor spacing," in *Proc. IEEE Int. Conf. Acoust. Speech Signal Process. (ICASSP)*, Florence, Italy, 2014, pp. 2267–2271.
- [57] T.-J. Shan, M. Wax, and T. Kailath, "On spatial smoothing for direction-of-arrival estimation of coherent signals," *IEEE Trans. Acoust. Speech Signal Process.*, vol. 33, no. 4, pp. 806–811, 1985.
- [58] Y. M. Chen, "On spatial smoothing for two-dimensional direction-of-arrival estimation of coherent signals," *IEEE Trans. Signal Process.*, vol. 45, no. 7, pp. 1689–1696, 1997.
- [59] Y. D. Zhang, M. G. Amin, and B. Himed, "Sparsity-based DOA estimation using co-prime arrays," in *Proc. IEEE Int. Conf. Acoust. Speech Signal Process. (ICASSP)*, Vancouver, Canada, 2013, pp. 3967–3971.
- [60] R. Jagannath and K. Hari, "Block sparse estimator for grid matching in single snapshot DOA estimation," *IEEE Signal Process. Lett.*, vol. 20, no. 11, pp. 1038–1041, 2013.
- [61] Z. Tan, P. Yang, and A. Nehorai, "Joint sparse recovery method for compressed sensing with structured dictionary mismatch," *IEEE Trans. Signal Process.*, vol. 62, no. 19, pp. 4997–5008, 2014.
- [62] M. E. Tipping, "Sparse Bayesian learning and the relevance vector machine," *J. Mach. Learn. Res.*, vol. 1, no. 9, pp. 211–244, 2001.
- [63] S. D. Babacan, R. Molina, and A. K. Katsaggelos, "Bayesian compressive sensing using Laplace priors," *IEEE Trans. Image Process.*, vol. 19, no. 1, pp. 53–63, 2010.



(a)



(b)

Fig. 6. RMSE versus the number of snapshots using the joint and two-step estimation methods ($Q = 2$ and $\text{SNR} = -5$ dB).
(a) RMSE_θ ; (b) RMSE_R

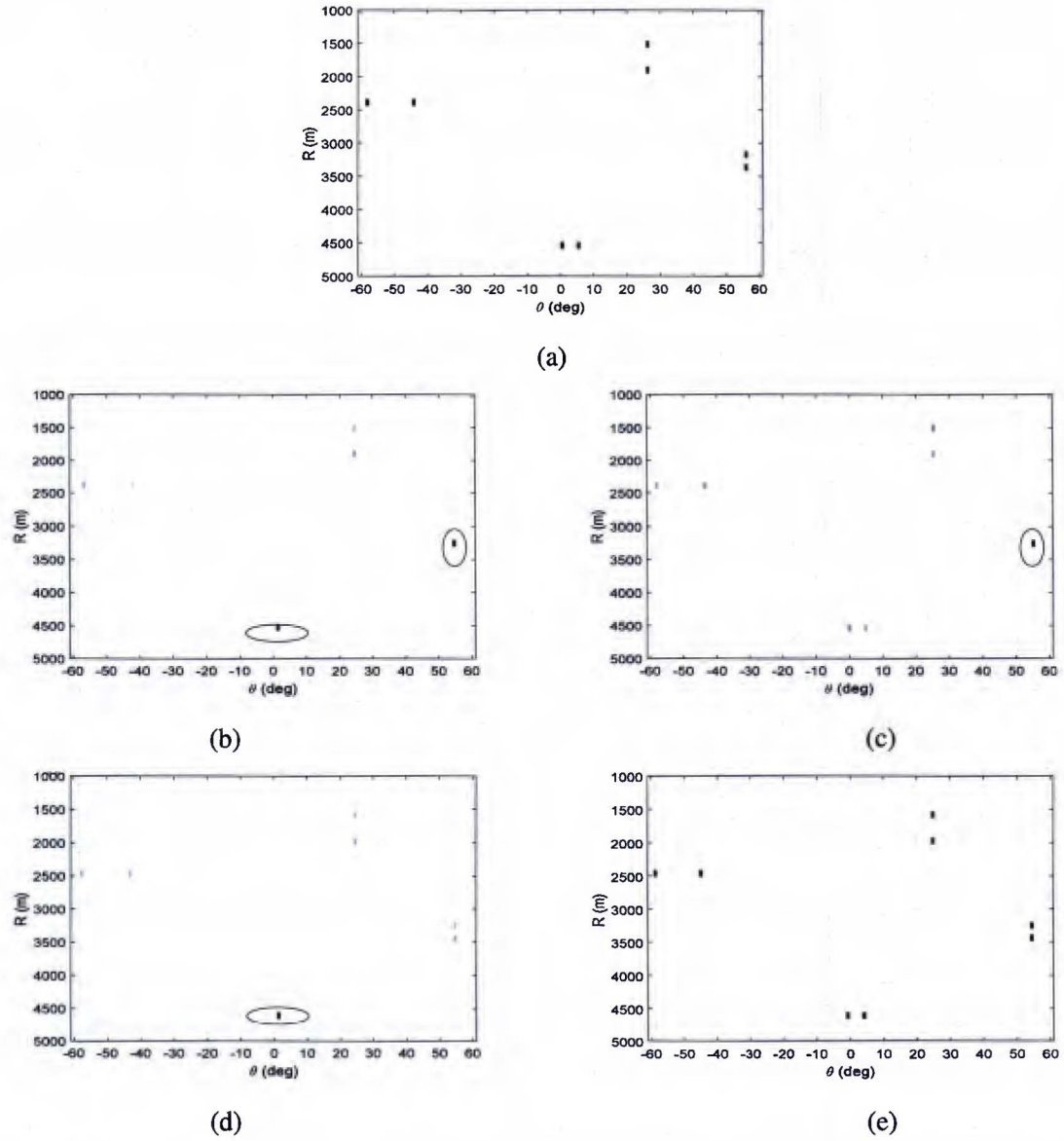
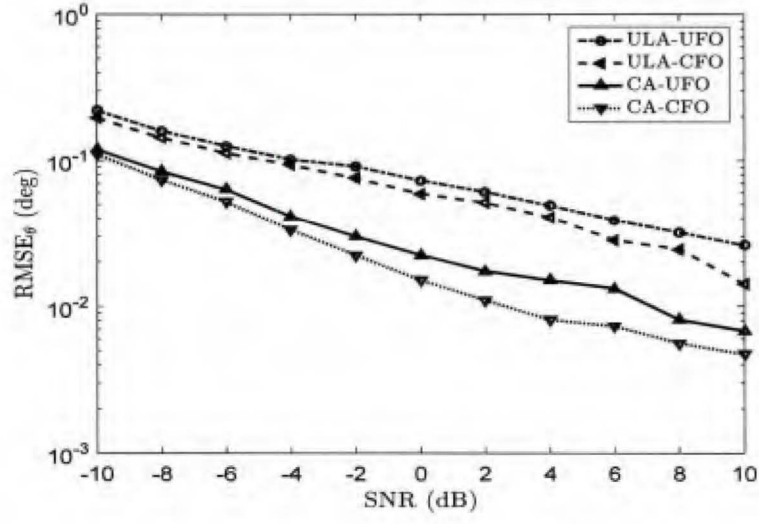
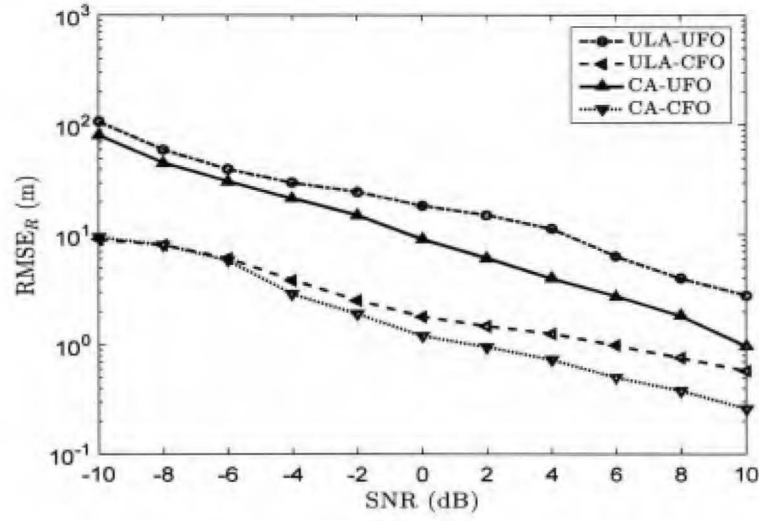


Fig. 7. The localization results using different schemes ($Q = 8$) (a) True; (b) ULA-UFO; (c) CA-UFO; (d) ULA-CFO; (e) CA-CFO.

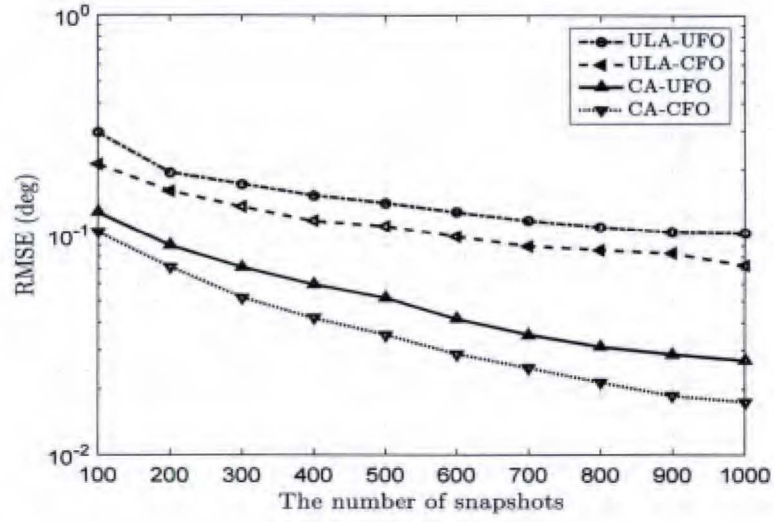


(a)

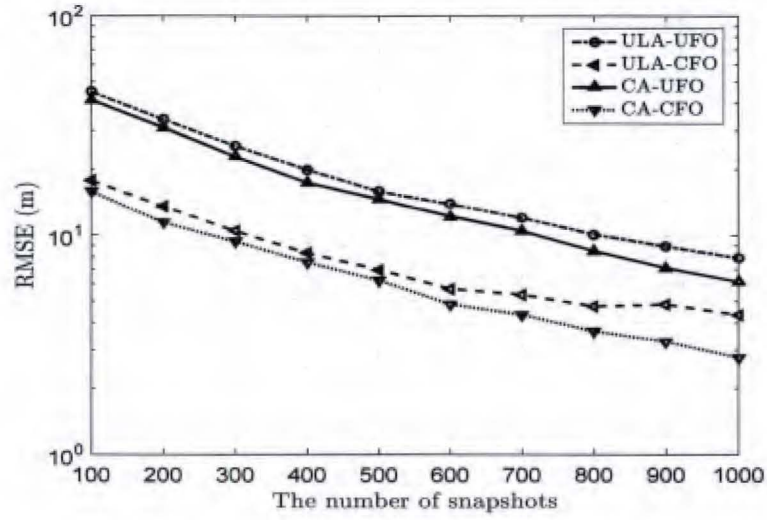


(b)

Fig. 8. RMSE versus SNR ($Q = 2$ and $T = 500$). (a) RMSE_θ ; (b) RMSE_R

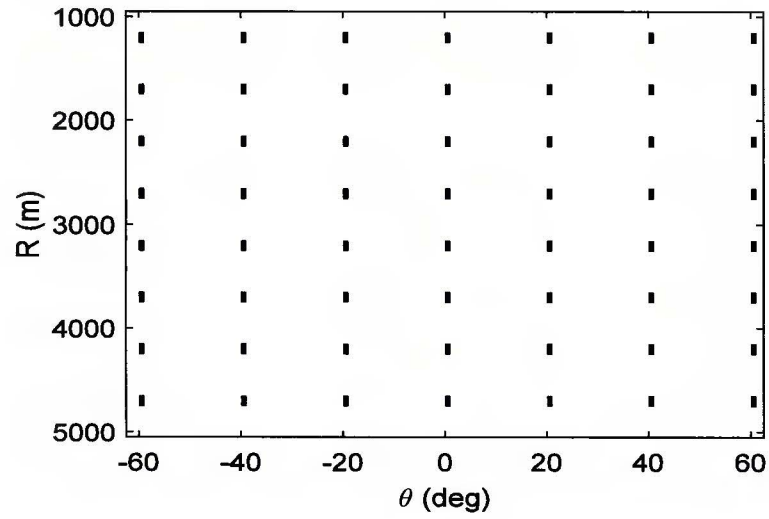


(a)

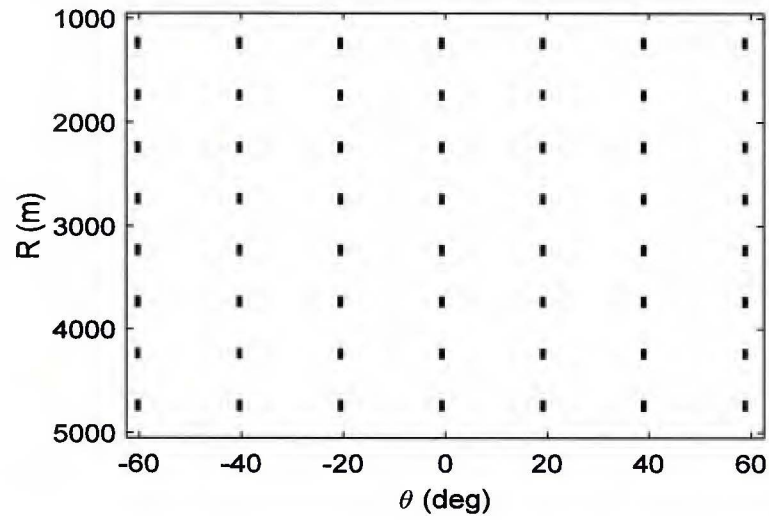


(b)

Fig. 9. RMSE versus the number of snapshots ($Q = 2$ and $\text{SNR} = -5$ dB). (a) RMSE_θ ; (b) RMSE_R

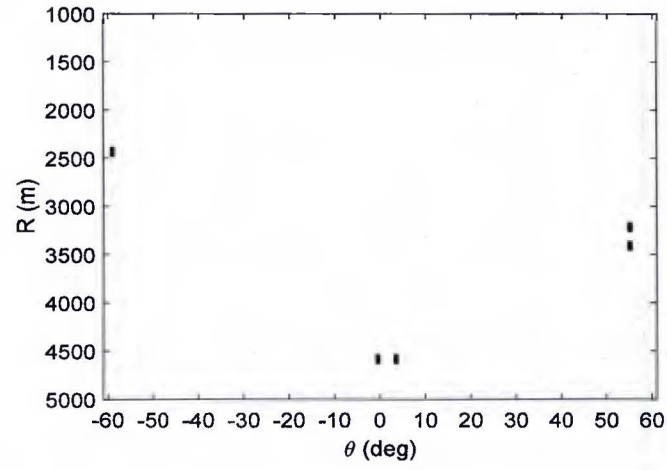


(a)

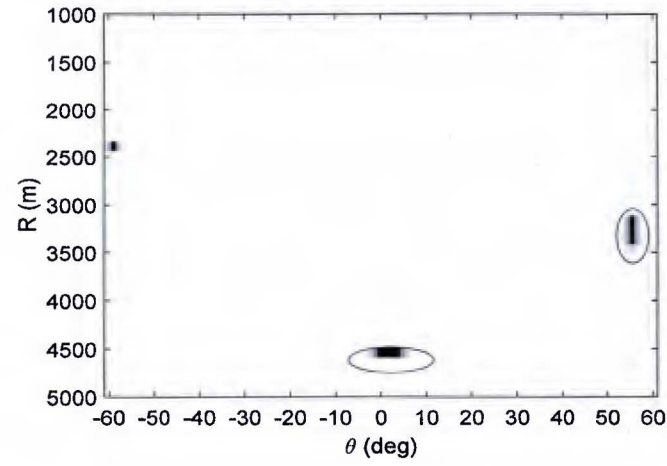


(b)

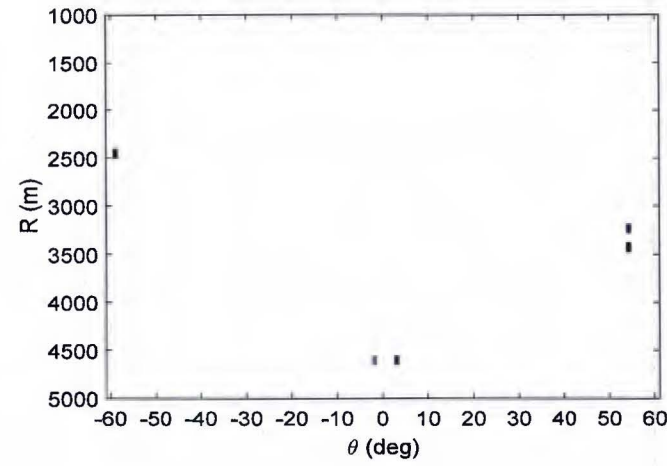
Fig. 10. The localization results using CA-CFO ($Q = 56$). (a) True; (b) Estimated



(a)

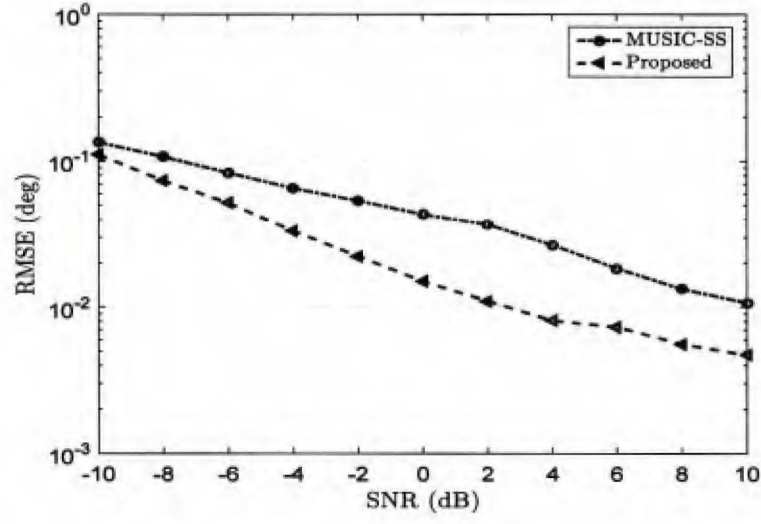


(b)

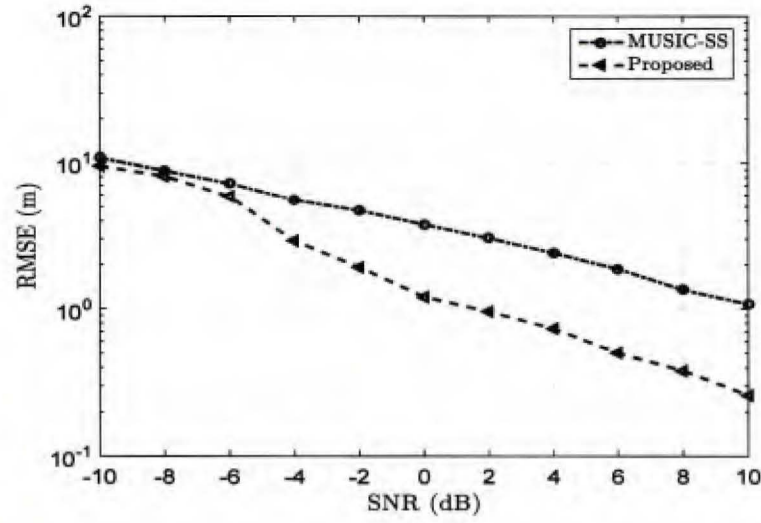


(c)

Fig. 11. The localization results for different methods using CA-CFO ($Q = 5$, $T = 500$, and $\text{SNR} = 0$ dB) (a) True; (b) MUSIC-SS; (c) Proposed.

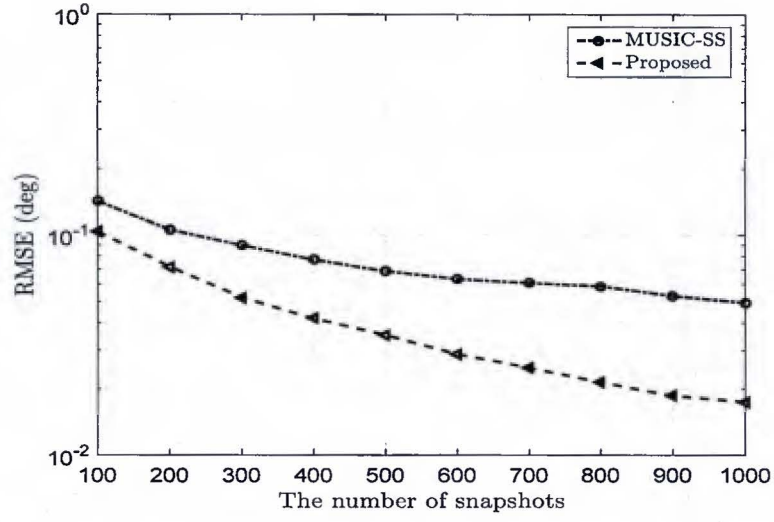


(a)

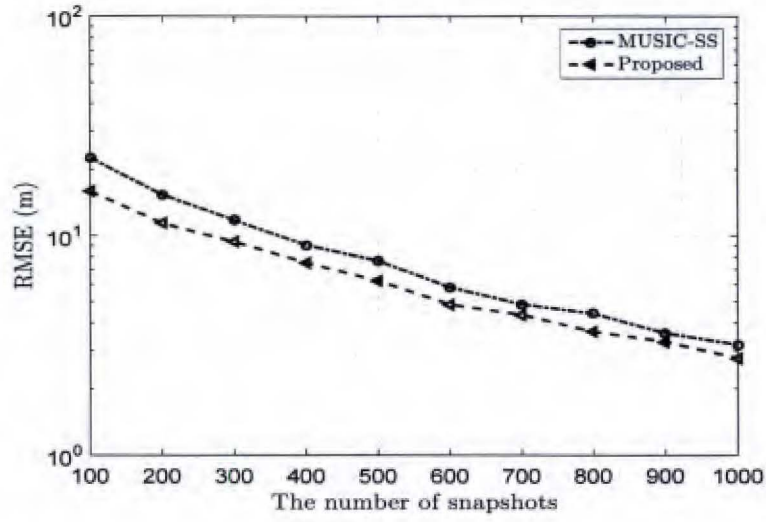


(b)

Fig. 12. RMSE versus SNR for different methods using CA-CFO ($Q = 2$ and $T = 500$). (a) RMSE_θ ; (b) RMSE_R



(a)



(b)

Fig. 13. RMSE versus the number of snapshots for different methods using CA-CFO ($Q = 2$ and $\text{SNR} = -5$ dB). (a) RMSE_θ ; (b) RMSE_R

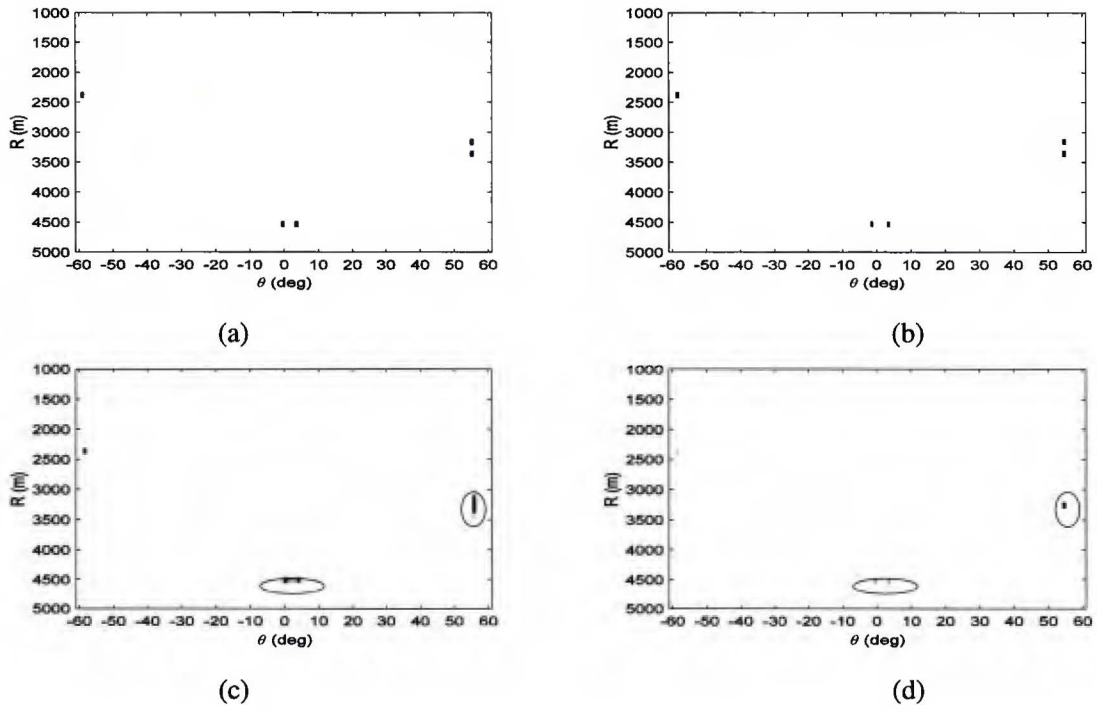
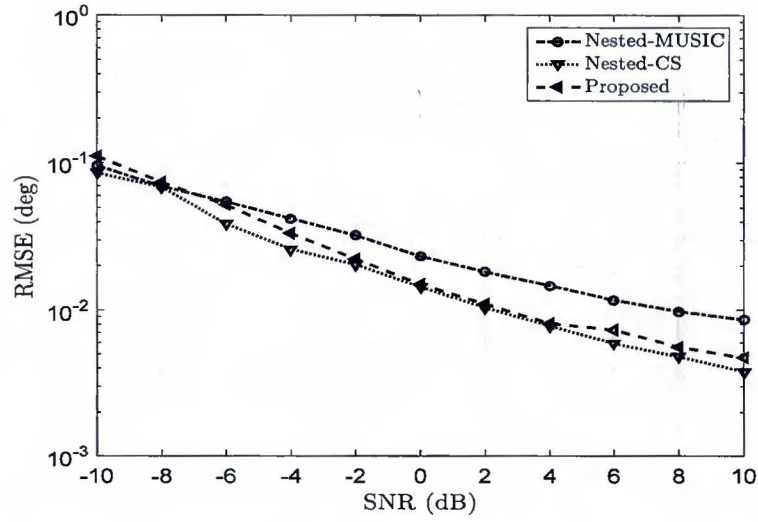
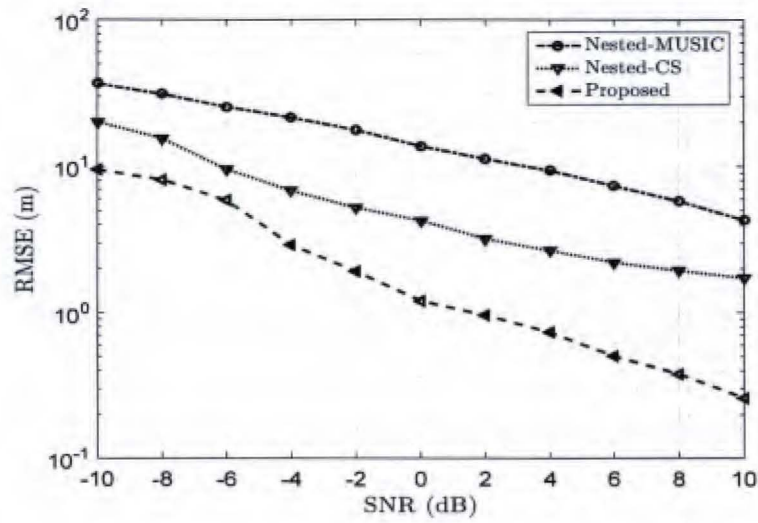


Fig. 14. The localization results for different methods ($Q = 5$, $T = 500$, and $\text{SNR} = 0$ dB) (a) True; (b) Proposed; (c) Nested-MUSIC; (d) Nested-CS.

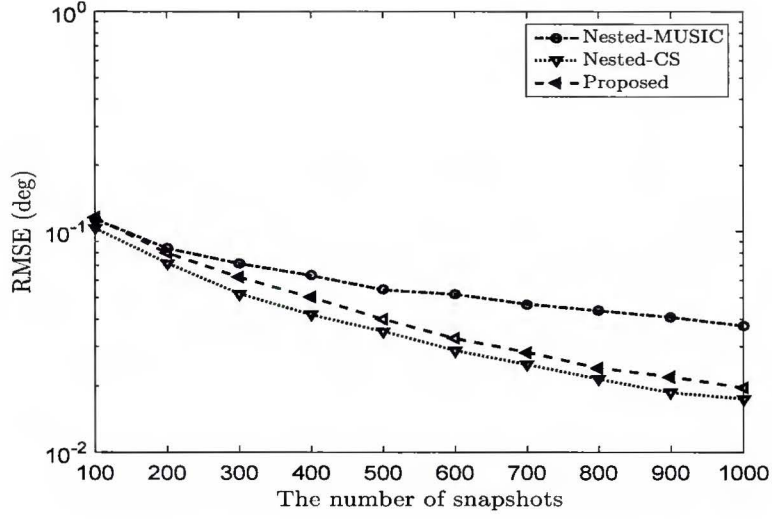


(a)

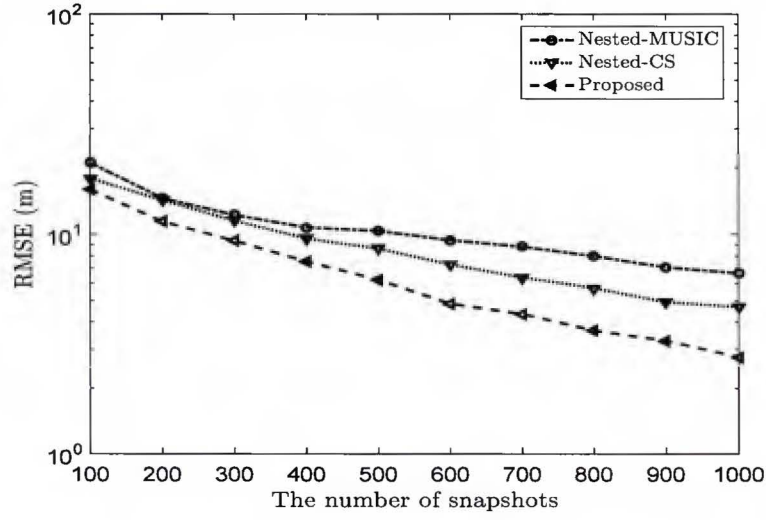


(b)

Fig. 15. RMSE versus the SNR for different methods ($Q = 2$ and $T = 500$). (a) RMSE_θ ; (b) RMSE_R



(a)



(b)

Fig. 16. RMSE versus the number of snapshots for different methods ($Q = 2$ and $\text{SNR} = -5$ dB). (a) RMSE_θ ; (b) RMSE_R

3.5. Sparsity-Based Direction Finding of Coherent and Uncorrelated Targets Using Active Nonuniform Arrays

Abstract

In this letter, direction-of-arrival (DOA) estimation of a mixture of coherent and uncorrelated targets is performed using sparse reconstruction and active nonuniform arrays. The data measurements from multiple transmit and receive elements can be considered as observations from the sum coarray corresponding to the physical transmit/receive arrays. The vectorized covariance matrix of the sum coarray observations emulates the received data at a virtual array whose elements are given by the difference coarray of the sum coarray (DCSC). Sparse reconstruction is used to fully exploit the significantly enhanced degrees-of-freedom offered by the DCSC for DOA estimation. Simulated data from multiple-input multiple-output minimum redundancy arrays and transmit/receive co-prime arrays are used for performance evaluation of the proposed sparsity-based active sensing approach.

I. INTRODUCTION

Direction-of-arrival (DOA) estimation is an important application of array signal processing and is an area of continued research interest [1-4]. The problem of DOA estimation becomes challenging in the presence of coherent sources or a mixture of coherent and uncorrelated sources, which often arise in the presence of multipath propagation. Traditional subspace-based DOA estimation techniques, such as MUSIC [5], can no longer be directly applied due to the rank deficiency of the noise-free covariance matrix. Spatial smoothing can be used to restore the rank of the covariance matrix [6]. However, it can only be applied to specific array structures and always results in reducing the degrees-of-freedom (DOF) that are available for DOA estimation.

Sparse reconstruction techniques have also been applied for DOA estimation of coherent sources [7–9]. In [7], an ℓ_1 – SVD method is proposed to perform sparsity-based DOA estimation. In this method,

the singular value decomposition (SVD) is employed to reduce the dimensionality of the signal model, followed by a mixed $\ell_{1,2}$ – norm minimization, which assumes group sparsity across the time snapshots. The number of resolvable sources in ℓ_1 – SVD is limited by the number of sensors in the array. Joint ℓ_0 approximation, which is a related method to ℓ_1 – SVD, has been proposed in [8]. This method uses a mixed $\ell_{0,2}$ – norm minimization, instead of $\ell_{1,2}$, in order to enforce sparsity in the reconstructed DOAs. Another sparsity-based method for DOA estimation of more correlated sources than sensors was presented in [9]. This method adopts a dynamic array configuration, wherein different sets of elements of a uniform linear array (ULA) are activated in different time slots, and uses sparse reconstruction to estimate the vectorized form of the source covariance matrix to resolve the sources.

All of the aforementioned schemes employ passive or receive-only arrays for DOA estimation. An active or transmit/receive sensing method was proposed in [10] for direction finding in a coherent environment. This method generalizes the spatial smoothing decorrelation technique to encompass active arrays, where the transmitters illuminate the field of view, and the receivers detect the reflections from the targets. The recorded data emulates measurements at the corresponding sum coarray. Using the coarray equivalence principle, the sum coarray measurements can be considered as originating from a virtual transmit/receive array, which, compared to the physical transmit/receive array, provides a different tradeoff between the number of resolvable targets and the maximum number of mutually coherent targets that can be resolved. The number of resolvable targets for this active sensing scheme is limited by the number of receivers in the virtual transmit/receive array. In [11], a sparse reconstruction scheme for DOA estimation in co-located multiple-input multiple-output (MIMO) radar was proposed. The received data is arranged in a vector which emulates measurements at the sum coarray, and either ℓ_1 – SVD or a reweighted minimization is applied to reconstruct the signal. For this method, the number of resolvable targets is limited by the number of sum coarray elements.

In this letter, we perform DOA estimation of a mixture of coherent and uncorrelated targets by using the covariance matrix of the data vector that emulates measurements at the sum coarray of active

nonuniform arrays. In so doing, the number of DOFs is significantly increased, owing to the fact that the vectorized covariance matrix of the sum coarray observations can be thought of as a single measurement at a virtual array whose elements are given by the difference coarray of the sum coarray (DCSC). The DCSC has a much higher number of elements compared to the sum coarray itself [12]. Sparse reconstruction is employed to fully exploit the enhanced DOFs by estimating the vectorized form of the source covariance matrix, which is linearly related to the vectorized data covariance matrix of the sum coarray observations. Two different nonuniform array geometries are considered for performance evaluation using simulated data. The first configuration is the MIMO minimum redundancy array (MRA), which maximizes the number of elements in the DCSC [12], whereas the second is the transmit/receive co-prime arrays [13, 14]. Simulation results clearly demonstrate the superior performance of the proposed scheme over existing methods in terms of the number of resolvable targets for a given number of transmitters/receivers.

The remainder of the letter is organized as follows. In Section II, the signal model for active sensing is reviewed, and the proposed sparsity-based DOA estimation approach is presented. The MIMO MRA and co-prime configurations are also discussed in this section. The performance of the proposed method is evaluated in Section III through numerical simulation, and Section IV concludes the letter.

II. PROPOSED DOA ESTIMATION APPROACH

A. Signal Model

We consider an M -element linear transmit array and an N -element linear receive array. The two arrays may or may not share common elements. These arrays are assumed to be co-located so that a target in the far-field appears to have the same direction at all transmitters and receivers. The scene is illuminated by multiple sequential narrowband transmissions of center frequency f_0 from the different transmitters. This group of transmissions, one from each transmitter, is referred to as a single “snapshot”. We assume the field of view to consist of Q point targets in directions $[\theta_1, \theta_2, \dots, \theta_Q]$, where θ is the

angle relative to broadside of the transmit or receive array. The target distribution consists of both uncorrelated and coherent targets. Then, the output of the receive array can be expressed as an $MN \times 1$ vector [15, 16]

$$\mathbf{x}(t) = \sum_{q=1}^Q \mathbf{a}_t(\theta_q) \otimes \mathbf{a}_r(\theta_q) s_q(t) + \mathbf{n}(t), \quad (1)$$

where the operator \otimes denotes the Kronecker product, $s_q(t)$ is the reflection coefficient of the q th target at snapshot t , and $\mathbf{a}_t(\theta_q)$ and $\mathbf{a}_r(\theta_q)$ are the steering vectors of the transmit and receive arrays corresponding to the direction of the q th target, respectively. The m th element of $\mathbf{a}_t(\theta_q)$ is given by $\exp(-jk_0 t_m \sin \theta_q)$ where t_m is the location of the m th transmitter and $k_0 = 2\pi f_0/c$ is the wavenumber at frequency f_0 with c being the speed of light, and the n th element of $\mathbf{a}_r(\theta_q)$ is given by $\exp(-jk_0 r_n \sin \theta_q)$ where r_n is the location of the n th receiver. The vector $\mathbf{n}(t)$ in (1) is the $MN \times 1$ noise vector. The noise is assumed to be independent and identically distributed following a complex Gaussian distribution.

The term $\mathbf{a}_t(\theta_q) \otimes \mathbf{a}_r(\theta_q)$ in (1) is equivalent to the steering vector of a virtual receive-only array, whose elements are given by the sum coarray of the transmit and receive arrays. The sum coarray elements are defined as the set $\{(r_n + t_m), 0 \leq n \leq N-1, 0 \leq m \leq M-1\}$ [17]. Let L be the number of unique elements in the sum coarray. Then, a new $L \times 1$ received data vector can be formed from (1) as

$$\mathbf{x}_{sum}(t) = \mathbf{A}_{sum} \mathbf{s}(t) + \mathbf{n}_{sum}(t), \quad (2)$$

where $\mathbf{A}_{sum} = [\mathbf{a}_{sum}(\theta_1), \mathbf{a}_{sum}(\theta_2), \dots, \mathbf{a}_{sum}(\theta_Q)]$ is the $L \times Q$ array manifold corresponding to the sum coarray, $\mathbf{s}(t) = [s_1(t), s_2(t), \dots, s_Q(t)]^T$, and $\mathbf{a}_{sum}(\theta_q)$ is the steering vector of the sum coarray in direction θ_q . It should be noted that if two or more transmit/receive element pairs contribute to the same sum coarray point, either the average or one of the corresponding measurements could be used in $\mathbf{x}_{sum}(t)$. The ℓ_1 -SVD method can be applied to the sum coarray data vector $\mathbf{x}_{sum}(t)$ for sparsity-based DOA estimation [11]. However, the maximum number of resolvable targets in this case is limited to the

number of unique elements in the sum coarray [18].

B. Correlation Matrix Based Sparse Reconstruction Approach

The $L \times L$ covariance matrix of the sum coarray data can be expressed as

$$\mathbf{R}_{sum} = E\{\mathbf{x}_{sum}(t)\mathbf{x}_{sum}^H(t)\} = \mathbf{A}_{sum}\mathbf{R}_{ss}\mathbf{A}_{sum}^H + \sigma_n^2\mathbf{I}, \quad (3)$$

where $E\{\cdot\}$ is the expectation operator, σ_n^2 is the noise variance, and \mathbf{I} is an $L \times L$ identity matrix. \mathbf{R}_{ss} is the $Q \times Q$ source correlation matrix, which contains the powers of the reflections from the targets on its main diagonal and the cross-correlations between the targets in the off-diagonal terms. In practice, the covariance matrix is estimated by a sample average over multiple snapshots.

In order to perform DOA estimation of the coherent and uncorrelated targets, we estimate \mathbf{R}_{ss} using \mathbf{R}_{sum} [9]. To this end, we proceed as follows. The angular region of interest is discretized into a finite set of $K \gg Q$ grid points, $\{\theta_{g_1}, \theta_{g_2}, \dots, \theta_{g_K}\}$, with θ_{g_1} and θ_{g_K} being the limits of the search space. The targets are assumed to be located on the grid. Several methods can be used to modify the model in order to deal with off-grid targets [7, 19]. We define the $L \times K$ array manifold $\tilde{\mathbf{A}}_{sum}$ whose columns are the steering vectors corresponding to the defined angles in the grid, and the $K \times K$ $\tilde{\mathbf{R}}_{ss}$ which holds the auto- and cross-correlation between the potential targets at the defined angles. Equation (3) can then be rewritten as

$$\mathbf{R}_{sum} = \tilde{\mathbf{A}}_{sum}\tilde{\mathbf{R}}_{ss}\tilde{\mathbf{A}}_{sum}^H + \sigma_n^2\mathbf{I}. \quad (4)$$

Since $K \gg Q$, $\tilde{\mathbf{R}}_{ss}$ is a sparse matrix. Sparse reconstruction can then be applied to estimate $\tilde{\mathbf{R}}_{ss}$, and consequently resolve the targets. The nonzero terms on the main diagonal of $\tilde{\mathbf{R}}_{ss}$ correspond to the powers of the target reflections present in the field of view, and the nonzero off-diagonal terms correspond to the correlations between the coherent targets. As a result, the target directions can be obtained by identifying the nonzero terms on the main diagonal.

The covariance matrix \mathbf{R}_{sum} is vectorized by stacking its columns to form a tall vector, which emulates a single snapshot at a virtual array whose elements are given by the DCSC of the transmit and receive arrays. With the sum coarray containing L unique elements at positions $x_\ell, \ell = 0, \dots, L-1$, the

DCSC elements are given by the set $\Omega = \{x_{\ell_1} - x_{\ell_2}, \ell_1 = 0, \dots, L-1 \text{ and } \ell_2 = 0, \dots, L-1\}$. It can be readily shown that the $L^2 \times 1$ vectorized form of the noise-free term of \mathbf{R}_{sum} can be expressed as [9, 20],

$$\text{vec}(\tilde{\mathbf{A}}_{sum} \tilde{\mathbf{R}}_{ss} \tilde{\mathbf{A}}_{sum}^H) = (\tilde{\mathbf{A}}_{sum}^* \otimes \tilde{\mathbf{A}}_{sum}) \text{vec}(\tilde{\mathbf{R}}_{ss}), \quad (5)$$

where $\text{vec}(\cdot)$ denotes the vectorization operation and the superscript $*$ denotes complex conjugation. Given the model in (5), the constrained optimization problem for reconstructing the $K^2 \times 1$ $\text{vec}(\tilde{\mathbf{R}}_{ss})$ can be expressed as [21],

$$\hat{\mathbf{R}}_{ss} = \arg \min_{\tilde{\mathbf{R}}_{ss}} \|\text{vec}(\mathbf{R}_{sum}) - (\tilde{\mathbf{A}}_{sum}^* \otimes \tilde{\mathbf{A}}_{sum}) \text{vec}(\tilde{\mathbf{R}}_{ss})\|_2 + \lambda \|\text{vec}(\tilde{\mathbf{R}}_{ss})\|_1, \quad (6)$$

where the ℓ_2 -norm is the least squares cost function to maintain data fidelity, and the ℓ_1 -norm encourages sparsity in the reconstructed vector. The regularization parameter λ is used to control the weight of the sparsity constraint in the overall cost function.

C. Maximum Number of Resolvable Targets

The maximum number of resolvable targets using the proposed method depends on the number of unique lags in the DCSC and the number of coherent targets. Each pair of coherent targets corresponds to two nonzero off-diagonal terms in $\tilde{\mathbf{R}}_{ss}$, and each target contributes a nonzero term on the main diagonal. Due to conjugate symmetry in $\tilde{\mathbf{R}}_{ss}$, only the lower triangle matrix can be estimated. This implies that, instead of K^2 terms, only $K(K+1)/2$ elements of $\tilde{\mathbf{R}}_{ss}$ need to be estimated. According to [22], the sparsity based minimization problem in (6) is guaranteed to have a unique solution under the condition $P \geq 2D$, where P is equal to the number of independent observations or the number of unique elements in the DCSC and D is the number of nonzero terms in the lower triangle of $\tilde{\mathbf{R}}_{ss}$, which can be expressed as $D = Q + C$, where C is the number of pairs of coherent targets.

The number of unique lags P in the DCSC is a function of the transmit and receive array geometries. For a given number of transmitters and receivers, active array configurations specifically designed to be optimal in the sense that the number of unique elements in the DCSC is maximized, would yield the highest number of resolvable sources. MIMO MRAs are one such type of arrays which are designed under the constraint that the DCSC has no holes [12]. However, the use of such optimal array

configurations is not mandatory, and the proposed technique can be applied to other nonuniform arrays, such as co-prime arrays. Co-prime arrays consist of two interleaved ULAs with co-prime number of elements and co-prime element spacing [13, 14]. Table I summarizes the number of unique elements in the sum coarray and the DCSC of three different implementations (Configurations A, B, and C) of a co-prime array comprising a $(2M_c - 1)$ element ULA with $N_c\lambda_0/2$ inter-element spacing and a second ULA having N_c elements spaced by $M_c\lambda_0/2$; M_c and N_c are co-prime integers, the two ULAs share the first element at 0, and λ_0 is the wavelength at the frequency f_0 . Configuration A uses the first ULA to transmit and the second ULA to receive. Configuration B employs the first ULA for transmission and both ULAs for reception. Configuration C uses the entire co-prime array to transmit and receive. These implementations provide different tradeoffs between cost, hardware complexity, and the maximum number of unique elements in the DCSC. We observe from Table I that the advantage of the proposed method over the ℓ_1 - SVD method applied directly to the sum coarray of the co-prime arrays is more evident for higher values of M_c and N_c . For large M_c and N_c values, a three-fold increase in the DOFs occurs for configurations B and C.

III. NUMERICAL RESULTS

In this section, DOA estimation results for the proposed sparse reconstruction technique using nonuniform active arrays are presented, and a comparison with the ℓ_1 - SVD method is also provided. Both MIMO MRAs and co-prime arrays are considered. The root mean square error (RMSE) with respect to the directions is used to compare the two methods.

In the first example, we consider a MIMO MRA, which consists of two receivers positioned at $[0, 7d_0]$ and three transmitters positioned at $[0, d_0, 3d_0]$, where $d_0 = \lambda_0/2$. Fig. 1 shows the corresponding sum coarray and the DCSC. The sum coarray consists of six elements positioned at $[0, 1, 3, 7, 8, 10]d_0$, whereas the DCSC consists of 21 consecutive virtual elements and its aperture extends from $-10d_0$ to $10d_0$. As such, ℓ_1 - SVD applied to the sum coarray measurements can estimate

up to six sources, whereas the proposed method can estimate up to ten nonzero elements in the lower triangle of the source covariance matrix. This is tested by first considering six targets at directions $[-60^\circ, -20^\circ, -15^\circ, 10^\circ, 30^\circ, 40^\circ]$, with the reflections from the first three targets being mutually coherent. The total number of snapshots is set to 500. Spatially and temporally white Gaussian noise is added to the observations, and the SNR for the six targets is set to $[10, 0, 5, 0, 10, 0]$ dB. The search space is discretized uniformly from -90° and 90° with 1° increment, and the regularization parameter λ is set empirically to 0.5 for the proposed method. The normalized spectrum obtained using ℓ_1 - SVD and averaged across the snapshots is shown in Fig. 2(a). Fig. 2(b) depicts the normalized values on the main diagonal of the estimated source covariance matrix using the proposed approach. The dashed vertical lines in both figures indicate the true target directions. We observe that the proposed method has correctly estimated the target directions. However, ℓ_1 - SVD misses two targets with low SNR, and produces biased estimates for the remaining targets. The RMSE is 0° for the proposed method.

Next, the same MIMO MRA is used, but the number of targets is increased to seven with the first three being mutually coherent. The targets are positioned at $[-55^\circ, -40^\circ, -15^\circ, 5^\circ, 20^\circ, 45^\circ, 65^\circ]$. A 10 dB SNR is used for all the targets. The regularization parameter λ is set to 0.3. Figs. 3(a) and 3(b) show the estimated spectra using ℓ_1 - SVD and the proposed method, respectively. Clearly, ℓ_1 - SVD fails to estimate the targets since the total number of targets exceeds the number of sum coarray elements. The proposed method, on the other hand, is successful since the number of nonzero elements in the lower triangle is equal to 10. The corresponding RMSE is 0.24° . The number of targets is then increased to 10, which is equal to the maximum number of nonzero elements in the lower triangle of the covariance matrix that can be estimated using the proposed method. The target directions are uniformly spaced between -50° and 50° . The reflections from all the targets are assumed to be uncorrelated in this example, and the other simulation parameters are kept the same as before. Fig. 4(a) shows the estimated spectrum using ℓ_1 - SVD, which fails to estimate the target directions because the number of targets is larger than the number of sum coarray elements. The estimated spectrum using the proposed approach is

shown in Fig. 4(b). As expected, this method correctly estimates all the DOAs, and the RMSE is equal to 0.2° in this example.

Next, we consider a co-prime array with $M_c = 3$ and $N_c = 4$, i.e., the first ULA consists of five physical sensors with positions $[4, 8, 12, 16, 20]d_0$, and the second ULA consists of four sensors positioned at $[0, 3, 6, 9]d_0$. Configuration B is considered, which implies that the first ULA is used to transmit and both ULAs are used to receive. The corresponding sum coarray consists of 25 elements, and the DCSC consists of 67 elements. We consider 30 targets, uniformly spaced between -0.95 and 0.95 in the reduced angular coordinate $\sin(\theta)$, with three targets being mutually coherent. The rest of the simulation parameters are the same as in the previous examples. Figs. 5(a) and 5(b) show the estimated spectra using ℓ_1 - SVD and the proposed method, respectively. We observe that ℓ_1 - SVD fails to estimate the target directions, since the number of targets exceeds the number of sum coarray elements. The proposed method correctly estimates the DOAs since the number of nonzero elements in the lower triangle of the source covariance matrix in this case is $D = Q + C = 30 + 3 = 33$, and the number of unique elements in the DCSC is $P = 67$ which is greater than $2D$. The corresponding RMSE is 0.03° .

IV. CONCLUSION

A sparse reconstruction method has been proposed for DOA estimation using active nonuniform arrays. The proposed approach offers a significant enhancement in the DOFs over the currently employed methods by using the covariance matrix of sum coarray measurements to emulate observations at the difference coarray of the sum coarray. The proposed method was tested using two nonuniform array configurations and was shown to successfully estimate the directions of a mixture of coherent and uncorrelated targets.

TABLE I
NUMBER OF UNIQUE ELEMENTS IN THE SUM COARRAY AND THE DCSA

	Sum Coarray Unique Elements	DCSA Unique Elements
Configuration A	$(2M_c - 1)N_c$	$(5M_c - 3)N_c - M_c$
Configuration B	$(2M_c - 1)(N_c + 1)$	$(7M_c - 5)N_c + M_c$
Configuration C	$(2M_c)(N_c + 1) - 1$	$(7M_c - 3)N_c + M_c$

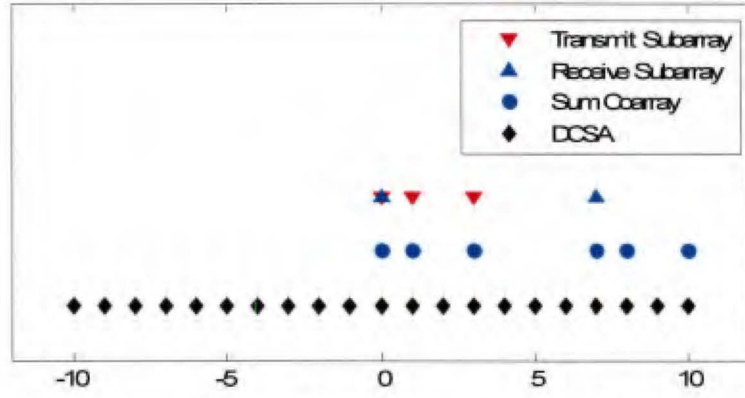


Figure 1. MIMO MRA, sum coarray and DCSA

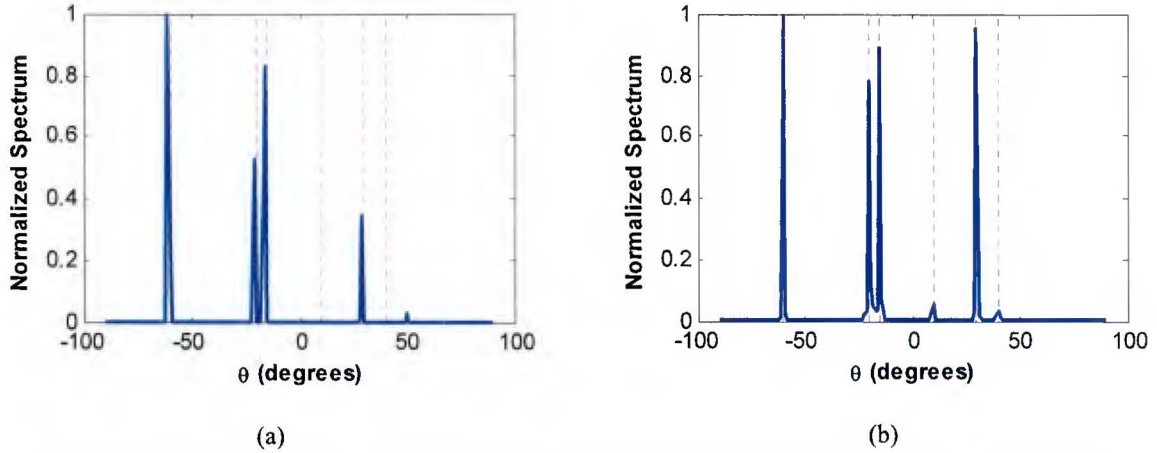


Figure 2. MIMO MRA, six targets (3 mutually coherent), (a) ℓ_1 - SVD, (b) Proposed method

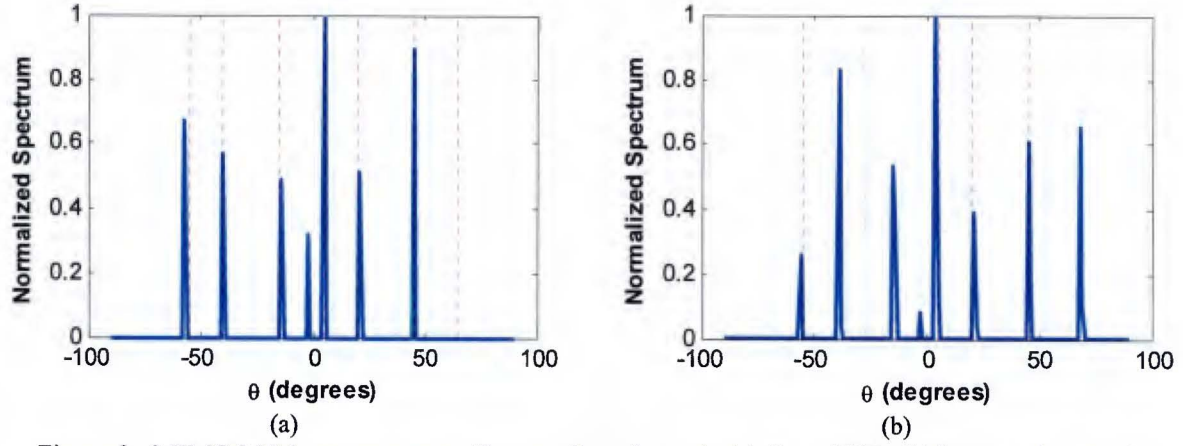


Figure 3. MIMO MRA, seven targets (3 mutually coherent), (a) ℓ_1 - SVD, (b) Proposed method

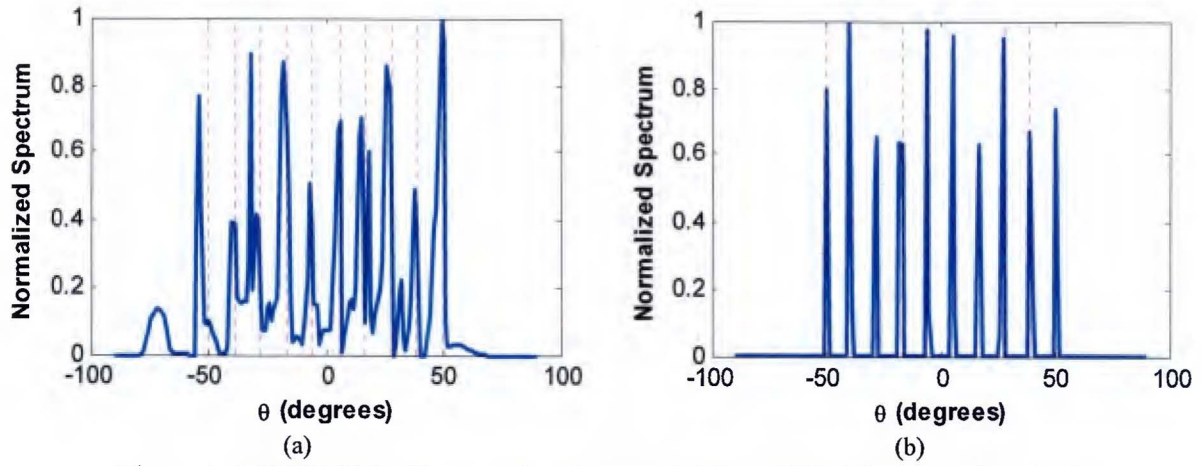


Figure 4. MIMO MRA, 10 uncorrelated targets, (a) ℓ_1 - SVD, (b) Proposed method

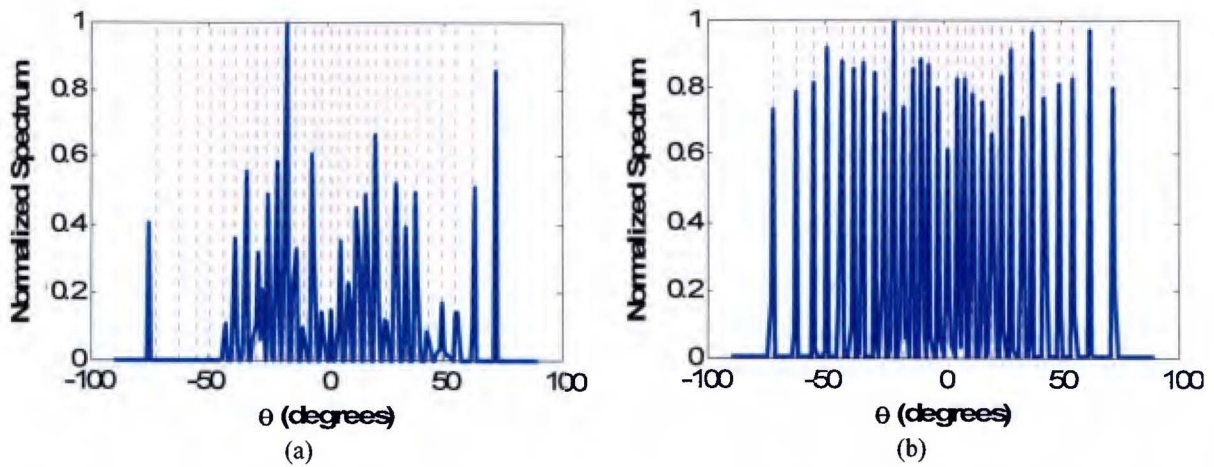


Figure 5. Co-prime array, 30 targets (3 coherent), (a) ℓ_1 - SVD, (b) Proposed method

REFERENCES

- [1] H. Krim and M. Viberg, "Two decades of array signal processing research: The parametric approach," *IEEE Signal Process. Mag.*, vol. 13, no. 7, pp. 67-94, 1996.
- [2] H.L. Van Trees, *Optimum Array Processing: Part IV of Detection, Estimation and Modulation Theory*, Wiley, New York, NY, 2002.
- [3] S. Chandran, *Advances in Direction-of-Arrival Estimation*, Artech House, Norwood, MA, 2006.
- [4] T.E. Tuncer and B. Friedlander, *Classical and Modern Direction-of-Arrival Estimation*, Academic Press (Elsevier), Boston, MA, 2009.
- [5] R. Schmidt, "Multiple emitter location and signal parameter estimation," *IEEE Trans. Antennas Propag.*, vol. 34 no. 3, pp. 276-280, 1986.
- [6] T.J. Shan, M. Wax, and T. Kailath, "On spatial smoothing for direction-of-arrival estimation of coherent signals," *IEEE Trans. Acoust., Speech, Signal Process.*, vol. 33 no. 4, pp. 806-811, 1985.
- [7] D. Malioutov, M. Cetin, and A. Willsky, "Sparse signal reconstruction perspective for source localization with sensor arrays," *IEEE Trans. Signal Process.*, vol. 53 no. 8, pp. 3010-3022, 2005.
- [8] M.M. Hayder and K. Mahata, "Direction-of-arrival estimation using a mixed $\ell_{2,0}$ norm approximation," *IEEE Trans. Signal Process.*, vol. 58 no. 9, pp. 4646-4655, 2010.
- [9] D.D. Arianada and G. Leus, "Direction of arrival estimation for more correlated sources than active sensors," *Signal Process.*, vol. 93, no. 12, pp. 3435-3448, 2013.
- [10] R.T. Hoor and S.A. Kassam, "High resolution coherent source location using transmit/receive arrays," *IEEE Trans. Image Process.*, vol. 1 no. 1, pp. 88-100, 1992.
- [11] X. Wang, W. Wang, J. Liu, X. Li, and J. Wang, "A sparse representation scheme for angle estimation in monostatic MIMO radar," *Signal Process.*, vol. 104, pp. 258-263, 2014.
- [12] C.-C. Weng and P.P. Vaidyanathan, "Nonuniform sparse array design for active sensing," in *Proc. Asilomar Conf. on Signals, Systems, and Computers*, Pacific Grove, CA, 2011.

- [13] P. P. Vaidyanathan and P. Pal, "Sparse sensing with co-prime samplers and arrays," *IEEE Trans. Signal Process.* vol. 59 no. 2, pp. 573-586, 2011.
- [14] P. Pal and P. P. Vaidyanathan, "Coprime sampling and the MUSIC algorithm," in *Proc. IEEE Dig. Signal Process. Workshop and IEEE Signal Process. Educ. Workshop*, Sedona, AZ, 2011.
- [15] X. Zhang and D. Xu, "Low-complexity ESPRIT-based DOA estimation for colocated MIMO radar using reduced-dimension transformation," *Electr. Lett.* vol. 47 no. 4, pp. 283-284, Feb. 2011.
- [16] X. Zhang, Y. Huang, C. Chen, J. Li, and D. Xu, "Reduced-complexity Capon for direction of arrival estimation in a monostatic multiple-input multiple-output radar," *IET Radar Sonar Navig.*, vol. 8 no. 5, pp. 796-801, Oct. 2012.
- [17] R. T. Hoor, and S. A. Kassam, "The unifying role of the coarray in aperture synthesis for coherent and incoherent imaging," *Proc. IEEE*, vol. 78 no. 4, pp. 735-752, 1990.
- [18] D. Malioutov, "A sparse signal reconstruction perspective for source localization with sensor arrays," M.S. thesis, EECS Dept., MIT, Cambridge, MA, 2003.
- [19] Z. Tan and A. Nehorai, "Sparse direction of arrival estimation using co-prime arrays with off-grid targets," *IEEE Signal Process. Lett.*, vol. 21, no. 1, pp. 26-29, 2014.
- [20] A.J. Laub, *Matrix Analysis for Scientists and Engineers*, SIAM, Philadelphia, PA, 2005.
- [21] R. Tibshirani, "Regression shrinkage and selection via the Lasso," *J. R. Stat. Soc.: Series B*, vol. 58, no. 1, pp. 267-288, 1996.
- [22] M. Davenport, M. Duarte, Y. Eldar, and G. Kutyniok, *Compressed Sensing: Theory and Applications*, Cambridge University Press, Cambridge, U.K, 2012.

3.6. Mutual Coupling Effect and Compensation in Non-Uniform Arrays for Direction-of-Arrival Estimation

Abstract

In this paper, we investigate the effect of mutual coupling on direction-of-arrival (DOA) estimation using non-uniform arrays. We compare and contrast the DOA estimation accuracy in the presence of mutual coupling for three different non-uniform array geometries, namely, minimum redundancy arrays (MRAs), nested arrays, and co-prime arrays, and for two antenna types, namely dipole antennas and microstrip antennas. We demonstrate through numerical simulations that the mutual coupling, if unaccounted for, can, in general, lead to performance degradation, with the MRA faring better against mutual coupling than the other two non-uniform structures for both antenna types. We also propose two methods that can compensate for the detrimental effects of mutual coupling, leading to accurate and reliable DOA estimation. Supporting numerical simulation results are provided which show the effectiveness of the proposed compensation methods.

I. INTRODUCTION

Antenna arrays are employed for direction-of-arrival (DOA) estimation in a broad range of applications including radar, sonar, and wireless communications [1-3]. High-resolution DOA estimation techniques, such as MUSIC [4], ESPRIT [5], and ℓ_1 - SVD [6], are widely used for direction finding. In real antenna arrays, these techniques, in their original implementations, suffer from a model mismatch which, among other factors, can be attributed to mutual coupling between the elements. Mutual coupling occurs when an external illuminating source induces a current on the surface of each array element, causing it to radiate. A portion of the radiated signal is captured by the remaining elements in the array. If unaccounted for, this interaction affects the characteristics and the performance of the array [7-8].

The mutual coupling between the array elements can be captured in a matrix called the mutual coupling matrix (MCM). Two major trends exist in the literature for performing DOA estimation in the presence of mutual coupling. The first deals with the case of perfectly known or modeled MCM, wherein the DOA estimation procedure is modified to account for the coupling [9]. In the second trend, the MCM is assumed to be unknown or imprecisely known with a specific structure, and is jointly estimated along with the source directions.

Electromagnetic theory and numerical or analytical modeling techniques are typically employed to characterize the MCM [8, 10-14]. The MCM depends on the self and mutual impedances between the array elements. One of the earliest methods that model the coupling matrix is the open-circuit method [8]. This method treats the array as a bilateral terminal network and relates the uncoupled voltages with the coupled voltages through a mutual impedance matrix. For dipole antennas, the elements in the mutual impedance matrix can be approximated by closed-form expressions [15]. An extension of the open-circuit method has been proposed in [10], where two types of mutual impedances are defined, namely, the transmission mutual impedance and the re-radiation mutual impedance. In [11], the receiving-mutual-impedance method (RMIM) is described for use in receive-only antenna arrays. As such, it provides a more accurate coupling model in DOA estimation applications. RMIM considers each antenna pair separately to compute the receiving mutual impedances. An enhancement of RMIM is presented in [12], which takes into account all the elements simultaneously in order to compute the receiving mutual impedances.

For a perfectly known or modeled MCM, DOA estimation algorithms can be modified to incorporate the coupling and compensate for it in order to achieve accurate source directions [9]. However, if the modeled MCM is not exact, the performance of the DOA estimation is degraded. Moreover, the MCM must be re-calibrated periodically to account for any changes in local conditions. For instance, the presence of a new scatterer in the vicinity of the antenna array changes the mutual coupling. Several methods have been proposed to circumvent these issues. These methods assume the coupling matrix to be unknown or imprecisely known and aim to jointly estimate the MCM along with the source DOAs [7, 16-17]. Ref. [7] presents an iterative method to estimate the MCM, the DOAs, and the antenna gains, wherein the cost

function is minimized with respect to one unknown quantity at a time while keeping the remaining two unknowns fixed. A maximum likelihood estimator for DOA estimation under unknown multipath and unknown mutual coupling has been proposed in [16]. Ref. [17] employs sparse reconstruction to perform DOA estimation in the presence of unknown mutual coupling. However, all of these aforementioned methods have been developed for uniform linear arrays (ULAs) and take advantage of the special structure of the corresponding MCMs. Although these methods can be modified and applied to non-uniform arrays, they fail to take advantage of the increased degrees-of-freedom (DOFs) offered by non-uniform arrays for DOA estimation [18-22]. Recall that an N_A - element non-uniform array can provide $O(N_A^2)$ DOFs, thereby permitting DOA estimation of more sources than sensors. An iterative method for DOA estimation using non-uniform arrays in the presence of mutual coupling was proposed in [23]. This method treats the non-uniform array as a subset of a ULA and, therefore, cannot take full advantage of the increased DOFs.

In this paper, we investigate the mutual coupling effect in non-uniform arrays. First, we examine the impact of coupling on the DOA estimation accuracy for different array geometries, including minimum redundancy arrays (MRA) [18], nested arrays [20], and co-prime arrays [21, 22]. The performance is evaluated for different array sizes and for two antenna element types, namely, dipole antenna and microstrip antenna. The latter is becoming increasingly popular in radar and wireless communications due to its low profile, ease of fabrication, low cost, and compatibility with radio frequency (RF) circuit boards. A computational electromagnetics software package, FEKO [24], is used to model the antenna arrays, and the RMIM [12] is used to compute the coupling matrices based on the obtained measurements. We show that the MRA provides superior performance compared to the nested and co-prime geometries, irrespective of the antenna type. Second, we propose two compensation methods that allow accurate DOA estimation using non-uniform arrays in the presence of mutual coupling. The first method assumes partial knowledge of the mutual coupling and employs an iterative approach to update the perturbed MCM and DOAs. Sparse signal reconstruction is used to find the source directions for a given coupling matrix, and a global optimization algorithm called covariance matrix adaptation evolution strategy (CMA-ES) [25] is used to update the MCM while keeping the DOAs fixed. The second method assumes unknown coupling and simultaneously

estimates the MCM, the source powers, and sources directions by minimizing a cost function using CMA-ES. Finally, the effectiveness of the proposed methods is evaluated through numerical examples.

The remainder of this paper is organized as follows. High-resolution DOA estimation using non-uniform arrays is briefly reviewed in Section II. The signal model in the presence of mutual coupling is also presented in the same section. In Section III, DOA estimation performance of different non-uniform array geometries is evaluated and compared for the case of uncompensated mutual coupling. Section IV discusses the two proposed compensation methods that allow accurate DOA estimation under mutual coupling and provides supporting numerical results. Section V concludes the paper.

II. DOA ESTIMATION USING NON-UNIFORM ARRAYS

A general N_A – element linear array is considered. The elements positions are assumed to be integer multiples of the unit spacing, i.e., $x_i = n_i d_0$, $i = 1, \dots, N_A$, where x_i is the position of the i th array element, n_i is an integer, and d_0 is the unit spacing which is usually set to half-wavelength at the operating frequency. Assume that D narrowband sources with directions $\{\theta_1, \theta_2, \dots, \theta_D\}$ and powers $\{\sigma_1^2, \sigma_2^2, \dots, \sigma_D^2\}$ impinge on the array, where θ is measured relative to broadside. In the absence of mutual coupling, the received data vector at snapshot t can be expressed as

$$\mathbf{x}(t) = \mathbf{A}\mathbf{s}(t) + \mathbf{n}(t), \quad (1)$$

where $\mathbf{s}(t)$ is the $D \times 1$ source signal vector, $\mathbf{n}(t)$ is the $N_A \times 1$ noise vector, and \mathbf{A} is the $N_A \times D$ array manifold matrix whose (i, d) th element is given by

$$[\mathbf{A}]_{i,d} = \exp(jk_0 x_i \sin \theta_d). \quad (2)$$

Here, k_0 is the wavenumber at the operating frequency and θ_d is the DOA of the d th source. Under the assumptions of uncorrelated sources and spatially and temporally white noise, the covariance matrix can be expressed as

$$\mathbf{R}_{xx} = E\{\mathbf{x}(t)\mathbf{x}(t)^H\} = \mathbf{A}\mathbf{R}_{ss}\mathbf{A}^H + \sigma_n^2 \mathbf{I}, \quad (3)$$

where $E\{\cdot\}$ is the expectation operator, $(\cdot)^H$ denotes conjugate transpose, $\mathbf{R}_{ss} = \text{diag}\{\sigma_1^2, \sigma_2^2, \dots, \sigma_D^2\}$ is the source covariance matrix, σ_n^2 is the noise variance, and \mathbf{I} is an $N_A \times N_A$ identity matrix.

Two approaches can be used for DOA estimation. The first approach is based on covariance matrix augmentation [26-28], while the second uses spatial smoothing [21-22]. Since the augmented covariance matrix in the first approach may not always be positive semidefinite, we consider spatial smoothing based approach in this paper, which is briefly reviewed below.

Vectorizing the covariance matrix in (3), we obtain

$$\mathbf{z} = \text{vec}\{\mathbf{R}_{xx}\} = \tilde{\mathbf{A}}\mathbf{p} + \sigma_n^2\tilde{\mathbf{I}}, \quad (4)$$

where $\mathbf{p} = [\sigma_1^2, \sigma_2^2, \dots, \sigma_D^2]^T$ is the source powers vector, $\tilde{\mathbf{A}} = \mathbf{A}^* \odot \mathbf{A}$, the symbol ' \odot ' denotes the Khatri-Rao product, the superscript ' $*$ ' denotes complex conjugate, and $\tilde{\mathbf{I}} = \text{vec}\{\mathbf{I}\}$ is the vectorized identity matrix. The vector \mathbf{z} emulates measurements at a longer array whose elements positions are given by the difference coarray of the non-uniform arrays, while the $N_A^2 \times D$ matrix $\tilde{\mathbf{A}}$ is the corresponding manifold matrix [29]. Assuming that the difference coarray has contiguous elements between $-Ld_0$ and $+Ld_0$, the data measurements can be rearranged to form a new $(2L + 1) \times 1$ vector \mathbf{z}_f , which contains measurements at these positions,

$$\mathbf{z}_f = \tilde{\mathbf{A}}_f\mathbf{p} + \sigma_n^2\tilde{\mathbf{I}}_f. \quad (5)$$

Since the sources are replaced by their powers in (5) and the noise is deterministic, the sources now appear as coherent, and subspace-based high-resolution methods can no longer be applied directly to perform DOA estimation. Spatial smoothing is used to build the rank of the covariance matrix of \mathbf{z}_f [30]. The filled part of the difference coarray is divided into $(L + 1)$ overlapping subarrays, each having $(L + 1)$ contiguous elements. The positions of the elements of the m th subarray are given by the following set

$$\{(l + 1 - m)d_0, \quad l = 0, 1, \dots, L\}. \quad (6)$$

The received data vector at the m th subarray is denoted by \mathbf{z}_{f_m} , and the spatially smoothed covariance matrix is then computed as

$$\bar{\mathbf{R}}_{zz} = \frac{1}{L + 1} \sum_{m=1}^{L+1} \mathbf{z}_{f_m} \mathbf{z}_{f_m}^H. \quad (7)$$

DOA estimation techniques, such as MUSIC, can now be applied to $\bar{\mathbf{R}}_{zz}$ to estimate up to L sources.

Thus far, mutual coupling has been ignored in the signal model. However, in practical antenna arrays, coupling between the antenna elements is a real issue and thus needs to be taken into account. The signal model in (1) can be modified to incorporate mutual coupling as

$$\mathbf{x}(t) = \mathbf{C}\mathbf{A}\mathbf{s}(t) + \mathbf{n}(t), \quad (8)$$

where \mathbf{C} is the $N_A \times N_A$ mutual coupling matrix. Note that the coupling-free model, discussed in (1), is a particular case of (8) corresponding to \mathbf{C} being an identity matrix. The covariance matrix of the measurements in (8) is given by

$$\mathbf{R}_{xx} = E\{\mathbf{x}(t)\mathbf{x}^H(t)\} = \mathbf{C}\mathbf{A}\mathbf{R}_{ss}\mathbf{A}^H\mathbf{C}^H + \sigma_n^2\mathbf{I}. \quad (9)$$

Proceeding with the vectorization and spatial smoothing, followed by DOA estimation without compensating for the MCM, is likely to degrade performance, owing to the mismatch between the assumed model (1) and the actual measurements (8). The severity of performance degradation, however, is a function of the array configuration and the choice of antennas, as shown in the following section.

III. MUTUAL COUPLING IMPACT ON DOA ESTIMATION

We quantify the performance degradations due to mutual coupling effect in terms of DOA estimation accuracy for three different non-uniform linear array configurations, namely, the minimum redundancy, nested, and co-prime geometries. Both MRAs and nested arrays have filled difference coarrays, whereas the difference coarray of a co-prime configuration contains a set of the consecutive lags. As such, spatial smoothing based approach can be applied to all three considered configurations for DOA estimation. For comparison, we also provide the performance of a uniform linear array in the presence of mutual coupling.

III.A. Considered Array Geometries

III.A.1. Uniform Linear Arrays (ULA)

A uniform linear array is an array whose elements lie along a straight line at equal intervals. An N_A – element ULA has elements with positions $[0, 1, \dots, N_A - 1]d_0$.

III.A.2. Minimum Redundancy Arrays (MRA)

An MRA maximizes the number of contiguous elements in the difference coarray for a given number N_A of antenna elements [18]. The corresponding difference coarray contains the lowest possible redundancy without any missing lags or ‘holes’.

III.A.3. Nested Arrays

An N_A – element nested array consists of a combination of two ULAs, where the inter-element spacing of the first ULA with N_1 elements is equal to the unit spacing d_0 while the $N_2 = N_A - N_1$ elements of the second ULA are separated by an integer multiple of d_0 [20]. That is, the first element of the second ULA is placed at $(N_1 + 1)d_0$ and the inter-element spacing is also set to $(N_1 + 1)d_0$. The corresponding difference coarray is filled and contains no holes.

III.A.4. Co-prime Arrays

A co-prime array comprises two spatially under-sampled ULAs with co-prime spatial sampling rates [21, 22]. In the basic co-prime configuration, the first array consists of M elements with inter-element spacing Nd_0 and the second array contains N elements with spacing Md_0 , with M and N being co-prime integers [21]. The elements of the two subarrays are arranged along a single line with the first elements coinciding, resulting in a co-prime array with $N_A = M + N - 1$ non-uniformly spaced physical elements. The corresponding difference coarray has holes, but is filled between $-(M + N - 1)d_0$ and $(M + N - 1)d_0$.

III.B. Mutual Coupling Matrix Modeling and Measurement

The mutual coupling matrix for each considered non-uniform array configuration is modeled using the receiving-mutual-impedance method (RMIM) [11]. Two conditions must be satisfied in order to render the application of this method feasible [11-12]. First, the array should be in the receiving mode. Second, the antenna elements should be terminated with a known load impedance Z_L . Assuming these conditions have been fulfilled, the received voltage across the terminal load of a particular antenna can be expressed as a superposition of two external excitations

$$v_i = Z_L i_i = w_i + \tilde{v}_i, i = 1, 2, \dots, N_A \quad (10)$$

where v_i is the terminal load voltage of the i th antenna, i_i is the current induced in the i th antenna, w_i is the voltage due to the external sources, and \tilde{v}_i is the voltage due to the mutual coupling from the other elements in the array. The coupled voltage \tilde{v}_i is given by

$$\tilde{v}_i = Z_{i,1}i_1 + Z_{i,2}i_2 + \dots + Z_{i,i-1}i_{i-1} + Z_{i,i+1}i_{i+1} + \dots + Z_{i,N_A}i_{N_A}, \quad (11)$$

where $Z_{i,j}$ is the receiving mutual impedance between the i th and j th elements. Substituting (10) in (11) and rearranging, the uncoupled voltages w_i , $i = 1, 2, \dots, N_A$ can be stacked in a vector \mathbf{w} as

$$\mathbf{w} = \mathbf{Z}\mathbf{v} = \begin{bmatrix} 1 & -Z_{1,2}/Z_L & \dots & -Z_{1,N_A}/Z_L \\ -Z_{2,1}/Z_L & 1 & \dots & -Z_{2,N_A}/Z_L \\ \vdots & \vdots & \ddots & \vdots \\ -Z_{N_A,1}/Z_L & -Z_{N_A,2}/Z_L & \dots & 1 \end{bmatrix} \begin{bmatrix} v_1 \\ v_2 \\ \vdots \\ v_{N_A} \end{bmatrix}, \quad (12)$$

where \mathbf{Z} is the mutual impedance matrix.

In order to determine the elements of \mathbf{Z} , K plane waves with different DOAs $\{\theta_1, \dots, \theta_K\}$ are individually used to excite the array, and the corresponding received voltages, $v_m^{(k)}$, $m = 1, \dots, N_A$, $k = 1, \dots, K$, are recorded. Note that $v_m^{(k)}$ denotes the received voltage at the m th array element when the k th plane wave is impinging on the array. The same set of plane waves is also used to excite each array element in isolation in order to measure the uncoupled voltages $w_m^{(k)}$. Given $v_m^{(k)}$ and $w_m^{(k)}$ for all k , the following system of linear equations is solved for each antenna element in order to compute the corresponding mutual impedance values.

$$\begin{bmatrix} v_m^{(1)} - w_m^{(1)} \\ v_m^{(2)} - w_m^{(2)} \\ \vdots \\ v_m^{(K)} - w_m^{(K)} \end{bmatrix} = \begin{bmatrix} v_1^{(1)} & \dots & v_{m-1}^{(1)} & v_{m+1}^{(1)} & \dots & v_{N_A}^{(1)} \\ v_1^{(2)} & \dots & v_{m-1}^{(2)} & v_{m+1}^{(2)} & \dots & v_{N_A}^{(2)} \\ \vdots & \ddots & \vdots & \vdots & \ddots & \vdots \\ v_1^{(K)} & \dots & v_{m-1}^{(K)} & v_{m+1}^{(K)} & \dots & v_{N_A}^{(K)} \end{bmatrix} \begin{bmatrix} Z_{m,1} \\ \vdots \\ Z_{m,m-1} \\ Z_{m,m+1} \\ \vdots \\ Z_{m,N_A} \end{bmatrix}. \quad (13)$$

In order to compute the mutual impedance between each element and the remaining elements in the array, the number of planes waves K should be greater than or equal to $(N_A - 1)$ [12]. Once the matrix \mathbf{Z} has been determined, the MCM is computed as $\mathbf{C} = \mathbf{Z}^{-1}$, where $(\cdot)^{-1}$ denotes matrix inverse.

III.C. Performance Comparisons

In this section, the effect of mutual coupling on the DOA estimation performance is investigated for the array configurations described in Section III.A. We consider two different antenna types, namely, a dipole antenna and a rectangular microstrip or the so-called patch antenna, as array elements. Each antenna is designed for operation at 3 GHz. The dipoles are chosen as half-wavelength at 3 GHz. Each rectangular patch element has dimensions $L_p = 31.18$ mm and $W_p = 46.64$ mm, where L_p and W_p correspond to the resonant length and radiating edge of the patch, respectively. The patch antenna is printed on a 2.87 mm lossless FR4 substrate with dielectric constant of 2.2, as shown in Fig. 1(a). The ground plane is assumed to be infinite. The patch antenna is modeled using FEKO and the corresponding gain pattern is shown in Fig. 1(b). This antenna is directive with a maximum gain at $\theta = 0^\circ$ and nulls at $\pm 90^\circ$. We assume that the patch elements in the array are positioned with their resonant edges facing each other, as shown in Fig. 1(c) which depicts a six-element uniform linear patch array with an inter-element spacing of half-wavelength at 3 GHz.

For each array geometry, we vary the number of elements, N_A , from four to ten with a step size of two. The element positions of the corresponding MRA configurations are provided in Table I, while those for nested and co-prime geometries are presented in Tables II and III, respectively. Note that, in the case of MRAs, more than one array structure is available for $N_A > 4$. We choose the configuration which has the least number of element pairs separated by half-wavelength. For co-prime arrays, we consider, for each N_A , the configuration with $M = N_A/2, N = M + 1$. This choice was shown to have operational advantages in [31] and [32]. Further, for nested arrays, we employ the configurations with $N_1 = N_2 = N_A/2$; this choice maximizes the DOFs for a given number of antennas [20]. FEKO is used to model the various microstrip and dipole array configurations and measure the required voltages for the RMIM. The corresponding mutual impedance and mutual coupling matrices are then computed for the different array geometries with varying number of elements. In the RMIM, the number of plane waves K is set to 16 for all array configurations. The directions of the plane waves are uniformly distributed between -74° and 76° .

For each combination of array configuration, antenna type, and total number of elements, we perform 1,000 Monte Carlo runs with two sources at a fixed separation in the reduced angular coordinate, $u = \sin \theta$. That is, for each run, the first source direction u_1 is randomly chosen to lie between -0.95 and 0.95 and the second source direction u_2 is selected so that $\Delta u = |u_1 - u_2|$ is kept constant. Two source separations, $\Delta u = 0.1$ and $\Delta u = 0.2$, are considered. The model in (8) is used to generate the array measurements, with the signal-to-noise ratio (SNR) set to 0 dB. The total number of snapshots per run is chosen as 10,000. This high number is selected to remove the influence of i) varying coarray redundancy of different array configurations, and ii) small sample size for correlation matrix estimation as a sample average. Spatial smoothing method is applied in conjunction with MUSIC to estimate the DOAs without compensating for the MCM. Note that in case of co-prime configurations, the DOA estimation only exploits the contiguous part of the coarray. The estimation accuracy is evaluated in terms of the average root-mean-square error (RMSE), which is given by

$$\overline{RMSE} = \frac{1}{D} \sum_{d=1}^D \sqrt{\frac{1}{N_{MC}} \sum_{n=1}^{N_{MC}} (\hat{u}_{d,n} - u_d)^2}, \quad (14)$$

where N_{MC} is the total number of Monte Carlo runs and $\hat{u}_{d,n}$ is the estimate of the d th source at the n th run.

III.C.1. Dipole Arrays

Fig. 2(a) depicts the average RMSE as a function of the number of elements for all considered geometries when $\Delta u = 0.1$, while the RMSE for $\Delta u = 0.2$ is plotted in Fig. 2(c). For reference, the corresponding RMSE plots in the coupling-free scenario are shown in Fig. 2(b) and Fig. 2(d), respectively. Comparing Fig. 2(a) to Fig. 2(b) and Fig. 2(c) to Fig. 2(d), we observe that the results for the coupling-free scenario exhibit much smaller RMSE values than those in the presence of mutual coupling. This confirms the detrimental effect of mutual coupling on the DOA estimation performance. By examining Fig. 2(a) and Fig. 2(c), several additional observations can be made. First, the estimation error decreases as the array size

increases for all configurations. Since mutual coupling depends on the distance between the array elements, larger arrays provide a much sparser MCM as compared to smaller arrays, thereby reducing the overall effect on performance. Second, irrespective of the number of elements, the ULA provides the worst performance while the MRA achieves the best performance for both source separations. This is expected because i) the ULA has the highest number of element pairs that are half-wavelength apart, ii) all considered MRAs have a reduced number of antenna pairs separated by half-wavelength, and iii) the MRAs provide both the largest array size for a given number of antennas and largest filled coarray aperture, leading to better resolution capability. Finally, for $\Delta u = 0.2$, the co-prime array provides better performance than the nested array for $N_A = 6, 8$, and 10 , as seen in Fig. 2(c). This is expected since the nested array has a greater number of element pairs separated by half-wavelength. For $N_A = 4$, however, the nested array outperforms the co-prime array. This can be explained by examining the two corresponding array structures in Tables II and III. We note that both arrays have three contiguous elements at half-wavelength spacing, while the fourth element is closer to its nearest neighbor in the co-prime array as compared to the nested array. In the case of $\Delta u = 0.1$, the roles are reversed for $N_A = 6$ and 8 , where the nested array outperforms the co-prime array. This is primarily due to the difference in the corresponding resolution capabilities. As mentioned earlier, since the difference coarray corresponding to a co-prime array has holes, a reduced coarray aperture is employed for spatial smoothing based DOA estimation. Even though the coupling effect is larger in nested arrays, its effect on the DOA estimation performance is outweighed by the resolution capability when the sources are closely separated.

III.C.2. Microstrip Arrays

The Monte Carlo experiments that were performed for dipole arrays are repeated for the microstrip arrays. Fig. 3 shows the obtained average RMSE plots for the different array configurations and different source separations both in the presence and absence of mutual coupling. By comparing the corresponding plots in Fig. 2 and Fig. 3, we observe an increase in the average RMSE when using microstrip arrays. This can be attributed to the proximity of the edges of the consecutive elements. Further, similar to the case of dipole

arrays, the microstrip MRA provides the smallest estimation error, while the microstrip ULA has the largest error for both source separations. In addition, the estimation error decreases with increasing number of array elements for all configurations. However, unlike the case of dipole arrays, nested arrays outperform the co-prime arrays for both source separations when microstrip antennas are employed. This performance difference between the co-prime and nested arrays for the two antenna types is due to the fact that mutual coupling in microstrip arrays comprises not only the edge coupling but also the coupling due to the presence of surface waves in the substrate. Since the aperture of co-prime arrays is smaller for the same number of antennas, the surface wave coupling influences the performance of co-prime arrays more than that of nested arrays.

To summarize, mutual coupling affects the DOA estimation performance. The degree of performance degradation depends on the array configuration, the number of elements and their types, the source directions, and the source separations.

IV. MUTUAL COUPLING COMPENSATION

The MCM modeling provides a characterization of the mutual coupling, which can be utilized to account for the coupling in DOA estimation methods. However, in practice, the model can suffer from inaccuracies and, as such, requires frequent re-calibration in order to account for any changes in local conditions. Maintaining an exact MCM model can be cumbersome, if not impossible, in many practical applications. In this section, we propose two compensation methods for accurate DOA estimation under unknown or imperfectly known MCMs. The first method treats the modeling imperfections as perturbations in the MCM and employs an iterative approach to estimate the source directions and the perturbed MCM. The second method performs joint estimation of the MCM and the source directions simultaneously.

IV.A. Iterative Approach

We model imperfections in the coupling matrix as arising from perturbations in the mutual impedance matrix, i.e., $\mathbf{Z}_{actual} = \mathbf{Z}_{model} + \Delta\mathbf{Z}$, where \mathbf{Z}_{actual} is the actual mutual impedance matrix, \mathbf{Z}_{model} is the initial modeled mutual impedance matrix, and $\Delta\mathbf{Z}$ is the perturbation matrix. We assume that the sources

are sparse in angle, which is true in general for direction finding applications. The angular region of interest is discretized into a finite set of Q grid points, where $Q \gg D$. Substituting $(\mathbf{Z}_{model} + \Delta\mathbf{Z})^{-1}$ for \mathbf{C} in (9) and vectorizing \mathbf{R}_{xx} yields

$$\begin{aligned} \text{vec}\{\mathbf{R}_{xx}\} &= \text{vec}\{\mathbf{C}\mathbf{A}\mathbf{R}_{ss}\mathbf{A}^H\mathbf{C}^H + \sigma_n^2\mathbf{I}\} \\ &= \{[(\mathbf{Z}_{model} + \Delta\mathbf{Z})^{-1}\mathbf{A}]^* \otimes [(\mathbf{Z}_{model} + \Delta\mathbf{Z})^{-1}\mathbf{A}]\}\text{vec}\{\mathbf{R}_{ss}\} + \sigma_n^2\mathbf{\tilde{I}}, \end{aligned} \quad (15)$$

where ‘ \otimes ’ denotes the Kronecker product. In order to solve for the unknowns, namely the perturbations $\Delta\mathbf{Z}$, source directions and powers, and noise variance, a nested optimization problem can be posed as

$$\begin{aligned} \min_{\Delta\mathbf{Z}} \min_{\text{diag}(\bar{\mathbf{R}}_{ss}), \sigma_n^2} & \|\text{vec}\{\hat{\mathbf{R}}_{xx}\} - \{[(\mathbf{Z}_{model} + \Delta\mathbf{Z})^{-1}\bar{\mathbf{A}}]^* \otimes [(\mathbf{Z}_{model} + \Delta\mathbf{Z})^{-1}\bar{\mathbf{A}}]\}\text{vec}\{\bar{\mathbf{R}}_{ss}\} \\ & - \sigma_n^2\mathbf{\tilde{I}}\|_2 + \lambda\|\text{diag}(\bar{\mathbf{R}}_{ss})\|_1 \end{aligned} \quad (16)$$

where $\hat{\mathbf{R}}_{xx}$ is the covariance matrix obtained as a sample average, $\bar{\mathbf{A}}$ is the $N_A \times Q$ array manifold matrix corresponding to the grid of potential directions, $\bar{\mathbf{R}}_{ss}$ is the covariance matrix of the potential sources, and λ is a Lagrange-type regularization parameter. The elements on the main diagonal of $\bar{\mathbf{R}}_{ss}$ are the powers of the potential sources. The D nonzero diagonal elements correspond to the powers of the actual sources.

The inner optimization in (16) over $\text{diag}(\bar{\mathbf{R}}_{ss})$ and σ_n^2 is convex and can be solved using sparse reconstruction techniques with the constraint that the unknowns are nonnegative. The ℓ_2 – norm term in (16) is the least squares cost function that maintains data fidelity, while the ℓ_1 – norm term encourages sparsity in the reconstructed power spectrum. The weight of the sparsity constraint in the overall cost function is controlled by λ . The choice of λ is tied to the source sparsity and the noise variance. Several methods have been proposed to estimate λ including cross-validation [33] and the discrepancy principle [6]. It is noted that the source directions are assumed to be located on the grid. However, several methods can be used to modify the model in order to deal with off-grid sources [6, 34]. The outer minimization over $\Delta\mathbf{Z}$ in (16) is non-convex and can be solved by general nonlinear optimization methods. The nested optimization in (16) is solved iteratively until the maximum number of iterations is reached or until the cost function stagnates.

In this paper, we solve the outer optimization problem in (16) using CMA-ES [25], which is a nature-

based global optimization algorithm. Nature-based optimization algorithms try to emulate natural phenomena, such as swarm intelligence and the Darwinian model of natural evolution, in order to find optimal solutions. These algorithms can deal with highly nonlinear cost functions, which require simultaneous optimization of a large number of parameters. Nature-based optimization algorithms include many categories, such as Genetic Algorithms [35], Particle Swarm Optimization [36], Evolutionary Programming [37], and Evolution Strategies [38]. CMA-ES has been shown to outperform other evolutionary algorithms in many complex electromagnetic problems [39].

CMA-ES is a self-adaptive evolution strategy which requires no parameter tuning. Fig. 4 shows the block diagram of the main operation of CMA-ES. The algorithm starts by initializing the parameters to their default values. It then samples a new generation of potential solutions from a multivariate Gaussian distribution using

$$\mathbf{y}_i^{(g+1)} \sim N\left(\mathbf{m}^{(g)}, \left(\sigma_c^{(g)}\right)^2 \mathbf{C}_c^{(g)}\right), \quad (17)$$

where $\mathbf{y}_i^{(g+1)}$ consists of the parameters of the i th potential solution at the $(g + 1)$ th generation, $\mathbf{m}^{(g)}$ is the mean parameter vector of the best performing members of the previous generation, $\sigma_c^{(g)}$ is the step size, and $\mathbf{C}_c^{(g)}$ is the covariance matrix of the parameters. The parameters of the multivariate Gaussian distribution are then updated sequentially using the best performing members of the generation [25]. The performance of the members is measured by their fitness value or score on the outer optimization in (16). This process is then repeated until a termination criterion is met. This criterion can be, for instance, a target fitness value or a maximum number of generations.

IV.B. Simultaneous Approach

In this approach, the sources directions and the MCM are simultaneously estimated rather than in an iterative fashion [40]. Starting with the covariance matrix in (9), the joint DOA and MCM estimation is achieved by solving

$$\min_{\boldsymbol{\theta}, \text{diag}(\mathbf{R}_{ss}), \mathbf{z}, \sigma_n^2} \|\hat{\mathbf{R}}_{xx} - \mathbf{C} \mathbf{A} \mathbf{R}_{ss} \mathbf{A}^H \mathbf{C}^H - \sigma_n^2 \mathbf{I}\|_F^2, \quad (18)$$

where $\|\cdot\|_F$ is the Frobenius norm, $\boldsymbol{\theta} = [\theta_1, \theta_2, \dots, \theta_D]^T$ contains the source DOAs, $\text{diag}(\mathbf{R}_{ss})$ consists of the source powers, and \mathbf{z} holds the unique elements in \mathbf{C}^{-1} . The total number of unknowns is $(2D + 1 + 2|\mathbf{z}|)$, where $|\mathbf{z}|$ is the number of unique elements in the mutual impedance matrix. The multiplier 2 in front of $|\mathbf{z}|$ is due to the entries of \mathbf{z} being complex valued. A mixed-parameter variation of CMA-ES is used to solve (18), since the sources DOAs are picked from a predetermined grid while the remaining unknowns are assumed to be continuous parameters [39, 41].

It should be noted that the perturbed mutual impedance matrix model can be employed in (18), with the minimization carried out with respect to $\boldsymbol{\theta}$, $\text{diag}(\mathbf{R}_{ss})$, σ_n^2 , and $\Delta \mathbf{Z}$.

IV.C. Supporting Results

In the first example, a dipole array with a six-element nested configuration is considered. The elements positions are given by $[1, 2, 3, 4, 8, 12]d_0$. The corresponding difference coarray extends from $-11d_0$ to $11d_0$ and is filled with no holes. The length of the dipoles is set to half-wavelength. The corresponding MCM is modeled using the RMIM and the signal model in (8) is used to generate the array measurements. The coupling matrix is then assumed to be unknown and is jointly estimated along with the DOAs using the simultaneous method. A total of 11 sources are considered. The sources are uniformly spaced between -0.85 and 0.8 in the reduced angular coordinate $u = \sin \theta$. Spatially and temporally white Gaussian noise is added to the observations, and the SNR is set to 10 dB. The total number of snapshots is fixed to 1,000. Mixed-parameter CMA-ES is used to minimize the cost function in (18), where the DOAs are assumed to fall on a grid with 1° step size and the remaining parameters are assumed to be continuous. The search space for the unknown mutual impedance matrix is restricted to be within 10% of the actual values. For the CMA-ES algorithm, the population size and the number of generations are each set to 1,000. Fig. 5 shows the estimated spectrum, with the vertical dashed lines indicating the true source locations. Clearly, the

proposed method is successfully able to compensate for the mutual coupling and estimate the correct source directions.

Next, we consider $D = 5$ sources with directions $[-58^\circ, -26^\circ, -1^\circ, 23^\circ, 53^\circ]$. The same six-element nested array configuration from the first example is employed to estimate the DOAs under varying number of snapshots and SNR values. Figs. 6(a) shows the success rate as a function of the number of snapshots with the SNR of all sources fixed at 10 dB. For each snapshot value, a total of 100 Monte Carlo runs are used. A solution is deemed successful if each DOA estimate is within 2° of the true DOA. Fig. 6(b) shows the average RMSE values corresponding to the successful solutions. Figs. 6(c) and 6(d) depict the success rate and the average RMSE as a function of SNR, respectively, with the number of snapshots fixed at 1,000. Again, 100 Monte Carlo runs are employed for each SNR value. From Fig. 6, it is evident that the performance of the proposed method improves with an increasing number of snapshots and increasing SNR. In addition, compared to the SNR, the number of snapshots has a larger effect on the performance. This is expected since the proposed method relies on a good estimate of the covariance matrix using the sample average. It should be noted that the performance can be further improved by increasing the population size and the number of generations of the CMA-ES algorithm.

In the third example, the iterative method is used to estimate the actual MCM along with the DOAs. A six-element microstrip array with an MRA configuration is used. The elements positions are given by $[0, 1, 6, 9, 11, 13]d_0$, and each microstrip element is similar to the one modeled in Section III.C. The MCM is modeled using the RMIM and the data measurements are generated using the model in (8). The MCM is then perturbed to emulate the effect of changes in local conditions. The perturbations are drawn from uniform distributions that assume values between -25% and 25% of the actual values. Eight sources, uniformly spaced between $u = -0.7$ and $u = 0.6$, are considered. The SNR of all sources is set to 10 dB and the number of snapshots is equal to 1,000. Fig. 7(a) shows the estimated spectrum using MUSIC with spatial smoothing without accounting for mutual coupling. Clearly, the estimation performance is severely degraded since the mutual coupling is not accounted for. Fig. 7(b) depicts the initial estimated spectrum, while Figs. 7(c) and 7(d) show the estimated spectra after the first and tenth iterations, respectively. The

initial estimated spectrum of Fig. 7(b) is based on solving the inner optimization problem in (16) with the perturbations set to zero. We observe that the initial spectrum completely misses one source, provides biased estimates for some sources, and exhibits spurious peaks. The estimated spectrum after the first iteration in Fig. 7(c) finds all the sources, but exhibits some spurious peaks. The performance of the method improves with increasing number of iterations, and after ten iterations, all the sources are correctly estimated, as shown in Fig. 7(d).

In order to validate the convergence of the proposed method, we perform 100 Monte Carlo runs with the aforementioned six-element microstrip MRA. The same source directions and powers as in the third example are considered. In each run, a new perturbation of the MCM is generated and the minimization is performed over 20 iterations. Fig. 8 shows the success rate as a function of the iteration number. We note that the success rate improves with an increasing number of iterations and reaches 100% after 20 iterations. It is to be noted that a faster convergence can be reached for smaller perturbations of the MCM.

In the final example, a six-element extended co-prime dipole array with $M = 2$ and $N = 3$ is considered. Note that an extended co-prime configuration comprises of two interleaved ULAs, one with $2M$ elements and the other with N elements, with the first element shared between them. The first subarray has elements at $[0, 3, 6, 9]d_0$ and the second one has elements at $[0, 2, 4]d_0$. The corresponding difference coarray is filled between $-7d_0$ and $7d_0$. The simultaneous compensation method is used to jointly estimate the MCM and the DOAs. A total of seven uniformly spaced sources between $u = -0.8$ and $u = 0.8$ are considered. The SNR is fixed to 10 dB for all sources and the number of snapshots is set to 1,000 for each run. Mixed-parameter CMA-ES with 1,000 population size and 1,000 generations is used to minimize the cost function. 100 Monte Carlo runs are performed to assess the ability of the proposed method to provide a unique solution. Fig. 9 shows the estimated spectrum of one of the successful runs. The DOA estimates of all 100 runs are superimposed in Fig. 10(a). It is evident that some of the runs result in wrong or biased estimates. The success rate as a function of the maximum bias of all estimates is plotted in Fig. 10(b). For instance, 76 percent of the runs result in a solution that has each estimated DOA within 2° of the actual

value. The success rate can be improved by increasing the number of generations used in CMA-ES. This is validated by increasing the number of generations to 5,000 and introducing restarts after each 1,000 generations. Fig. 11 shows the corresponding results. We observe that runs in excess of 60 percent result in unbiased estimates, while all 100 runs produce solutions having each source estimate within 2° of the actual value.

V. CONCLUSION

The impact of mutual coupling on DOA estimation performance using non-uniform arrays was investigated in this paper. Direction finding accuracy was compared for three different non-uniform array configurations and two antenna element types. The MRA configuration was shown to provide superior estimation performance compared to nested and co-prime array configurations. Further, choice of dipole antennas as array elements fared better in terms of RMSE over microstrip antennas; the latter suffer from additional coupling arising from surface waves in the substrate. Additionally, two mutual coupling compensation methods were proposed for non-uniform arrays. The first method is iterative in nature and assumes imprecisely known MCM. The second method simultaneously estimates the coupling matrix and the DOAs and is better suited to scenarios where no prior knowledge of the MCM is available. Numerical examples were used to demonstrate the effectiveness of the proposed compensation methods.

REFERENCES

- [1] S. Chandran, *Advances in Direction-of-Arrival Estimation*, Norwood, MA: Artech House, 2006.
- [2] H.L. Van Trees, *Optimum Array Processing: Part IV of Detection, Estimation and Modulation Theory*, New York, NY: Wiley, 2002.
- [3] T.E. Tuncer and B. Friedlander, *Classical and Modern Direction-of-Arrival Estimation*, Boston, MA: Academic Press (Elsevier), 2009.
- [4] R. Schmidt, "Multiple emitter location and signal parameter estimation," *IEEE Trans. Antennas Propag.*, vol. 34, no. 3, pp. 276–280, 1986.
- [5] R. Roy and T. Kailath, "ESPRIT-Estimation of signal parameters via rotational invariance techniques," *IEEE Trans. Acoust., Speech, Signal Processing*, vol. 37, no. 7, pp. 984–995, 1989.
- [6] D. Malioutov, M. Cetin, and A. Willsky, "Sparse signal reconstruction perspective for source localization with sensor arrays," *IEEE Trans. Signal Process.*, vol. 53, no. 8, pp. 3010–3022, 2005.
- [7] B. Friedlander and A.J. Weiss, "Direction finding in the presence of mutual coupling," *IEEE Trans. Antennas Propag.*, vol. 39, no. 3, pp. 273–284, 1991.
- [8] I.J. Gupta and A.A. Ksienski, "Effect of mutual coupling on the performance of adaptive arrays," *IEEE Trans. Antennas Propag.*, vol. 31, no. 5, pp. 785–791, 1983.
- [9] C.-C. Yeh, M.-L. Leou, and D.R. Ucci, "Bearing estimations with mutual coupling present," *IEEE Trans. Antennas Propag.*, vol. 37, no. 10, pp. 1332–1335, 1989.
- [10] H. Yamada, Y. Ogawa, and Y. Yamaguchi, "Mutual impedance of receiving array and calibration matrix for high-resolution DOA estimation," in *Proc. IEEE/ACES International Conference on Wireless Communications and Applied Computational Electromagnetics*, Honolulu, HI, 2005, pp. 361–364.
- [11] H.T. Hui, "Improved compensation for the mutual coupling effect in a dipole array for direction finding," *IEEE Trans. Antennas Propag.*, vol. 51, no. 9, pp. 2498–2503, 2003.
- [12] H.S. Lui and H.T. Hui, "Effective mutual coupling compensation for direction-of-arrival estimation using a new, accurate determination method for the receiving mutual impedance," *J. of Electromagn. Waves and Appl.*, vol. 24, pp. 271–281, 2010.
- [13] R.S. Adve and T.K. Sarkar, "Compensation for the effects of mutual coupling on direct data domain adaptive algorithms," *IEEE Trans. Antennas Propag.*, vol. 48, no. 1, pp. 86–94, Jan. 2000.
- [14] H. Singh, H.L. Sneha, and R.M. Jha, "Mutual coupling in phased arrays: A review," *International J. Antennas Propag.*, vol. 2013, Article ID 348123, 2013.
- [15] C. A. Balanis, *Antenna Theory: Analysis and Design, 3rd Ed*, New York: John Wiley and Sons, 2005.
- [16] Q. Bao, C.C. Ko, and W. Zhi, "DOA estimation under unknown mutual coupling and multipath", *IEEE Trans. Aerosp. Electron. Syst.*, vol. 41, no. 2, pp. 565–573, 2005.
- [17] J. Dai, D. Zhao, and X. Ji, "A sparse representation method for DOA estimation with unknown mutual coupling," *IEEE Antennas Wireless Propag. Lett.*, vol. 11, pp. 1210–1213, 2012.
- [18] A. Moffet, "Minimum-redundancy linear arrays," *IEEE Trans. Antennas Propag.*, vol. AP-16, no. 2, pp. 172–175, Mar. 1968.

- [19] G.S. Bloom and S.W. Golomb, "Application of numbered undirected graphs," *Proc. IEEE*, vol. 65, no. 4, pp. 562–570, Apr. 1977.
- [20] P. Pal and P.P. Vaidyanathan, "Nested arrays: a novel approach to array processing with enhanced degrees of freedom," *IEEE Trans. Signal Process.*, vol. 58, no. 8, pp. 4167–4181, Aug. 2010.
- [21] P. P. Vaidyanathan and P. Pal, "Sparse sensing with co-prime samplers and arrays," *IEEE Trans. Signal Process.*, vol. 59, no. 2, pp. 573–586, 2011.
- [22] P. Pal and P. P. Vaidyanathan, "Coprime sampling and the music algorithm," in *Proc. IEEE Digital Signal Processing Workshop and IEEE Signal Processing Education Workshop*, Sedona, AZ, 2011, pp. 289–294.
- [23] J. Dai, D. Zhao, and Z. Ye, "DOA estimation and self-calibration algorithm for nonuniform linear array," in *Proc. International Symposium on Intelligent Signal Processing and Communications Systems*, Chengdu, China, 2010.
- [24] FEKO Suite 6.3, EM Software & Systems – S.A. (Pty) Ltd.
- [25] N. Hansen and A. Ostermeier, "Completely derandomized self-adaptation in evolutionary strategies," *Evolutionary Computation*, vol. 9, no. 2, pp. 159–195, 2001.
- [26] S.U. Pillai, Y. Bar-Ness, and F. Haber, "A new approach to array geometry for improved spatial spectrum estimation," *Proc. IEEE*, vol. 73, pp. 1522–1524, Oct. 1985.
- [27] Y.I. Abramovich, D.A. Gray, A. Y. Gorokhov, and N. K. Spencer, "Positive-definite Toeplitz completion in DOA estimation for nonuniform linear antenna arrays. I. Fully augmentable arrays," *IEEE Trans. Signal Process.*, vol. 46, pp. 2458–2471, Sep. 1998.
- [28] Y.I. Abramovich, N.K. Spencer, and A. Y. Gorokhov, "Positive-definite Toeplitz completion in DOA estimation for nonuniform linear antenna arrays. II. Partially augmentable arrays," *IEEE Trans. Signal Process.*, vol. 47, pp. 1502–1521, Jun. 1999.
- [29] R.T. Hoorntje and S.A. Kassam, "The unifying role of the coarray in aperture synthesis for coherent and incoherent imaging," *Proc. IEEE*, vol. 78, no. 4, pp. 735–752, Apr. 1990.
- [30] T.J. Shan, M. Wax, and T. Kailath, "On spatial smoothing for direction-of-arrival estimation of coherent signals," *IEEE Trans. Acoust., Speech, Signal Process.*, vol. 33, no. 4, pp. 806–811, 1985.
- [31] K. Adhikari, J.R. Buck, and K.E. Wage, "Beamforming with extended co-prime sensor arrays," in *Proc. IEEE International Conference on Acoustics, Speech, and Signal Processing*, Vancouver, BC, May 2013, pp. 4183–4186.
- [32] E. BouDaher, Y. Jia, F. Ahmad, and M. G. Amin, "Multi-frequency co-prime arrays for high-resolution direction-of-arrival estimation," *IEEE Trans. Signal Process.*, vol. 63, no. 14, pp. 3797–3808, Jul. 2015.
- [33] R. Tibshirani, "Regression shrinkage and selection via Lasso," *J. R. Stat. Soc. Ser. B Methodol.*, vol. 58, no. 1, pp. 267–288, 1996.
- [34] Z. Tan and A. Nehorai, "Sparse direction of arrival estimation using co-prime arrays with off-grid targets," *IEEE Signal Process. Lett.*, vol. 21, no. 1, pp. 26–29, Jan. 2014.
- [35] D.E. Goldberg, *Genetic Algorithms in Search, Optimization and Machine Learning*, Reading, MA: Addison-Wesley, 1989.
- [36] J. Kennedy and R. Eberhart, "Particle swarm optimization," in *Proc. IEEE International Conference on Neural Networks*, Perth, WA, 1995, pp. 1942–1948.

- [37] G.B. Fogel and D.B. Fogel, "Continuous evolutionary programming: Analysis and experiments," *Cybern. Syst.*, vol. 26, pp. 79-90, 1995.
- [38] H.P. Schwefel, *Evolution and Optimum Seeking, Sixth Generation Computer Technology Series*, New York: Wiley, 1995.
- [39] E. BouDaher and A. Hoorfar, "Electromagnetic optimization using mixed-parameter and multiobjective covariance matrix adaptation evolution strategy," *IEEE Trans. Antennas Propag.*, vol. 63, no. 4, pp. 1712–1724, Apr. 2015.
- [40] E. BouDaher, F. Ahmad, M. Amin, and A. Hoorfar, "DOA estimation with co-prime arrays in the presence of mutual coupling," in *Proc. 23rd European Signal Processing Conference*, 2015, pp. 2830–2834.
- [41] N. Hansen, "A CMA-ES for mixed integer nonlinear optimization," *Institut National de Recherche en Informatique et en Automatique*, no. 7751, 2011.

TABLE I
MINIMUM REDUNDANCY ARRAY CONFIGURATIONS

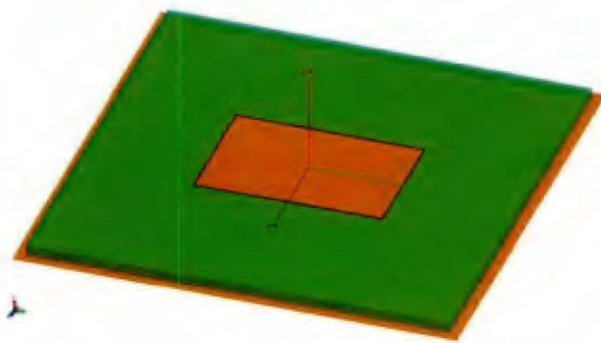
N_A	Positions
4	$[0, 1, 4, 6]d_0$
6	$[0, 1, 6, 9, 11, 13]d_0$
8	$[0, 1, 4, 10, 16, 18, 21, 23]d_0$
10	$[0, 1, 3, 6, 13, 20, 27, 31, 35, 36]d_0$

TABLE II
NESTED ARRAY CONFIGURATIONS

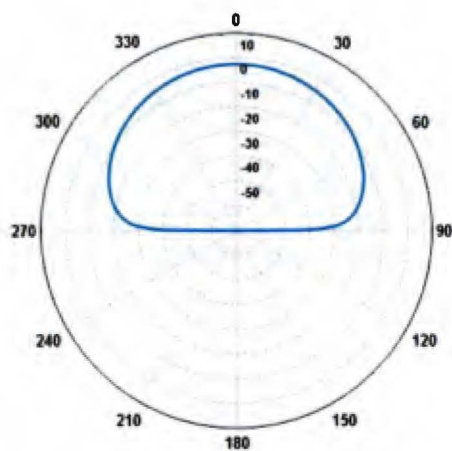
N_A	Positions
4	$[0, 1, 2, 5]d_0$
6	$[0, 1, 2, 3, 7, 11]d_0$
8	$[0, 1, 2, 3, 4, 9, 14, 19]d_0$
10	$[0, 1, 2, 3, 4, 5, 11, 17, 23, 29]d_0$

TABLE III
CO-PRIME ARRAY CONFIGURATIONS

N_A	M	N	Positions
4	2	3	$[0, 2, 3, 4]d_0$
6	3	4	$[0, 3, 4, 6, 8, 9]d_0$
8	4	5	$[0, 4, 5, 8, 10, 12, 15, 16]d_0$
10	5	6	$[0, 5, 6, 10, 12, 15, 18, 20, 24, 25]d_0$



(a)



Total Gain [dBi] (Frequency = 3 GHz, Phi = 90 deg)

(b)

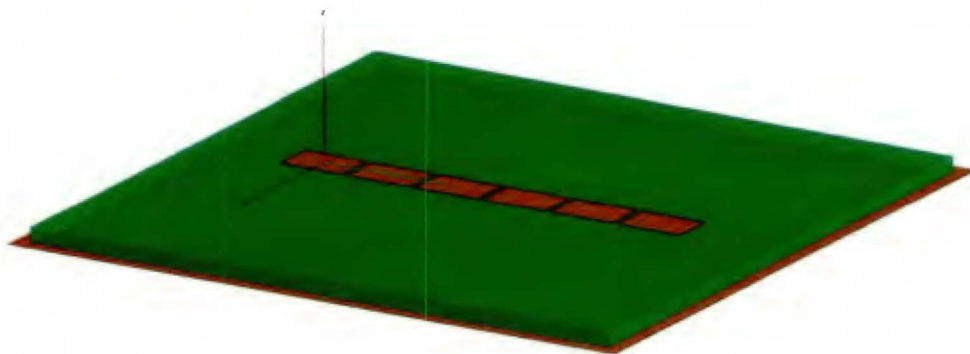


Figure 1. (a) Patch antenna, (b) Gain pattern (dBi) of a single element in isolation, (c) Six-element uniform linear patch array.

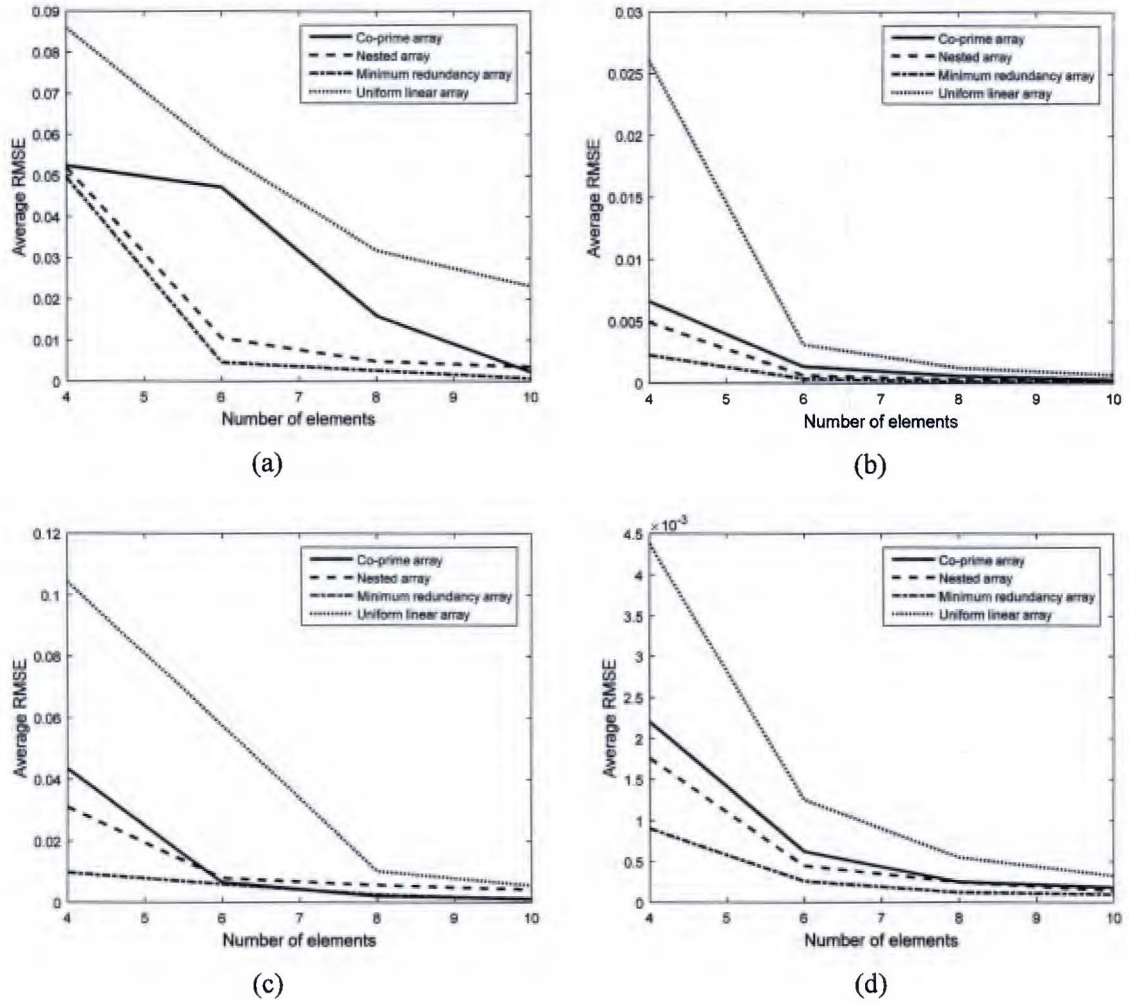


Figure 2. Dipole arrays: Average RMSE for different array geometries and different number of elements at SNR = 0dB, (a) $\Delta u = 0.1$ in the presence of mutual coupling, (b) $\Delta u = 0.1$ in the absence of mutual coupling, (c) $\Delta u = 0.2$ in the presence of mutual coupling, (d) $\Delta u = 0.2$ in the absence of mutual coupling.

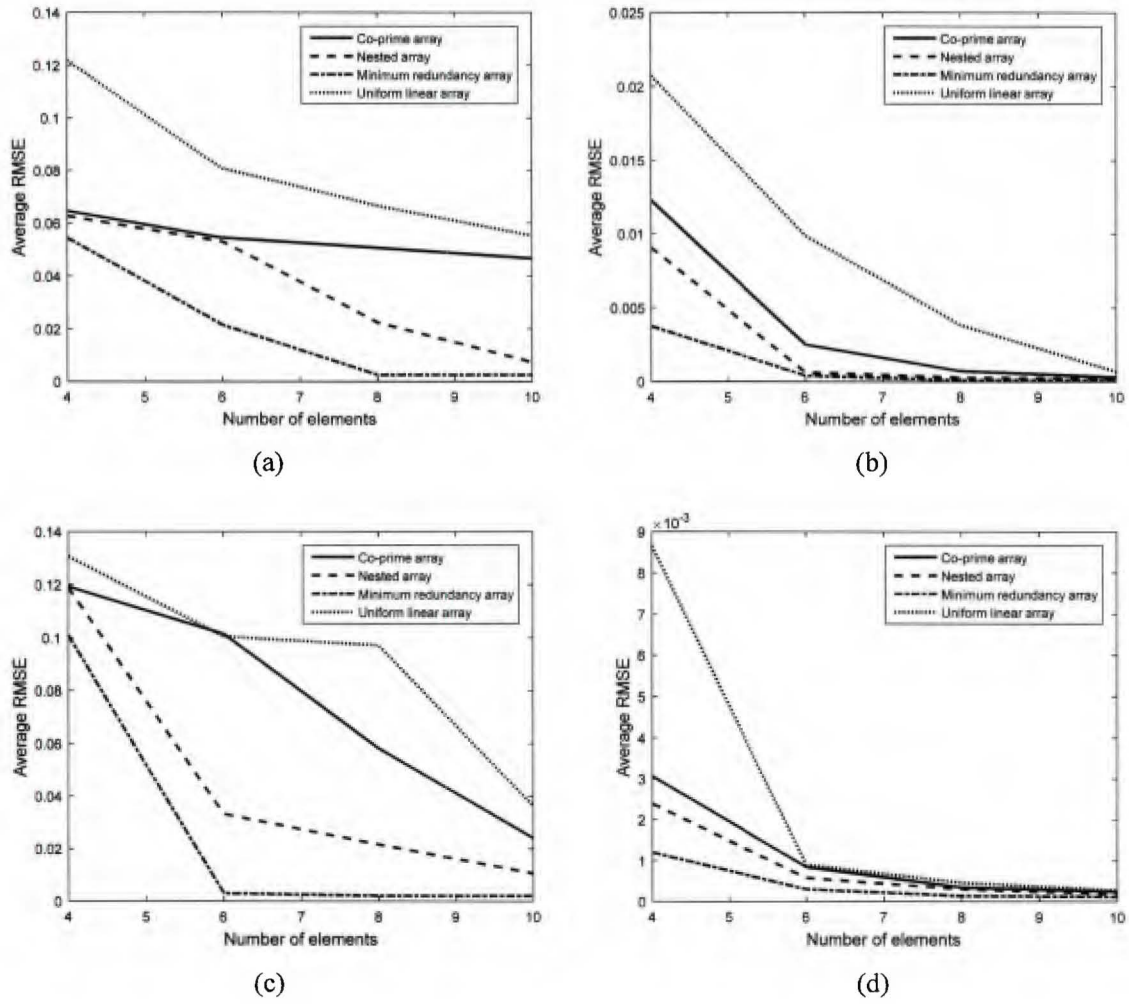


Figure 3. Microstrip arrays: Average RMSE for different array geometries and different number of elements at SNR = 0dB, (a) $\Delta u = 0.1$ in the presence of mutual coupling, (b) $\Delta u = 0.1$ in the absence of mutual coupling, (c) $\Delta u = 0.2$ in the presence of mutual coupling, (d) $\Delta u = 0.2$ in the absence of mutual coupling.

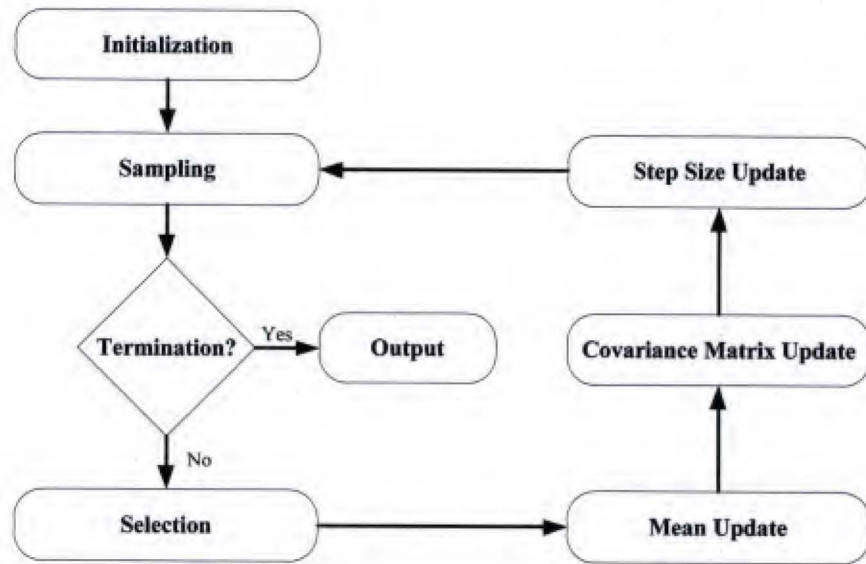


Figure 4. CMA-ES block diagram.

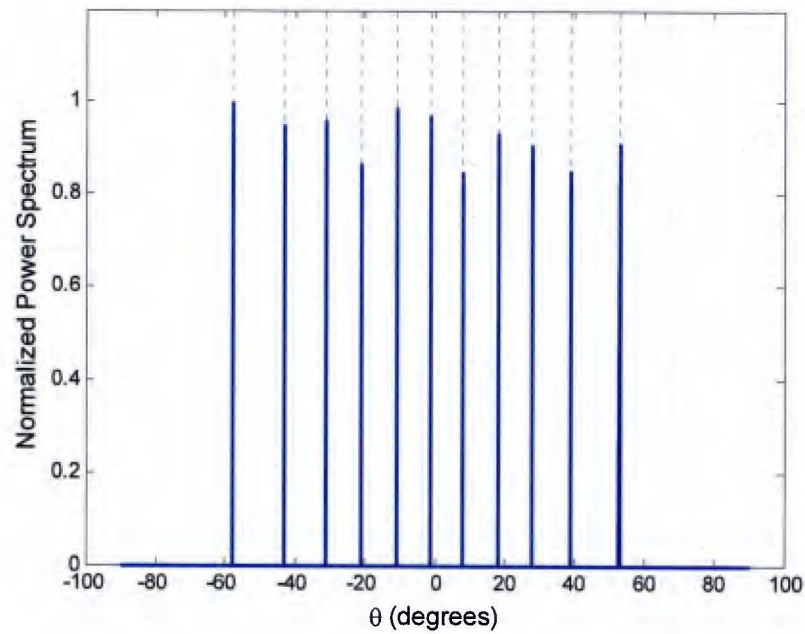
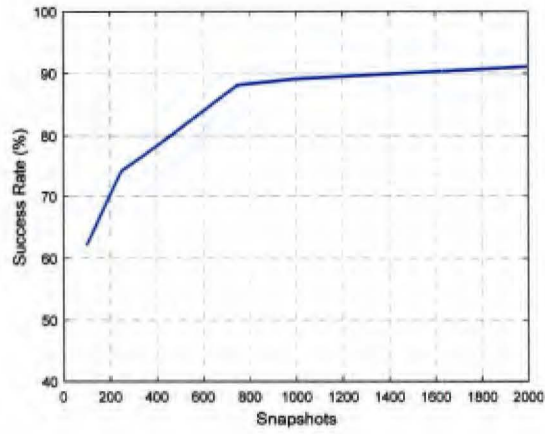
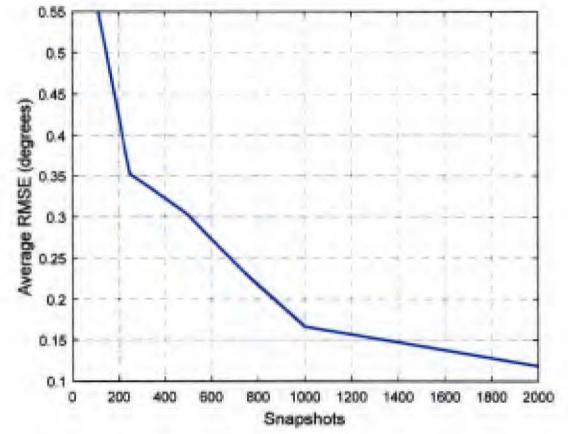


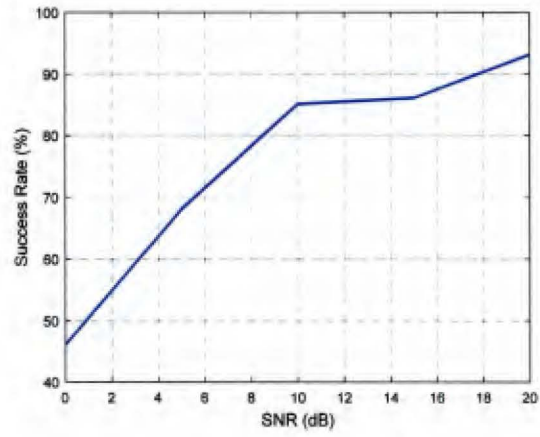
Figure 5. Simultaneous approach estimated spectrum: Six-element nested-array, $D = 11$.



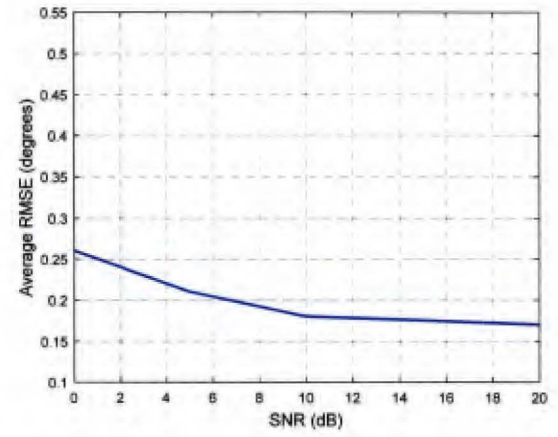
(a)



(b)

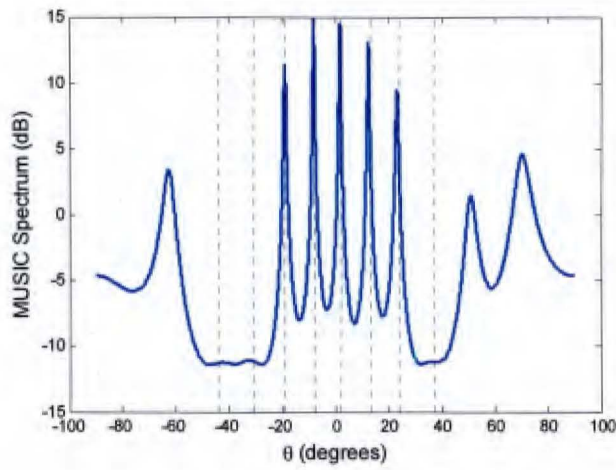


(c)

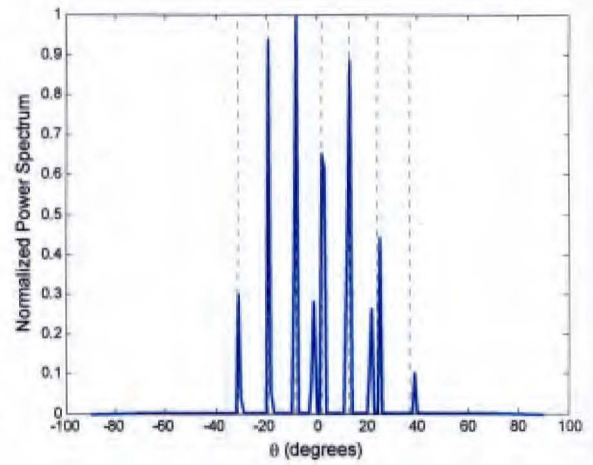


(d)

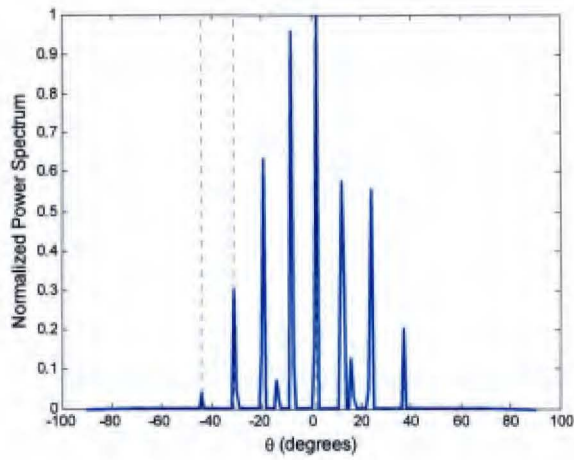
Figure 6. Simultaneous approach: Six-element nested-array, $D = 5$; (a) SNR = 10 dB, success rate vs. snapshots, (b) SNR = 10 dB, average RMSE vs. snapshots (c) $T = 1000$ snapshots, success rate vs. SNR, (d) $T = 1000$ snapshots, average RMSE vs. SNR.



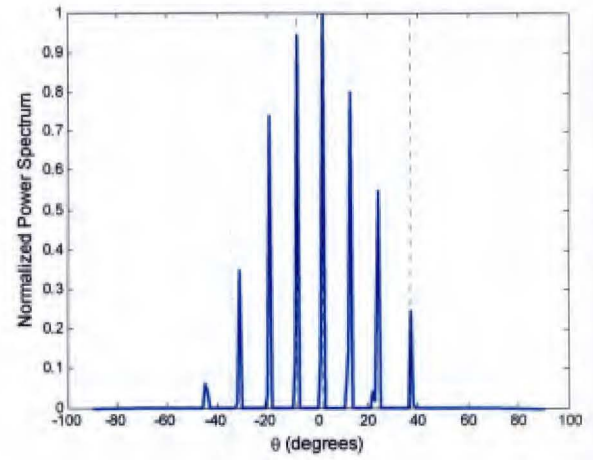
(a)



(b)



(c)



(d)

Figure 7. Six-element microstrip array (a) MUSIC with spatial smoothing without accounting for mutual coupling, Iterative method: (b) initial estimated spectrum, (c) estimated spectrum after first iteration, (d) estimated spectrum after tenth iteration.

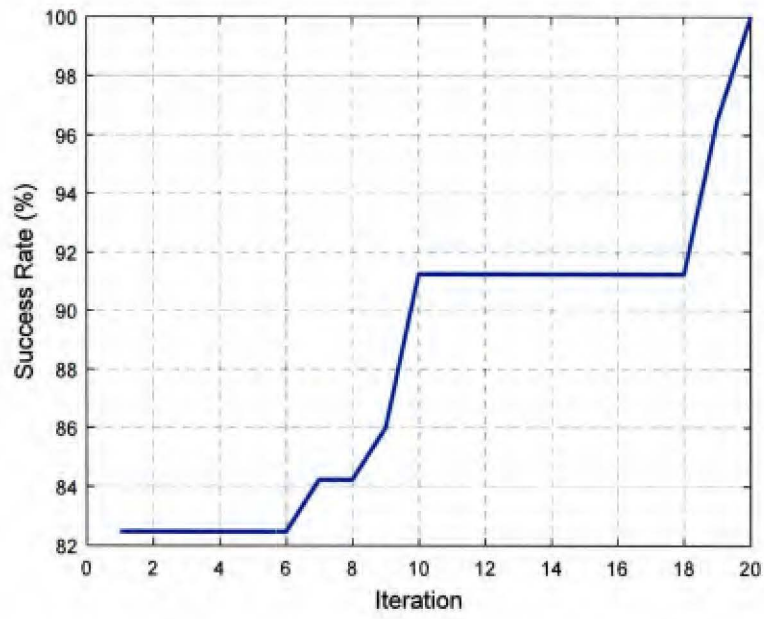


Figure 8. Six-element microstrip array: Success rate vs. iteration number.

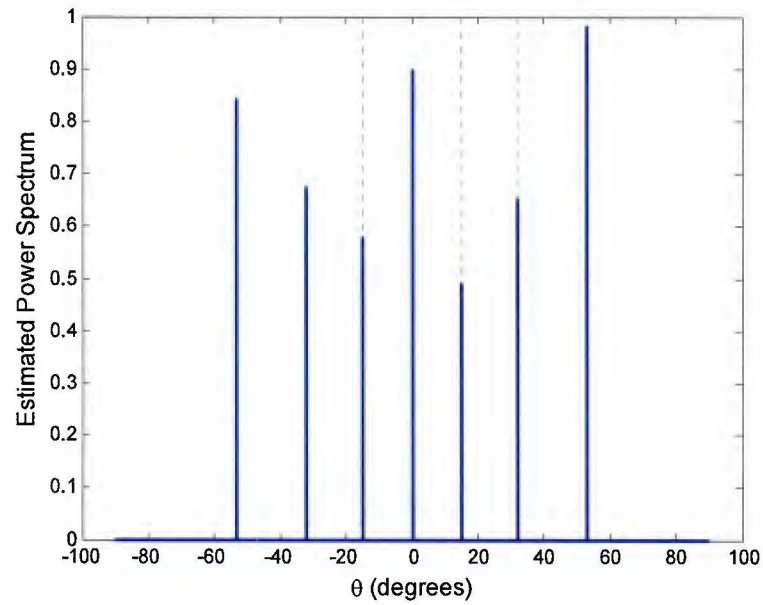
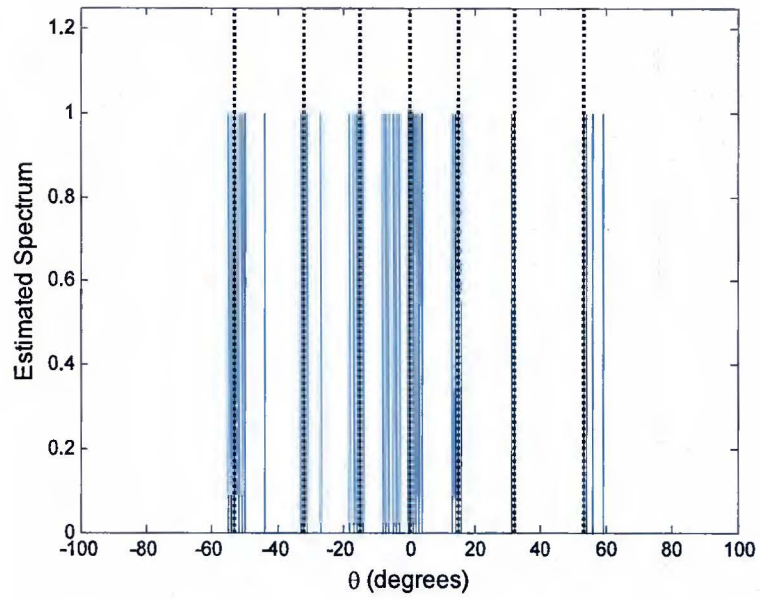
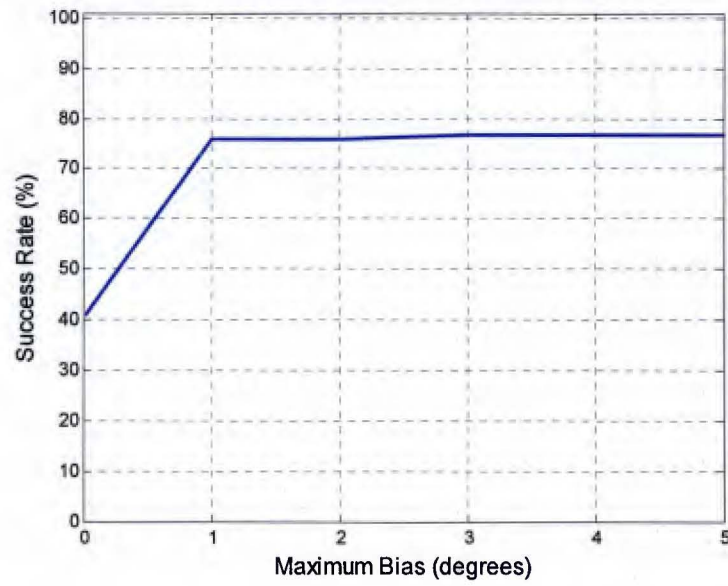


Figure 9. Estimated spectrum: Extended co-prime array with $M = 2$, $N = 3$, $D = 7$.

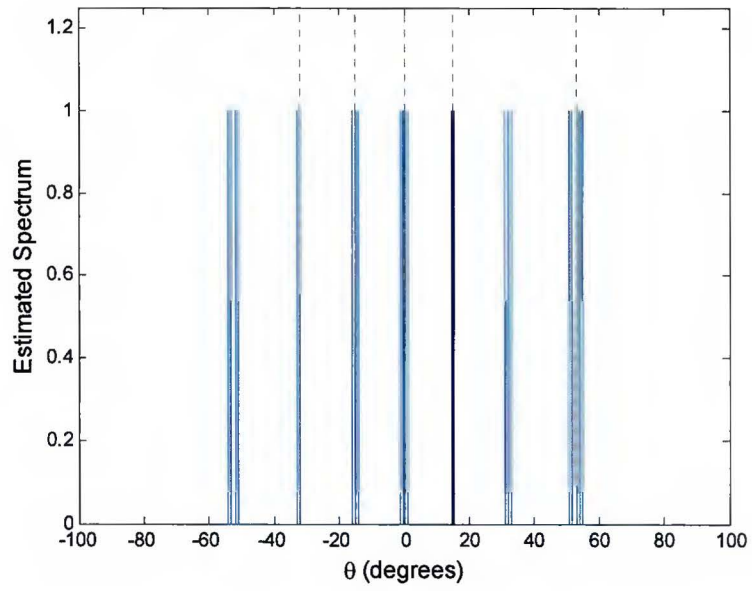


(a)

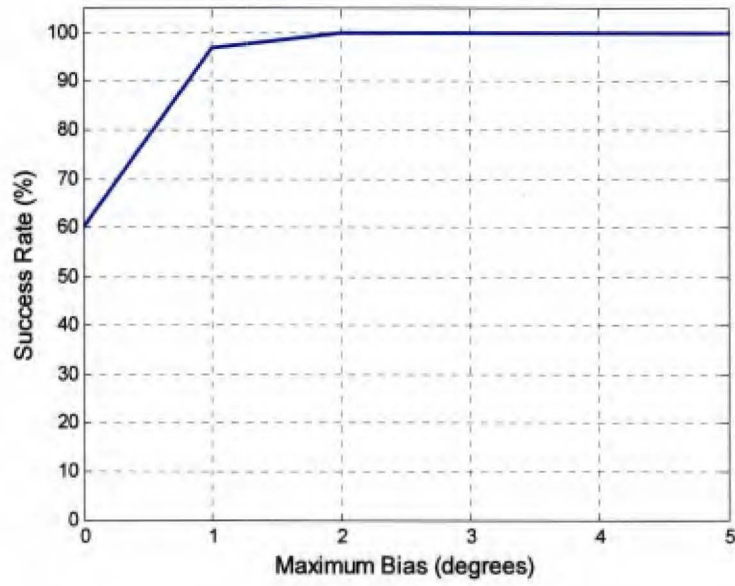


(b)

Figure 10. CMA-ES population size: 1000 with no restarts, (a) Estimated DOAs of 100 the Monte Carlo runs, (b) Success rate of the obtained solutions.



(a)



(b)

Figure 11. CMA-ES population size: 5000 with five restarts, (a) Estimated DOAs of 100 the Monte Carlo runs, (b) Success rate of the obtained solutions.

3.7. Generalized Coprime Sampling of Toeplitz Matrices for Spectrum Estimation

Abstract

Increased demand on spectrum sensing over a broad frequency band requires a high sampling rate and thus leads to a prohibitive volume of data samples. In some applications, e.g., spectrum estimation, only the second-order statistics are required. In this case, we may use a reduced data sampling rate by exploiting a low-dimensional representation of the original high dimensional signals. In particular, the covariance matrix can be reconstructed from compressed data by utilizing its specific structure, e.g., the Toeplitz property. Among a number of techniques for compressive covariance sampler design, the coprime sampler is considered attractive because it enables a systematic design capability with a significantly reduced sampling rate. In this paper, we propose a general coprime sampling scheme that implements effective compression of Toeplitz covariance matrices. Given a fixed number of data samples, we examine different schemes on covariance matrix acquisition for performance evaluation, comparison and optimal design, based on segmented data sequences.

Index Terms

Compressive covariance sampling, structured matrix, coprime sampling, overlapping data segmentation

I. INTRODUCTION

Various applications require spectrum sensing over a broad frequency band, which demand on the sampling rate and produce a large amount of data. In some cases, the original signal is known to be sparse. This property allows the exploitation of compressive sensing and sparse sampling approaches that enable effective sparse signal reconstruction [3], [4], with no loss of information. The signal reconstruction can be carried out by a number of algorithms, such as orthogonal matching pursuit (OMP), least absolute shrinkage and selection operator (LASSO), and Bayesian compressive sensing [5]–[8].

Spectrum estimation based on the second-order statistics adds to the abovementioned applications for signal reconstruction. In this case, the covariance function and the covariance matrix can be constructed as low-dimensional representations of the original high-dimensional signals [9], [10]. This fact has motivated the development of an alternate framework, referred to as compressive covariance sampling, in which the signal sparsity is not a requirement [11]–[13].

In this paper, we consider spectrum estimation of wide-sense stationary (WSS) processes utilizing the Toeplitz property of the covariance matrix. Note that, while our focus in this paper is limited to the second-order statistics, extension to techniques based on high-order statistics [14] is straightforward.

Several methods have been developed to tackle similar compressive Toeplitz matrix sampling. For example, a generalized nested sampler [15] was proposed to recover Toeplitz matrices from a compressed covariance matrix. However, this approach assumes an infinite number of data samples and does not consider the achievable reconstruction performance when the number of samples is finite. In addition, it imposes a minimum sampling interval that follows the Nyquist criterion, which makes it ineffective to implement low sampling rate systems for wideband spectrum estimation. In [16], a minimal sparse sampler was proposed through a set of properly designed analog filters and then down-sampling the signals at a reduced rate. A finite number of outputs was divided into multiple blocks without overlapping, and the compressed covariance was estimated by averaging over these blocks. However, the requirement of using the designed analog filters complicates the implementation. In addition, the effect of utilization of overlapping blocks were not considered.

The proposed work is based on the recently developed coprime sampling structure [17], which utilizes only two uniform samplers to sample a WSS process with sampling intervals, M and N . The integers M and N , which represent the down-sampling rates, are chosen to be coprime. As a result, it generates two sets of uniformly spaced samples with a rate substantially lower than the nested [18] and with fewer samplers than the schemes in [19]–[21].

In this paper, we design a sampling matrix to compress Toeplitz matrices based on a coprime sampling scheme. In particular, our focus is on effective estimations of the Toeplitz covariance matrix and signal spectrum from a finite number of samples of a WSS sequence. Toward this objective, we generalize the coprime sampling approach to achieve a higher number of degrees of freedom (DOFs) and low estimation error. The generalization is carried out in the following two aspects: (a) The first generalization is to use multiple coprime units to obtain a higher number of DOFs and improved power spectrum density (PSD) estimation performance. This is achieved through the use of an integer factor p , where a coprime unit is defined as a full period of the output sample pattern between $x[bMN]$ and $x[(b+1)MN-1]$ for any non-negative integer b . (b) The second generalization is to exploit overlapping blocks in performing sample averaging, enabling an increased number of blocks to be used for sample averaging, leading to a reduced estimation variance.

The concept of generalized coprime sampling was first developed in [1] where only the abovementioned first generalization is considered, whereas the second generation was introduced in [2]. In this paper, we extend these preliminary results by providing comprehensive theoretical support and performance bound

analysis of the developed techniques, and describe the spectrum estimation algorithm based on the cross-covariance between the outputs of the two samplers. A number of simulation results are presented to clearly reveal the relationship between the achieved performance and various parameters related to the sampling strategies and signal conditions.

The rest of the paper is organized as follows. We first introduce the signal model in Section II. Generalized coprime sampling that exploits multiple coprime units is presented in Section III. Section IV describes spectrum estimation based on the generalized coprime sampling scheme, and the corresponding spectrum identifiability, compression factor, and Cramér-Rao bound (CRB) are examined. In Section V, we propose the exploitation of overlapping samples, and show analytically that the overlapping sampling scheme achieves reduced variance in the estimated covariance matrix and signal spectrum. Simulation results are provided in Section VI to numerically verify the effectiveness of the proposed generalization and the analysis. Section VII concludes the paper.

Notations: We use lower-case (upper-case) bold characters to denote vectors (matrices). In particular, \mathbf{I}_N denotes the $N \times N$ identity matrix. $(\cdot)^*$ implies complex conjugation, whereas $(\cdot)^T$ and $(\cdot)^H$ respectively denote the transpose and conjugate transpose of a matrix or a vector. $\mathbb{E}(\cdot)$ is the statistical expectation operator and \otimes denotes the Kronecker product. \mathbb{R} and \mathbb{C} denote the set of real values and complex values, respectively, while \mathbb{N}^+ denotes the set of positive integers. $x \sim \mathcal{CN}(a, b)$ denotes that random variable x follows the complex Gaussian distribution with mean a and variance b . $\lfloor \cdot \rfloor$ denotes the floor function which returns the largest integer not exceeding the argument. $\text{diag}(\mathbf{x})$ denotes a diagonal matrix that uses the elements of \mathbf{x} as its diagonal elements, and $\text{Tr}\{\mathbf{A}\}$ returns the trace of matrix \mathbf{A} .

II. SIGNAL MODEL

Assume that a zero-mean WSS process $X(t), t \in \mathbb{R}$, which consists of signals corresponding to a number of sparse frequencies, is confined within a bandwidth B_s . To obtain its PSD, the covariance matrix needs to be provided from a specific realization of $X(t), t = 0, \dots, T-1$. It suffices to consider the discrete-time random process, $X[l]$, obtained by sampling the analog signal $X(t)$, with a Nyquist sampling rate $f_s = 2B_s$. Note that the discrete-time process $X[l]$ remains WSS in the discrete-time sense. Let $\mathbf{x}_L[l] = [x[l], x[l+1], \dots, x[l+L-1]]^T$ be a realized vector of $X[l]$. Then, the resulting

semi-positive definite, Hermitian and Toeplitz covariance matrix can be given by

$$\begin{aligned}\mathbf{R}_x &= \mathbb{E} [\mathbf{x}_L[l] \mathbf{x}_L^H[l]] \\ &= \begin{pmatrix} r[0] & r[-1] & \dots & r[-L+1] \\ r[1] & r[0] & \dots & r[-L+2] \\ \vdots & \vdots & \dots & \vdots \\ r[L-2] & r[L-3] & \dots & r[-1] \\ r[L-1] & r[L-2] & \dots & r[0] \end{pmatrix},\end{aligned}\quad (1)$$

in which the entry $r[\tau] = \mathbb{E} [x[l]x^*[l-\tau]]$ only depends on the lags $\tau = -L+1, \dots, L-1$. It is clear from (1) that $r[-\tau] = r^*[\tau]$. In addition, the Toeplitz structure of \mathbf{R}_x implies that many of its elements are redundant. As a result, \mathbf{R}_x can be obtained from a sparsely sampled data sequence. This fact motivated compressive covariance sampling [11]–[13].

In this paper, we consider the problem of estimating an $L \times L$ covariance matrix of $\mathbf{x}_L[l]$ and the signal PSD from an observation of $X(t)$ with an available length of KT_s , where $K \in \mathbb{N}^+$ and $K \geq L$. When sampled at the Nyquist interval $T_s = 1/f_s$, it yields K samples of discrete-time observations $x[k], k = 0, \dots, K-1$. A common practice for covariance matrix estimation is to segment the entire discrete-time observation of length K into multiple length- L blocks, and average the respectively sample covariances [22]. As shown in Fig. 1, the entire observation period is segmented into multiple, possibly overlapping, blocks. In Section III-B, we first consider the non-overlapping segmentation to illustrate the signal model, as shown in Fig. 1(a), whereas the overlapping case depicted in Fig. 1(b) will be discussed in Section III-C. Denote B as the number of data blocks for the non-overlapping case. We assume for convenience that the B blocks cover the entire sequence, i.e., $BL = K$.

Denote by $x_b[l] = x[l + (b-1)L], l = 0, \dots, L-1$, and $\mathbf{x}_b = [x_b[0], \dots, x_b[L-1]]^T$ for $b = 1, \dots, B$. We sparsely sample each data block using a $V \times L$ sampling matrix \mathbf{A}_s to obtain $\mathbf{y}_b = \mathbf{A}_s \mathbf{x}_b$, where $V \ll L$. The estimated covariance matrix obtained by averaging the available B blocks and is expressed as

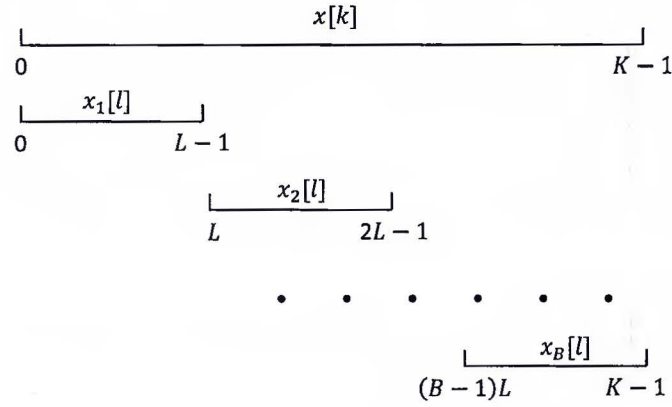
$$\hat{\mathbf{R}}_y = \frac{1}{B} \sum_{b=1}^B \mathbf{y}_b \mathbf{y}_b^H = \mathbf{A}_s \left(\frac{1}{B} \sum_{b=1}^B \mathbf{x}_b \mathbf{x}_b^H \right) \mathbf{A}_s^H = \mathbf{A}_s \hat{\mathbf{R}}_x \mathbf{A}_s^H, \quad (2)$$

where $\hat{\mathbf{R}}_x$ is an estimated covariance matrix of \mathbf{R}_x . The compressed covariance matrix $\hat{\mathbf{R}}_y$ with size $V \times V$ can be exploited to reconstruct the $L \times L$ matrix $\hat{\mathbf{R}}_x$, provided that it includes all lags $\tau = 0, \dots, L-1$. Note that covariances corresponding to negative lags $\tau = -L+1, \dots, -1$ can be obtained through the Hermitian operation $r[\tau] = r^*[-\tau]$ and thus does not contain additional information. Reconstruction of full covariance matrix \mathbf{R}_x from the compressed covariance matrix $\hat{\mathbf{R}}_y$ can be made possible by designing

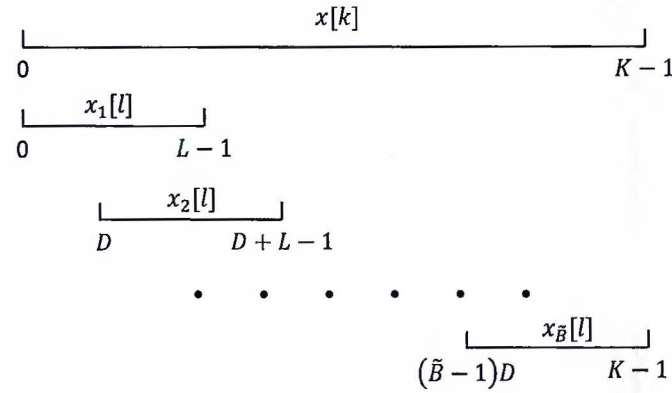
a proper sampling matrix \mathbf{A}_s . It is clear that, since there are V^2 entries in $\hat{\mathbf{R}}_y$, the number of samples required to enable reconstruction of the Hermitian Toeplitz matrix $\hat{\mathbf{R}}_x$ is $\mathcal{O}(\sqrt{L})$. In this end, $\hat{\mathbf{R}}_x$ can be reconstructed as

$$\hat{\mathbf{R}}_x = \begin{pmatrix} \hat{r}[0] & \hat{r}[-1] & \dots & \hat{r}[-L+1] \\ \hat{r}[1] & \hat{r}[0] & \dots & \hat{r}[-L+2] \\ \vdots & \vdots & \dots & \vdots \\ \hat{r}[L-2] & \hat{r}[L-3] & \dots & \hat{r}[-1] \\ \hat{r}[L-1] & \hat{r}[L-2] & \dots & \hat{r}[0] \end{pmatrix}, \quad (3)$$

where $\hat{r}[\tau], \tau = -L+1, \dots, L-1$ are estimated by averaging all the entries with the same lag τ in $\hat{\mathbf{R}}_y$.



(a)



(b)

Fig. 1. Illustration of segmentations. (a) Non-overlapping segmentation; (b) Overlapping segmentation.

III. GENERALIZED COPRIME SAMPLING

Coprime sampling exploits two uniform sub-Nyquist samplers with sampling period being coprime multiples of the Nyquist sampling period [17], [23]. In this section, the generalized coprime sampling scheme is presented in two operations. A multiple coprime unit factor $p \in \mathbb{N}^+$ [1], aiming to increase the number of lags in the compressed covariance matrix, is first introduced. Then, the utilization of overlapping samples between blocks is pursued to yield a reduced estimation variance through the use of a non-overlapping factor $q \in \mathbb{N}^+$.

A. The concept of coprime sampling

In coprime sampling, the sampling matrix \mathbf{A}_s can be denoted as $\mathbf{A}_s = [\mathbf{A}_{s1}^T \ \mathbf{A}_{s2}^T]^T$, where \mathbf{A}_{s1} and \mathbf{A}_{s2} are the sub-sampling matrices corresponding to the two coprime samplers.

Definition 1: The (i, j) th entry of the sampling matrices \mathbf{A}_{s1} and \mathbf{A}_{s2} can be designed as:

$$[\mathbf{A}_{s1}]_{i,j} = \begin{cases} 1, & j = Mi, \quad i \in \mathbb{N}^+, \\ 0, & \text{elsewhere,} \end{cases}$$

and

$$[\mathbf{A}_{s2}]_{i,j} = \begin{cases} 1, & j = Ni, \quad i \in \mathbb{N}^+, \\ 0, & \text{elsewhere,} \end{cases} \quad (4)$$

where $M \in \mathbb{N}^+$ and $N \in \mathbb{N}^+$ are coprime integers.

From a data acquisition perspective, there are two sets of uniformly spaced samples of the input WSS signal $X(t), t = 0, \dots, T$, from two samplers with sampling intervals MT_s and NT_s , respectively, as illustrated in Fig. 2. Without loss of generality, we assume $M < N$. Then, the highest sampling rate of the system is $1/(MT_s) = f_s/M$ and the two sampled stream outputs can be given as

$$\begin{aligned} y_1[k_1] &= x[Mk_1] = X(Mk_1T_s), \\ y_2[k_2] &= x[Nk_2] = X(Nk_2T_s). \end{aligned} \quad (5)$$

Note that, due to the coprime property of M and N , there are no overlapping outputs between the two sets other than $x[bMN]$ for any non-negative integer b . The outputs between $x[(b-1)MN]$ and $x[bMN-1]$ are referred to as a coprime unit, positioned at

$$\mathbb{P}_b = \{bMN + Mk_1\} \cup \{bMN + Nk_2\}. \quad (6)$$

Over an observation with an available length of KT_s , K/MN coprime units can be obtained, each consists of $M + N$ physical samples. As such, the total number of physical samples is given by

$$K_s = K \left(\frac{M+N}{MN} \right) = K \left(\frac{1}{M} + \frac{1}{N} \right). \quad (7)$$

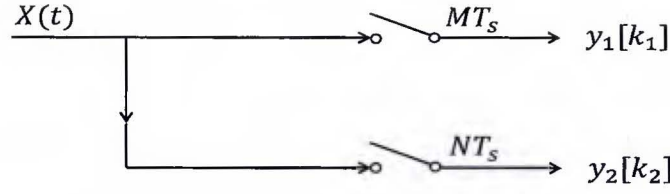


Fig. 2. Coprime sampling structure.

For illustration, an example is presented in Fig. 3, where two coprime samplers with $M = 3$ and $N = 4$ are considered. The length of $K = 60$ output streams consist of 5 coprime units, and $K_s = 35$ physical samples are distributed between $x[12(b-1)]$ and $x[12b-1]$, for $b = 1, \dots, 5$, where 5 pairs of samples overlap between the output of the two samplers at positions 0, 12, 24, 36, and 48.

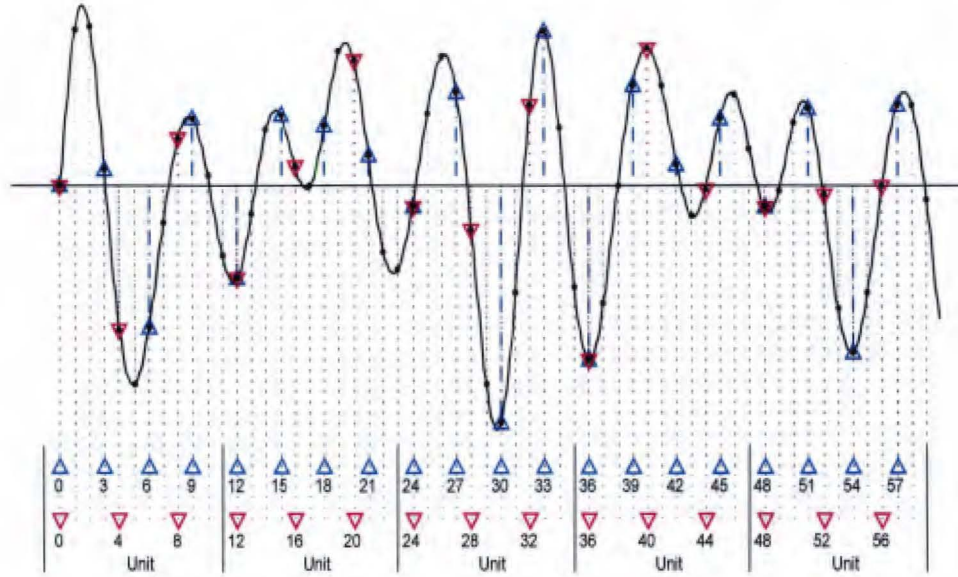


Fig. 3. An example for coprime sampling ($M = 3$, and $N = 4$; •: Nyquist sampler; △: first sampler outputs; ▽: second sampler outputs.)

Denote $\mathbf{y}_{b_1} = [y_{b_1}[0], \dots, y_{b_1}[N-1]]^T$ as an $N \times 1$ vector, and $\mathbf{y}_{b_2} = [y_{b_2}[0], \dots, y_{b_2}[M-1]]^T$ as an $M \times 1$ vector, with $y_{b_1}[k_1] = x[(b-1)MN + Mk_1]$ and $y_{b_2}[k_2] = x[(b-1)MN + Nk_2]$, where $0 \leq k_1 \leq N-1$ and $0 \leq k_2 \leq M-1$, for $1 \leq b \leq K/(MN)$. In addition, let $\mathbf{y}_b = [\mathbf{y}_{b_1}^T \ \mathbf{y}_{b_2}^T]^T$. As

such, the $(M + N) \times (M + N)$ covariance matrix \mathbf{R}_y can be expressed as

$$\mathbf{R}_y = \begin{pmatrix} \mathbf{R}_{y_{11}} & \mathbf{R}_{y_{12}} \\ \mathbf{R}_{y_{21}} & \mathbf{R}_{y_{22}} \end{pmatrix} = \begin{pmatrix} E[\mathbf{y}_{b_1} \mathbf{y}_{b_1}^H] & E[\mathbf{y}_{b_1} \mathbf{y}_{b_2}^H] \\ E[\mathbf{y}_{b_2} \mathbf{y}_{b_1}^H] & E[\mathbf{y}_{b_2} \mathbf{y}_{b_2}^H] \end{pmatrix}. \quad (8)$$

In \mathbf{R}_y , matrices $\mathbf{R}_{y_{11}}$ and $\mathbf{R}_{y_{22}}$ contains self-lags of the two sampler output streams, while their cross-lags are included in matrices $\mathbf{R}_{y_{12}}$ and $\mathbf{R}_{y_{21}}$. Note that $\mathbf{R}_{y_{21}} = \mathbf{R}_{y_{12}}^*$. In addition, because the two sampler outputs share the first sample in each coprime unit, the self-lags can be taken as cross-lags between every sample from one sampler and the first sample from the other sampler. As such, the self-lags form a subset of the cross-lags. Thus, \mathbf{R}_x can be reconstructed by using only $\mathbf{R}_{y_{12}}$, whose cross-lags (including the negated ones) are given by the following set,

$$\mathbb{L} = \{\tau | \tau = \pm(Mk_1 - Nk_2)\}, \quad (9)$$

where $0 \leq k_1 \leq N - 1$ and $0 \leq k_2 \leq M - 1$.

The prototype scheme uses one coprime unit samples to generate all lags in \mathbb{L} . However, it should be noticed that they are distributed in the range $[-M(N - 1), M(N - 1)]$ with some missing integers at $(aM + bN)$, where $a \geq 1$ and $b \geq 1$, as shown in Fig. 4(a), for $M = 3$ and $N = 4$. That is, they are not sufficient to reconstruct $\hat{\mathbf{R}}_x$ with dimension $L = MN$. To overcome this limitation, two coprime units from the first sampler and one coprime unit from the second sampler are used to form one block in [17], and the resulting lags are contiguous in the range $[-MN - N + 1, MN + N - 1]$, as depicted in Fig. 4(b). This scheme is referred in this paper to as the conventional scheme. In this case, the maximum achievable L is $L_{\max} = MN + N$.

B. Generalized coprime sampling scheme using non-overlapping blocks

In the sequel, an integer factor $p \geq 2$, representing the number of multiple coprime units, is first introduced to achieve a higher value of L . In each block, outputs from p coprime units from both samplers, i.e., $p(M + N)$ physical samples spanning a time period of $pMNT_s$, are used to estimate the covariance matrix. In this case, the resulting lags fall into the following set,

$$\tilde{\mathbb{L}} = \{\tau | \tau = \pm(Mk_1 - Nk_2)\}, \quad (10)$$

for $0 \leq k_1 \leq pN - 1$ and $0 \leq k_2 \leq pM - 1$. Note that varying p changes the set $\tilde{\mathbb{L}}$. The following proposition about the set $\tilde{\mathbb{L}}$ reveals the property of the resulting lag positions.

Proposition 1: The set $\tilde{\mathbb{L}}$ contains all integer lags in the range $-(p - 1)MN - M - N + 1 \leq \tau \leq (p - 1)MN + M + N - 1$.

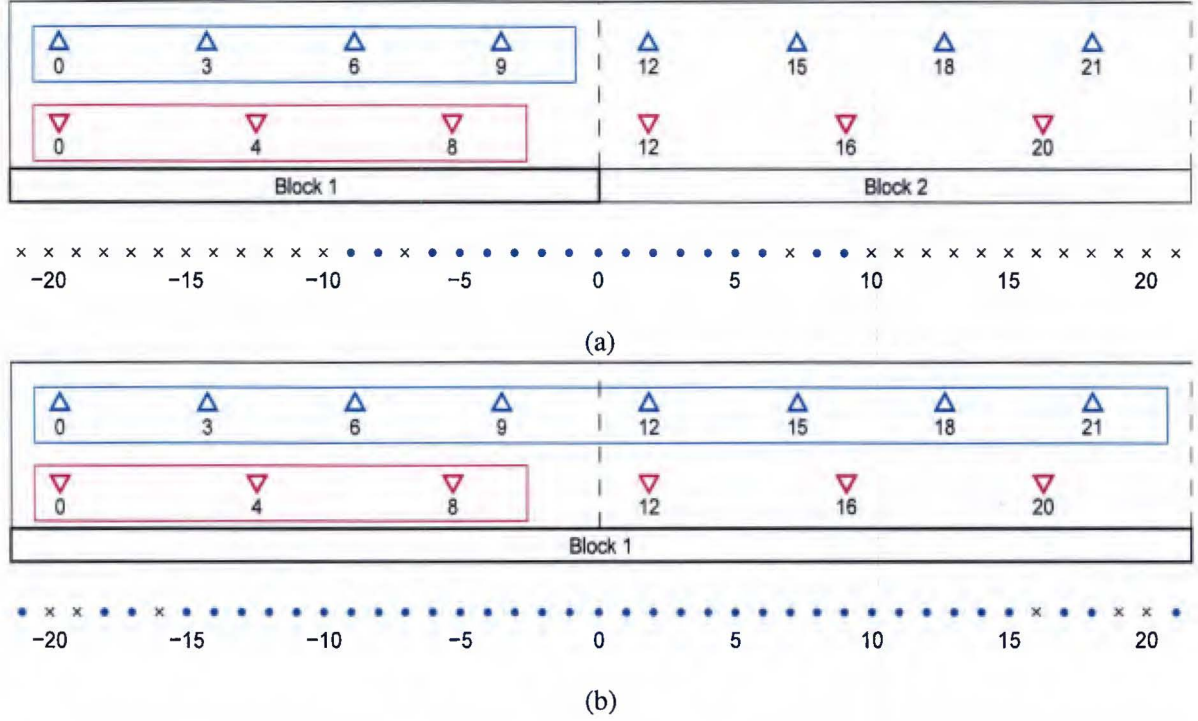


Fig. 4. An example for different schemes ($M = 3$, and $N = 4$; \triangle : first sampler outputs; ∇ : second sampler outputs; \bullet : lags; \times : holes. (a) Prototype; (b) Conventional.)

The proof is provided in Appendix A. Note that, all resulting lags using conventional scheme are included in $\tilde{\mathcal{L}}$ as a special case of $p = 2$. For the generalized scheme, the maximum achievable value of L becomes

$$\tilde{L}_{\max} = (p - 1)MN + M + N, \quad (11)$$

and the number of the corresponding non-overlapping blocks is given by

$$B = \left\lfloor \frac{K}{pMN} \right\rfloor. \quad (12)$$

An example for different values of p is illustrated in Fig. 5, where $K = 120$, $M = 3$, and $N = 4$ are assumed. For the case of $p = 2$, i.e., the conventional scheme, each block forms consecutive lags within $[-18, 18]$. That is, $\hat{\mathbf{R}}_{\mathbf{x}}$ can be reconstructed with a maximum of dimension $\tilde{L}_{\max} = 19$ by averaging $B = 5$ blocks. For the case of $p = 5$, $\tilde{L}_{\max} = 55$ can be obtained by a consecutive lag range of $[-54, 54]$ in each block, whereas the number of the blocks is reduced to $B = 2$.

We examine the compression factor, which is defined as the ratio of the number of entries in $\hat{\mathbf{R}}_{\mathbf{x}}$ over the corresponding number in $\hat{\mathbf{R}}_{\tilde{\mathbf{y}}_{12}}$, expressed as

$$\kappa = \frac{L \times L}{pM \times pN} = \frac{L^2}{p^2 MN}. \quad (13)$$

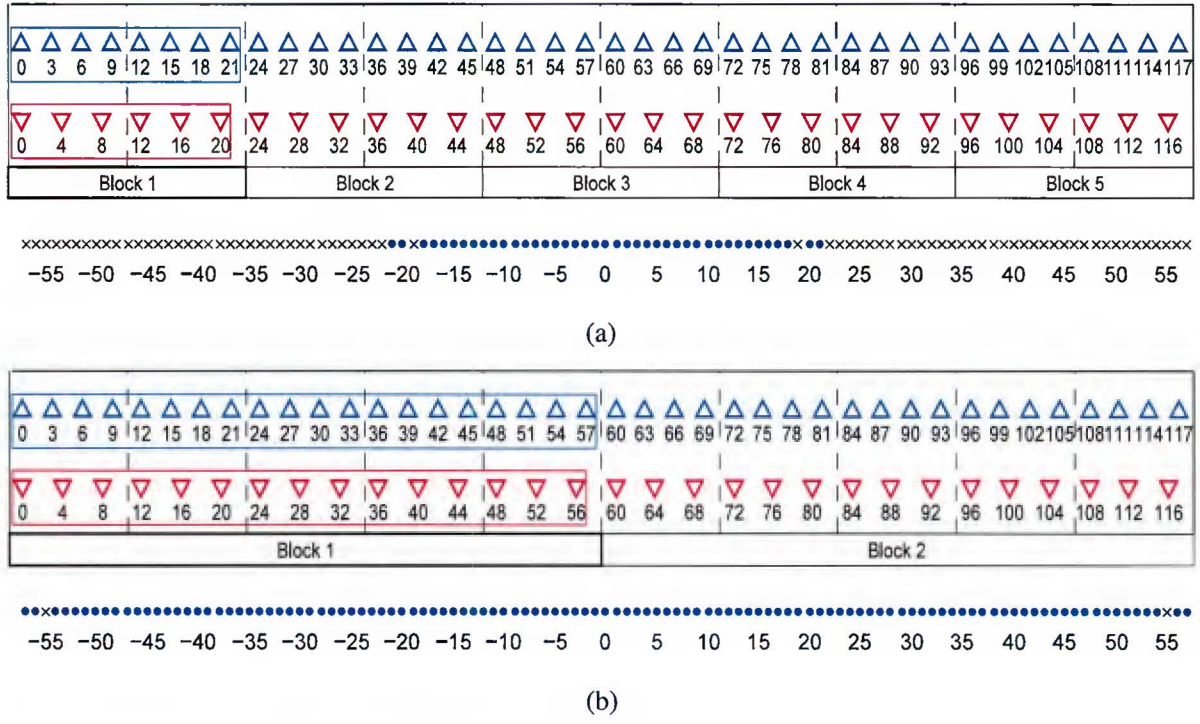


Fig. 5. An example for different values of p ($K = 120$, $M = 3$, and $N = 4$; (a) $p = 2$; (b) $p = 5$.)

Because the maximum value of L is $\tilde{L}_{\max} = (p-1)MN + M + N$, the maximum achievable value of κ is given by

$$\kappa_{\max} = \frac{[(p-1)MN + M + N]^2}{p^2 MN}. \quad (14)$$

Fig. 6 shows κ_{\max} , as a function of M , N , and p . It is clear that κ_{\max} improves as M and N increase. Notice that, while the number of entries in $\hat{\mathbf{R}}_{\tilde{\mathbf{y}}_{12}}$ increases with p , κ_{\max} does not significantly change. It asymptotically approaches MN when $p \gg 1$.

For a given number of compression factor, i.e., the constant value of MN , the optimal coprime pair in terms of total number of physical samples, K_s , can be derived by solving the optimization problem:

$$\begin{aligned} &\text{Minimize} \quad K_s = K \left(\frac{1}{M} + \frac{1}{N} \right) \\ &\text{subject to} \quad MN = \text{constant}, \\ &\quad \quad \quad 0 < M < N. \end{aligned} \quad (15)$$

It is demonstrated in [23], [31] that the valid optimal coprime pair is the one that has M and N as close as possible. This is satisfied by choosing $N = M + 1$. This relationship is assumed in the remainder of

the paper. In this case, K_s becomes

$$K_s = K \left(\frac{1}{M} + \frac{1}{M+1} \right), \quad (16)$$

and the corresponding compression factor, κ_{\max} , can be expressed as

$$\kappa_{\max} = \frac{\tilde{L}_{\max}^2}{p^2 M(M+1)} \propto M^2, \quad (17)$$

with $\tilde{L}_{\max} = (p-1)M^2 + (p+1)M + 1$.

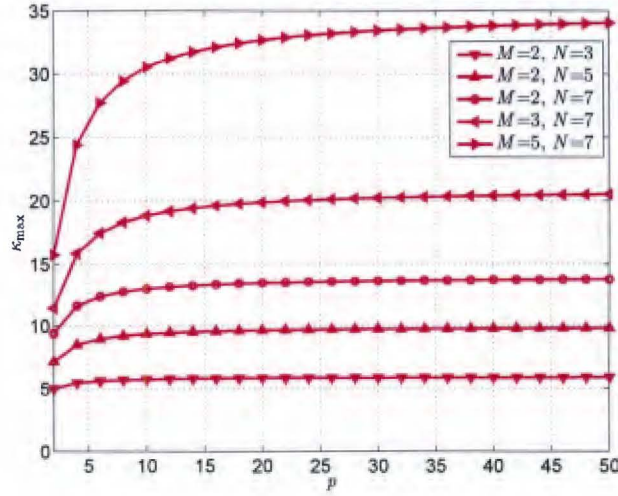


Fig. 6. κ_{\max} , as a function of M , N , and p .

C. Utilization of overlapping blocks

The variance of the estimated covariance and spectrum is generally reduced by utilizing a higher number of averaging blocks. In addition to averaging over non-overlapping segments, as discussed earlier, a general and more effective alternative for spectrum estimation is to exploit overlapping segments. In so doing, the number of applicable blocks for sample averaging can be substantially increased. The overlapping samples used are set by non-overlapping factor $q \in \mathbb{N}^+$.

As shown in Fig. 1(b), we maintain the same segment length $pM(M+1)$, and let the starting points of two adjacent blocks $D = qM(M+1)$ units apart, where $1 \leq q \leq p$. Similarly, we assume, for convenience, that $(\tilde{B}-1)D + pM(M+1) = K$ covers the entire recorded sequence.

Definition 2: Assume that D consists of the length of q coprime units, i.e., $D = qM(M+1)$, where $1 \leq q \leq p$. Then, the number of blocks can be expressed as

$$\begin{aligned}\tilde{B} &= \left\lfloor \frac{K - pM(M+1)}{D} \right\rfloor + 1 = \left\lfloor \frac{K}{qM(M+1)} - \frac{p}{q} \right\rfloor + 1 \\ &= \left\lfloor \frac{p}{q}B - \frac{p}{q} \right\rfloor + 1.\end{aligned}\quad (18)$$

It is straightforward to confirm that $\tilde{B} \geq B$ since $q \leq p$. In addition, \tilde{B}/B approaches p/q when B is large. As such, p/q can be considered as the overlapping ratio that approximately describes the level of additional blocks used for sample averaging. It is clear that \tilde{B} increases as q decreases and is maximized when $q = 1$. Note that the non-overlapping case can be considered as a special case of $q = p$ and $\tilde{B} = B$.

For illustration, an example of $p = 5$ and $q = 1$ is considered in Fig. 7, where K and M are assumed to be the same as those in Fig. 5. It is shown that $\tilde{B} = 6$ blocks can be used in Fig. 7, whereas only $B = 2$ blocks are obtained in the corresponding non-overlapping scenario, as depicted in Fig. 5(b).

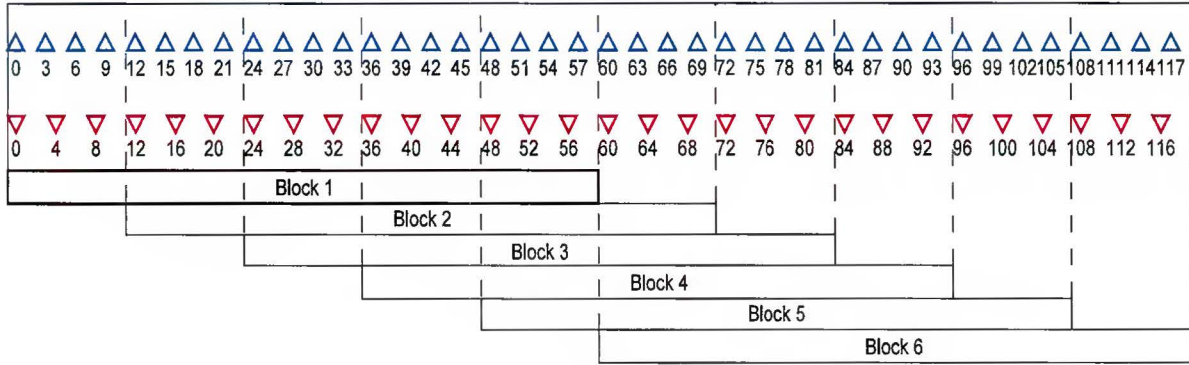


Fig. 7. An example of utilization of overlapping samples ($K = 120$, $M = 3$, $p = 5$, and $q = 1$.)

Denote $\tilde{y}_{b_1}[k_1] = x[(b-1) \times qM(M+1) + Mk_1]$ and $\tilde{y}_{b_2}[k_2] = x[(b-1) \times qM(M+1) + (M+1)k_2]$, where $0 \leq k_1 \leq p(M+1) - 1$ and $0 \leq k_2 \leq pM - 1$, for $1 \leq b \leq \tilde{B}$. In addition, let $\tilde{\mathbf{y}}_{b_1} = [\tilde{y}_{b_1}[0], \dots, \tilde{y}_{b_1}[p(M+1) - 1]]^T$ and $\tilde{\mathbf{y}}_{b_2} = [\tilde{y}_{b_2}[0], \dots, \tilde{y}_{b_2}[pM - 1]]^T$. The covariance matrix $\hat{\mathbf{R}}_{\tilde{\mathbf{y}}_{12}}$, using the generalized scheme, can be estimated as

$$\hat{\mathbf{R}}_{\tilde{\mathbf{y}}_{12}} = \frac{1}{\tilde{B}} \sum_{b=1}^{\tilde{B}} \tilde{\mathbf{y}}_{b_1} \tilde{\mathbf{y}}_{b_2}^H. \quad (19)$$

Note that, for each $1 \leq b \leq \tilde{B}$, the entries $r_b(k_1, k_2) = \tilde{y}_{b_1}[k_1] \tilde{y}_{b_2}^*[k_2]$ corresponding to the same position (k_1, k_2) in covariance matrix are still independent. As discussed above, the value of \tilde{B} is increased from that of B approximately by a factor of p/q . Thus, utilizing overlapping blocks for averaging, the variance of the estimated covariance is generally reduced to q/p of the corresponding non-overlapping case.

Then, $\hat{\mathbf{R}}_{\mathbf{x}}$ with dimension $L \times L$, where $L \leq \tilde{L}_{\max}$, can be reconstructed as

$$\hat{\mathbf{R}}_{\mathbf{x}} = \begin{pmatrix} \hat{r}[0] & \hat{r}[-1] & \dots & \hat{r}[-L+1] \\ \hat{r}[1] & \hat{r}[0] & \dots & \hat{r}[-L+2] \\ \vdots & \vdots & \dots & \vdots \\ \hat{r}[L-2] & \hat{r}[L-3] & \dots & \hat{r}[-1] \\ \hat{r}[L-1] & \hat{r}[L-2] & \dots & \hat{r}[0] \end{pmatrix}, \quad (20)$$

where $\hat{r}[\tau], \tau = -L+1, \dots, L-1$, are estimated by averaging all the entries with the same lag τ in $\hat{\mathbf{R}}_{\tilde{\mathbf{y}}_{12}}$.

We make the following two remarks:

1. In the generalized coprime sampling scheme, $(\tilde{B}-1)qM(M+1) + pM(M+1) = K$, where $p, q \in \mathbb{N}^+$, is assumed to cover the entire recorded sequence. When $\tilde{B} = 1$, factor q does not have a physical meaning. Thus, $\tilde{B} \geq 2$ needs to be guaranteed, which is equivalent to

$$p + q \leq \frac{K}{M(M+1)}. \quad (21)$$

As such, the range of the pair of (p, q) falls into the following set,

$$\Pi_{p,q} = \left\{ (p, q) \mid p + q \leq \frac{K}{M(M+1)}, 1 \leq q \leq p, p, q \in \mathbb{N}^+ \right\}. \quad (22)$$

2. The covariance matrix $\mathbf{R}_{\tilde{\mathbf{y}}_{12}}$ is estimated using the \tilde{B} available samples. In practice, p and q are generally chosen to yield the large number of blocks \tilde{B} to achieve to rigid estimation of $\mathbf{R}_{\tilde{\mathbf{y}}_{12}}$.

3. As p increases, a higher number of DOFs in the compressed covariance matrix $\mathbf{R}_{\tilde{\mathbf{y}}_{12}}$ can be achieved. As a result, we can reconstruct covariance matrix $\hat{\mathbf{R}}_{\mathbf{x}}$ with a higher dimension, yielding an improved spectrum resolution and estimation accuracy. When q increases, the estimation accuracy can be improved because a higher number of blocks are used in the averaging. However, such higher dimension and higher number of blocks result in a higher computational complexity.

IV. SPECTRUM ESTIMATION AND THE CRB

Spectrum estimation deals with the problem of estimating the PSD of a random process, and finds applications in the context of dynamic spectrum sharing [24]. In this case, a broad frequency band should be sensed in order to locate the unoccupied spectrum before establishing a communication link. Sub-Nyquist sampling for cognitive radios is a widely studied topic, e.g., in [25]–[30].

Generally, power spectrum sensing can be classified into two major categories. The first category reconstructs the signal waveforms and then estimate the power spectrum, whereas the second category estimates the power spectrum from the signal covariance, i.e., the second-order statistics. The approach

discussed in [25]–[27] belongs to the former where the signals are assumed to be sparse in some domain and sub-Nyquist sampling is implemented to recover the signal waveforms through compressive sensing. The approach adopted in this paper, along with [28]–[30] and several other references [11]–[13], [15], [16] belong to the second category. Note, however, that this paper makes significant difference to the papers in its category, as our major contribution is the generalization of the coprime sampling, where the multiple unit factor p is used to improve the degrees-of-freedom (DOFs) and spectrum resolution, and the non-overlapping factor q is used to improve the estimation accuracy. Such generalization and the related analyses are novel.

A. Spectrum estimation

The well-known Wiener-Khinchin theorem proves that the PSD of a signal and the covariance function form a Fourier transform pair, expressed as

$$P[f] = \sum_{\tau=-\infty}^{\infty} r[\tau] e^{-j2\pi\tau f/f_s}. \quad (23)$$

Therefore, once $\hat{\mathbf{R}}_{\mathbf{x}}$ is reconstructed, then $P[f]$ can be estimated by employing the discrete Fourier transform which does not require the assumptions of signal sparsity in the frequency domain. The applicability to continuous spectrum signals will be demonstrated using a simulation example in Section V.

For signals with sparse and discrete spectrum, however, we can further achieve high-resolution spectrum estimation by exploiting subspace-based spectrum estimation techniques, in lieu of the Fourier transform. As such, in the following, we focus on the spectrum estimation of sparse spectrum signals which consist of a sum of multiple sinusoids, and the corresponding CRB analysis is provided.

Assume that $x[k]$, for $k = 0, 1, \dots, K-1$, are samples of the analog signal $X(t)$, which can be presented as a sum of I independent frequency components

$$x[k] = \sum_{i=0}^{I-1} \sigma_i e^{\frac{-j2\pi k f_i}{f_s}} + n[k], \quad (24)$$

of frequency f_i and complex magnitudes σ_i , $i = 0, \dots, I-1$. The additive noise $n[k]$ is assumed to be an independent and identically distributed (i.i.d.) random variable following the zero-mean complex Gaussian distribution with a variance σ_n^2 , i.e., $n[k] \sim \mathcal{CN}(0, \sigma_n^2)$.

Using the generalized coprime sampling scheme, in the b th block, $0 \leq b \leq \tilde{B} - 1$, the received outputs at the two coprime samplers can be respectively written as

$$\begin{aligned}\tilde{y}_{b_1}[k_1] &= x[(b-1) \times qM(M+1) + Mk_1] \\ &= \sum_{i=0}^{I-1} \sigma_i e^{\frac{-j2\pi[(b-1) \times qM(M+1) + Mk_1]f_i}{f_s}} + n_{b_1}[k_1],\end{aligned}\quad (25)$$

$$\begin{aligned}\tilde{y}_{b_2}[k_2] &= x[(b-1) \times qM(M+1) + (M+1)k_2] \\ &= \sum_{i=0}^{I-1} \sigma_i e^{\frac{-j2\pi[(b-1) \times qM(M+1) + (M+1)k_2]f_i}{f_s}} + n_{b_2}[k_2],\end{aligned}\quad (26)$$

where $0 \leq k_1 \leq p(M+1) - 1$, $0 \leq k_2 \leq pM - 1$, and the range of the pair (p, q) is given in $\Pi_{p,q}$. Stacking $\tilde{y}_{b_1}[k_1]$ for $0 \leq k_1 \leq p(M+1) - 1$ and $\tilde{y}_{b_2}[k_2]$ for $0 \leq k_2 \leq pM - 1$, yields the following received vector data

$$\begin{aligned}\tilde{\mathbf{y}}_{b_1} &= \sum_{i=0}^{I-1} \mathbf{a}_{b_1}(f_i) e^{\frac{-j2\pi[(b-1) \times qM(M+1)]f_i}{f_s}} \sigma_i = \mathbf{A}_{b_1} \mathbf{s} \Phi + \mathbf{n}_{b_1}, \\ \tilde{\mathbf{y}}_{b_2} &= \sum_{i=0}^{I-1} \mathbf{a}_{b_2}(f_i) e^{\frac{-j2\pi[(b-1) \times qM(M+1)]f_i}{f_s}} \sigma_i = \mathbf{A}_{b_2} \mathbf{s} \Phi + \mathbf{n}_{b_2},\end{aligned}\quad (27)$$

where $\mathbf{s} = [\sigma_1, \dots, \sigma_I]^T$, $\mathbf{A}_{b_1} = [\mathbf{a}_{b_1}(f_1), \dots, \mathbf{a}_{b_1}(f_I)]$, and $\mathbf{A}_{b_2} = [\mathbf{a}_{b_2}(f_1), \dots, \mathbf{a}_{b_2}(f_I)]$ with

$$\mathbf{a}_{b_1}(f_i) = \left[1, e^{\frac{-j2\pi M f_i}{f_s}}, \dots, e^{\frac{-j2\pi[p(M+1)-1]M f_i}{f_s}} \right]^T, \quad (28)$$

$$\mathbf{a}_{b_2}(f_i) = \left[1, e^{\frac{-j2\pi(M+1)f_i}{f_s}}, \dots, e^{\frac{-j2\pi(pM-1)(M+1)f_i}{f_s}} \right]^T. \quad (29)$$

In addition, Φ is a diagonal matrix given by

$$\Phi = \text{diag}\left(e^{\frac{-j2\pi[(b-1) \times qM(M+1)]f_1}{f_s}}, \dots, e^{\frac{-j2\pi[(b-1) \times qM(M+1)]f_I}{f_s}}\right). \quad (30)$$

Note that the noise vectors \mathbf{n}_{b_1} and \mathbf{n}_{b_2} follow the complex Gaussian distribution $\mathcal{CN}(0, \sigma_n^2 \mathbf{I}_{pM})$ and $\mathcal{CN}(0, \sigma_n^2 \mathbf{I}_{p(M+1)})$, respectively. Then, the compressed covariance matrix $\mathbf{R}_{\tilde{\mathbf{y}}_{12}}$ is obtained as

$$\begin{aligned}\mathbf{R}_{\tilde{\mathbf{y}}_{12}} &= \mathbb{E}[\tilde{\mathbf{y}}_{b_1} \tilde{\mathbf{y}}_{b_2}^H] = \mathbf{A}_{b_1} \mathbf{R}_{ss} \mathbf{A}_{b_2}^H + \sigma_n^2 \mathbf{i}_{\tilde{\mathbf{y}}_{12}} \\ &= \sum_{i=0}^{I-1} \sigma_i^2 \mathbf{a}_{b_1}(f_i) \mathbf{a}_{b_2}^H(f_i) + \sigma_n^2 \mathbf{i}_{\tilde{\mathbf{y}}_{12}},\end{aligned}\quad (31)$$

where $\mathbf{i}_{\tilde{\mathbf{y}}_{12}}$ returns a $pM \times p(M+1)$ matrix with ones on the main diagonal and zeros elsewhere. Note that, the following vector with elements corresponding to different lags, $\mathbf{a}(f_i) = [1, e^{\frac{-j2\pi f_i}{f_s}}, e^{\frac{-j4\pi f_i}{f_s}}, \dots, e^{\frac{-j2(L-1)\pi f_i}{f_s}}]^T$, can be extracted based on $\mathbf{a}_{b_1}(f_i) \otimes \mathbf{a}_{b_2}^*(f_i)$ for $1 \leq i \leq I$. Thus, $\mathbf{R}_{\mathbf{x}} \in \mathbb{C}^{L \times L}$, where $L \leq \tilde{L}_{\max}$, can be reconstructed and expressed as

$$\mathbf{R}_{\mathbf{x}} = \sum_{i=0}^{I-1} \sigma_i^2 \mathbf{a}(f_i) \mathbf{a}^H(f_i) + \sigma_n^2 \mathbf{I}_L. \quad (32)$$

In practice, $\hat{\mathbf{R}}_{\tilde{\mathbf{y}}_{12}}$ is estimated by averaging the available \tilde{B} blocks as in (19), and $\hat{\mathbf{R}}_{\mathbf{x}}$ is reconstructed as in (20). The spectrum can be estimated using a variety of methods (e.g., [33]), with respect to $\hat{\mathbf{R}}_{\mathbf{x}}$. It is well known that subspace-based methods are popular candidates to achieve a high spectrum resolution with a moderate computational complexity. The multiple signal classification (MUSIC) algorithm [34] is used to evaluate the performance of our approach. Note that the extension of other spectrum estimation techniques [35], [36] is straightforward.

The MUSIC approach is based on eigen-decomposition of the reconstructed covariance matrix $\hat{\mathbf{R}}_{\mathbf{x}}$, given by

$$\hat{\mathbf{R}}_{\mathbf{x}} = \hat{\mathbf{U}} \hat{\mathbf{\Lambda}} \hat{\mathbf{U}}^H, \quad (33)$$

where $\hat{\mathbf{\Lambda}} = \text{diag}\{\hat{\lambda}_1, \hat{\lambda}_2, \dots, \hat{\lambda}_L\}$ is the diagonal matrix of the eigenvalues in a descending order, and the $L \times L$ matrix $\hat{\mathbf{U}}$ contains the corresponding eigenvectors. The MUSIC algorithm requires the information of the rank of the signal subspace, i.e., the number of carrier frequencies of the signal arrivals. Various mathematical criteria, such as Akaike information criterion (AIC) [37], minimum description length (MDL) [38], and Bayesian information criterion (BIC) [39], can be employed to achieve the rank estimation. In this paper, we apply the BIC on $\hat{\mathbf{R}}_{\mathbf{x}}$ to obtain the value of I . It was shown that that BIC based methods [40]–[42] generally outperform other methods, such as those developed based on AIC and MDL [43]–[45] due to the stronger consistency, particularly when the number of array sensors is large and the number of samples is small. Then, Eqn. (33) can be decomposed as

$$\hat{\mathbf{R}}_{\mathbf{x}} = \hat{\mathbf{U}}_s \hat{\mathbf{\Lambda}}_s \hat{\mathbf{U}}_s^H + \hat{\mathbf{U}}_n \hat{\mathbf{\Lambda}}_n \hat{\mathbf{U}}_n^H, \quad (34)$$

where $\hat{\mathbf{U}}_s \in \mathbb{C}^{L \times I}$ and $\hat{\mathbf{U}}_n \in \mathbb{C}^{L \times (L-I)}$ contain the signal and noise subspace sample eigenvectors, respectively, and the corresponding sample eigenvalues are included in the diagonal matrices $\hat{\mathbf{\Lambda}}_s = \text{diag}\{\hat{\lambda}_1, \hat{\lambda}_2, \dots, \hat{\lambda}_I\}$ and $\hat{\mathbf{\Lambda}}_n = \text{diag}\{\hat{\lambda}_{I+1}, \hat{\lambda}_{I+2}, \dots, \hat{\lambda}_L\}$. Then, the spectrum can be estimated as

$$\hat{P}(f) = \frac{1}{\mathbf{a}^H(f) \hat{\mathbf{U}}_n \hat{\mathbf{U}}_n^H \mathbf{a}(f)}, \quad (35)$$

where f is defined as the collection over all possible grids in the spectrum and the values of f that produce peaks in the estimator $\hat{P}(f)$ are taken as estimates of the frequencies $f_i, i = 1, \dots, I$. The spectrum identifiability and resolution are improved as L increases, and they are optimized when $L = \tilde{L}_{\max}$. This relationship is assumed in the remainder of the paper.

B. The Cramér-Rao Bound (CRB)

The CRB offers a lower bound on the variances of unbiased estimates of the parameters. The specific CRB expressions given in [46]–[48] are valid only when the number of frequencies is less than the number

of physical samples ($I < K_s$). This is because the expressions are based on the inverse of the matrix $\mathbf{A}^H \mathbf{A}$, where \mathbf{A} is the so-called array or frequency manifold matrix. However, the assumption $I < K_s$ is not requirement for the existence of CRB, because even when $I \geq K_s$, with proper prior information, the Fisher information matrix (FIM) can remain nonsingular (invertible) under a much broader range of conditions. Thus, we use the inverse of FIM as the CRB expression. After we have submitted the previous version of the manuscript, several papers have been published on the CRB analysis of the directions of arrival estimation when more sources than the number of sensors are handled in the context of coarrays. We have cited these papers as references [49]–[51]. However, none of these papers provide revealing solutions in a compact matrix form.

For a set of vectors $\tilde{\mathbf{y}}_b = [\tilde{\mathbf{y}}_{b_1}^T \ \tilde{\mathbf{y}}_{b_2}^T]^T$, $b = 1, \dots, \tilde{B}$, the CRB is calculated by the well-known expression [47] involving the FIM elements

$$F_{\alpha_i \alpha_j} = \tilde{B} \text{Tr} \left\{ \mathbf{R}_{\tilde{\mathbf{y}}}^{-1} \frac{\partial \mathbf{R}_{\tilde{\mathbf{y}}}}{\partial \alpha_i} \mathbf{R}_{\tilde{\mathbf{y}}}^{-1} \frac{\partial \mathbf{R}_{\tilde{\mathbf{y}}}}{\partial \alpha_j} \right\}, \quad (36)$$

for unknown variables α_i and α_j , where $\mathbf{R}_{\tilde{\mathbf{y}}}$ is expressed as

$$\mathbf{R}_{\tilde{\mathbf{y}}} = \text{E}[\tilde{\mathbf{y}}_b \tilde{\mathbf{y}}_b^H] = \sum_{i=0}^{I-1} \sigma_i^2 \mathbf{a}_b(f_i) \mathbf{a}_b^H(f_i) + \sigma_n^2 \mathbf{I}_{p(2M+1)}, \quad (37)$$

and $\mathbf{a}_b(f_i) = [\mathbf{a}_{b_1}^T(f_i) \ \mathbf{a}_{b_2}^T(f_i)]^T$.

In the underlying case, the unknown parameters are the I signal frequencies f_i and powers σ_i^2 for $i = 1, \dots, I$, as well as the noise power σ_n^2 . Therefore, the elements in the $(2I+1) \times (2I+1)$ Fisher matrix \mathbf{F} can be written in terms of the block matrices, for $i, j = 1, \dots, I$, given by

$$\begin{aligned} F_{i,j} &= \tilde{B} \text{Tr} \left\{ \mathbf{R}_{\tilde{\mathbf{y}}}^{-1} \frac{\partial \mathbf{R}_{\tilde{\mathbf{y}}}}{\partial f_i} \mathbf{R}_{\tilde{\mathbf{y}}}^{-1} \frac{\partial \mathbf{R}_{\tilde{\mathbf{y}}}}{\partial f_j} \right\}, \\ F_{i,j+I} &= \tilde{B} \text{Tr} \left\{ \mathbf{R}_{\tilde{\mathbf{y}}}^{-1} \frac{\partial \mathbf{R}_{\tilde{\mathbf{y}}}}{\partial f_i} \mathbf{R}_{\tilde{\mathbf{y}}}^{-1} \frac{\partial \mathbf{R}_{\tilde{\mathbf{y}}}}{\partial \sigma_j^2} \right\}, \\ F_{i,2I+1} &= \tilde{B} \text{Tr} \left\{ \mathbf{R}_{\tilde{\mathbf{y}}}^{-1} \frac{\partial \mathbf{R}_{\tilde{\mathbf{y}}}}{\partial f_i} \mathbf{R}_{\tilde{\mathbf{y}}}^{-1} \frac{\partial \mathbf{R}_{\tilde{\mathbf{y}}}}{\partial \sigma_n^2} \right\}, \\ F_{i+I,j} &= \tilde{B} \text{Tr} \left\{ \mathbf{R}_{\tilde{\mathbf{y}}}^{-1} \frac{\partial \mathbf{R}_{\tilde{\mathbf{y}}}}{\partial \sigma_i^2} \mathbf{R}_{\tilde{\mathbf{y}}}^{-1} \frac{\partial \mathbf{R}_{\tilde{\mathbf{y}}}}{\partial f_j} \right\}, \\ F_{i+I,j+I} &= \tilde{B} \text{Tr} \left\{ \mathbf{R}_{\tilde{\mathbf{y}}}^{-1} \frac{\partial \mathbf{R}_{\tilde{\mathbf{y}}}}{\partial \sigma_i^2} \mathbf{R}_{\tilde{\mathbf{y}}}^{-1} \frac{\partial \mathbf{R}_{\tilde{\mathbf{y}}}}{\partial \sigma_j^2} \right\}, \\ F_{i+I,2I+1} &= \tilde{B} \text{Tr} \left\{ \mathbf{R}_{\tilde{\mathbf{y}}}^{-1} \frac{\partial \mathbf{R}_{\tilde{\mathbf{y}}}}{\partial \sigma_i^2} \mathbf{R}_{\tilde{\mathbf{y}}}^{-1} \frac{\partial \mathbf{R}_{\tilde{\mathbf{y}}}}{\partial \sigma_n^2} \right\}, \\ F_{2I+1,2I+1} &= \tilde{B} \text{Tr} \left\{ \mathbf{R}_{\tilde{\mathbf{y}}}^{-1} \frac{\partial \mathbf{R}_{\tilde{\mathbf{y}}}}{\partial \sigma_n^2} \mathbf{R}_{\tilde{\mathbf{y}}}^{-1} \frac{\partial \mathbf{R}_{\tilde{\mathbf{y}}}}{\partial \sigma_n^2} \right\}, \end{aligned} \quad (38)$$

where

$$\begin{aligned}\frac{\partial \mathbf{R}_{\tilde{\mathbf{y}}}}{\partial f_i} &= \sigma_i^2 \left[\frac{\partial \mathbf{a}_b(f_i)}{\partial f_i} \mathbf{a}_b^H(f_i) + \mathbf{a}_b(f_i) \frac{\partial \mathbf{a}_b^H(f_i)}{\partial f_i} \right], \\ \frac{\partial \mathbf{R}_{\tilde{\mathbf{y}}}}{\partial \sigma_i^2} &= \mathbf{a}_b(f_i) \mathbf{a}_b^H(f_i), \\ \frac{\partial \mathbf{R}_{\tilde{\mathbf{y}}}}{\partial \sigma_n^2} &= \mathbf{I}_{p(2M+1)}.\end{aligned}\tag{39}$$

Then, the CRB of estimated frequencies is obtained as

$$\text{CRB}(f_i) = [\mathbf{F}^{-1}]_{i,i}.\tag{40}$$

V. SIMULATION RESULTS

For illustrative purposes, we demonstrate the spectrum estimation performance under different choices of the arguments within the generalized coprime sampling scheme. Assume that I frequency components with identical powers are distributed in the frequency band $[-500, 500]$ MHz. Assume that $K = 50000$ samples are generated with a Nyquist sampling rate $f_s = 1$ GHz. In addition, the noise power is assumed to be identical across the entire spectrum. The MUSIC method is used to estimate the power spectrum. Our benchmarks are the spectrum DOFs and their statistical performance. The latter is evaluated in terms of average relative root mean square error (RMSE) of the estimated frequencies, defined as

$$\text{Relative RMSE}(f_i) = \frac{1}{f_s} \sqrt{\frac{1}{500I} \sum_{n=1}^{500} \sum_{i=1}^I (\hat{f}_i(n) - f_i)^2},\tag{41}$$

where $\hat{f}_i(n)$ is the estimate of f_i from the n th Monte Carlo trial, $n = 1, \dots, 500$.

A. The performance of coprime sampling

We first illustrate the performance of coprime sampling. Herein, the conventional coprime sampling scheme is considered, i.e., $p = 2$. In addition, $M = 3$ is assumed. As such, the $L \times L = 19 \times 19$ covariance matrix $\hat{\mathbf{R}}_{\mathbf{x}}$ can be reconstructed from $\hat{\mathbf{R}}_{\tilde{\mathbf{y}}_{12}}$ with dimension $pM \times p(M+1) = 6 \times 8$. Thus, the resulting compression factor is $\kappa_{\max} \approx 7.52$ and up to $L - 1 = 18$ frequencies can be estimated.

In Fig. 8, we consider $I = 18$ frequencies with $\delta_f = 50$ MHz separation in the presence of noise with a 0 dB SNR. It is evident that all 18 frequencies can be identified correctly. In Fig. 9, the RMSE results are shown as a function of the input SNR, where $I = 1$ is assumed. As expected, it displays a strong inverse semi-logarithmic dependence on the input SNR. It is also observed that there is a gap between the RMSE and CRB even in the high SNR region, due to estimation bias. The errors are mainly generated in two aspects. On one hand, $\hat{\mathbf{R}}_{\tilde{\mathbf{y}}_{12}}$ is used to reconstruct $\hat{\mathbf{R}}_{\mathbf{x}}$. On the other hand, only consecutive lag entries in $\hat{\mathbf{R}}_{\tilde{\mathbf{y}}_{12}}$ are exploited. It is observed that the bias errors increase with I due to a higher frequency components, as shown in Fig. 10, where the input SNR is set to 0 dB.

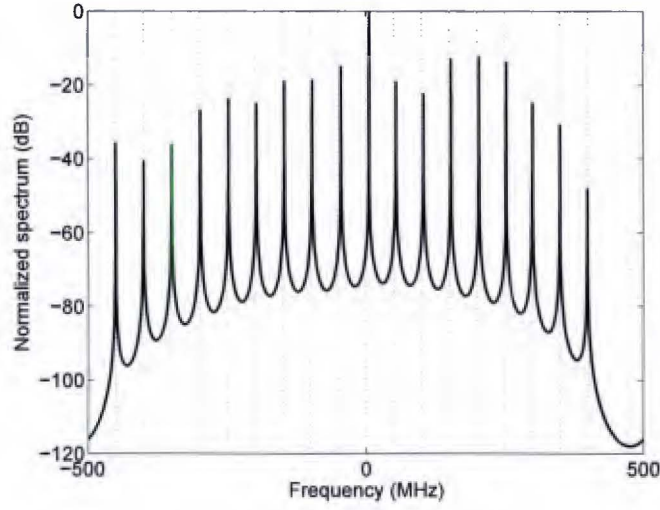


Fig. 8. Estimated spectrum ($I = 18$ and input SNR=0 dB).

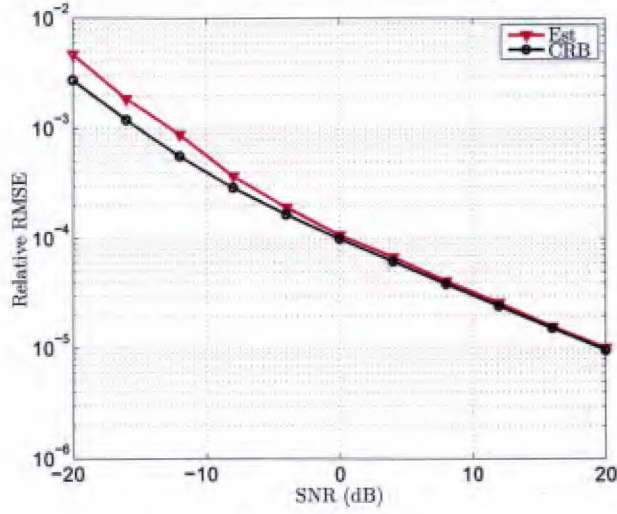


Fig. 9. Relative RMSE versus SNR ($I = 1$).

B. The generalized coprime sampling scheme versus other schemes

Next, we compare the generalized coprime sampling scheme with the nested sampler and the sparse ruler based sampler, where the same number of physical samples is assumed. For the coprime sampler, we set $M = 3$, and thus there are $2M + 1 = 7$ physical samples in each coprime unit. The sampling patterns corresponding to the nested sampler and the sparse ruler based sampler that yield the same 7-sample unit

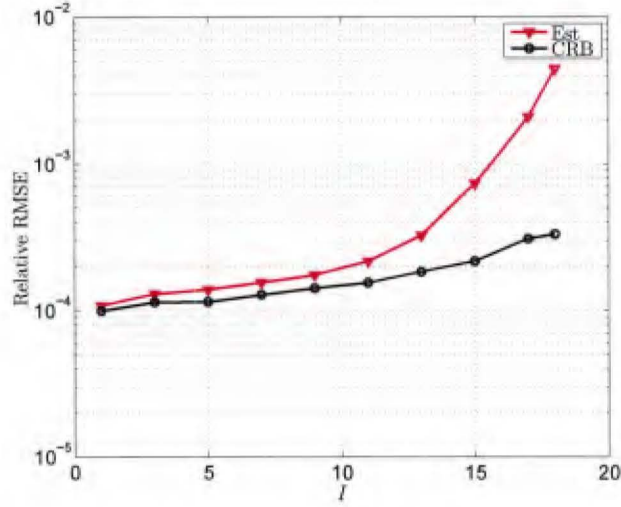


Fig. 10. Relative RMSE versus I (SNR=0 dB).

are $[0 \ 1 \ 2 \ 3 \ 7 \ 11 \ 15]$ and $[0 \ 1 \ 4 \ 10 \ 12 \ 15 \ 17]$, respectively. In this simulation, $p = 3$ coprime units are used to form the covariance matrix for the generalized coprime scheme, whereas the nested sampler and minimal sparse ruler based sampler each uses one unit as in [15] and [12]. Their relative RMSEs are depicted as a function of input SNR in Fig. 11, where $I = 5$ frequencies are considered. It is clear that the generalized coprime scheme outperform the other two sampling schemes due to the higher number of DOFs and improved resolution.

C. Relative RMSE for various p

In Figs. 12–14, we compare the performance corresponding to different choices of p under different criteria, where non-overlapping segmentation is used.

Figs. 12 and Fig. 13 examine the performance for different choices of p , based on the same compression factor, where $M = 3$ is assumed. In Fig. 12, the distinction on spectrum identifiability is depicted for the cases of $p = 10$ and $p = 45$. We consider $I = 100$ frequencies with $\delta_f = 2$ MHz separation in the presence of noise with a 0 dB SNR. It is evident that only the scenario of $p = 45$ can resolve all frequencies correctly, although in the case of $p = 10$ the number of DOFs $L - 1 = 114$, is slightly higher than the number of frequency components. Fig. 13 presents the RMSE and CRB with respect to p , where $I = 5$ is assumed. It is observed that the estimation performance is improved as p increases. In addition, the bias error between the estimated frequency and the CRB becomes smaller, since the ratio between the number of consecutive lags and the number of total lags in $\hat{\mathbf{R}}_{\tilde{\mathbf{y}}_{12}}$ increases with p . In summary, a

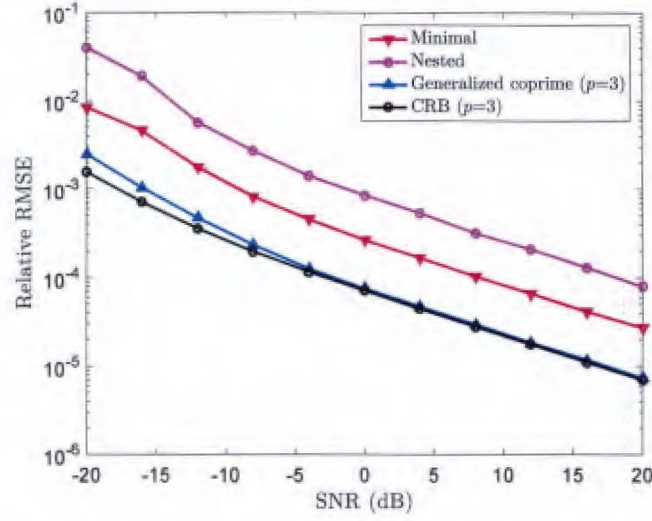


Fig. 11. Relative RMSE versus SNR for different sampling schemes ($I=5$).

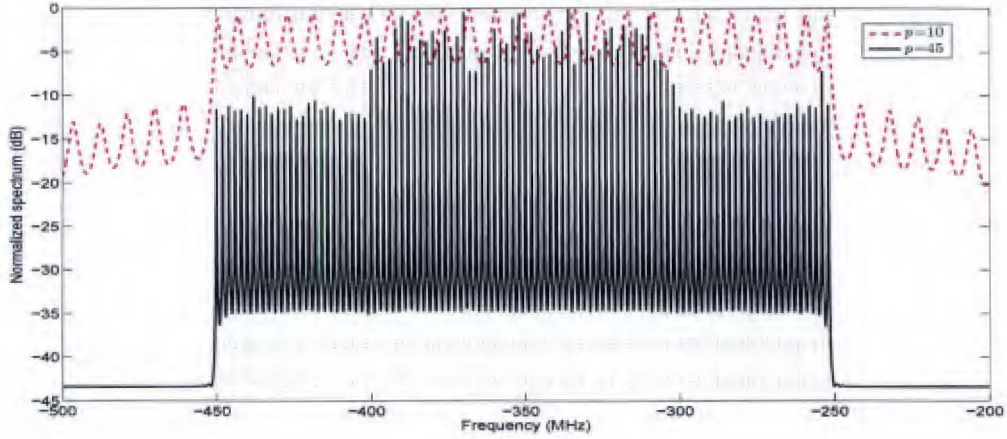


Fig. 12. Estimated spectra for the cases of $p = 10$ and $p = 45$ ($M = 3$ and input SNR=0 dB).

higher value of p can improve DOFs and spectrum estimation performance under the same compression factor. However, the requirement of storage space and the computational load become higher, due to the resulting higher value of L .

In Fig. 14, we present the relative RMSE as a function of the input SNR for different values of (p, M) pairs, where the dimension of the covariance matrix is $L = (p - 1)M^2 + (p + 1)M + 1 = 161$, and the number of frequencies is $I = 5$. It is clear that, as the value of M decreases (and so does the compression factor κ_{\max} because $\kappa_{\max} \propto M^2$), the estimated relative RMSE is reduced since a higher number of

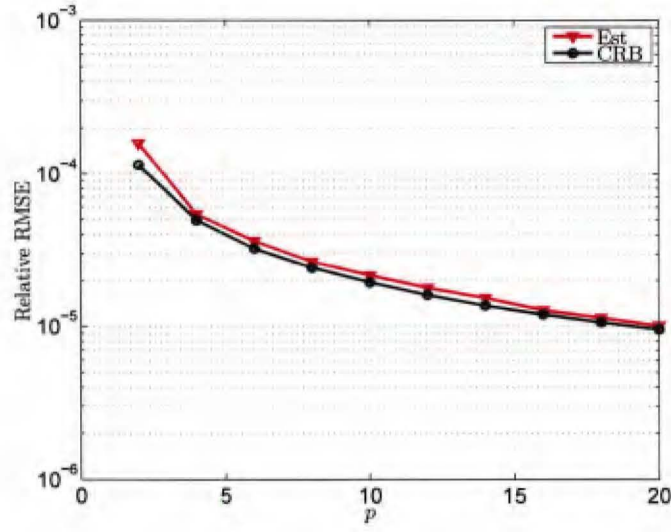


Fig. 13. Relative RMSE versus p , based on the same M ($I = 5$ and $M = 3$).

physical samples ($K_s = K(1/M + 1/(M + 1))$) can be used.

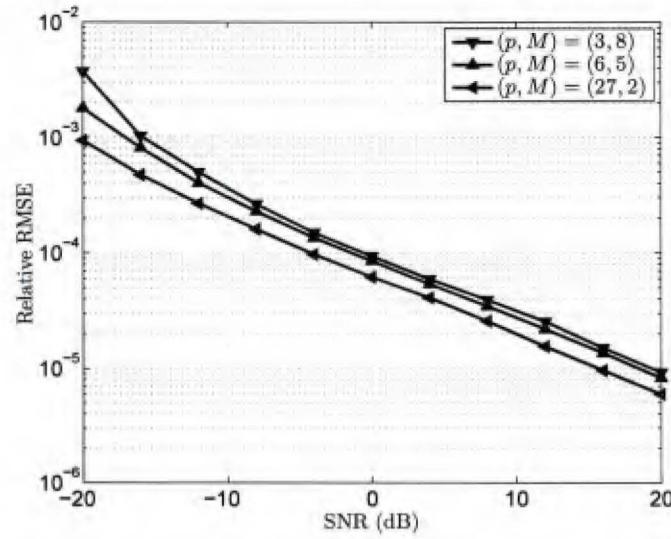


Fig. 14. Relative RMSE versus SNR, based on the same L ($I = 5$ and $L = 161$).

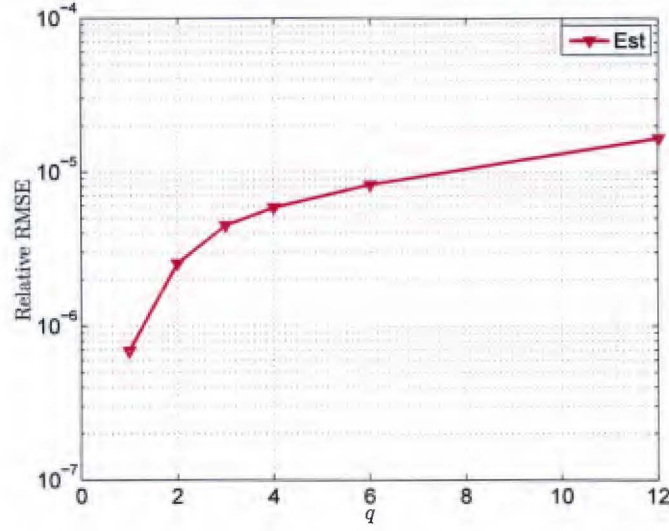


Fig. 15. Relative RMSE versus q ($M = 3$, $p = 12$, and $I = 5$).

D. Relative RMSE for various q

Finally, the advantage of utilization of overlapping blocks is demonstrated in Fig. 15, where $M = 3$ and $p = 12$ are assumed and $I = 5$ frequency is considered with a 0 dB SNR. In addition, q is chosen within the range of $\{1, 2, 3, 4, 6, 12\}$. It is evident that the estimation performance can be improved as q decreases, compared to the non-overlapping case, i.e., $q = p = 12$.

E. Relative RMSE versus K

In Fig. 16, we present the relative RMSE performance with respect to K , where $M=3$ is assumed, and $I=5$ frequencies with a 0 dB input SNR are considered. It is evident that the estimated relative RMSE performance is improved as K increases because a higher number of blocks is used to reduce the noise effect. Asymptotically, when K is large, the relative RMSE asymptotically decreases with a factor of $1/\sqrt{K}$. In addition, various cases with different values of p and q are compared in this figure. By assuming a large value of p and a small value of q , the generalized coprime sampling scheme improves the RMSE performance as it benefits from the high dimension of the reconstructed covariance matrix and the utilization of overlapping blocks, respectively.

F. Estimation for continuous spectrum

Finally, we consider an example of continuous spectrum signals in Fig. 17, where $x(t)$ is assumed to have continuous rectangular spectrum supports in $[-350, -230]$ MHz and $[150, 280]$ MHz. Multiple

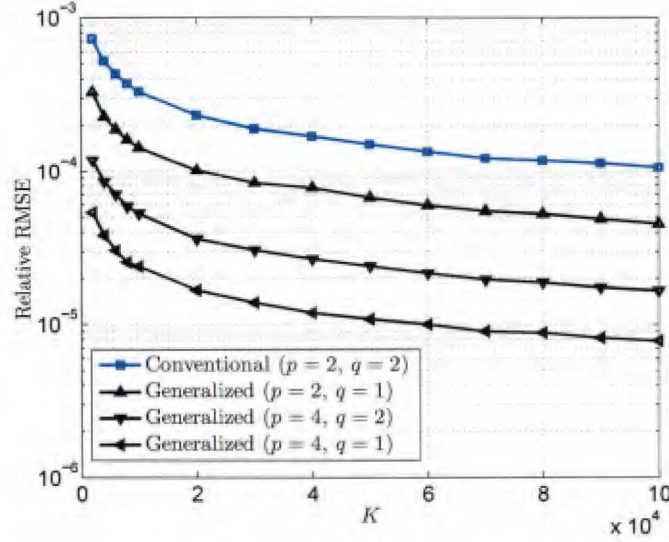


Fig. 16. Relative RMSE versus K ($M=3$ and $I=5$).

coprime unit factors of $p = 2, 3, 7$ are considered. As p increases, it is clear that the mainlobe becomes closer to the ideal signal bandwidth due to the larger dimension of the reconstructed matrix $\hat{\mathbf{R}}_{\mathbf{x}}$. For comparison, the case of $p = 7$ and $q = 1$ generally outperforms the case of $p = 7$ and $q = 7$ because a higher number of blocks, achieved by using overlapping segmentation, become available for averaging.

VI. CONCLUSIONS

We proposed an effective approach to compressively sample wide-sense stationary processes. The coprime sampling matrix was used to obtain a compressed representation for their second-order statistics. Using a fixed number of data, different schemes for the acquisition of a covariance matrix were presented, based on segmenting the data sequence. The performance of these schemes was compared and numerically evaluated. The effectiveness of the proposed technique was evidently verified using simulation results.

VII. APPENDIX

Proof of Proposition 1

For the convenience of presentation, we define the function $\Gamma([k_{1_{\min}}, k_{1_{\max}}], [k_{2_{\min}}, k_{2_{\max}}])$ as the operation $\pm(Mk_1 - Nk_2)$ with $k_1 \in [k_{1_{\min}}, k_{1_{\max}}]$ and $k_2 \in [k_{2_{\min}}, k_{2_{\max}}]$. Denote

$$\tilde{\mathbb{L}}_1 = \{\tau_1 | \Gamma([0, pN - 1], [0, M - 1])\}, \quad (42)$$

$$\tilde{\mathbb{L}}_2 = \{\tau_2 | \Gamma([0, N - 1], [0, pM - 1])\}, \quad (43)$$

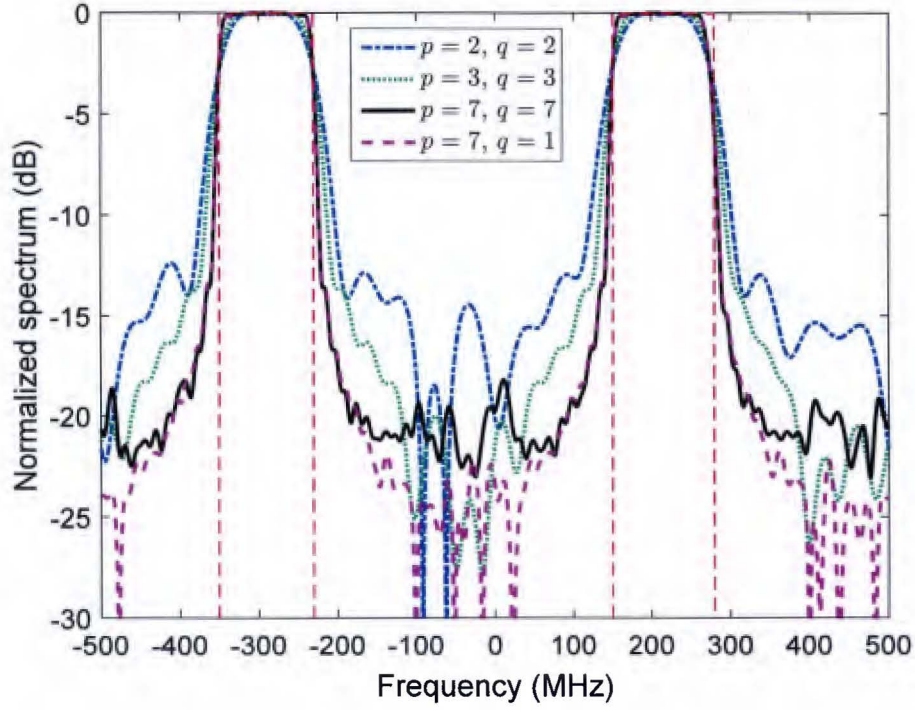


Fig. 17. Estimated spectrum.

and the proposition 1 can be obtained by proving the following propositions:

- 1(a) $\tilde{\mathbb{L}} = \tilde{\mathbb{L}}_1 \cup \tilde{\mathbb{L}}_2$.
- 1(b) For the set $\tilde{\mathbb{L}}_1$, it contains all integer lags in the range $-(p-1)MN - N + 1 \leq \tau_1 \leq (p-1)MN + N - 1$, and the “holes” are located at $\pm[(p-1)MN + aM + bN]$, where $a \geq 0$ and $b > 0$ are integers.
- 1(c) For the set $\tilde{\mathbb{L}}_2$, it contains all integer lags in the range $-(p-1)MN - M + 1 \leq \tau_2 \leq (p-1)MN + M - 1$, and the “holes” are located at $\pm[(p-1)MN + aM + bN]$, where $a > 0$ and $b \geq 0$ are integers.
- 1(d) The first pair of holes $\pm[p-1)MN + bN]$ in $\tilde{\mathbb{L}}_1$, where $b \geq 0$, can be aligned by the non-consecutive element in $\tilde{\mathbb{L}}_2$.

Proof of proposition 1(a): The lag set

$$\begin{aligned}
\tilde{\mathbb{L}} &= \{\Gamma([0, pN - 1], [0, pM - 1])\}, \\
&= \bigcup_{p_1=1}^p \{\Gamma([0, pN - 1], [(p_1 - 1)M, p_1M - 1])\} \cup \\
&\quad \bigcup_{p_2=1}^p \{\Gamma([(p_2 - 1)N, p_2N - 1], [0, pM - 1])\} \\
&= \tilde{\mathbb{L}}_1 \cup \left(\bigcup_{p_1=2}^p \{\Gamma([0, pN - 1], [(p_1 - 1)M, p_1M - 1])\} \right) \cup \\
&\quad \tilde{\mathbb{L}}_2 \cup \left(\bigcup_{p_2=2}^p \{\Gamma([(p_2 - 1)N, p_2N - 1], [0, pM - 1])\} \right). \tag{44}
\end{aligned}$$

Note that the union of the sets $\bigcup_{p_1=2}^p \{\Gamma([0, pN - 1], [(p_1 - 1)M, p_1M - 1])\}$ and $\bigcup_{p_2=2}^p \{\Gamma([(p_2 - 1)N, p_2N - 1], [0, pM - 1])\}$ is the subset of $\tilde{\mathbb{L}}_1 \cup \tilde{\mathbb{L}}_2$. Therefore, (44) can be simplified as

$$\tilde{\mathbb{L}} = \tilde{\mathbb{L}}_1 \cup \tilde{\mathbb{L}}_2. \tag{45}$$

Proof of proposition 1(b): Given any integer τ_1 satisfying

$$0 \leq \tau_1 \leq (p - 1)MN + N - 1, \tag{46}$$

we need to prove that there exist integers $k_1 \in [0, pN - 1]$ and $k_2 \in [0, M - 1]$ such that $\tau_1 = Mk_1 - Nk_2$ holds. The requirement $k_2 \in [0, M - 1]$ is equivalent to

$$0 \leq Nk_2 \leq MN - N. \tag{47}$$

Because $Mk_1 = \tau_1 + Nk_2$, we obtain the following relationship by combining (46) and (47),

$$0 \leq Mk_1 \leq pMN - 1 < pMN. \tag{48}$$

This result can be equivalently expressed as $0 \leq k_1 < pN$. Because k_1 is an integer, this requirement is equivalent to

$$0 \leq k_1 \leq pN - 1, \tag{49}$$

which is satisfied in the underlying coprime array configuration.

Next, we prove the hole positions by contradiction. We suppose $Mk_1 - Nk_2 = (p - 1)MN + aM + bN$ holds for some integers $k_1 \in [0, pN - 1]$ and $k_2 \in [0, M - 1]$, where $a \geq 0$ and $b > 0$ are integers, then relationship

$$\frac{M}{N} = \frac{k_2 - M + b}{k_1 - pN - a} \tag{50}$$

must be valid. From $k_1 \in [0, pN-1]$ and $a \geq 0$, we find $Mk_1 - Nk_2 = (p-1)MN + aM + bN < pMN$, and then $b < M$. As a result, $|k_2 - M + b| < M$. Due to the coprimality between M and N , we cannot find a k_1 to satisfy (50). Therefore, $Mk_1 - Nk_2 \neq (p-1)MN + aM + bN$, i.e., there are holes at $(p-1)MN + aM + bN$ in $\tilde{\mathbb{L}}_1$.

Due to the symmetry of $\tilde{\mathbb{L}}_1$, we can draw the conclusions that $\tilde{\mathbb{L}}_1$ all integer lags in the range $-(p-1)MN - N + 1 \leq \tau_1 \leq (p-1)MN + N - 1$, and the “holes” are located at $\pm[(p-1)MN + aM + bN]$, where $a \geq 0$ and $b > 0$ are integers.

Proof of proposition 1(c): We omit the proof of proposition 1(c), which can be proved by using the same method as in the proof of proposition 1(b).

Proof of proposition 1(d): Based on the proposition 1(b), there are holes $(p-1)MN + aM + bN$ in $\tilde{\mathbb{L}}_1$, where $a \geq 0$ and $b > 0$ are integers. If the holes are aligned by the elements in $\tilde{\mathbb{L}}_2$, the following relationship

$$(p-1)MN + aM + bN = \pm(Mk_1 - Nk_2) \quad (51)$$

must be valid for $k_1 \in [0, N-1]$ and $k_2 \in [0, pM-1]$. The requirement is equivalent to

$$(p-1)MN + aM + (b+k_2)N = Mk_1,$$

or

$$(p-1)MN + (a+k_1)M + bN = Nk_2,$$

i.e.,

$$b = -k_2, \quad \text{or} \quad a = -k_1. \quad (52)$$

It is only possible for $a = k_1 = 0$ when $k_1 \in [0, N-1]$, $k_2 \in [0, pM-1]$, $a \in [0, \infty)$, and $b \in (0, \infty)$. Then, the requirement further becomes

$$(p-1)M + b = k_2. \quad (53)$$

In the proof of proposition 1(b), it is shown that $b < M$, i.e., $b \leq M-1$. As such, $k_2 \in ((p-1)M, pM-1] \subseteq [0, pM-1]$. Therefore, the holes $(p-1)MN + bN$ ($a = 0$) in $\tilde{\mathbb{L}}_1$ are aligned by the element in $\tilde{\mathbb{L}}_2$ for some integers $k_2 \in [0, pM-1]$. As a result, the first hole outside the consecutive range of $\tilde{\mathbb{L}}$ becomes $(p-1)MN + M + N$. Then, the set $\tilde{\mathbb{L}}$ contains all integer lags in the range

$$-(p-1)MN - M - N + 1 \leq \tau \leq (p-1)MN + M + N - 1. \quad (54)$$

REFERENCES

- [1] S. Qin, Y. D. Zhang, and M. G. Amin, "High-resolution frequency estimation using generalized coprime sampling," in *Proc. SPIE Mobile, Multimedia/Image Process., Secur. Appl. Conf. (SPIE)*, Baltimore, MD, 2015, vol. 9497, pp. 94970K1–94970K7.
- [2] S. Qin, Y. D. Zhang, M. G. Amin, and A. M. Zoubir, "Generalized coprime sampling of Toeplitz matrices," in *Proc. IEEE Int. Conf. Acoust. Speech Signal Process. (ICASSP)*, Shanghai, China, 2016, pp. 4468–4472.
- [3] E. J. Candes, J. Romberg, and T. Tao, "Robust uncertainty principles: exact signal reconstruction from highly incomplete frequency information," *IEEE Trans. Inf. Theory*, vol. 52, no. 2, pp. 489–509, 2006.
- [4] D. L. Donoho, "Compressed sensing," *IEEE Trans. Inf. Theory*, vol. 52, no. 4, pp. 1289–1306, 2006.
- [5] J. A. Tropp and A. C. Gilbert, "Signal recovery from random measurements via orthogonal matching pursuit," *IEEE Trans. Inf. Theory*, vol. 53, no. 12, pp. 4655–4666, 2007.
- [6] R. Tibshirani, "Regression shrinkage and selection via the lasso," *J. R. Stat. Soc., Ser. B*, vol. 58, no. 1, pp. 267–288, 1996.
- [7] S. Ji, D. Dunson, and L. Carin, "Multitask compressive sensing," *IEEE Trans. Signal Process.*, vol. 57, no. 1, pp. 92–106, 2009.
- [8] Q. Wu, Y. D. Zhang, M. G. Amin, and B. Himed, "Multi-task Bayesian compressive sensing exploiting intra-task dependency," *IEEE Signal Process. Lett.*, vol. 22, no. 4, pp. 430–434, 2015.
- [9] G. Dasarathy, P. Shah, B. N. Bhaskar, and R. Nowak, "Sketching sparse matrices, covariances, and graphs via tensor products," *IEEE Trans. Inf. Theory*, vol. 61, no. 3, pp. 1373–1388, 2015.
- [10] Y. Chen, Y. Chi, and A. Goldsmith, "Exact and stable covariance estimation from quadratic sampling via convex programming," *IEEE Trans. Inf. Theory*, vol. 61, no. 7, pp. 4034–4059, 2015.
- [11] G. Leus and Z. Tian, "Recovering second-order statistics from compressive measurements," in *Proc. IEEE Int. Workshop on Comp. Adv. in Multi-Sensor Adaptive Process. (CAMSAP)*, San Juan, Puerto Rico, 2011, pp. 337–340.
- [12] D. D. Ariananda and G. Leus, "Compressive wideband power spectrum estimation," *IEEE Trans. Signal Process.*, vol. 60, no. 9, pp. 4775–4789, 2012.
- [13] D. Romero and G. Leus, "Compressive covariance sampling," in *Proc. Inf. Theory Appl. Workshop (ITA)*, San Diego, CA, 2013, pp. 1–8.
- [14] C. L. Nikias and J. M. Mendel, "Signal processing with higher-order spectra," *IEEE Signal Process. Mag.*, vol. 10, no. 3, pp. 10–37, 1993.
- [15] H. Qiao and P. Pal, "Generalized nested sampling for compression and exact recovery of symmetric Toeplitz matrices," in *Proc. IEEE Global Conf. Signal Inf. Process. (GlobalSIP)*, Atlanta, GA, 2014, pp. 443–447.
- [16] Z. Tian, Y. Tafesse, and B. M. Sadler, "Cyclic feature detection with sub-Nyquist sampling for wideband spectrum sensing," *IEEE J. Sel. Top. Signal Process.*, vol. 6, no. 1, pp. 58–69, 2012.

- [17] P. P. Vaidyanathan and P. Pal, "Sparse sensing with co-prime samplers and arrays," *IEEE Trans. Signal Process.*, vol. 59, no. 2, pp. 573–586, 2011.
- [18] P. Pal and P. P. Vaidyanathan, "Nested arrays: A novel approach to array processing with enhanced degrees of freedom," *IEEE Trans. Signal Process.*, vol. 58, no. 8, pp. 4167–4181, 2010.
- [19] M. A. Lexa, M. E. Davis, J. S. Thompson, and J. Nikolic, "Compressive power spectral density estimation," in *Proc. IEEE Int. Conf. Acoust. Speech Signal Process. (ICASSP)*, Prague, Czech Republic, 2011, pp. 3884–3887.
- [20] Y. L. Polo, Y. Wang, A. Pandharipande, and G. Leus, "Compressive wide-band spectrum sensing," in *Proc. IEEE Int. Conf. Acoust. Speech Signal Process. (ICASSP)*, Taipei, Taiwan, 2009, pp. 2337–2340.
- [21] D. D. Ariananda, G. Leus, and Z. Tian, "Multi-coset sampling for power spectrum blind sensing," in *Proc. Int. Conf. Digit. Signal Process. (DSP)*, Corfu, Greece, 2011, pp. 1–8.
- [22] P. D. Welch, "The use of fast Fourier transform for the estimation of power spectra: a method based on time-averaging over short, modified periodograms," *IEEE Trans. Audio Electroacoust.*, vol. 15, no. 2, pp. 70–73, 1967.
- [23] S. Qin, Y. D. Zhang, and M. G. Amin, "Generalized coprime array configurations for direction-of-arrival estimation," *IEEE Trans. Signal Process.*, vol. 63, no. 6, pp. 1377–1390, 2015.
- [24] Q. Zhao and B. M. Sadler, "A survey of dynamic spectrum access," *IEEE Signal Process. Mag.*, vol. 24, no. 3, pp. 79–89, 2007.
- [25] M. Mishali and Y. Eldar, "From theory to practice: Sub-Nyquist sampling of sparse wideband analog signals," *IEEE J. Sel. Top. Signal Process.*, vol. 4, no. 2, pp. 375–391, 2010.
- [26] R. Venkataramani and Y. Bresler, "Perfect reconstruction formulas and bound on aliasing error in sub-Nyquist nonuniform sampling of multiband signals," *IEEE Trans. Inf. Theory*, vol. 46, no. 6, pp. 2173–2183, 2000.
- [27] M. Mishali and Y. Eldar, "Blind multiband signal reconstruction: Compressed sensing for analog signals," *IEEE Trans. Signal Process.*, vol. 57, no. 3, pp. 993–1009, 2009.
- [28] H. Sun, W. Y. Chiu, J. Jiang, A. Nallanathan and H. V. Poor, "Wideband spectrum sensing with sub-Nyquist sampling in cognitive radios," *IEEE Trans. Signal Process.*, vol. 60, no. 11, pp. 6068–6073, 2012.
- [29] D. Cohen and Y. C. Eldar, "Sub-Nyquist sampling for power spectrum sensing in cognitive radios: A unified approach," *IEEE Trans. Signal Process.*, vol. 62, no. 15, pp. 3897–3910, 2014.
- [30] M. Shaghaghi and S. A. Vorobyov, "Finite-length and asymptotic analysis of averaged correlogram for undersampled data," *Appl. Comput. Harmon. Anal.*, <http://dx.doi.org/10.1016/j.acha.2016.02.001>.
- [31] K. Adhikari, J. R. Buck and K. E. Wage, "Extending coprime sensor arrays to achieve the peak side lobe height of a full uniform linear array," *EURASIP J. Wireless Commun. Netw.*, doi:10.1186/1687-6180-2014-148, 2014.
- [32] P. Stoica and A. Nehorai, "MUSIC, maximum likelihood, and Cramér-Rao bound," *IEEE Trans. Acoust. Speech Signal Process.*, vol. 37, no. 5, pp. 720–741, 1989.
- [33] P. Stoica and R. L. Moses, *Spectrum Analysis of Signals*, Upper Saddle River, NJ: Prentice-Hall, 2005.

- [34] R. Schmidt, "Multiple emitter location and signal parameter estimation," *IEEE Trans. Antennas Propag.*, vol. 34, no. 3, pp. 276–280, 1986.
- [35] R. Roy and T. Kailath, "ESPRIT – Estimation of signal parameters via rotation invariance techniques," *IEEE Trans. Acoust. Speech Signal Process.*, vol. 17, no. 7, pp. 984–995, 1989.
- [36] Y. Hua and T. K. Sarkar, "Matrix pencil method for estimating parameters of exponentially damped/undamped sinusoids in noise," *IEEE Trans. Acoust. Speech Signal Process.*, vol. 38, no. 5, pp. 814–824, 1990.
- [37] H. Akaike, "A new look at the statistical model identification," *IEEE Trans. Autom. Control*, vol. 19, no. 6, pp. 716–723, 1974.
- [38] M. Wax and T. Kailath, "Detection of signals by information theoretic criteria," *IEEE Trans. Acoust. Speech Signal Process.*, vol. 33, no. 2, pp. 387–392, 1985.
- [39] G. Schwarz, "Estimating the dimension of a model," *Ann. Statist.*, vol. 6, no. 2, pp. 461–464, 1978.
- [40] Z. Lu and A. M. Zoubir, "Generalized Bayesian information criterion for source enumeration in array processing," *IEEE Trans. Signal Process.*, vol. 61, no. 6, pp. 1470–1480, 2013.
- [41] Z. Lu and A. M. Zoubir, "Source enumeration in array processing using a two-step test," *IEEE Trans. Signal Process.*, vol. 63, no. 10, pp. 2718–2727, 2015.
- [42] L. Huang, Y. Xiao, K. Liu, H. C. So, and J.-K. Zhang, "Bayesian information criterion for source enumeration in large-scale adaptive antenna array," *IEEE Trans. Veh. Technol.*, vol. 65, no. 5, pp. 3018–3032, 2016.
- [43] K. Han and A. Nehorai, "Improved source number detection and direction estimation with nested arrays and ULAs using jackknifing," *IEEE Trans. Signal Process.*, vol. 61, no. 23, pp. 6118–6128, 2013.
- [44] C. D. Giurcaneanu, S. A. Razavi, and A. Liski, "Variable selection in linear regression: Several approaches based on normalized maximum likelihood," *Signal Process.*, vol. 91, no. 8, pp. 1671–1692, 2011.
- [45] L. Huang and H. C. So, "Source enumeration via MDL criterion based on linear shrinkage estimation of noise subspace covariance matrix," *IEEE Trans. Signal Process.*, vol. 61, no. 19, pp. 4806–4821, 2013.
- [46] H. L. Van Trees, *Optimum Array Processing: Part IV of Detection, Estimation, and Modulation Theory*. New York: Wiley, 2002.
- [47] P. Stoica and A. Nehorai, "Performance study of conditional and unconditional direction-of-arrival estimation," *IEEE Trans. Acoust. Speech Signal Process.*, vol. 38, no. 10, pp. 1783–1795, 1990.
- [48] M. Shaghghi and S. A. Vorobyov, "Cramer-Rao bound for sparse signals fitting the low-rank model with small number of parameters," *IEEE Signal Process. Lett.*, vol. 22, no. 9, pp. 1497–1501, 2015.
- [49] C.-L. Liu and P. P. Vaidyanathan, "Cramer-Rao bounds for coprime and other sparse arrays, which find more sources than sensors," *Digital Signal Process.*, doi: 10.1016/j.dsp.2016.04.011, 2016.
- [50] M. Wang and A. Nehorai, "Coarrays, MUSIC, and the Cramer-Rao bound," arXiv:1605.03620, 2016.
- [51] A. Koochakzadeh and P. Pal, "Cramer-Rao bounds for underdetermined source localization," *IEEE Signal Process. Lett.*, vol. 23, no. 7, pp. 919–923, 2016.

REPORT DOCUMENTATION PAGE				Form Approved OMB No. 0704-0188	
<p>The public reporting burden for this collection of information is estimated to average 1 hour per response, including the time for reviewing instructions, searching existing data sources, gathering and maintaining the data needed, and completing and reviewing the collection of information. Send comments regarding this burden estimate or any other aspect of this collection of information, including suggestions for reducing the burden, to Department of Defense, Washington Headquarters Services, Directorate for Information Operations and Reports (0704-0188), 1215 Jefferson Davis Highway, Suite 1204, Arlington, VA 22202-4302. Respondents should be aware that notwithstanding any other provision of law, no person shall be subject to any penalty for failing to comply with a collection of information if it does not display a currently valid OMB control number.</p> <p>PLEASE DO NOT RETURN YOUR FORM TO THE ABOVE ADDRESS.</p>					
1. REPORT DATE (DD-MM-YYYY) 10/03/2018		2. REPORT TYPE Final		3. DATES COVERED (From - To) 01-01-2013 - 31-12-2017	
4. TITLE AND SUBTITLE Co-Prime Frequency and Aperture Design for HF Surveillance, Wideband Radar Imaging, and Nonstationary Array Processing				5a. CONTRACT NUMBER	
				5b. GRANT NUMBER N00014-13-1-0061	
				5c. PROGRAM ELEMENT NUMBER	
6. AUTHOR(S) Amin, Moeness, G (PI), Ahmad, Fauzia (Co-PI), Zhang, Yimin, D (Co-PI)				5d. PROJECT NUMBER	
				5e. TASK NUMBER	
				5f. WORK UNIT NUMBER	
7. PERFORMING ORGANIZATION NAME(S) AND ADDRESS(ES) Villanova University 800 Lancaster Avenue, Villanova, PA 19085				8. PERFORMING ORGANIZATION REPORT NUMBER 527934	
9. SPONSORING/MONITORING AGENCY NAME(S) AND ADDRESS(ES) Office of Naval Research Code 331 875 North Randolph Street Arlington, VA 22203-1995				10. SPONSOR/MONITOR'S ACRONYM(S)	
				11. SPONSOR/MONITOR'S REPORT NUMBER(S)	
12. DISTRIBUTION/AVAILABILITY STATEMENT DISTRIBUTION STATEMENT A. Approved for public release. Distribution is unlimited.					
13. SUPPLEMENTARY NOTES					
14. ABSTRACT The research objectives are to develop novel co-prime sampling and array design strategies that achieve high-resolution estimation of spectral power distributions and signal direction-of-arrivals (DOAs), and their applications in various surveillance, radar imaging applications, and array processing. The focus of our studies has been in the following five areas: (i) Generalized co-prime array design; (ii) Wideband DOA estimation and radar sensing; (iii) Active sensing using co-prime arrays; (iv) Mutual coupling effect and mitigation; (v) Spectrum estimation based on co-prime sampling.					
15. SUBJECT TERMS Array signal processing, spectrum estimation, co-prime array, direction-of-arrival estimation, radar imaging					
16. SECURITY CLASSIFICATION OF:			17. LIMITATION OF ABSTRACT	18. NUMBER OF PAGES	19a. NAME OF RESPONSIBLE PERSON
a. REPORT	b. ABSTRACT	c. THIS PAGE			19b. TELEPHONE NUMBER (Include area code)
UU	UU	UU	UU	211	